UNIVERSITY OF CALIFORNIA,
IRVINE

Aqueous Ionic Photovoltaics from Photoacid-Sensitized Ion-Selective Polymers

DISSERTATION

Submitted in partial satisfaction of the requirements
for the degree of

DOCTOR OF PHILOSOPHY

in Chemistry

by

Christopher Douglas Sanborn

Dissertation Committee:
Assistant Professor Shane Ardo, Chair
Chancellor's Professor Reginald M. Penner
Associate Professor Matthew D. Law

2017

DEDICATION

To my family

for their unconditional love and unwavering support.

TABLE OF CONTENTS

List of Schemes

List of SI Schemes

List of Equations

List of SI Equations

List of Figures

List of SI Figures

List of Tables

List of SI Tables

List of common acronyms and abbreviations

AHA	commercial monopolar anion-exchange membrane (NEOSEPTA)
aq	aqueous
Ar	argon
ATR	attenuated total reflectance
b.p.	boiling point
Boc	tert-butyloxycarbonyl
bpy	2,2′-bipyridine
C	Carbon
C	Coulomb
$CDCl_3$	deuterated chloroform
cm	centimeter
CO_2	carbon dioxide
conc.	concentrated
cPFSA	perfluorosulfonic acid ionomer membrane containing covalently bound photoacids
Cu	copper

D	diffusion coefficient
d	doublet
DCM	dichloromethane
dd	doublet of doublets
DMF	dimethylformamide
DMSO	dimethyl sulfoxide
dt	doublet of triplets
E_a	activation energy
E_c	minimum energy of the effective electronic states near the bottom of the conduction band
EDA	ethylenediamine
EDC HCl	*N*-(3-dimethylaminopropyl)-*N*′-ethylcarbodiimide hydrochloride
E_g	electronic bandgap energy
E_{oc}	steady-state open-circuit potential across the membrane in the dark
Equiv.	equivalents

EtOH	ethanol
EV	electron volt
Ev	maximum energy of the effective electronic states near the top of the valence band
EW	equivalent weight
FTIR	Fourier-transform infrared spectroscopy
fwhm	full width half maximum
g	grams
GaAs	gallium arsenide
RO H_2O	reverse osmosis water
HMTA	hexamethylenetetramine
InGaP	indium gallium phosphide
iPFSA	ionomer membranes containing ionically associated photoacids
KCl	potassium chloride
kV	kilovolt
L	Liter

l_{diff}	maximum distance that minority charge-carrier hydroxides can diffuse to the space-charge region prior to recombination
M	molarity
m	multiplet
MeCN	acetonitrile
mequiv.	milliequivalents
MES	*N*-(2-aminoethyl)-4-methylbenzenesulfonamide
mM	millimolar
mmol	millimole
N	nitrogen
nA	nanoampere
NaOH	sodium hydroxide
N_c	effective electronic states near the bottom of the conduction band
N_v	effective electronic states near the top of the valence band
O	oxygen

p	pentet
P1	working electrode 1
P2	working electrode 2
Pd/C	palladium on carbon
PET	polyethylene terephthalate
PFSA	perfluorosulfonic acid ionomer membrane
PFSF	precast Nafion sulfonyl fluoride poly-(perfluorosulfonyl fluoride) membrane
q	elementary charge
q	quartet
r.t.	room temperature
RBF	round bottom flask
RE	reference electrode
RP-HPLC	reverse-phase high-performance liquid chromatography
s	seconds
s	singlet
S	sulfur

SCE	Saturated Calomel Electrodes
SD	standard deviation
$SOCl_2$	thionyl chloride
t	triplet
TEA	triethylamine
TFA	trifluoroacetic acid
TiO_2	titanium dioxide
Tosyl	4-toluenesulfonyl
Tris	2-amino-2-(hydroxymethyl)propane-1,3-diol
UV–Vis	Ultraviolet–Visible
V	Volts
V_{oc}	open-circuit photovoltage
WE	working electrode
Xe	xenon
XPS	X-ray photoelectron spectroscopy
μL	microliter
μmol	micromoles

Acknowledgments

Foremost, I want to thank Professor Shane Ardo for his tutelage, guidance, and friendship that was exceedingly responsible for my development as a scientist. Moreover, Shane has been one of my role models in life and I want to thank him for my personal development as well. Shane is altruistic, passionate about teaching, and tenacious about research. He has a genial, gregarious aura to him that makes him always pleasant to be around, and with this charisma, he is able to motivate and inspire. My favorite inspirational Shane-quote is, “It’s gotta work,” which was typically said after a very loquacious and informative discussion about how to perform an upcoming experiment. More often than not, it did work. And occasionally Shane would lend his hand in lab to help troubleshoot the experiments that did not work. This is just one-example of how Shane was always there for his students, and I could not image a better mentor to have.

As the first pupil in the Group, I witnessed the birth of a new research team and all its projects. Our successes and our happiness were due to the tremendous efforts that each member contributed. Henceforth, I would like to thank all past and current members of Team Ardo for their support. Together, we survived the tribulations of graduate school and for that, I am thankful.

I want to thank all the UCI faculty and staff that helped me along the way. I want to give a special thanks to Zuzanna Siwy and Alan Heyduk for allowing me to conduct research in their labs for an extended period, that occurred before the construction of the Ardo labs. I want to express additional gratitude to Dmitry Fishman and Jenu Chacko whom trained me in the field of photophysical science.

The most difficult challenge about my graduate life has been moving from coast to coast, leaving my family behind. I would like to thank everyone who has made me feel at home. I am most thankful for meeting Amy Babbush, who is now my fiancé. She has been a blessing in my life and has helped me keep my sanity throughout the years. I have been especially fond of our escapades, walking the dog, Harper, and having quaint picnics on the beach. Her fun-loving and free spirit has helped me appreciate the things outside of graduate school and helped me discover who I am. I am also thankful for her family, which has already accepted me into the fold. Randy and Suzanne Babbush, thank you for your generosity, kindness, and support; I am forever grateful for having a family away from home.

To my family at home, I am thankful their support and enduring compassion. I was fortunate to be raised by two loving parents who were able to instill the best in me, and to have siblings that drove friendly competition. Together, we learned to laugh, play, and seek adventure. No matter how far away from you, I will carry you in my heart.

Lastly, I want to thank my friends. Collectively, you have made me into a better person and kept a smile on my face. Cheers!

Curriculum Vitae

Contact: 240-925-8486 | cdsanbor@uci.edu

EDUCATION

Doctor of Philosophy | Chemistry December 2017
University of California, Irvine (UCI)
Irvine, California

Bachelor of Arts in Chemistry | Minor in Mathematics May 2012
St. Mary's College of Maryland
St. Mary's City, Maryland

TECHNICAL SKILLS

- Photoelectrochemistry: Four-electrode photoelectrochemical ion-transport measurements, Cyclic voltammetry, Chronopotentiometry, Chronoamperometry, Electrochemical impedance spectroscopy.
- Spectroscopy/Spectrometry: 1-Dimensional NMR and 2-Dimensional NMR, FTIR-ATR, UV-VIS, Photoluminescence, Single-photon fluorescence microscopy, Two-photon fluorescence microscopy, X-ray fluorescence, X-ray diffraction, Mass spectrometry, Scanning electron microscopy, Energy-dispersive x-ray spectroscopy, Raman.
- Schlenk-line and glove-box techniques.
- Controlled synthesis of organic molecules under inert conditions.
- Chromatography: Gas, Liquid, RP-HPLC, TLC.
- Additional techniques: Bomb calorimetry, Differential scanning calorimetry, Polarimetry.

RESEARCH AND PROFESSIONAL EXPERIENCE

PTD Module and Integration Device Yield Engineer
Intel, Hillsboro, OR 2018

- Lead scientific research enabling manufacture of innovative device architectures.
- Design, execute, analyze experiments necessary to meet engineering specifications for their process.

Research Assistant, PhD Candidate
Professor Shane Ardo Group, UCI 2013–2017

- Synthesized and characterized new visible-light-absorbing photoacid dye molecules.
- Developed, characterized, and evaluated the performance of artificial light-driven proton pumps that utilized the aforementioned photoacid dyes.
- Developed novel bipolar electrochemical techniques to evaluate the photocatalytic properties of single semiconductor nanoparticles wetted by electrolyte.

Engineering Technician
Naval Air Systems Command, Patuxent River 2009–2012

- Researched and developed corrosion resistant primers based on non-passivating metallic pigments for the United States Navy.

- Synthesized coating additives such as self-healing agents, for their incorporation into galvanic sacrificial coatings.
- Developed anodizing methods for the electrolytic passivation of steel and aluminum alloys.
- Analyzed the performance of hexavalent-chromium-free passivation techniques.
- Conducted coating weathering experiments for both non-military and military corporations.

Research Assistant
Professor Andrew Koch Group, St. Mary's College of Maryland 2009 – 2012

- Explored new methodologies employing polyvalent iodonium compounds. Used polyvalent iodonium compounds as oxidizing agents, catalysts for organoiodine applications, and recyclable reagents.
- Utilized an array of hypervalent aromatic iodonium compounds to incorporate nucleophiles onto aromatic and heteroaromatic compounds (via a reductive elimination pathway).

Research Assistant
St. Mary's Project, St. Mary's College of Maryland 2011– 2012

- Developed syntheses for the incorporation of nucleophiles onto nitrogenous bases utilizing polyvalent iodonium reagents.

PUBLICATIONS, PATENTS, PRESENTATIONS

Peer-Reviewed Publications

Sanborn, C.;# Tkacz, K.;# Ardo, S. "Photoelectrochemical measurements on several TiO_2 nanoparticles permanently affixed in conical nanopores in poly(ethylene terephthalate)." *Research in progress*. (# Co-first author)

Sanborn, C.; Ardo, S. "Optimal carbodiimide conditions for the coupling of amines to polyethylene terephthalate nanopores." *Research in progress*.

Sanborn, C.; Chacko, J. V.; Ardo, S. "Pyrenol Photoacids Covalently Bound to Polymer Nanopores as Models for Light-Driven Proton Pumps: Observation of Undesired Decrease in Acidity of the Excited-State" *J. Am. Chem. Soc. To be submitted shortly*.

White, W.; **Sanborn, C.**; Fabian, D.; Ardo, S. "Conversion of Visible-Light to Ionic Power Using Photoacid-Dye-Sensitized Bipolar Ion-Exchange Membranes." *Joule,* 2017, http://dx.doi.org/10.1016/j.joule.2017.10.015.

White, W.;# **Sanborn, C.**;# Reiter, R.; Fabian, D.; Ardo, S. "Observation of Photovoltaic Action from Photoacid-Modified Nafion Due to Light-Driven Ion Transport" *J. Am. Chem. Soc.,* 2017, 139, 34, 11726-11733. (# Co-first author)

Sanborn, C.; Koch, A. S.; DiMagno S. Hypervalent Iodine Reagents for Nucleophilic Addition to Aromatic Amines. Bachelor's Thesis, St. Mary's College of Maryland, St. Mary's City, MD, 2012.

Patents

White, W; **Sanborn, C.**; Cardon, J.; Ardo, S. Light-Driven Ion-Pumping Membrane Systems. U. S. Provisional Patent 62,384,503, Sep 07, 2016.

Oral Presentations

Sanborn, C.; Ardo, S. "Alteration of photoacidic behavior of pyrenol dyes covalently bound in the nanoconfined, electrostatically-complicated tips of asymmetric nanopores" American Chemical Society National Meeting, San Francisco, CA, April 3, 2017.

Sanborn, C.; Ardo, S. "Visible light-driven proton pumps utilizing photoacid molecules in polymeric nanopore scaffolds" American Chemical Society National Meeting, San Diego, CA, March 13, 2016.

Sanborn, C.; Ardo, S. "Artificial light-driven proton pump." Southern California Inorganic Photochemistry Symposium, Catalina Island, CA, September 4, 2014.

Sanborn, C.; Ardo, S. "Enhancing the lifetime of excited-state proton transfer reactions using electric fields: Toward a light-driven proton pump." Southern California Inorganic Photochemistry Symposium, Catalina Island, CA, September 4, 2013.

Poster Presentations

Sanborn, C.; Koch, A. S.; DiMagno S. "Asymmetric Triaryl Iodonium Compounds." American Chemical Society National Meeting, Anaheim, CA, March 28, 2011.

TEACHING, LEADERSHIP, AND OUTREACH EXPERIENCE

Laboratory Safety Officer	UCI, Ardo laboratory	2013 – present
Mentor for Undergraduate Researchers*	UCI, Ardo laboratory	2014 – present
Volunteer Organic Chemistry Tutor	UCI	2012 – present
Tech-trek Outreach	UCI	2012 – present
LEAPS Outreach	UCI	2012 – present
ESCAPE Outreach	UCI	2012 – present
Organic Chemistry Teaching Assistant	UCI	2012 – 2015
Inorganic Seminar Committee Member	UCI, Ardo laboratory	2013
Solar Decathlon Program Promoter	UCI, Ardo laboratory	2013
Organic Chemistry Teaching Assistant	St. Mary's College of Maryland	2011 – 2012
Lead Research Assistant	St. Mary's College, Koch laboratory	2011 – 2012
Volunteer Organic Chemistry Tutor	St. Mary's College of Maryland	2009 – 2012
Youth Group Leader	First Saints Community Church	2008 – 2012
Repaired homes for low-income families	Appalachia Service Project	2004 – 2012
Repaired homes for low-income families	SoMD Rebuilding Together	2004 – 2012

Abstract of the dissertation.

Aqueous Ionic Photovoltaics from Photoacid-Sensitized Ion-Selective Polymers

By

Christopher Douglas Sanborn

Doctor of Philosophy in Chemistry

University of California, Irvine, 2017

Professor Shane Ardo, Chair

This Thesis provides the seminal work towards the development of new technologies for ionic power generation and solar saltwater desalination. Central to the approach is the transformation of optically-inactive ion-exchange membranes used in electrochemical technologies into optically-active power-producing membranes.

Chapter 1 provides a brief description of anthropogenic emissions and human induced global warming and climate change. It is desired that these human induced calamities can be mitigated by replacing fossil fuel energies with solar energy conversion technologies.

Chapter 2 presents studies on a model system of optically-active membranes. Included is the synthesis of an exemplary visible-light absorbing photoacid dye and its covalent attachment to a nanoporous membrane. Basic materials characterization and more specialized photophysical techniques were used to characterize the dyes dissolved in solution and the dyes covalently bound to membranes. The study suggests that ion

transport initiated by photoacids bonded to mesoporous materials will require careful molecular engineering to enable efficient light-to-ionic energy conversion.

Chapter 3 shows the first demonstration of photovoltaic action from a covalently sensitized ion-exchange membrane. Photoelectrochemical measurements quantified the photocurrent and photovoltage production and control studies suggested that the power production is a result of photo-generated ions produced from the photoacid dye. Results were consistent with protons being transported against a pH gradient opposite to the thermodynamically favored direction; albeit, no net power was generated because of a rapid and continuous ion crossover across the membrane due to use of a single monopolar ion-exchange membrane with a large pH gradient across it.

The arrangement of these optically-active cation-exchange membranes adjacent to anion-exchange membranes is the focus of Chapter 4. The bipolar membranes showed enhanced photovoltaic efficiencies as compared to the monolithic counterpart and analogies from the physics of solar cells was used to elucidate the mechanism of photovoltaic action. The obtained photovoltages are more than half that needed to desalinate the sodium chloride in sea water to potable water and all that needed to convert moderately saline brackish water to potable water.

The Thesis concludes with Chapter 5, which presents the ongoing solar-energy conversion optimization tactics for these devices.

Chapter 1. Introduction.

Chapter 1.1. Anthropogenic energy consumption.

The total energy consumption of the World from 2016 to 2017 was reported to be 575×10^{15} British thermal units,[1] which equates to 19.2 terawatts of power. The world energy consumption has projected to increase by an average rate of ~1.1% per year until 2040, with more than half of the energy consumption attributed to the increasingly prosperous economies of China and India.[2,3] Regardless of source, the total power consumption of 2040 would be approximately 24.7 terawatts. Twenty-four terawatts of electricity could power $\sim 1 \times 10^{12}$ 25-watt light emitting diodes (LED) each operating at 3000 lumens for a total output of $\sim 3 \times 10^{15}$ lumens. These values are miniscule with respect to the solar energy or solar radiance absorbed by the surface of the Earth. On average, the surface of the Earth absorbs 164 watts of solar radiation per cubic meter per day.[4] The surface area of Earth is $\sim 5 \times 10^{14}$ cubic meters and so in a given year the surface absorbs $\sim 3 \times 10^{19}$ watts of solar radiation. This is 1.6 million times greater than the projected energy consumption. In terms of brightness, the equivalent amount of lumens absorbed by the surface of the Earth is $\sim 3 \times 10^{21}$ because solar radiation has a luminous efficacy of 93 lumens per watt.[5] Therefore, the amount of solar radiation prior to absorption would be about 1 million times brighter than the $\sim 1 \times 10^{12}$ 25-watt LEDs.

The yearly anthropogenic energy demand could be met within less than an hour if all the sunlight reaching the surface of the Earth was converted into useable energy.[6] Albeit, solar energy provides $< 1\%$ of the global consumption needs in 2017 and the bulk

of the energy demand is met by non-renewables, particular fossil fuels.[7] The high consumption of fossil fuels has been common practice for the United States (Figure 1.1).[8] In general, ~80% of the total primary energy consumption has been from the burning of fossil fuels. And as of 2017, fossil fuels account for ~81% of the primary energy consumed, where the percent of coal, natural gas, petroleum consumed are 14, 29, 37, respectively.[8] Only within the last 20 years did the usage of renewable energy sources, such as biomass, hydroelectric, wind, solar, and geothermal, begin to increase.

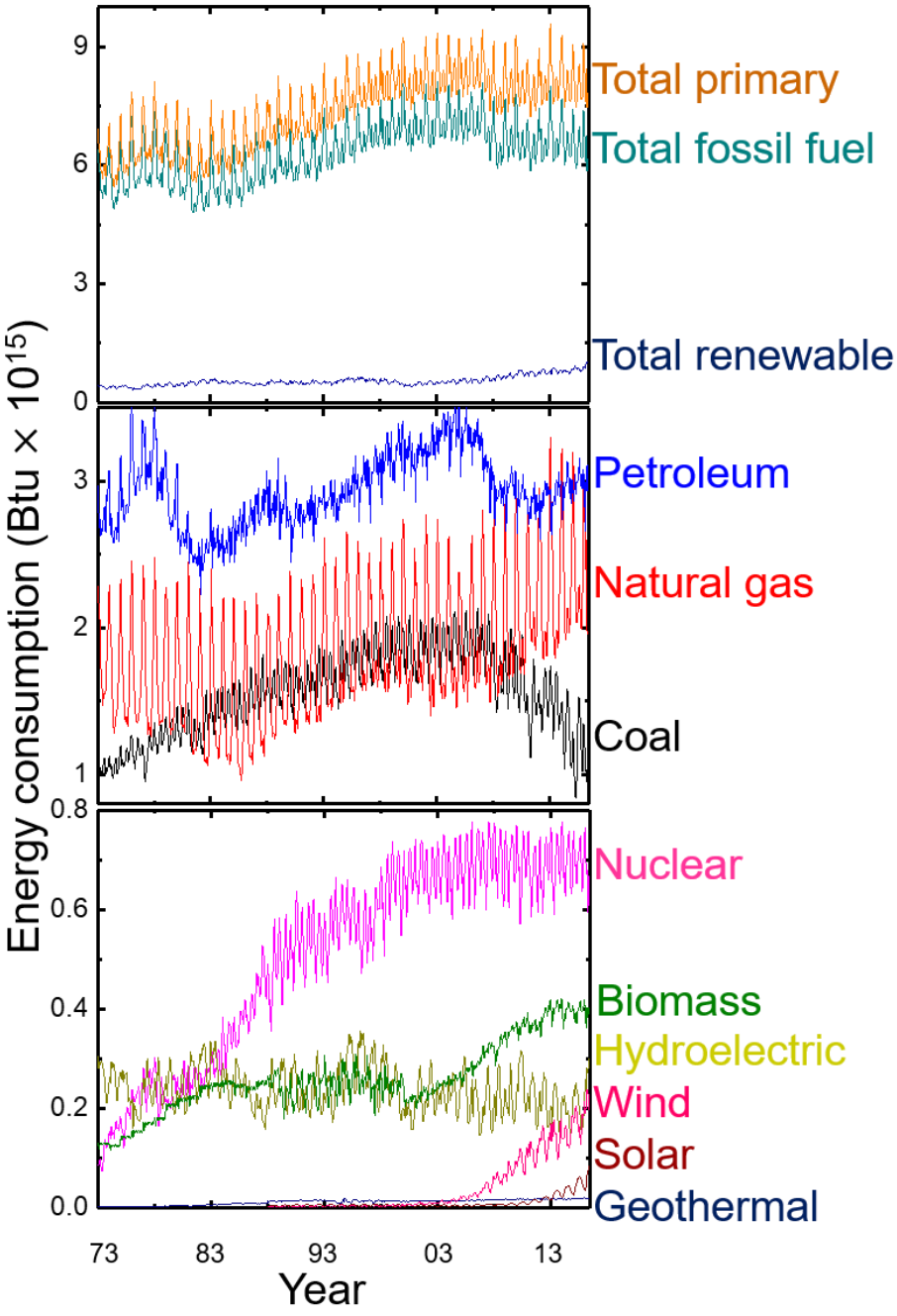

Figure 1.1. Energy consumption timeline depicted for United States.[8]

Derivatives of Figure 1.1 are shown in Figure 1.2. This shows that the rate of renewable energy consumption has increased at a rate of ~0.3 quadrillion Btu a year from 2010 to 2016, and solar energy consumption grew ~0.09 quadrillion Btu within the last year. Additionally, the rate of non-renewable energy consumption has been in decline

since 2005, while the consumption of all primary energy sources has levelized. This suggests that renewable green energy sources are replacing non-renewable energy sources.

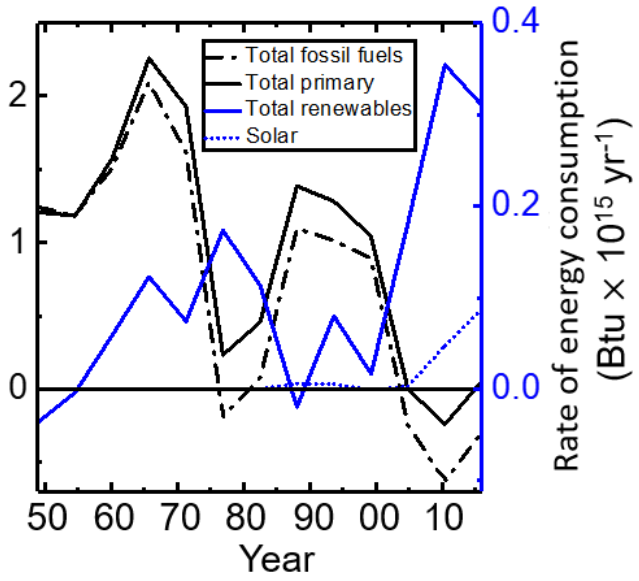

Figure 1.2. Rate of consumption of primary energy sources in the United States.

Chapter 1.2. Anthropogenic carbon dioxide emissions.

Energy security is particularly important as certain non-renewable energy sources become scarcer. For example, the total global reserves and resource base of oil, natural gas, and fossil fuels are predicted to deplete in 50-150 years, 60-160 years, and 1000-2000 years.[8] Not only does substituting non-renewable energy sources with renewable energy sources promote energy security, but it also advances national security, economic security, and most importantly, environmental security.[6] Greater than 97% of publishing climate scientists have reached the following census on the cause of global warming,[9–12]

humans are the cause. Scientists have statistically quantified that anthropogenic emissions are the cause of global warming and climate change to a 95-100% certainty.[13] Briefly, anthropogenic emissions perturbed the equilibrium of the carbon cycle and it is this perturbation that is the main driving force behind global climate change.[14–16] Global climate changes include the global temperature increase, rising sea levels, ocean acidification, and worsening of extreme weather intensities.[14–16] The health, environmental, and climate benefits of switching to green alternative energies has been monetarily quantified to be $10/MWh to $100/MWh.[17] If the energy demand of the all humans were met in the beginning of 2017 via green sources, then the global savings would mass to ~$1.6 trillion to $16 trillion dollars by the end of the year. This is due to the mitigation of CO_2, fugitive methane emissions, sulfur dioxide, nitrous oxides, and particle pollution.

Under natural conditions, carbon dioxide (CO_2) is beneficial to supporting life. Without it, life as we know it would not exist. For example, photosynthesis would cease, and free oxygen production would halt. Therefore, all photosynthetic and respiratory-relying organisms would perish. Carbon dioxide is also responsible for keeping the planet warm; without it, the temperature at the surface of the Earth would be -18 °C.[18] As of 2017, the concentration of CO_2 is 403 ppm, whereas for the last 800,000 years the concentration hovered between ~200 ppm and 250 ppm (Figure 1.3). This suggests that the concentration of CO_2 has almost doubled its natural values. Under natural conditions, the CO_2 concentration is related to the temperature fluctuates through changes in the orbit of the Earth. The orbit of the Earth changes in eccentricity, obliquity, and precession throughout 100,000-year cycles (Milankovitch cycle). Therefore the Earth experiences

long term changes in incident solar radiation at different seasons.[19] The change in incident solar radiation is also a function of longitude and latitude. Warming cycles occur when high latitudes receive more incident sunlight. This causes cascade of effects. Ice melts, oceans flood with the melted, unsalted ice water, oceanic currents are perturbed such that the distribution of heat among the hemispheres changes,[20] forcing a change in the solubility of CO_2 in the oceans of the Southern Hemisphere,[21] that results in emission of the CO_2 into the atmosphere of the Southern Hemisphere,[22] and the emitted CO_2 mixes into the Northern Hemisphere.[23] Lastly, the emission of CO_2 amplifies the original heating associated with the change in orbital cycles by ~90%, but there is a ~1,000 year delay associated with this temperature increase.[24]

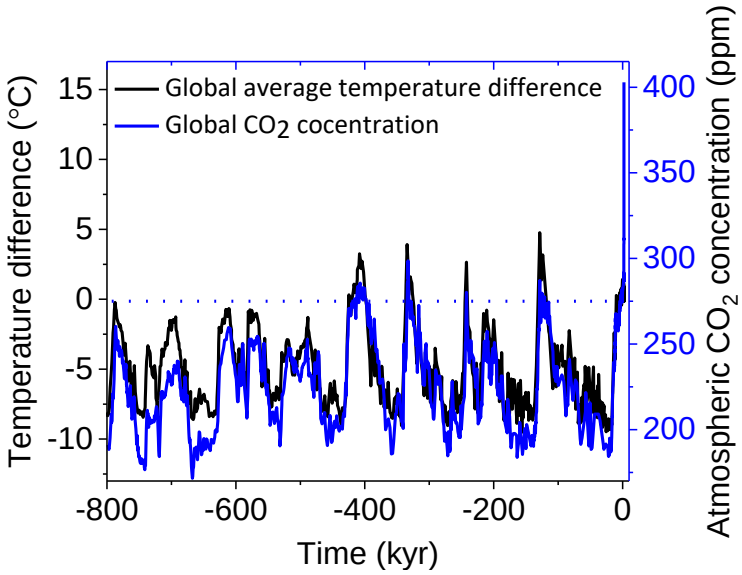

Figure 1.3. Global temperature difference with respect to the global temperature in 1850 (common era), and the atmospheric CO_2 concentration from the year 800,000 (before common era) to 2016 (common era). Reproduce with permission from © 2008 Nature Publishing Group. Lüthi, D.; Floch, M. L.; Bereiter, B.; Blunier, T.; Barnola, J. M.; Siegenthaler, U.; Raynaud, D.; Jouzel, J.; Fischer, H.; Kawamura, K.; Stocker, T. F. *Nature*. **2008**. 453, 379-382.[25]

Chapter 1.3. Forcing elements.

The temperature change as a function of CO_2 has followed the same natural trend from 800,000 BCE to ~1849 (Figure 1.4). However, beginning from 1850 CE, a new trend was set correlating to anthropogenic emission. The two trends are different because CO_2 is just a single component of an ensemble of effects that affect temperature changes. The ensemble of effects is a summation of forcing factors.[26] An ensemble of forcing factors and their effect on temperature change from the years of 2000 to 2012 are presented in Figure

1.4b. Greenhouses gases include carbon dioxide, methane, 1,1-difluoroethane, nitrous oxide, tetrafluoromethane, and sulfur hexafluoride. These gases combined with tropospheric ozone, solar, volcanic activity, and stratospheric water vapor would contribute to a ~1.8 °C increase if not counteracted by the ~0.9 °C decrease from the cumulative forcing of black and organic carbon, stratospheric ozone, direct aerosols, and indirect aerosols. The individual forcing elements were also categorized by their origins. Natural emissions contributed to a ~0.2 °C increase, whereas anthropogenic emissions contributed to a ~0.6 °C increase, that is, humans caused ~80% of the observed global warming.

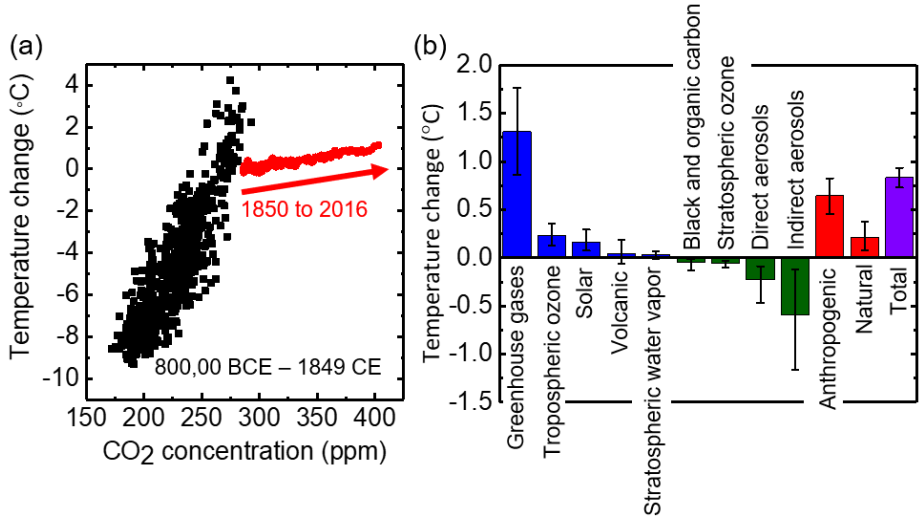

Figure 1.4. (a) Temperature change with respect to 1850 CE versus CO2 concentration.[25] (b) Individual forcing agents and the influence on the temperature change from 2000 CE to 2012 CE with respect to 1850 CE. Panel b reproduced with permission from © 2011 Macmillan Publishers Limited. Huber, M.; Knutti. *Nature Geoscience*. **2012**, 5, 31-36.[27]

The measured temperature anomaly from the years 1850 to 2016 is presented in Figure 1.5. The individual contributions of natural and anthropogenic forcing elements were calculated, and the total of the individual contributions coincided with the measured temperature changes. Shown across these presented 160 years, anthropogenic elements have been the primary constituent of the temperature increase.

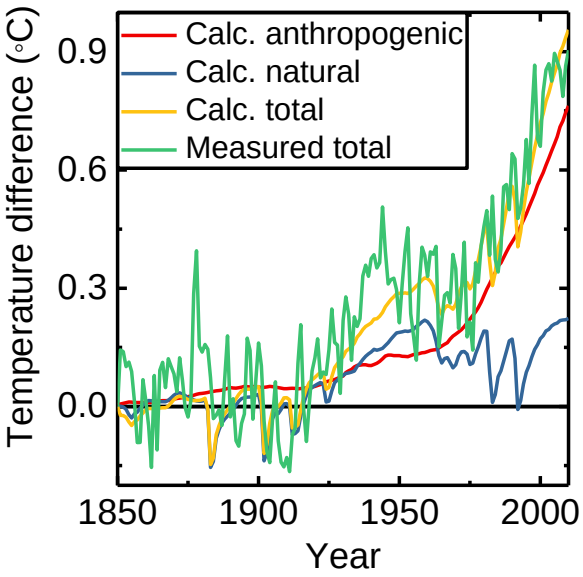

Figure 1.5. Global temperature anomaly with respect to 1850 to 2010. Reproduced with permission from © 2011 Macmillan Publishers Limited. Huber, M.; Knutti. *Nature Geoscience*. **2012**, 5, 31-36.[27]

It is important to realize the full forcing effect that CO_2 has on temperature has not been experienced yet. This is because the Earth has not reached a new point of equilibrium.[18] Predictions of the change in temperature once the new equilibrium is reached are generally consistent with temperature increases of 2 °C to 4.5 °C by 2100.[18]

At which, it is with high certainty that the temperature increase will cause severe, global, and irreversible impacts.[28] One way to mitigate further temperature increases is to reduce greenhouse gas emission. In 2017, ~1.9×10^{10} tonnes of CO_2 equivalent emissions were released into the air by the United States. This was calculated by multiplying the energy which the United States consumes in 2017 (Figure 1.1) by the pollution emitted during power consumption; these numbers[29] are in the parenthesis of Figure 1.6. Moreover, the percent of CO_2 equivalent emissions released by the consumption of fossil fuel sources in the United States is slightly greater than 99% of the total CO_2 equivalent emissions. This stresses alternative, green energy technologies need to make strong headway to replace the CO_2 emission culprits.

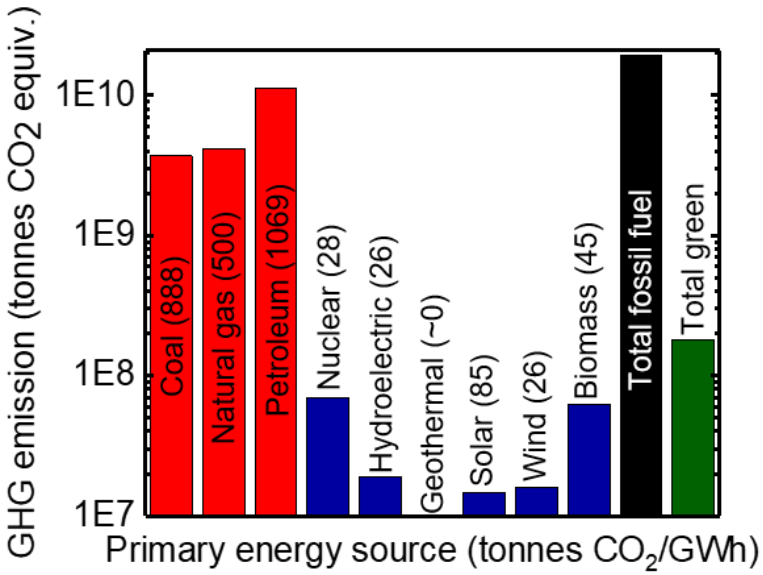

Figure 1.6. Greenhouse gas emissions generated by the consumption of primary energy sources in the United States in 2016. Tonnes CO_2/Gwh reported by World Nuclear Association.[29]

Chapter 1.4. Solar power.

Installing commercially available solar cells with ~14% efficiencies across approximately 20% of Nevada could power the United States.[30] Likewise, the energy demand of the planet could be met with solar cells that have a ~9% conversion efficiency covering a total area of ~910,000 km^2 focused in deserts with high incident irradiances (> 260 W/m^2). Figure 1.7 displays such optimal locations in North America (Great Basin), South America (Atacama), Africa (Sahara), Middle-East (Arabian), China (Takla Makan), and Australia (Great Sandy). This map could become a reality in part to SunShot Initiative and like-minded enterprises.

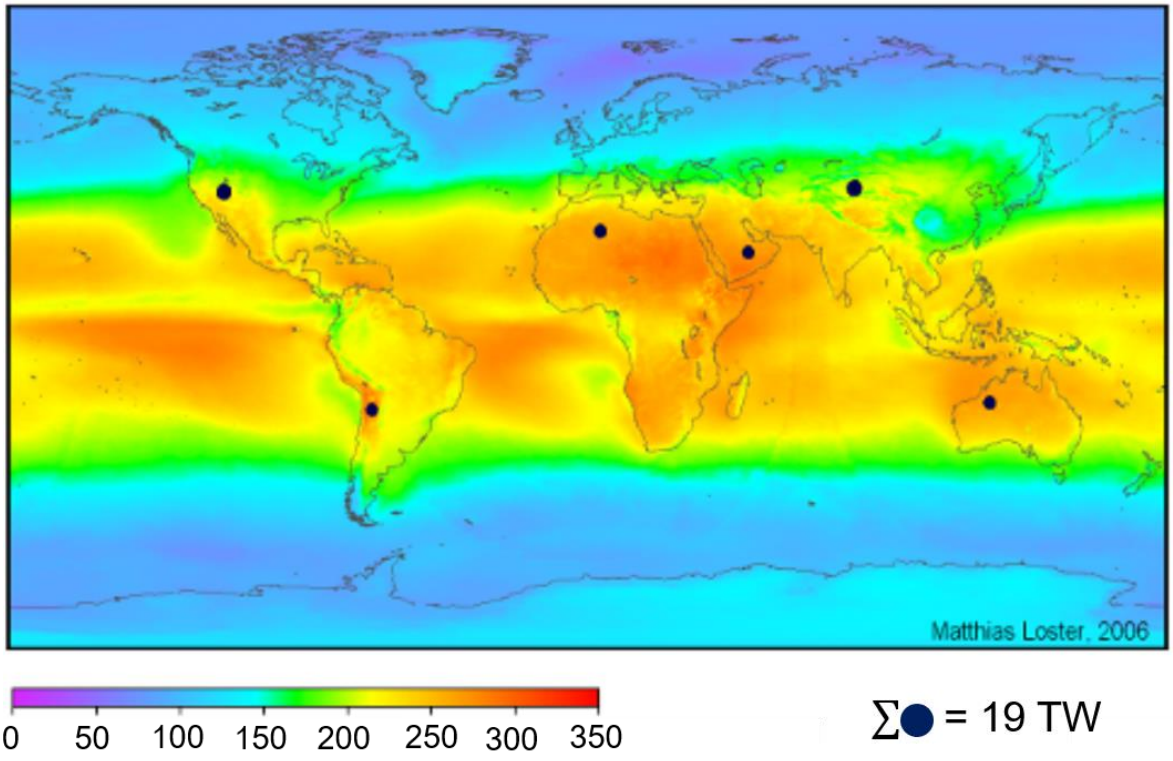

Figure 1.7. Sunlight hitting blue circles could provide enough power for the entire world. Colors show a three-year average of solar irradiance, including night and cloud coverage.[31]

The United States Department of Energy (DOE) launched the SunShot Initiative in 2011 with the mission of reducing the cost of solar-produced electricity to that of conventionally generated electricity by 2020 via research and development efforts.[32] The Initiative achieved its goal three years early announcing in September of 2017 that the average price of utility-scale solar power decreased to $0.06 per kilowatt hour (kWh) without price adjustments from feed-in tariffs.[32] The Initiative now seeks to reach half of this price by 2030 upon which a utility-scale solar facility would cost less than most fossil fuel power plants.[32] Moreover, the Initiative will address grid reliability, resilience, and storage issues making utility-scale facilities more practical in the future.[32]

Utility-scale facilities may not be as essential if photovoltaics were integrated into commercial and residential settings. Photovoltaics can be integrated into rooftops, facades, awnings, and windows.[33] This strategy utilizes on-site electricity generation and utilization which reduces electrical transmission losses and the need for utility-scale energy storages. Importantly, residential photovoltaics produce electricity at approximately $0.09 per kilowatt hour (kWh), which is about the same as the direct coast of coal.[32] In 2015, installing a residential solar system with an output of 3 - 9 kW would cost $15,000 - $40,000.[34] The total cost of solar cell is broken down into material costs, labor, permits and inspection fees, and operational costs. The cost of material consists of the photovoltaic panel and all other components, known as balance of systems, and their percent of the overall cost is 30 and 20, respectively.[34] The balance of system includes the wiring, switches, mounting system, DC to AC converter, battery bank, and a battery charger. The labor costs and permit and inspection fees contribute equal to the price, both at 15% of the total costs.[34] About 20% of the costs are from operational sources such as

maintenance, repairs, insurance, and overhead.[34] Research and development decreased the material costs considerably with increases in solar cell efficiencies, better fabrication processes, and use of more economical materials.

Specifically, solar photovoltaics have made huge strides since Bell Telephone Laboratories introduced the first practical solar cell in 1954.[35] From its debut to today, the single-junction solar cell efficiency increased from 6% to 28.8%.[36] The theoretical maximum efficiency of a single-junction solar cell is ~34%, as described by the detailed balance radiative limit.[37] Therefore, the most efficient single-junction solar cell of today is 85% of its theoretical maximum value. The bounds of the theoretical maximum efficiency are extended by layering multiple junctions in tandem. For example, the maximum theoretical efficiencies of two-, three-, and infinity-junction cells are 42%, 49%, and 68%, respectiviley.[38] Figure 1.8 displays the world-record efficiencies of various kinds of solar cells dating back to 1975. Included are a variety of cells using semiconductor materials such as silicon (Si), gallium arsenide (GaAs), cadmium telluride (CdTe), and copper indium gallium selenide (CIGS). Emerging technologies include organic and inorganic dye molecules, perovskites, and quantum dots.

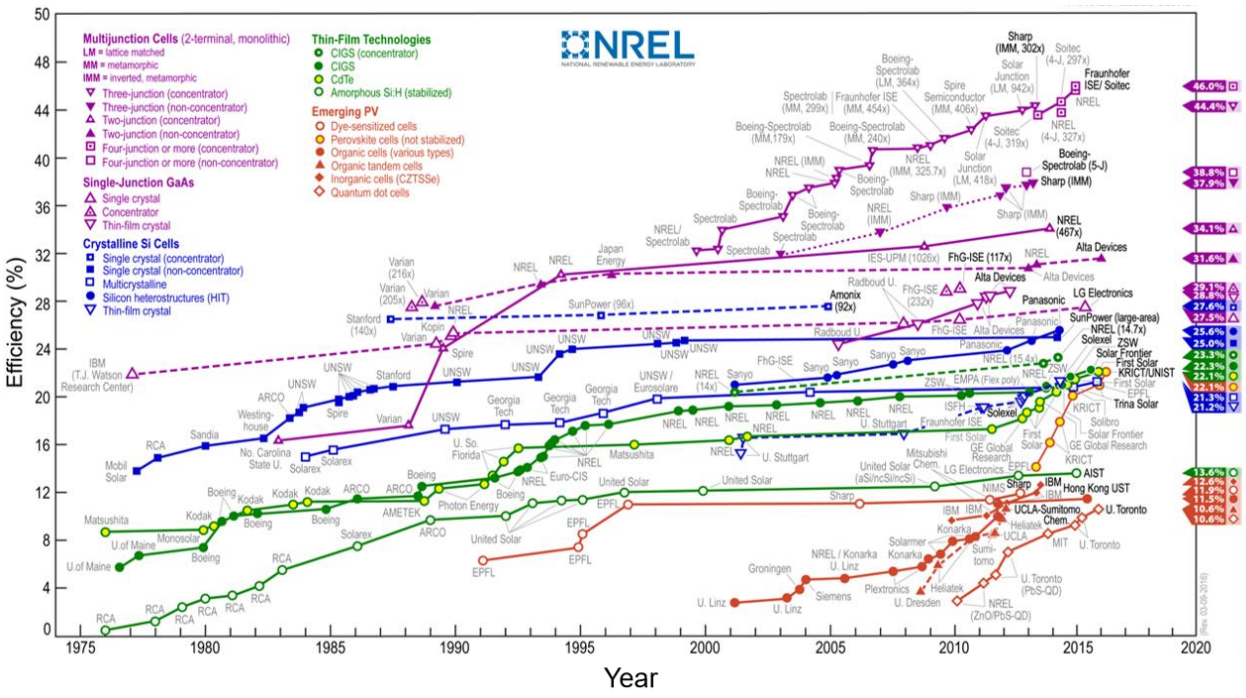

Figure 1.8. Best research cell efficiencies. This plot is courtesy of the National Renewable Energy Laboratory, Golden, CO.

Chapter 1.5. Proton-based photovoltaics.

In traditional artificial photovoltaics, sunlight energy is converted into electrical or electrochemical energy via electronic circuits. Light absorbing materials capture photon energy which generates excited electrons and vacant occupancies, called holes. The excited electrons and holes are separated by electric fields or changes in electron affinity propagating in the photovoltaic material. Upon separation and collection, electrons are transferred through an external circuit to perform work.

In nature, photosynthetic systems absorb light with molecular systems and the excited electron energy is converted into the unidirectional movement of protons. Protons flow across the membrane of a closed vesicle resulting in a proton gradient that powers the release of the energy storage molecule, adenosine triphosphate (ATP), from the enzyme, ATP synthase. The important distinguish between artificial and biological systems is that their circuit components are entirely different. This has made the development of biomimetic photovoltaics particularly challenging to the scientific community.

In the year 2000, Tributsch announced that there was no fundamental reason why artificial systems could not use light-driven proton gradients as an energy source,[39] and because the thermodynamic limit of photon to electrical energy and photon to chemical energy are equivalent,[40] such systems should be studied. And so in his studies a closed loop electrochemical cell utilizing Nafion membranes and pyrite as a photoactive proton conductor, was used to generate 150 mV of photopotential.[39]

The first relatively-practical wireless photovoltaic was achieved by Dan Nocera in 2011. The devices was coined the 'artificial leaf,' which had a wireless solar-driven water-

splitting efficiency of 2.5% under 1 Sun of air mass 1.5 simulated sunlight.[41] The 'artificial leaf' was a commercially bought triple-junction amorphous silicon with a cobalt catalyst for oxygen evolution and a ternary alloy (Nickel Molybdenum Zinc [NiMoZn]) for hydrogen evolution interfaced on opposite sides.[41] The listed materials are Earth abundant and the 'artificial leaf' was estimated to produce hydrogen at $6.5 per kilogram, which was $0.5 per kilogram cheaper than hydrogen driven by a traditional solar panel powering an electrolysis unit at the time.[42] The startup, Sun Catalytix, sought to improve the performance of the 'artificial leaf' but halted research and development after realizing the actual costs were higher, and the device was not safe because there was not a mechanism to prevent explosive mixtures of hydrogen and oxygen.

Later in 2015 Nate Lewis developed the first practical wireless solar fuels device using a tandem junction gallium arsenide (GaAs [bottom cell])/ indium gallium phosphide (InGaP [top cell]) photoanode coated with an amorphous titanium dioxide (TiO_2) protection layer for hydrogen-evolution and a nickel-molybdenum counter electrode for oxygen-evolution.[43] The electrodes were compartmentalized by an anion-exchange membrane (AHA-type, NEOSEPTA) and consequently separated the flows of hydrogen and oxygen gas, thereby preventing the buildup of explosive mixtures.[43] A 1 cm^2 prototype exhibited a rate of hydrogen production of 0.81 $\mu L\ s^{-1}$ and a solar-to-hydrogen efficiency of 8.6% under 1 sun illumination.[43] Incorporating a bipolar membrane in place of the monolithic anion-exchange membrane, allowed the solar-to-hydrogen efficiencies to reach 10% for >100 hours even with the inherent potential loss due to the resistivity of the membrane (~450 mV at a membrane current of ~4.4 mA cm^{-2}, or ~1 V at a membrane current of 10 mA cm^{-2}).[44] Moreover, the use of a bipolar membrane facilitated the solar-

driven reduction of 1 atmosphere of CO_2 to formate at an energy conversion efficiency of 10% and an operational current density of 8.5 mA cm^{-2}.[45] A GaAs/InGaP/TiO_2/Ni photoanode was immersed in 1 M KOH (aq) to drive oxygen-evolution at an overpotential of ~320 mV and a titanium (Ti) mesh coated with nanoparticles of palladium on carbon (Pd/C) was immersed in 2.8 M potassium bicarbonate to drive the reduction of CO_2 to formate (94% Faradaic efficiency) at an overpotential of <100 mV.[45]

Other examples of photovoltaic devices capable of driving protons vectorially have included long-lived (photobleached) photoacids or sacrificial molecules. Recently, such a system was published by Bakker and co-workers whereby long-lived photoacids were embedded in a synthetic membrane.[46] The system created a proton/counterion flux and exhibited an open-circuit photovoltage of ~210 mV mostly due to the gradient of chemical potential of protons manifested as a pH gradient of ~3.6 pH units. However, as in most previous demonstrations of light-driven protonic circuits, to assist charge separation and collection an asymmetry in potential had to be generated which required an energy input from something other than unidirectional solar illumination. In this case, it was excitation of each side of the membrane with a different color of light. The goal of the research presented herein is to design a light-driven protonic circuit that can demonstrate proton conduction in a pre-defined direction irrespective of the direction of optical excitation, akin to a traditional inorganic photovoltaic.

Chapter 2. Pyrenol Photoacids Covalently Bound to Polymer Nanopores as Models for Light-Driven Proton Pumps

Chapter 2.1. Overview.

The ability for light to drive directional ion transport on the nanoscale has implications for various applications, including light-to-ionic energy conversion, neuron triggering, and biomimetic processes. Reported herein are results from fundamental studies conducted on photoacid-modified nanoporous polymers capable of energizing protons in response to optical excitation. Pyrenol photoacid dye molecules with terminal ammonium groups for polymer attachment were synthesized and characterized by absorption and fluorescence spectroscopy as a function of pH. When dissolved in aqueous solution, their ground-state pK_a ≈ 6 and their thermally equilibrated excited-state pK_a ≈ -1, meaning that photoexcitation resulted in a change in the free energy of the hydroxyl group by ~7 pH units. These photoacids were also covalently bonded within conical nanopores that had been track etched in poly(ethylene terephthalate) (PET) films and their photophysical, photochemical, and electrochemical properties were characterized by absorption spectroscopy, two-photon fluorescence microscopy, and cyclic voltammetry. The results indicate that ~90% of the nanopore surface was modified with photoacids, which were on average linked to PET through three sulfonamide groups. In comparison to photoacids dissolved in solution, the data suggest that photoacids bound to PET are stronger acids in their ground-state (pK_a ≈ 5) but that photoacids bound to the nanoporous tip region are weaker acids in their ground-state (pK_a ≈ 7) due to a 100 mV surface potential. Moreover,

the bound photoacids are weaker acids in their excited-state ($pK_a^* \approx 0$ in aqueous 100 mM KCl or $pK_a^* \approx 2$ in water with no supporting electrolyte), and with shorter excited-state lifetimes (from ~4-6 ns to ~1 ns), signifying an increase in the rate of non-radiative decay. Results from these pioneering studies suggest that ion transport initiated by photoacids bonded to mesoporous materials will require careful molecular engineering to enable efficient light-to-ionic energy conversion.

Chapter 2.2. Introduction.

Control of the direction and timing of energy and charge transport on the nanoscale and macroscale has allowed for various innovations, from advanced microelectronics and photovoltaics, to life. While in most artificial systems energy and charge are transported using electronic processes,[47] nature also uses ionic processes.[48,49] For example, action potential is transmitted along neurons via a series of orchestrated ion fluxes across lipid bilayers,[50] and the photosynthetic processes in Photosystem II of green plants involve vectoral transport of both electrons and protons.[51] In each of these biological systems the materials contain a built-in asymmetry which leads to current rectification, i.e. a preferential direction for charge transport.[52–55]

Several artificial systems have also been shown to rectify ionic current: ion-exchange membranes,[9] nanopores,[58–68] and nanopipettes.[69–72] Utilizing the rectification properties that arise from device asymmetry, several light-driven proton pumps have emerged.[46,73–75] However, until very recently,[76,77] none of these materials were covalently functionalized with photoacid dye molecules to explore the possibility of creating a light-

driven proton pump that operates like a solar cell and exhibits photovoltaic action. An illuminated photoacid dye molecule undergoes a decrease in the pK_a of one of its protic functional groups, therefore becoming more acidic in its excited-state. This results in the liberation of a proton charge carrier that will then be transported in a direction defined by the asymmetry of the material to which it is bound. If the built-in asymmetry of the material results in ionic current rectification due to the presence of selective contacts on each side of the material,[78] light should be able to impart vectoral pumping of ions. Recently, photoacid-dye-modified Nafion ion-exchange membranes were used to demonstrate photovoltaic action through light absorption.[76,77] Illumination of photoacids generated a small photovoltage by converting visible light energy into a change in the local concentration of protons,[79,80] thus perturbing the system away from equilibrium. The observation of a photocurrent was consistent with directional ion transport of the photo-liberated protons driven by an electrostatic asymmetry in the Nafion ion-exchange membrane. However, the photovoltaic performance is not optimized and the mechanisms are not well understood, therefore prompting further study of the fundamental photophysical properties of photoacid dye molecules bound to hydrated charged polymers.

Herein, we utilize charged polymer nanopores as model systems for ion-exchange membranes to further interrogate the photovoltaic ion-pumping process previously observed in photoacid-dye-modified Nafion. Nanopores are ideal models for ion-exchange membranes like Nafion, because Nafion phase segregates into columnar porous hydrophilic regions that consist of micelle-like cylindrical channels with diameters on the order of 4 nm and bearing negatively-charge covalently bound (fixed) sulfonate groups

on their interior.[81,82] The model systems that we utilized consisted of ion-rectifying track-etched nanopores in poly(ethylene terephthalate) (PET) with diameters ~5 nm and bearing negatively-charge fixed carboxylate groups on their interior. Through careful characterization of these model nanoporous rectifying materials functionalized with custom photoacid molecules we further elucidated the role that confinement plays on the (photophysical) properties of the bound photoacid dye molecules, which may help explain some of the limitations in light-driven ion pumping observed using photoacid-dye-modified Nafion membranes.

Chapter 2.3. Results and discussion.

Chapter 2.3.1. Molecular synthesis.

Custom photoacid, tris(sulfonamide) pyrenol **2.1**, was synthesized from pyranine using a four-step synthesis (Scheme 2.1). Pyranine was treated with acetic anhydride under basic conditions to afford the acetyl-protected hydroxyl group followed by refluxing in excess thionyl chloride with catalytic *N,N*-dimethylformamide to activate the three sulfonate groups as sulfonyl chlorides. In a solution of 2:7:1 THF:MeCN:H_2O (v/v/v), two equivalents of *N*-Boc-ethylenediamine per sulfonyl chloride were added such that one equivalent formed the sulfonamide and HCl, which was neutralized by the other equivalent. The product was then deacetylated via addition of NaOH and the Boc protecting group was removed via trifluoroacetic acid treatment to yield **2.1**. Additional purification was achieved with RP-HPLC.

Scheme 2.1 Synthesis of **2.1** by sulfonate activation from pyranine.

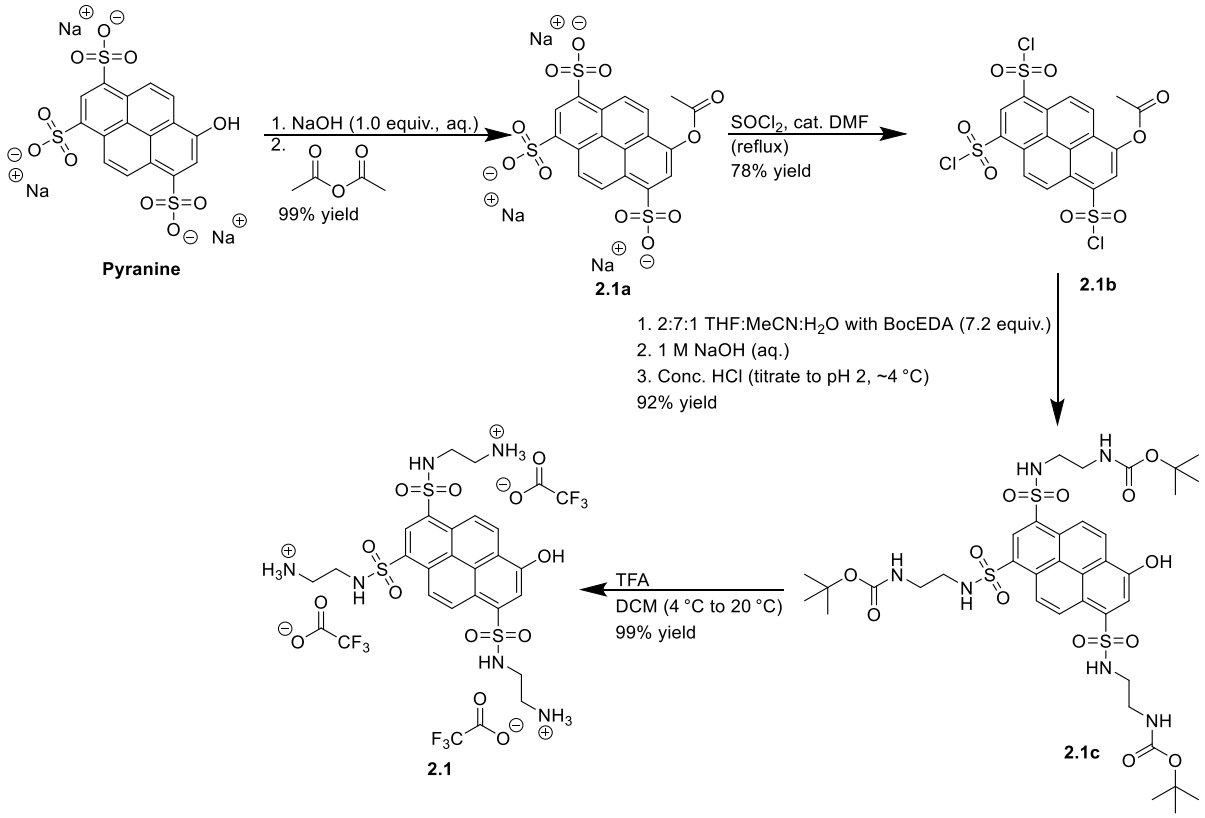

Chapter 2.3.2. Solution pK_a values.

The most acidic pK_a value of **2.1** dissolved in a buffered aqueous solution was determined to be ~5.8 via an acid/base titration procedure with spectrophotometric detection and non-linear least-squares fitting of the data to the Hill equation (Figure 2.1a-b),

$$\theta = \frac{1}{1 + 10^{\,n(\mathrm{pH} - \mathrm{p}K_a)}} \qquad \text{Equation 2.1}$$

where θ is the fraction of protonated/deprotonated species and n is the Hill coefficient, a stretch parameter used to account for non-ideal titration behavior.[83] For solution titrations the absolute value of the Hill coefficient should be close to its ideal value (i.e.

one); however, inclusion of this parameter affords a simple means to incorporate non-ideality into fits of the titration data. A positive (negative) value for the Hill coefficient means the spectral features decreased (increased) as the pH increased. The pK_a value was calculated as the average of the pH values at θ = 0.5 (the inflection points of the titration curves) for the protonated and deprotonated species.

The calculated pK_a value of 5.8 is similar to values reported for deprotonation of hydroxyl groups on tris(sulfonamide) pyrenols,[84] and therefore is assigned to deprotonation of the hydroxyl group of **2.1**. Spectral changes associated with this (de)protonation reaction were completely reversible and isosbestic points were maintained for all pH values reported. Three less acidic pK_a values for **2.1** dissolved in aqueous solution were determined to be ~8.6, ~10.5, and ~12.3 (Figure 2.1c-d). These pK_a values were assigned to deprotonation of the three ammonium functional groups of **2.1**. Spectral changes associated with this reaction were completely reversible; however, isosbestic points were not maintained for pH values greater than 8 because of the proximity of the pK_a values.

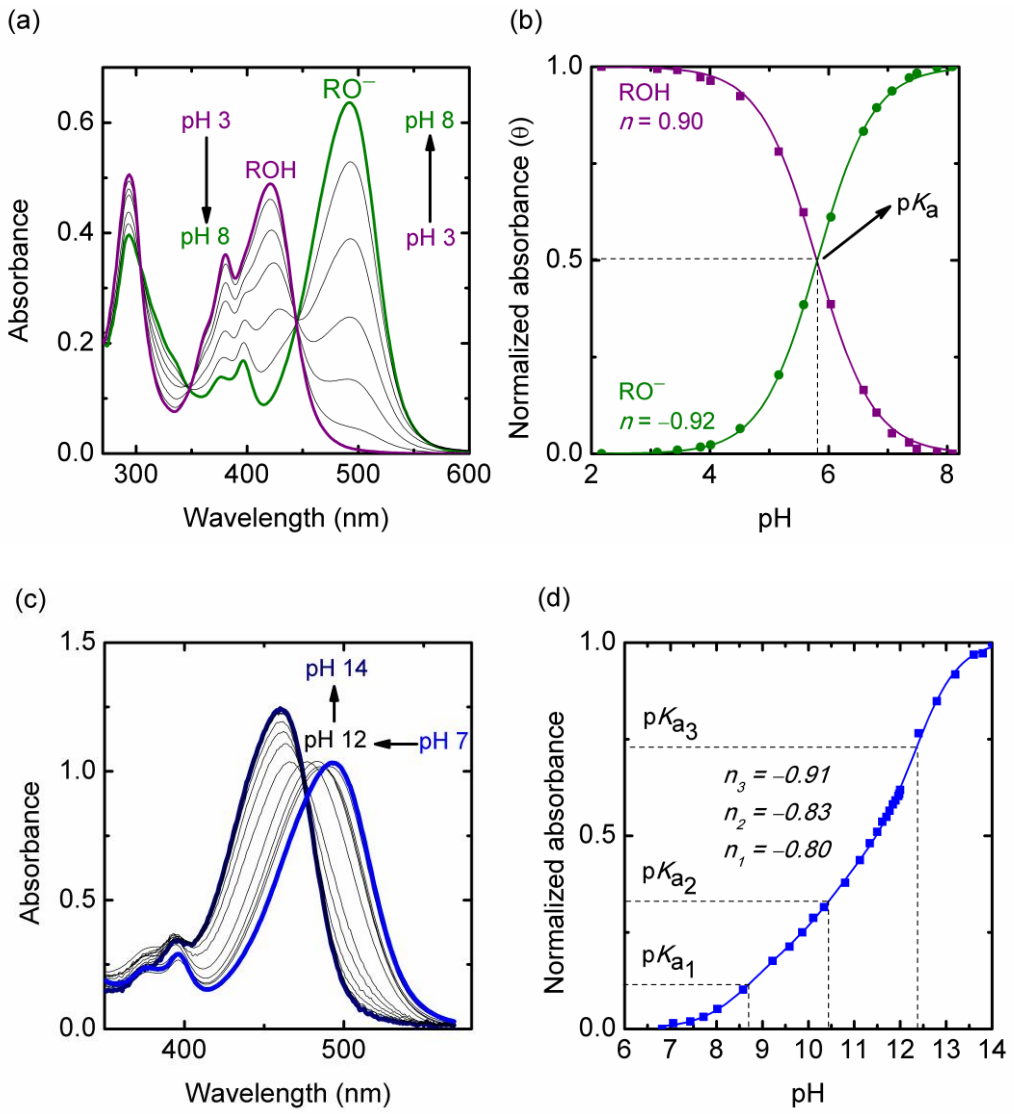

Figure 2.1. (a) Electronic absorption spectra of **2.1** dissolved in an aqueous buffer solution. The completely protonated and deprotonated ground-state spectra are bolded, colored, and are labeled with ROH and RO^-, respectively. (b) Plot of normalized absorbance (θ) at the λ_{max} (421 nm and 492 nm) for each species as a function of pH, and displayed with non-linear least square best fits to the Hill equation (Equation 2.1). (c) Electronic absorption spectra of **2.1** dissolved in aqueous solution without buffer. (d) Plot of normalized absorbance at 460 nm as a function of pH, and displayed with non-linear least square best fit to a linear combination of three Hill equations (Equation SI 2.1**Error! Reference source not found.**).

The excited-state pK_a, pK_a^*, of **2.1** dissolved in acidic aqueous solution was estimated to be -1.0 via the Förster cycle analysis (Equation 2.2,. Figure SI 2.2Figure SI 2.3)

$$pK_a^* = pK_a - \frac{N_A hc(\nu_{ROH} - \nu_{RO^-})}{(\ln 10)RT} \qquad \text{Equation 2.2}$$

where N_A is Avogadro's number (6.022 x 10^{23} molecules mol^{-1}), h is Planck's constant (6.626 x 10^{-34} J s), c is the speed of light in vacuum (2.998 x 10^8 m s^{-1}), ν_{ROH} and ν_{RO^-} are the energies of the 0-0 electronic transitions of ROH and RO^-, respectively, and are expressed in inverse meters (m^{-1}), R is the ideal gas constant (8.314 J mol^{-1} K^{-1}), and T is the temperature (K; room temperature, 298.15 K). This analysis results in an approximation of the change in the acidity between the equilibrated ground-state and the thermally equilibrated excited-state.[85,86]

This approximate pK_a^* was further corroborated by an experimental acid/base titration procedure with photoluminescence detection (Figure 2.2, Equation SI 2.5). Over the range of pH and Hammett acidity values (H_0) reported in the figure, the photoacid hydroxyl groups remained protonated in their ground-states (ROH). Under strongly acidic conditions, emission occurred exclusively from the protonated excited-state (ROH^*); however, at intermediate H_0 values, excitation of ROH resulted in emission predominantly from the deprotonated excited-state species (RO^{-*}). The latter behavior is indicative of an intermediate excited-state proton-transfer (ESPT) step occurring within the lifetime of the excited-state. The pK_a^* value obtained from Equation 2.2, i.e. -1.1, and the excited-state Hammett acidity value, H_0^*, obtained from the photoluminescence

titration data and Equation SI 2.5, i.e. -1.3, are similar to those reported for tris(sulfonamide) pyrenols.[84]

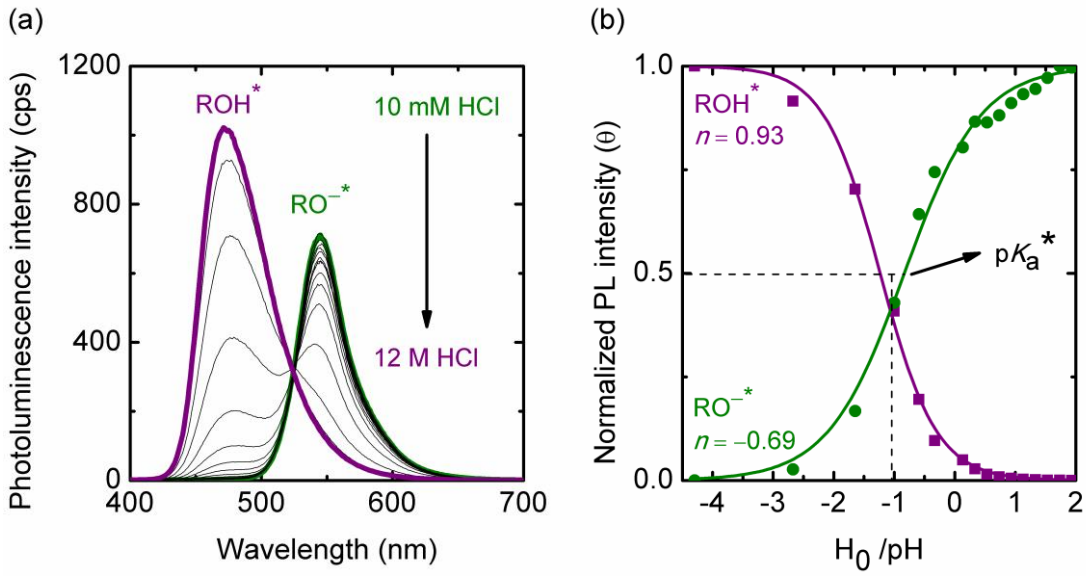

Figure 2.2. (a) Photoluminescence spectra of **2.1** dissolved in differing concentrations of aqueous HCl. The excitation wavelength (λ_{ex}) was 379 nm. Emission from the completely protonated and deprotonated excited-states are represented by ROH^* and RO^{-*}, respectively. (b) Plot of normalized photoluminescence (PL) intensity (θ) at the λ_{max} for each species (476 nm and 545 nm) as a function of Hammett acidity (H_0 >1 M HCl) and pH (< 1 M HCl). Displayed with non-linear least square best fits to the Hill equation (Equation 2.1).

Chapter 2.3.3. Polymer functionalization.

Conical nanopores in poly(ethylene terephthalate) (PET) films were etched using a previously reported procedure[87–89] with minor modifications to yield films with between 1 pore per film and 100,000,000 pores per cm^2. The conical nanopores were calculated to have base diameters of 130 – 1000 nm and tip diameters of 4 – 20 nm; the base diameters were estimated on the basis of the bulk etching rates and the tip diameters were estimated on the basis of the resistance of the pores immersed in 1 M aqueous KCl, according to Vlassiouk's and Siwy's practice.[89] 1-Ethyl-3-(3-dimethylaminopropyl)carbodiimide was employed to covalently anchor **2.1** to the inside of the conical nanopores to yield a PET_n/**2.1** film, where 10^n is the projected areal coverage of nanopores (pores cm^{-2}).

Localization of **2.1** within PET pores was supported by data obtained using two-photon fluorescence microscopy of PET_8/**2.1** (Figure 2.3). Fluorescence microscopy allowed selective excitation of photoacids bound in the pore tips and emission was clearly observable from regions coincident with pores. However, this technique did not afford information on the chemical identity of the bound species. Photoacid **2.1** has three free amine functional groups that can be covalently linked to PET through carboxylates to form up to three amide linkages. Knowing the approximate number of amide linkages formed between **2.1** and PET provides a more complete picture of the electrostatic and chemical environment in PET_n/**2.1**, which we describe below.

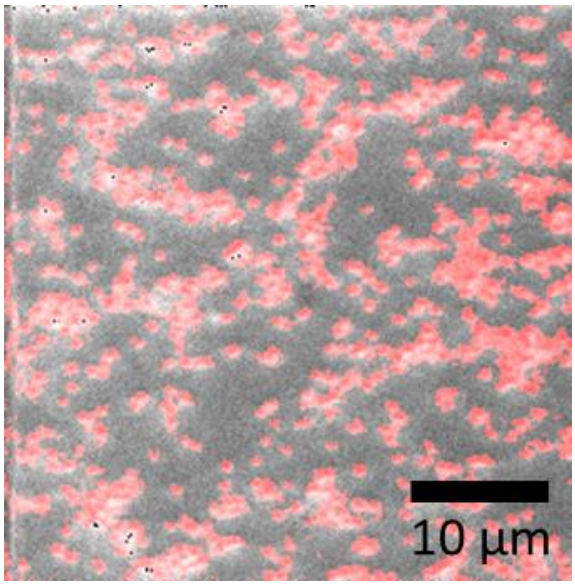

Figure 2.3. Optical microscopy reflection image of PET$_8$/**2.1** immersed in aqueous pH 3 solution and overlaid with emission from **2.1** (red) resulting from two-photon absorption (λ_{ex} = 900 nm). Photoluminescence intensity from **2.1** was greater than photoluminescence intensity from the PET polymer. The optical microscopy reflection image is shown as Figure SI 2.5 and clearly depicts the pore openings (dark spots, base side) that would be directly underneath the photoluminescence observed here.

PET$_8$/**2.1** had maximum absorbance values at 426 nm and 498 nm and all major absorption peaks exhibited ~5 nm bathochromic shifts as compared to those observed in solution (Figure 2.4a). Across the pH range tested, changes in absorption were consistent with data in solution for deprotonation of the hydroxyl group of **2.1**, which suggests that **2.1** did not bind to PET through the hydroxyl group (Figure 2.4). No hypsochromic shifts in absorption were observed at pH 8 – 10.5, which suggests that the ammonium groups of **2.1** were not deprotonated across this pH range tested, even though pK_a values of these

ammonium groups observed for **2.1** in solution are 8.6, 10.5, 12.3 (Figure 2.1c-d). This suggests that at least 66% of the ammoniums reacted with PET to form covalent bonds and the pK_a of unreacted ammonium groups was > ~11.5. A summary of all spectral features from the solution and film studies are presented in Table SI 2.1.

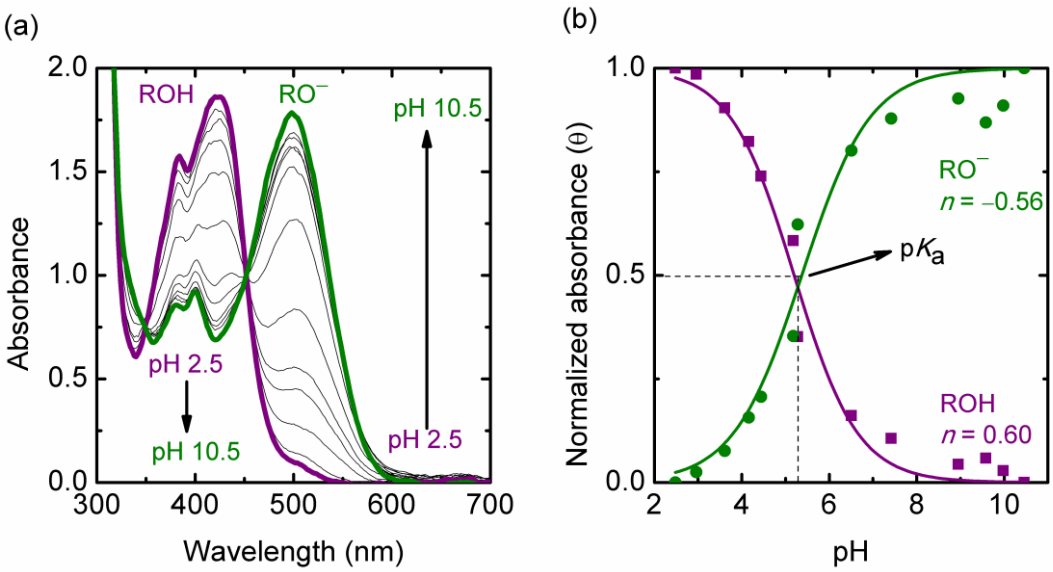

Figure 2.4**.** (a) Electronic absorption spectra of PET_8/**2.1** wetted with aqueous buffer solution. (b) Plot of normalized absorbance (θ) at the λ_{max} for each species (426 nm and 498 nm) as a function of pH, and displayed with non-linear least square best fits to the Hill equation (Equation 2.1).

Chapter 2.3.4. Ground-state pK_a values in polymers.

For photoacid-functionalized nanopores to serve as light-driven ion pumps, ideally **2.1**, when anchored to the conical nanopores, would be a weak ground-state acid and strong excited-state photoacid. The hydroxyl pK_a of **2.1** covalently bound as PET$_8$/**2.1** immersed in an aqueous buffered solution was determined to be 5.1 via an acid/base titration procedure with spectrophotometric detection (Figure 2.4); this value is 0.7 pH units more acidic than the hydroxyl pK_a of **2.1** dissolved in solution, but consistent with the shift observed for a model of PET$_n$/**2.1**, i.e. mono-methyl-terephthalate capped **2.1** (photoacid **2.2**) in aqueous solution, whose hydroxyl pK_a ≈ 5.4 (Scheme SI 2.1).

The acid/base titration procedure with spectrophotometric detection (Figure 2.4) gave the average pK_a of all photoacid molecules bound to the PET surface but did not provide information about the pK_a of photoacids bound specifically at the tips of nanopores. The tip region is reported to be a major contributor to the ionic current rectification and is proposed to contain a built-in potential,[61,62,66,90–94] therefore suggesting that photoacids in this region may enable demonstration of ion-based photovoltaic action. Studies have shown that the tip region of native PET nanopores have surface charges of 0.1-1 C m^{-2} for pore diameters 10-100 nm,[88,95,96] and assuming a Debye length of 1.1 nm for a pore wetted by 100 mM KCl aqueous electrolyte,[97] implies that the conical nanopores used in our studies have built-in surface potentials of 0.15-1.5 V (Equation SI 2.7). Cyclic voltammetry of PET$_0$/**2.1** as a function of solution pH was used to assess the net charge in the tip region of the nanopore (Figure 2.5), because the net charge affects the current–potential behavior.[68,89,98–100] Data pertaining to the titration of an ensemble of pores, PET$_8$/**2.1**, was fit to Equation SI 2.1

(Figure 2.6). The inflection points in the fit likely represent pK_a values of functional groups that line the inside of nanopore tips and thus, pK_a values were 3.5, 6.9, >10. The largest pK_a value was too basic to measure because the alkaline conditions beyond those values assessed (i.e. pH > 10) would have hydrolyzed the PET polymer.

The net charge in the tip region of nanopores is also diagnostic of the number of amide bonds formed between **2.1** and PET, therefore the net charge of PET_0/**2.1** and PET_8/**2.1** were probed as a function of pH (Figure 2.5;Chapter 2.6.7). Under acidic conditions (pH 2), current rectification consistent with a net positively charged tip of PET_0/**2.1** was observed. This behavior strongly suggests that at least some of **2.1** are covalently bound in the tip region with (at least) one free cationic ammonium group and a neutral hydroxyl group. As the pH was titrated to more basic values (pH = 2 – 5.5), the current–potential response became ohmic and highly resistive. This behavior occurred at pH values smaller than those measured for the deprotonation of the hydroxyl group of **2.1** bound to PET_8/**2.1** (Figure 2.4) and therefore a logical conclusion is that this process was deprotonation of unreacted terephthalic acid groups in the tip of the nanopore which aided in the charge neutralization of ammonium groups. Upon further titration of the pH toward more basic values (pH = 5.5 – 10) current rectification returned but this time the behavior was consistent with a net negatively charged tip of PET_n/**2.1** likely caused by the deprotonation of the hydroxyl group of **2.1**. These positive–neutral–negative surface features were consistently observed during the titration of another 11 individual PET_0/**2.1** (Chapter 2.6.8Chapter 2.6.9).

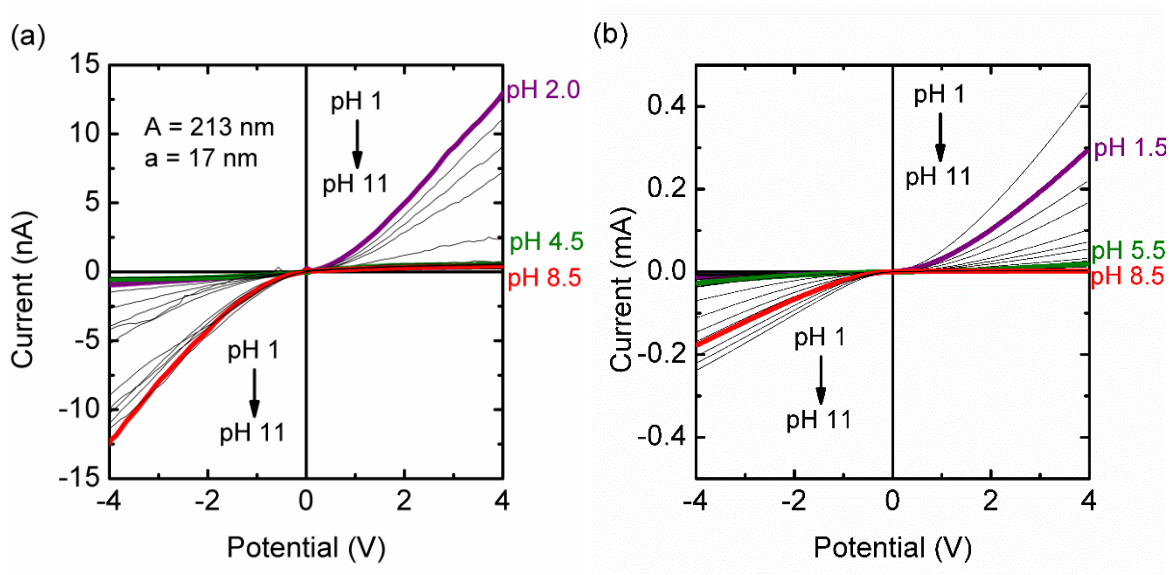

Figure 2.5.Cyclic voltammograms of (a) PET_0/**2.1** and (b) PET_8/**2.1** immersed in aqueous 100 mM KCl. Also shown are the large (A) and small (a) diameters of the conical nanopore.

The titration data were further analyzed to determine the binding mode and the binding coverage of **2.1** to the nanopore surface by converting the extreme current values into rectification ratios (Figure 2.6a) and plotting them as a function of pH, consistent with previous reports.[100–104] Data obtained from PET_0/**2.1** lacked the sigmoidal character expected for this analysis. Therefore, data from the ensemble of pores in the PET_8/**1** was fitted to a linear combination of three Hill equations (Equation SI 2.1). Three Hill equations were required to account for changes in surface charge due to protonation of carboxylates, alkoxides, and primary amines (Figure 2.6). Based on the best-fit weightings for each Hill equation, the total number of carboxylic acids and primary ammoniums were approximately equal and that there were 3.6 times more hydroxyls (3.6:1:1 ROH: $R'NH_3^+$ R''COOH [Table SI 2.2]). Because there are three amines and one hydroxyl per photoacid molecule, and no

hydroxyls were bound to PET, this implies that for every 10.8 amines (3.6 x 3) there was one unreacted amine and one unreacted carboxylic acid on PET and therefore that 91% of the amines and 91% of the carboxylic acids on the surface of the PET nanopore reacted to bond the photoacid to PET. Furthermore, knowing that there is approximately one carboxylate per nm^2 in the native PET film[105] helped elucidate that the binding coverage of **2.1** was ~0.3 photoacids nm^{-2} (Equation SI 2.9), which was further substantiated by the a two-step coupling/hydrolysis method (Chapter 2.6.10). Collectively, these data suggest that pK_a value of the hydroxyl group on **2.1** is more basic when **2.1** is bound in the tip region (p$K_a \approx 6.9$) by ~2 pH units in comparison to **2.1** bound to bulk polymer lacking a built-in potential (p$K_a \approx$ 5.1) and by ~1 pH unit in comparison to **2.1** dissolved in aqueous electrolyte (p$K_a \approx 5.8$). The ~2 pH unit shift for the pK_a value of **2.1** in the tip region versus bulk PET is consistent with an electrostatic hypothesis. A 2 pH unit shift would arise from a 120 mV potential drop (2 x $2.303RT/F$). When the pH equals the hydroxyl pK_a (6.9), ~8% of the PET surface has unbalanced fixed negative charges and therefore, the potential drop is ~8% of 1.5 V (the reported tip potentials for nanopores with tip diameters of 10 nm), or ~120 mV. A summary of the pK_a values measured in this work is presented in Table 2.1.

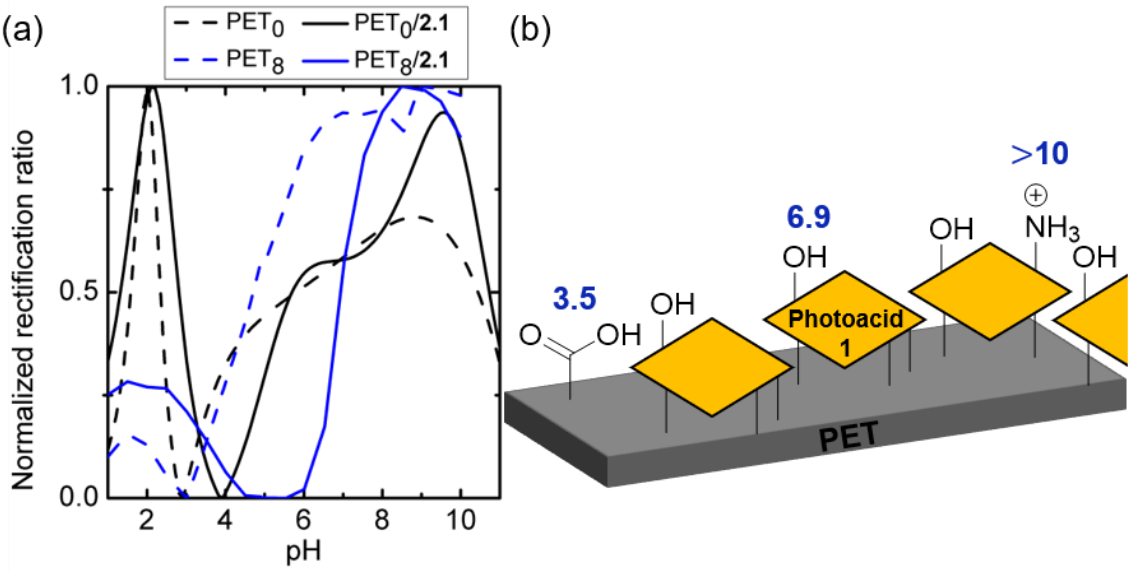

Figure 2.6. (a) Rectification ratio as a function of pH for PET$_n$ immersed in aqueous 100 mM KCl. (b) Representative arrangement of species in the modified tip surface region of PET$_8$/**2.1**based on values obtained from best-fits of the data in panel a. Numbers shown correspond to approximate pK_a values obtained from inflection points of the best-fit of the PET$_8$/**2.1** data in panel a to Equation SI 2.1 (fit shown for clarity in Figure SI 2.9).

Table 2.1. Ground-state and excited-state hydroxyl pK_a values for **2.1** and PET$_n$/**2.1** in the presence and absence of salt.

Sample	**2.1**	PET$_8$/**2.1**		
[KCl] (M) (aq.)	100	100	100	0
Region probed	Dissolved photoacid	Nanopore tip	Entire film	Nanopore tip
pK_a	5.80 ± 0.03[a]	6.9[d]	5.06 ± 0.16[a]	n/a
pK_a^* (H_0^*)	-0.57 ± 0.02[b] (-1.30 ± 0.11)[b] -1.05[c] (-4.12)[c]	0.17[e] -1.41[c] (-9.58)[c]	n/a	1.62[e]

Chapter 2.3.5. Excited-state pK_a values and excited-state lifetimes in polymers.

Measurement of pKa* in the nanopores required that only the tip of the nanopores be functionalized. To accomplish this, taurine (T) was used to cap the free carboxylates in other regions of the PET film so that they would be unreactive (for PET_8/T+**2.1**). Similar to the solution studies, the Förster cycle analysis was first used to calculate an approximate pK_a^*, which was determined to be ~ -1.4 (Chapter 2.6.12), consistent with pK_a^* calculated for **2.1** in solution (pK_a^* ≈ -1.1). Also, analogous to **2.1** in solution, PET_8/T+**2.1** films that contained ROH species and were immersed in weakly acidic aqueous solutions exhibited photoluminescence from RO^{-*} species (Figure 2.7) indicating that **2.1** underwent ESPT, that is **2.1** operated as a photoacid while covalently bound within the PET nanopores. However, under these weakly acidic conditions, emission from ROH* was also observed for PET_8/T+**2.1** which is a stark contrast to photoluminescence spectra from **2.1** dissolved in solution and the results from the simple Förster cycle analysis. For instance, at pH 3, ~40% of the emission was from ROH* for PET_8/T+**2.1** (Figure 2.7and Figure SI 2.13b) whereas for **2.1** in solution > 99% of the emission was from ROH* (Figure 2.2). Also, full photoluminescence pH titrations results are shown in Table 2.1 and indicated that in contrast to pK_a^* of **2.1** in solution (pK_a^* ≈ -1), pK_a^* of PET_8/T+**2.1** (pK_a^* ≈ 1.6 when taken in absence of supporting electrolyte) was highly non-ideal in the which is most likely caused by a distribution of pore sizes or distribution of microenvironments. Spectral changes associated with this excite-state (de)protonation reaction were completely reversible and isoemissive points were maintained for all pH

values reported. A summary of the pK_a^* values measured in this work is presented in Table 2.1.

To rationalize the observed excited-state behavior, several hypotheses were evaluated. In PET_8/T+**2.1** films the ratio of emission from ROH^* and RO^{-*} was found to be independent of the intensity of the excitation illumination (Figure SI 2.14). Therefore, changes in local acidity due to laser photoexcitation did not occur even at bulk pH values as basic as ~3. Moreover, confined charged pores are known to exhibit Donnan exclusion of ions which could result in a nanopore pH that differed from that of the bulk solution. Addition of 100 mM supporting electrolyte further supported the notion that Donnan exclusion was operative, because then the salt concentration was approximately equal to that of the concentration of fixed charges in the nanopores. Specifically, the addition of 100 mM KCl allowed the observation of a near zero value for pK_a^* value, that is pK_a^* value of **2.1** in PET approached the pK_a^* value of **2.1** in dissolved in solution (Figure 2.7c-d). These changes are consistent with the idea that the electrostatic environment of the tip effects both the ground-state and excited state pK_a.

Another hypothesis that might be operative too is that the change in pK_a is attributed to nanoconfinement. Fayer and coworkers studied the water environment in confined areas of Nafion[106,107] and sodium 1,4-bis(2-ethylhexyl) sulfosuccinate (AOT) reverse micllese[106] using the photoacid HPTS. In these systems containing nanoscopic water environments,[106,107] sluggish hydrogen bond dynamics prevented water from properly solvating RO^{-*} and H^+ formed from the ESPT step and consequently the equilibrium was shifted toward the excited protonated species and the driving force for net ESPT was depressed.[108–110] This observation is consistent with the data reported

herein where for **2.1** in solution, pK_a^* ~ -1 while for PET_8/T+**2.1** (with 100 mM KCl), pK_a^* ~0. Collectively, these data support that pK_a^* of **2.1** bound in the tips of nanopores becomes less acidic, coinciding with the changes in the ground-state pK_a (6.9) of **1** in the same tip region wetted by the same supporting electrolyte. Moreover, the decrease pK_a^* values were likely due to electrostatic effects or slow excited-state reorganization of **2.1**. Irrespective of the mechanism, **2.1** is a weaker photoacid in confined nanopores.

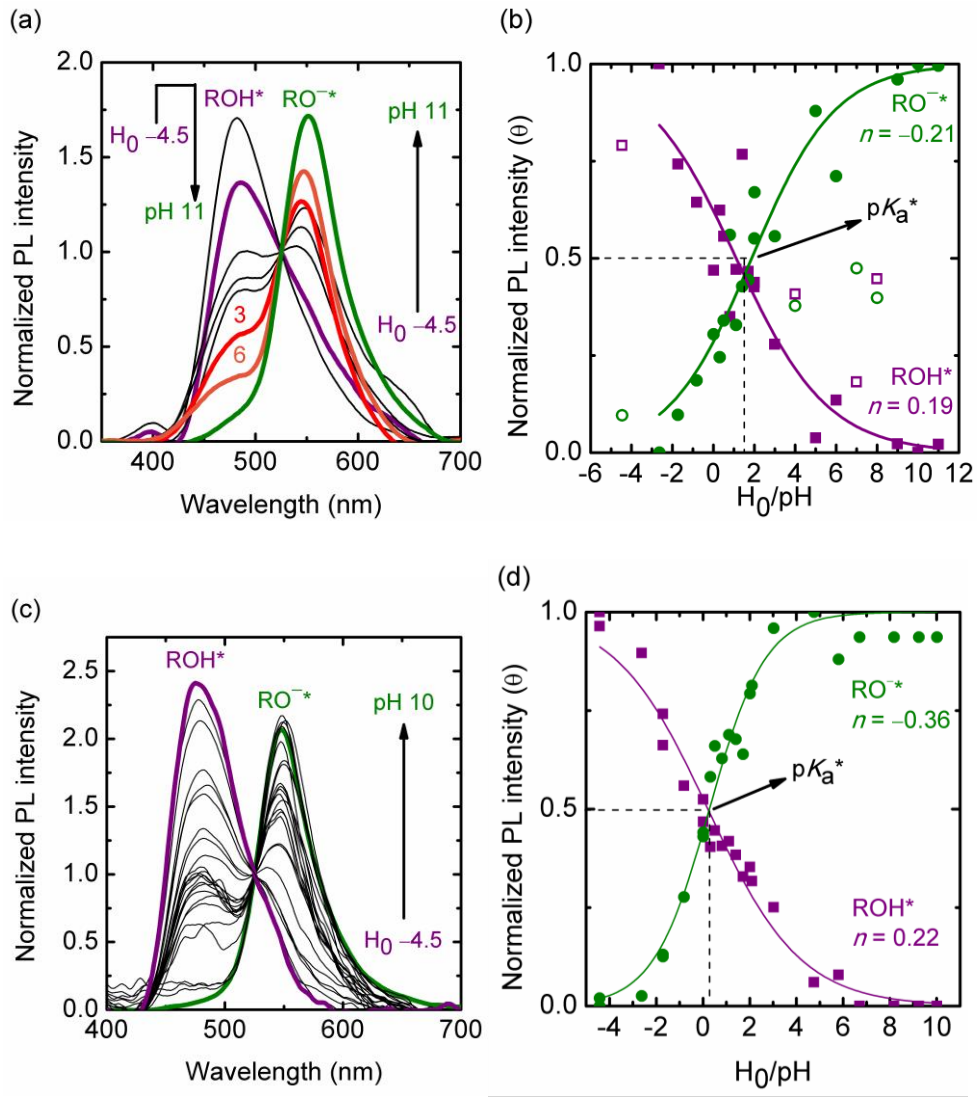

Figure 2.7. (a) Photoluminescence (PL) spectra of PET_8/T+**2.1** immersed in aqueous solutions without supporting electrolyte and (c) with 100 mM KCl supporting electrolyte. Two-photon-absorption excitation wavelength (λ_{ex}) was 900 nm. Emission from the completely protonated and deprotonated excited-states are represented by ROH^* and RO^{-*}, respectively. (b) Plot of normalized photoluminescence (θ) derived from spectral modeling as a function of pH, and displayed with non-linear-least-squares best fits to Equation 2.1 for titration done without supporting electrolyte and (d) with 100 mM KCl supporting electrolyte. Unfilled shapes were not fit to Equation 2.1. H_0 >1 M HCl, and pH < 1 M HCl.

Fluorescence-lifetime imaging microscopy was used to measure the excited-state lifetime of PET_8/**2.1** immersed in concentrated HCl and aqueous pH 10; the measured excited-state lifetimes were 1.0 ns for ROH^* and 1.2 ns for RO^{-*}. A radiative lifetime of 1.9 ns was measured at pH 3, conditions that would allow ESPT. Because the excited-state lifetimes of **2.1** in concentrated aqueous HCl, pH 3, and pH 10 were 3.9 ns, 5.9 ns, and 5.8 ns, respectively, it is implies that when **2.1** is bound to PET, faster non-radiative relaxation channels exist. PET_8/T lifetimes were also measured in the similar conditions, and an excited-state lifetime of ~2.7 ns were observed.

Recent studies by White, Sanborn, et al. suggest that photoacid-modified Nafion exhibits photovoltaic action (Chapter 2-3).[76,77] However, the photocurrent was at least in part limited by an increase in pK_a* for dyes bound in the nanopores of Nafion.[76] The nanopores reported herein are nearly ideal models for these systems because their small diameters are on the same size scale as those reported in Nafion (< 10 nm). [76,77] The results above suggest that the ground-state pK_a values of photoacids bound to materials vary with surface potential. But more importantly, the excited-state pK_a values become less acidic. This is undesired for the ultimate application of these materials and suggests that alternative photoacids (smaller pK_a*) or ion-exchange materials (larger pH) will likely be required in order to realize an effective combination that results in large yields for light-to-ionic energy conversion. Nevertheless, studies are currently underway to assess the feasibility of using membranes/nanopores with altered surface chemistries and/or using photoacids with smaller pK_a^* values, with larger magnitudes for ΔpK_a, and/or that prefer to be localized in the center of nanochannels where the characteristics of water more closely resemble that of bulk water.

Chapter 2.4. Conclusions.

Water soluble photoacid molecules with terminal ammonium groups were synthesized. The terminal ammonium groups allowed for facile coupling to carboxylic acids on nanoporous PET surfaces. Spectrophotometric titration curves showed that the hydroxyl pK_a of photoacid **2.1** was 5.8 in aqueous solution. Electrochemical measurements and electronic absorption spectroscopy suggested that the hydroxyl pK_a value of **2.1** bound to PET nanopores was ~5 in areas with low surface potential and ~7 at the tip regions where surface potentials were high (~0.1 V and surface charge of ~0.07 C m^{-2}). Also, a majority of **2.1** was attached via three out of three amine groups, the PET surface was ~90% modified, and **2.1** had a binding coverage of 0.3 photoacids nm^{-2}. Förster cycle approximations and photoluminescence titration measurements indicated that the hydroxyl pK_a^* of **2.1** in solution was ~ -1. Fluorescence microscopy was used to show that **2.1** bound to PET was localized within nanopores and **2.1** still operated as a photoacid. The apparent pK_a^* was ~0 when 100 mM KCl was added, where this value was 1.7 when no supporting electrolyte was present. Moreover, PET$_n$/**2.1** exhibited a titration curve that followed highly non-ideal behavior postulated to be due to an accumulation of confinement effects, distribution in pore geometries, and differences in microenvironments. Additionally, the excited-state lifetime of **2.1** significantly decreases upon binding (4-6 ns to 1 ns). These observations suggest that ESPT in small nanopores (diameter < 10 nm) occurs at lower efficiencies. Use of these systems for application in

light-driven proton pumps requires further advances but could conceivably be improved by incorporating different photoacids and membranes.

Chapter 2.5. Experimental methods.

General Synthetic Procedures. Unless otherwise stated, all reactions were run under an inert atmosphere of nitrogen in oven dried flasks equipped with Teflon-coated magnetic stir bars. All chemicals were obtained from commercial suppliers and used with no further purification. Reactions were monitored by thin-layer chromatography (TLC) on TLC Silica gel 60 F_{254} aluminum sheets using ultraviolet light for visualization or by time-of-flight mass spectrometry.

Reagents: Pyranine (>85%, TCI America), acetic anhydride (99%, EMD Millipore), sodium hydroxide (≥95%, Macron Fine Chemicals), potassium chloride (≥99%, Fisher Scientific), 1-(3-dimethylaminopropyl)-3-ethylcarbodiimide hydrochloride (98%, Alfa Aesar), 1-boc-ethylenediamine (98%, Combi-Blocks), thionyl chloride (≥99%, Sigma-Aldrich), propylamine (98%, Sigma-Aldrich), ethylenediamine (99%, Acros Organics), MES hydrate (99%, Oakwood Chemical), tris base (≥99.8%, Fisher Scientific), potassium phosphate monobasic (≥99.5%, Fisher Scientific), sodium tetraborate decahydrate (≥99.5%, Fisher Scientific), citric acid anhydrous (≥99.5%, Fisher Scientific), hydrochloric acid 36.5-38% (EMD Millipore), trifluoroacetic acid (99%, Oakwood Chemical), formic acid (88%, Fisher Scientific), dimethylsulfoxide (≥99.9%, EMD Millipore), taurine (99%,

Sigma-Aldrich), mono-methyl terephthalate (97%, Sigma-Aldrich), *N*-hydroxy succinimide (98% Sigma-Aldrich).

Spectroscopic Characterization. NMR Spectra were collected at 298 K at 400 MHz using a Bruker AVANCE400 Spectrometer or at 500 MHz using a Bruker CRYO500 Spectrometer. Chemical shifts are reported using the standard δ notation in parts per million (ppm) relative to solvent peaks (^{1}H, ^{13}C). Peak multiplicities are listed as follows: s, singlet; d, doublet; t, triplet; q, quartet; m, multiplet. The *J*-coupling constants are reported in Hertz. Infrared spectra were recorded on a Perkin-Elmer Spectrum One FTIR Spectrophotometer; samples were prepared as KBr pellets.

Chemical Syntheses.

Sodium 8-acetoxypyrene-1,3,6-trisulfonate (2.1a): Sodium hydroxide (0.80 g, 20 mmol) was added to a stirring solution of pyranine (9.59 g, 18 mmol) dissolved in water (10 mL). The solution was stirred for 15 minutes and then concentrated under vacuum to dryness. A heated water bath was used to assist the distillation process. Acetic anhydride (100 mL) was added. The suspension was heated to reflux and stirred for 14 hours. A white powder was collected via filtration and washed with dichloromethane and acetone; the powder was dried under vacuum (10.7 g, 18 mmol, quantitative yield). ^{1}H NMR (500 MHz, D_2O) δ 9.24 (s, 1H), 9.23 (d, *J* = 10.0, 2H), 9.17 (d, *J* = 10.0, 1H), 9.13 (d, *J* = 9.5, 1H), 8.56 (s,1H), 8.51 (d, *J* = 9.5, 1H), 2.65 (s, 3H); ^{13}C NMR (500 MHz, D2O) δ 173.4, 144.5, 138.3, 136.2, 136.1, 129.7, 129.0, 127.1, 126.4, 125.6, 125.5, 125.3, 125.0, 125.0, 124.7,

123.4, 120.2, 20.5; FTIR (KBr pellet) ν 3470 (st) cm^{-1}, 2959 cm^{-1}, 1736 (m) cm^{-1}, 1569 (m) cm^{-1}, 1206 (st) cm^{-1}, 1060 (st) cm^{-1}.

3,6,8-tris(chlorosulfonyl)pyren-1-yl acetate (2.1b): While stirring, pyrene **2.1a** (4.352 g, 7.684 mmol) was slowly added to a solution of thionyl chloride (10 mL) containing three drops of *N*,*N*-dimethylformamide. The reaction was refluxed for 5 h. The crude product was poured onto an aqueous ice slurry and dissolved with dichloromethane. The organic layer was separated and concentrated *in vacuo* to obtain a yellow powder (3.312 g, 5.400 mmol, 78%). ^{1}H NMR (500 MHz, $CDCl_3$) δ 9.68 (d, *J* = 10.0, 1H), 9.62 (s, 1H), 9.51 (d, *J* = 10.0, 1H), 9.45 (d, *J* = 9.7, 1H), 8.91 (s, 1H), 8.83 (d, *J* = 9.7, 1H), 2.67 (s, 3H); ^{13}C NMR (500 MHz, $CDCl_3$) δ 168.7, 147.2, 140.8, 137.4, 137.2, 133.1, 131.9, 129.9, 128.2, 128.1, 127.6, 126.5, 126.1, 125.5, 125.4, 124.7, 123.4, 21.3.

***tert*-butyl-(2-((6,8-bis(N-(2-((*tert*-butoxycarbonyl)amino)ethyl)sulfamoyl)-3-hydroxypyrene)-1-sulfonamido)ethyl)carbamate (2.1c):** *N*-boc-ethylenediamine (4.5704 g, 28.52 mmol) was added to a solution of H_2O (2 mL), tetrahydrofuran (4 mL), and acetonitrile (14 mL). While stirring, pyrene **2.1b**(2.184 g, 3.938 mmol) was added. An additional solution of H_2O (2 mL), tetrahydrofuran (4 mL), and acetonitrile (14 mL) was added. The resulting red-violet solution was stirred for 19 hours at room temperature. Consequently, NaOH pellets (0.3 g) were added to the mixture and stirred for 2.5 hours before an additional NaOH pellets (0.4 g) were added. After 1.5 hours, 100 mL of chloroform and 100 mL of 1 M NaOH was added and vigorously shaken (with occasional venting) until the red product dissolved completely into the aqueous layer. The aqueous

solution was washed with chloroform (200 mL x 4). The aqueous layer was separated, ice was added to the directly to the solution, and then acidified with a chilled solution of HCl (concentrated HCl added directly to ice in a 1:3 volume ratio). The resulting yellow precipitate was collected via vacuum filtration and dried under vacuum (3.224 g, 3.643 mmol, 92%). ^{1}H NMR (500 MHz, CD_3OD) δ 9.21 (s, 1H), 9.18 (d, *J* = 9.8, 1H), 8.90 (d, *J* = 9.6, 1H), 8.94 (d, *J* = 9.8, 1H), 8.80 (d, *J* = 9.6, 1H), 8.30 (s, 1H), 2.98 (coalescing m, 12H), 1.15 (coalescing s, 27H).

2,2',2''-((8-hydroxypyrene-1,3,6-trisulfonyl)tris(azanediyl))tris(ethan-1-aminium) tris(trifluoroacetate) (2.1): Trifluoroacetic acid (10 mL) was diluted with dichloromethane (50 mL) and then chilled on ice. Pyrene **2.1c** (3.088 g, 3.489 mmol) was then added to the chilled solution and then stirred for 1 hour, off ice. The reaction mixture was concentrated *in vacuo*. Residual trifluoroacetic acid was codistilled with 5 x 20 mL dichloromethane and the resulting orange powder was dried further under high vacuum. For further purification, the powder was dissolved in a 5% MeCN:95% water mixture spiked with 0.1% TFA. The solution was passed through a 0.2 μm filter and then injected into a preparatory RP-HPLC where the gradient was set from 5% MeCN (aq, 0.1% TFA) to 90% MeCN (aq, 0.1% TFA) over a 30-minute duration. The flow rate was set to 15 mL/min. Pyrenol **2.1** was collected from 15% to 33% MeCN. Note that the preparatory RP-HPLC used has a maximum capacity of ~0.8 grams of solute; therefore, the product was divided into 4 equal portions less than 0.8 grams. Each portion was dissolved in 4.5 mL of the 5% MeCN:95% water mixture, and a total of 4 runs were made to collect the entire batch of product. The desired fractions were concentrated *in vacuo* to obtain a

yellow solid (3.201 g, 3.454 mmol, 99%).^{1}H NMR (600 MHz, DMSO-D_6) δ 9.19 (d, *J* = 9.7, 1H), 9.15 (s, 1H), 9.02 (d, *J* = 9.6, 1H), 8.92 (d, *J* = 9.7, 1H), 8.84 (d, *J* = 9.6, 1H), 8.76 (broad, 1H), 8.69 (broad, 1H), 8.66 (broad, 1H), 8.41 (s, 1H), 7.90 (broad, 9H), 3.07 (broad q, *J* = 5.9, 2H), 3.01 (broad m, 4H), 2.86 and 2.84 (coalescing, 6H); ^{13}C NMR (600 MHz, DMSO-D_6) δ 158.6 (q, *J* = 126, trifluoroacetate), 158.5 (q, *J* = 126, trifluoroacetate), 155.0, 136.9, 131.7, 130.5, 130.4, 130.3, 128. 6, 128.1, 126.2, 125.8, 125.5, 123.3, 121.2, 120.4, 118.4, 117.1 (q, *J* = 1188, trifluoroacetate), 117.1 (q, *J* = 1188, trifluoroacetate), 115.7, 40.0, 39.9, 38.6. The *m* / *z* calculated for $[M+H]^+$ was 585.1260, found 585.1270. Acceptable Δ = 2.9 mDa, observed Δ = 1.0 mDa.

Electronic absorption characterization of 2.1 in aqueous buffered solution. Equal amounts of **2.1** were portioned into three separate volumetric flasks. The three flasks were made to contain an acidic (12 M HCl), basic (pH ~13), and weakly acidic (pH ~5) aqueous solution of 0.1 M sodium tetraborate decahydrate, 0.1 M citric acid anhydrous, 0.1 M tris(hydroxymethyl)aminomethane, 0.1 M potassium phosphate monobasic, and 0.1 M potassium chloride. The weakly acidic solution was made using the acidic and basic solutions to reach the desired pH; the pH was measured using a Fisher Scientific pH/Ion 510. Ultraviolet–Visible electronic absorption spectra were recorded on a Cary 60 UV-Vis Spectrophotometer. Samples consisted of aliquots dispensed in a quartz cuvette (1 cm path length) and were kept at room temperature. Spectra were subtracted by a blank-buffering solution. The titration was performed four times to obtain an average value and standard deviation. The procedure was also replicated using a less extreme buffer system;

the aqueous solvent contained 1 mM potassium dihydrogen phosphate and no supporting electrolyte (Chapter 2.6.2).

Photoluminescence characterization of 2.1 in aqueous acidic solution. Equal amounts of **2.1** were portioned into two separate volumetric flasks. The two flasks were made to contain concentrated HCl, and deionized water titrated with concentrated aqueous HCl to pH 3. Ultraviolet–visible electronic absorption spectra were recorded on both samples. Samples consisted of aliquots dispensed in a quartz cuvette (1 cm path length) and were kept at room temperature. The smallest difference in absorbance occurred at a wavelength of 379 nm and thus 379 nm was chosen as the excitation wavelength for photoluminescence titration studies; the difference in absorbance at 379 nm was 0.009 units. Further samples were prepared by making mixtures of the two solutions. A known volume of pH 3 solution was titrated using known volumes of concentrated aqueous HCl which allowed the calculation of intermediate pH values. For each sample, an ultraviolet–visible electronic absorption spectrum and photoluminescence emission spectra were recorded. The ultraviolet–visible electronic absorption spectra were recorded on a Cary 50 Ultraviolet–Visible Spectrophotometer. Photoluminescence emission spectra were recorded using a Cary Eclipse Spectrophotometer using the following excitation (ex) and emission (em) parameters: λ_{ex} = 379 nm, $slit_{ex}$ = 5 nm, $slit_{em}$ = 5 nm, PMT = 600 V. The spectra were reported after corrections for changes in refractive indices (see Supporting Information). The titration was performed three times to obtain an average value and standard deviation.

Preparation of PET_8/2.1 with cylindrical pores used in electronic absorption measurements. Films containing 10^8 cylindrical pores cm^{-2} were prepared by the track-etching technique similar to those described in previous reports.[88,89,111] Templates were prepared by bombarding the 12 μm PET film with uranium ions of energy of 11.4 MeV per nucleon to generate 10^8 latent tracks cm^{-2} that spanned the thickness of the film (UNILAC, GSI Darmstadt, Germany). Cylindrical pores were then produced by an alkaline chemical etching procedure. For better etching results, the films were first irradiated with longwave ultraviolet light on both sides, rinsed with isopropanol, methanol, followed by a deionized water rinse. The nonporous transparent films were stirred in aqueous 9 M aqueous NaOH at ~80 ^{0}C for 15 minutes to create a porous white opaque film.

Successful coupling of **2.1** was achieved through a two-step procedure using conditions similar to those described by Nakajima and Ikada for 1-ethyl-3-(3-dimethylaminoproypl)carbodiimide (EDC) chemistry in aqueous media.[112] First, the film was rinsed with an unbuffered aqueous solution, titrated with concentrated aqueous HCl to pH 4. Next, the film was placed in an aqueous solution of 0.1 M EDC, 0.1 M NHS, 0.1 M MES buffer (pH 5.0, titrated with HCl) to activate the surface i.e. convert the carboxylic acids on the PET surface into *o*-acylisourea esters. The films were rinsed with distilled water and then stirred in an aqueous solution of 0.05 M **2.1**, pH 9 (pre-titrated with aqueous NaOH solution) for ≥ 24 hours.

Electronic absorption measurements on PET_8/2.1 with cylindrical pores. An aqueous solution of 0.1 M sodium tetraborate decahydrate, 0.1 M citric acid anhydrous, 0.1 M tris(hydroxymethyl)aminomethane, 0.1 M potassium phosphate monobasic, and

0.1 M potassium chloride was produced. The solution was titrated with concentrated aqueous HCl or 9 M aqueous NaOH to the desired pH; the pH was measured using a Fisher Scientific pH/Ion 510. After titrating the solution to the desired pH, the film was stirred for ~1 minute in the buffered solution. The film was removed and while dripping wet, pushed flush against the aperture. Ultraviolet–Visible spectra were recorded on a Cary 60 spectrophotometer. To account for the inhomogeneity of the film, each reported spectrum is an average of 10 scans taken at different locations on the film. Lastly, the spectra were baselined with a PET_8/ethylenediamine film.

Preparation of single conical nanopores used in electrochemical measurements. Single conical-pore PET templates were prepared by the track-etching technique as described in previous reports.[88,89,111] Templates were prepared by bombarding the 12 μm PET film with uranium ions of energy of 11.4 MeV per nucleon to generate a single latent track (up to 10^8 latent tracks/cm^2) that spanned the thickness of the film (UNILAC, GSI Darmstadt, Germany). The conical nanopore was then produced by a chemical etching procedure. For better etching results, the films were irradiated with longwave UV light on both sides, rinsed with isopropanol, methanol, followed by a rinse with deionized water. The film was then placed in a clean two chamber cell for subsequent etching; 9 M aqueous NaOH was placed on one side of the film to etch the latent track. To halt the reaction, an aqueous stopping medium containing 1 M formic acid and 1 M KCl was placed on the other side of the membrane. A platinum (Pt) electrode was placed on both sides of the membrane. A 1 V bias was applied from the anode which was immersed in the 9 M aqueous NaOH solution. A decrease in the resistance across the film signified pore

breakthrough and completed synthesis of a conical nanopore. The reaction was usually halted when a current of ~200 pA was observed. The resulting nanopore has a large pore opening with diameter A, which was approximated based on the bulk etch rate (for the described etching scenario) of 2.13 nm/min. The diameter of the small pore opening, a, was approximated by the following equation:

$$R = \frac{4L}{\pi g A a} \qquad \text{Equation 2.3}$$

where R is the resistance of a nanopore, L is the length of the pore, and g is the specific conductivity of the electrolyte (10 S/m for 1 M KCl aqueous solution). R was determined by calculating the slope of the linear current–voltage data between -0.1 V and 0.1 V to obtain the electrical conductance, and then reciprocating it. For pores presented herein, $a \approx 8 - 40$ nm and $A \approx 260 - 1000$ nm.

A PET_0 film was placed in a two-chamber cell. The cell was rinsed with a pH 4.0, 100 mM KCl aqueous electrolyte. An aqueous solution of 0.1 M EDC, 0.1 M N-hydroxysuccinimide, and 0.01 M MES buffer was titrated to pH 5.0 with dilute aqueous HCl. The EDC solution was placed on both sides and allowed to react for 1 hour. Without disassembling the cell, the EDC solution was then removed and electrochemical cell chambers were rinsed twice with deionized water. In a separate beaker, an aqueous 0.05 M **1** solution was titrated to pH 9.0 and placed on both sides of the film for ≥ 24 hours. Without disassembling the cell, the solution was removed and the film was rinsed five

times with deionized water. The membrane was stored in the cell using pH 7.0, 100 mM KCl, 1 mM tris aqueous electrolyte.

Electrochemical characterization on PET_0/2.1 and PET_8/2.1. Experiments were carried out using a VSP-300 potentiostat (Bio-Logic Science) equipped with low-current cables and a Faraday cage (Bio-Logic Science). The PET_0/**2.1** was placed in a two-chamber cell. A four-electrode setup was utilized. Two Pt wires served as the working and counter electrodes, while two standard calomel electrodes (KCl saturated) (SCEs) served as the reference electrodes. One of each was placed in chambers on either side of the membrane.

A 0.1 M KCl stock solution was purged via stirring and the vigorous bubbling of argon. The pH was continuously measured via a Fisher Scientific pH/Ion 510 probe that was constantly immersed in the solution. The stock solution was purged for 20 minutes before the initial cyclic voltammetric titration run. The assembled two-chamber cell was rinsed with deionized water five times, and then carefully rinsed with purged electrolyte solution five times. Cyclic voltammogram were recorded using the following parameters: a scan rate of 50 mV/s, scan range of 4 V to −4 V *vs* reference, the scan started and ended at 0 V *vs* reference, the scan cycle was repeated three times, current was measured over the last 50% of the step duration, recorded current was averaged over 10 voltage steps, the voltage resolution was set to 200 μV, and the current resolution range was set to 10 nA. The electrolyte solution in the cell was not purged during the measurement to prevent interference from bubbles. However, the stock solution was continuously purged during the cyclic voltammogram measurements. Titrations employed aqueous solutions of either HCl or KOH. Salt buildup was attenuated by titrating one purged stock solution from pH

~6 to ~1 with only HCl, and titrating another purged stock solution from pH ~6 to ~11 with only KOH. Measurements were performed from pH ~6 to ~1, and then from pH ~6 to ~11.

Determining binding coverage of photoacid in nanopores. As described above, conical pores in a PET_0 film and PET_8 film were prepared, and the two films were completely modified with **2.1** to form PET_0/**2.1** and PET_8/**2.1**. Separately, **2.1** was hydrolyzed from both modified films using 5 mL of aqueous 1 M NaOH. The absorbance spectra of both samples were recorded on a Cary 60 UV-Visible spectrophotometer. The binding surface coverage of **2.1** inside a single nanopore was calculated using the Equation SI 2.10.

Synthesis and electronic absorption measurements on trimethyl 4,4',4''-(((((8-hydroxypyrene-1,3,6-trisulfonyl)tris(azanediyl))tris(ethane-2,1-diyl))tris(azanediyl))tris(carbonyl))tribenzoate (2.2): Mono-methyl terephthalate (0.006 g, 0.03 mmol), EDC (0.008 g, 0.05 mmol), NHS (0.006 g, 0.05 mmol), MES buffer (0.005 g, 0.03 mmol) was added to a mixture of 5 mL of water and 5 mL of MeOH. The reaction was stirred at room temperature for 1.5 hours. Then **2.1** (0.006 g, 0.006 mmol) was added and stirred at room temperature for 0.5 hours. The reaction vessel was heated to 60 ^{0}C and stirred for four days. The solution was diluted with water so that major absorption peaks were ~0.3 units. UV-Visible spectra were recorded on a Cary 60 UV-Visible spectrophotometer and baselined with deionized water. The cocktail containing **2.2** was titrated using concentrated aqueous HCl and 9 M aqueous NaOH to minimize changes to the concentration of **2.2**.

Preparation of PET_8/2.1 with conical pores used in fluorescence microscopy measurements. Conical-pore PET templates were prepared by the track-etching technique as described in previous reports.[88,89,111] Templates were prepared by bombarding the 12 μm PET film with uranium ions of energy of 11.4 MeV per nucleon to generate a single latent track (up to 10^8 latent tracks/cm^2) that spanned the thickness of the film (UNILAC, GSI Darmstadt, Germany). The conical nanopore was then produced by a chemical etching procedure. For better etching results, the films were irradiated with longwave ultraviolet light on both sides, rinsed with isopropanol, methanol, followed by a deionized water rinse. The film was then placed in a clean two chamber cell for subsequent etching; 9 M aqueous NaOH was placed on one side of the film to etch the latent track. To halt the reaction, an aqueous stopping medium containing 1 M formic acid and 1 M KCl was placed on the other side of the membrane. A Pt electrode was placed on both sides of the membrane. A 1 V bias was applied from the anode which was immersed in 9 M aqueous NaOH. A decrease in the resistance across the film signified pore breakthrough and complete synthesis of a conical nanopore. The reaction was usually halted when a current of ~1 μA was observed.

The areal surface of a PET_8 film was modified with non-fluorescent taurine molecules followed by **2.1** such that **2.1** was located primarily inside the tips of the nanopores (PET_8/T+**2.1**). The PET_8 film was placed in a two-chamber cell. The cell was rinsed with a pH 4.0, 100 mM KCl aqueous electrolyte. Reverse osmosis water was placed on the large pore side of the film. An aqueous solution of 0.1 M EDC, 0.1 M N-hydroxysuccinimide, and 0.01 M MES buffer was titrated to pH 5.0 with dilute aqueous

HCl. The EDC solution was placed at the tip side of the film and allowed to react for 0.5 minutes. Without disassembling the cell, the EDC solution was then removed and electrochemical cell chambers were rinsed twice with deionized water. In a separate beaker, an aqueous 0.05 M taurine was titrated to pH 9.0 and placed on both sides of the film for ≥ 4 hours. The cell was rinsed with a pH 4.0, 100 mM KCl aqueous electrolyte. Deionized water was placed on the base side of the film. An aqueous solution of 0.1 M EDC, 0.1 M N-hydroxysuccinimide, and 0.01 M MES buffer was titrated to pH 5.0 with dilute aqueous HCl. The EDC solution was placed at the small tip side of the film and allowed to react for 20 minutes. Without disassembling the cell, the EDC solution was then removed and electrochemical cell chambers were rinsed twice with deionized water. In a separate beaker, an aqueous 0.05 M **2.1** solution was titrated to pH 9.0 and placed on both sides of the film for ≥ 24 hours. Without disassembling the cell, the solution was removed and the film was rinsed with deionized water five times. The membrane was stored in the cell, wetted with pH 4.0, 100 mM KCl aqueous electrolyte.

Two-photon fluorescence microscope setup for spectral imaging. A custom built two-photon excitation microscope based on an Olympus FV1000 (Olympus Corporation, Tokyo, Japan) was used for all fluorescence microscopy experiments. The microscope was equipped with an Olympus 60X UPlanApo objective (NA = 1.2 WI) (Olympus Corporation, Tokyo, Japan). A mode-locked 80 MHz Ti:Sapphire laser Chameleon Ultra (Coherent Inc., Santa Clara, CA) tunable in the range from 690 nm to 1040 nm was used for multiphoton excitation. The laser power was controlled by an acoustic optical modulator driven by SimFCS (LFD,UCI). A grating based spectrograph (Andor SRS303i) with a 512 channel

ultrafast EMCCD (Andor iXon Ultra) was used to collect spectrum from every pixel with a dispersion of 50 lines/600 nm blaze. In order to ensure spectral acquisition was synced to the frame clock and sampled to the pixel clock, the Olympus FV1000 galvo scanning mirrors was driven externally by SimFCS (LFD, UCI) using a data acquisition controller board (IOTECH DAQboard 3001). The spectral images of 256 x 256 pixels were collected with a pixel dwell time of 32 microseconds. The spectra are corrected with a spectral response curve of the system calibrated using a tungsten lamp, by a technique reported by Chen and coworkers.[113] The multiphoton imaging measurements were carried out with an open pinhole and the luminescent photons from the microscope were delivered to the spectrograph using a 200 μm multimode optical fiber.

Data processing of spectral images from two-photon fluorescence microscopy. All data was obtained and analyzed using SimFCS software (Laboratory for Fluorescence Dynamics, UCI, http://www.lfd.uci.edu/globals/, Irvine, CA).

Sample preparation for two-photon fluorescence microscopy. PET films were cut to <0.5 cm × <0.5 cm rectangles and placed flat on a glass bottom microwell dish (MatTek Corporation). The small tip side of the nanopores were face down. A titrated solution was pipetted on the film; the solutions did not contain buffer or salt. Solutions were pre-titrated with concentrated aqueous solutions of either HCl or NaOH. The film was completely immersed and the solution was pipetted back and forth over the film several times as a means to mix the solution into the nanopores. A glass microscope coverslip was cut and pressed on the top of the film. Solution that protruded from the coverslip side was

pipetted away. Enough solution was present in-between the glass microwell dish and glass coverslip to completely wet the nanopores.

Unmodified PET films and PET_8 films that were surface modified with taurine molecules via carbodiimide chemistry (PET_8/T) displayed excitation wavelength-dependent emission (Table S2). An excitation wavelength of 900 nm was used to excite the single-photon isosbestic point (~450 nm, Figure 2.1). Raw emission spectra from PET_8/T+**1** were individually subtracted by scaled emission spectra of PET_8/T.

Chapter 2.6. Supporting Information.

Chapter 2.6.1. Determination of pK_a values.

Several processes for analyzing titration data to determine pK_a values have been reported.[114,115] We carefully analyzed several methods and in detail compared the two that could enable analysis of the formation/loss of both the acidic and basic form of the molecule. For this, we used the maximum absorbance for each species and full spectral modeling.[114,115] The maximum absorbance method was used for all simple cases where spectral features changed in ideal manners (Figure 2.1Figure 2.2,Figure 2.4,Figure SI 2.1,Figure SI 2.4,Figure SI 2.11) whereas full spectral modeling was used when spectral features did not transition uniformly (Figure 2.7). Irrespective of the method, data was obtained for the fraction of each species, θ, as a function of pH which was fit to the modified Henderson–Hasselbalch equation, that is Hill equation, Equation 2.1. The pK_a value was calculated as the average of the pH values at θ = 0.5 (the inflection points of the titration curves) for the protonated and

deprotonated species. Data convoluted by three pK_a values was fit to a linear combination of three Hill equations:

$$\theta = \frac{A_{o_1}}{1 + 10^{\,n_1(\mathrm{pH}-\mathrm{p}K_{a_1})}} \pm \frac{A_{o_2}}{1 + 10^{\,n_2(\mathrm{pH}-\mathrm{p}K_{a_2})}} \pm \frac{A_{o_3}}{1 + 10^{\,n_3(\mathrm{pH}-\mathrm{p}K_{a_3})}} \qquad \text{Equation SI 2.1}$$

where θ is the total fraction for all three sets of protonated/deprotonated species, n_i are the Hill coefficients, and A_{o_i} are weights of each (de)protonation event. For solution studies the combinations were additive; however, when the equation was used to fit electrochemical data, the plus (minus) signs were changed to account for the positive (negative) surface polarity each functional group would impose.

Chapter 2.6.2. Intramolecular stabilization of the ground-state pK_a of 2.1.

The main text shows the titration of tris(sulfonamide) pyrenol **2.1** in a highly buffered system with supporting electrolyte, which was in part done to shield the charged ammonium groups thereby preventing the influence of the ammonium groups on the lowest energy electronic transitions of the dye. A less extreme buffer system was employed to fully understand the effect of non-shielded ammonium groups. The titration of **2.1** in an aqueous solvent with 1 mM potassium dihydrogen phosphate and no supporting electrolyte is shown below (Figure SI 2.1). The data suggest that pK_a of the hydroxyl is 4.6, which is 1.2 units more acidic than the dye dissolved in the buffered system with supporting electrolyte. Potentially, the increased acidity is due to intramolecular stabilization of the nearby ammonium group

on the hydroxyl conjugate base. Similar intermolecular stabilization of has been seen in 8-hydroxypyrene-1,3,6-trisulfonate (HPTS). Halder and colleagues showed that the pK_a of HPTS decreased from 7.3 in solution to 6.9 when lysozyme enzymes were added to solution.[116] The lysozyme enzymes formed 1:1 complexes with HPTS molecules and interacting amino acids stabilized the conjugate base through hydrogen bonds, van der Waals interactions, and electrostatic interactions.[116]

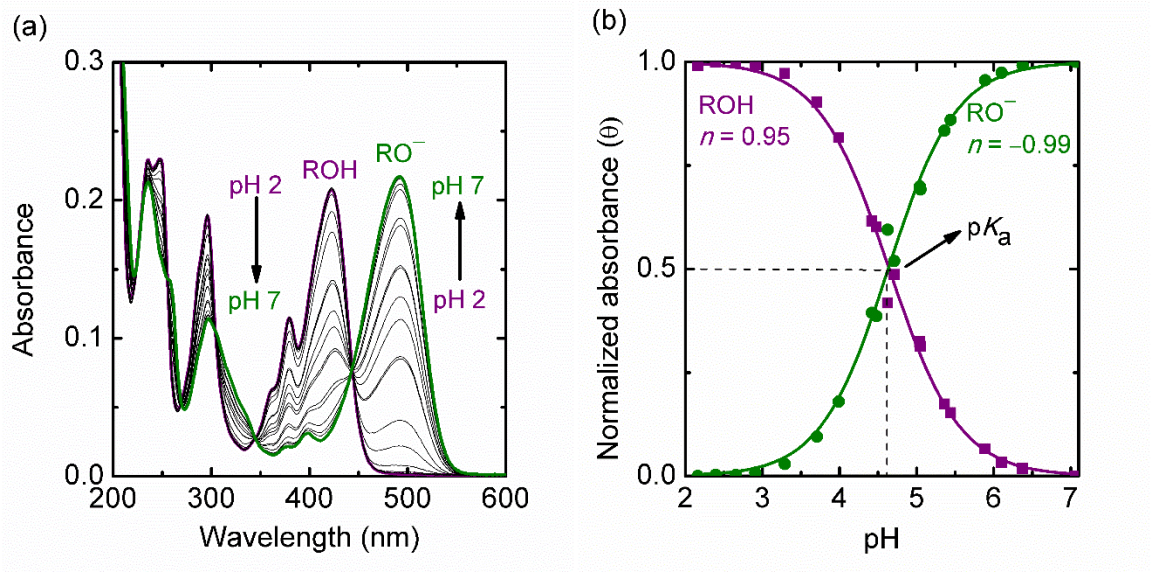

Figure SI 2.1. (a) Electronic absorption spectra of **2.1** dissolved in aqueous 1 mM KH_2PO_4. The completely protonated and deprotonated ground-state spectra are bolded and colored and are labeled with ROH and RO^-, respectively. (b) Plot of normalized absorbance (θ) at the λ_{max} (421 nm and 492 nm) for each species as a function of pH, and displayed with non-linear least square best fits to the Hill equation (Figure 2.1).

Chapter 2.6.3. Determination of pK_a^* values by Förster cycle analysis.

The Förster cycle (Figure SI 2.2) analysis is an indirect method used to approximate excited-state acid–base equilibria based on differences in molar enthalpy between the protonated and deprotonated species and energies of the 0-0 electronic transitions ($E_{0\text{-}0}$). This analysis is only valid if the (*i*) excited-state protonated and deprotonated species equilibrate during their excited-state lifetimes,[117,118] (*ii*) both excited-state species fluoresce,[119] (*iii*) both species emit at equivalent quantum yields,[119] (*iv*) the entropy associated with proton dissociation in the ground-state and excited-state are the same,[120] and (*v*) the energies of $E_{0\text{-}0}$ are determined precisely.[121] For example, the calculated pK_a^* differs by more than 0.5 units when the wavelength used to calculate $E_{0\text{-}0}$ is misinterpreted by 5 nm from a hypothetical value of 450 nm, a ~0.03 eV change. The $E_{0\text{-}0}$ can be approximated solely on the absorption spectra or fluorescence spectra, or by using a combination of the two.[117,119] The latter method is superior such that when used in the Förster cycle analysis, the obtained pK_a^* value is most comparable to the pK_a^* value determined via fluorescence titration.[6] This method estimates $E_{0\text{-}0}$ as the average of the lowest transition energies measured from the absorption and emission spectra, and when combined with the Förster cycle analysis is the protocol used herein as a first approximation to pK_a^* values (Equation 2.2, Figure SI 2.2).

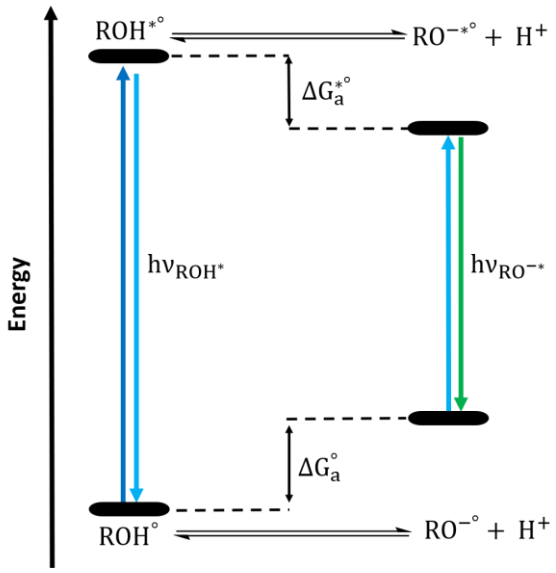

Figure SI 2.2. Förster cycle showing free-energy changes due to acid–base equilibria of hydroxyl photoacids in the ground-state (ΔG_a°) and excited-state ($\Delta G_a^{*\circ}$). When p*K*a > 0, ΔG is positive (unfavorable), because this plot assumes standard-state conditions for protons, i.e. $a_{H^+} = 1 \approx 1$ M.

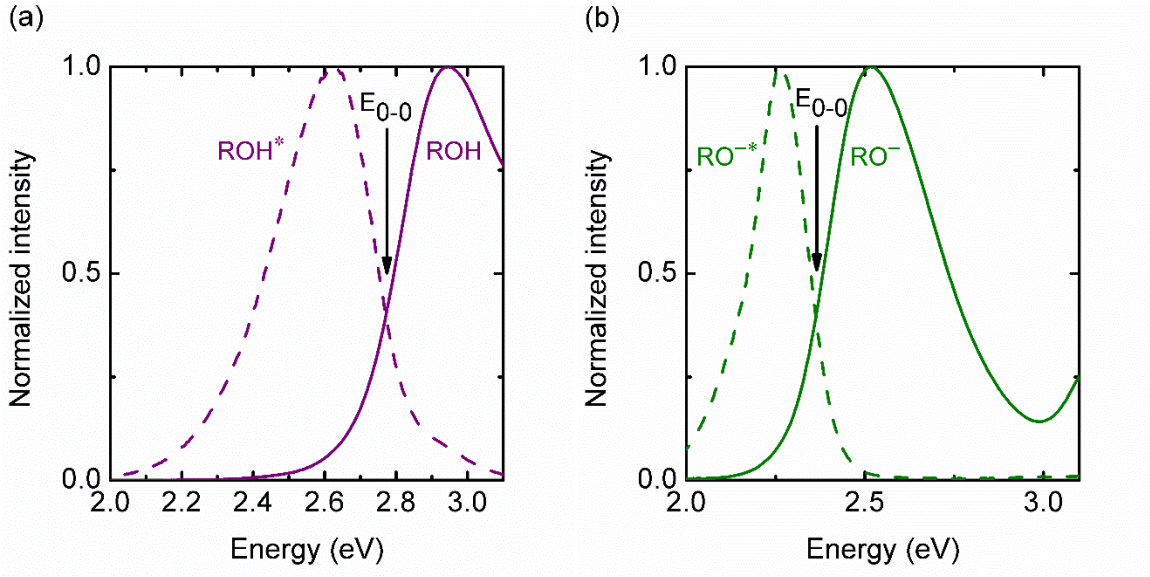

Figure SI 2.3. Normalized absorbance (solid) and photoluminescence intensity (dashed) spectra used to determine the energy of the 0-0 electronic transitions of **2.1** in solution for (a) the protonated photoacid (ROH and ROH*, 2.77 eV) and (b) deprotonated photoacid (RO^- and RO^{-*}, 2.36 eV).

Figure SI 2.3 was derived from absorbance and photoluminescence intensity spectra by converting abscissa values using the Planck relation:

$$E = \frac{hc}{e\lambda} \qquad \text{Equation SI 2.2}$$

where E is the energy (eV), h is Planck's constant (6.626 x 10^{-34} J s), c is the speed of light in vacuum (2.998 x 10^{8} m s^{-1}), e is the elementary charge (1.602 x 10^{-19} C), and λ is the wavelength (m). The absorbance ordinate values were normalized, while the

photoluminescence ordinate values were transformed by the Jacobian equation (Equation SI 2.3)[122,123] and then normalized. This transformation converts signal per unit wavelength into a signal per unit energy.

$$\text{Intensity} = \text{PL}_{\text{observed}}\left(\frac{hc}{E^2}\right) \qquad \text{Equation SI 2.3}$$

Chapter 2.6.4. Acid–base titration procedure with photoluminescence detection.

Acid–base titration with photoluminescence detection is superior to the Förster cycle analysis at determining pK_a^* values. All photoluminescence spectra were corrected using Equation SI 2.4. The first term is the raw photoluminescence intensities corresponding to abscissa coordinate. The second term corrects for inner filter effects, specifically the fluctuations in photoluminescence intensity due to changes in the amount of excitation light absorbed and the absorption of emitted light.[114] This factor was necessary when sample transmittance values were <85% at wavelengths equal to and greater than the excitation wavelength. The third term corrects for differences in the intensity of photoluminescence reaching the detector caused by differences in refractive indices of mediums.[124] The fourth term is a correction factor that corrects for wavelength detection dependencies.

$$\text{PL}_{\text{corrected}} = \text{PL}_{\text{observed}}\left(10^{\left(\frac{\text{A}_{\text{ex}}+\text{A}_{\text{em}}}{2}\right)}\right)\left(\frac{\eta^2_{\text{pH X}}}{\eta^2_{\text{pH 2}}}\right)(\text{C}) \qquad \text{Equation SI 2.4}$$

where A_{ex} is the absorbance value of sample at the excitation wavelength and A_{em} is the absorbance value of the sample at the emission wavelength; $\eta_{pH\ X}$ is the refractive index of the solution tested at some given pH and $\eta_{pH\ 2}$ is the refractive index of water at pH 2 which was used normalize the data, which in this case was 1.333; C is the correction factor due to attenuation of observed photoluminescence introduced by the monochromator, lamp, detector, and/or reflectance from the optics.

Photoluminescence titration data does not provide a direct measurement of the pK_a^* because the experiments occur at steady-state (as opposed to equilibrium) and therefore the experiments do not account for differences in the rates of excited-state relaxation of the emitting species, i.e. ROH* and RO^{-*}. Assuming the excited-states reach a quasi-equilibrium, which is not always true especially for photoacids with short-lived excited-states,[115] the actual pK_a^* can be calculated from the observed pK_a^* by correcting for the lifetimes of each excited-state species (Equation SI 2.5).[121]

$$pK_a^* = pK_{a_{obs}}^* + \log\left(\frac{\tau_{ROH}\ *}{\tau_{RO^-}\ *}\right) \qquad \text{Equation SI 2.5}$$

where τ is lifetime and $pK_{a_{obs}}^*$ is the pH value at which θ = 0.5. The lifetimes of ROH* and RO^{-*} of **2.1** were determined to be ~4 ns and ~6 ns, respectively, via fluorescence lifetime imaging. For **2.1** in solution, $pK_{a_{obs}}^*$ = -0.37 (Figure SI 2.4c) and using Equation SI 2.5, pK_a^* = -0.55. However, the conventional pH scale is less appropriate for concentrated acidic

solutions because the effective activity of protons increases at a more drastic rate as a function of increasing proton concentration.[125,126] Therefore, Hammett and Devrup developed the Hammett acidity function, H_0, to account for the highly acidic solutions (Figure SI 2.4d).[125] Consequently, photoluminescence data in the main text taken using acid concentrations greater than 1 M were plotted and reported using c after conversion using Equation SI 2.6 (Figure 2.2)Figure 2.2. (a) Photoluminescence spectra of **2.1** dissolved in differing concentrations of aqueous HCl. The excitation wavelength (λ_{ex}) was 379 nm. Emission from the completely protonated and deprotonated excited-states are represented by ROH^* and RO^{-*}, respectively. (b) Plot of normalized photoluminescence (PL) intensity (θ) at the λ_{max} for each species (476 nm and 545 nm) as a function of Hammett acidity (H_0 >1 M HCl) and pH (< 1 M HCl). Displayed with non-linear least square best fits to the Hill equation (Equation 2.1).

$$H_0 = -0.3763445x + 0.09397265 \qquad \text{Equation SI 2.6}$$

where H_0 is the Hammett acidity and x is the concentration of protons (M). Using Hammett acidities and lifetime correction, a more accurate pK_a^* was obtained for **2.1** in solution, pK_a^* = -0.57 (H_0 = 1.31,Figure 2.2) instead of $pK_{a_{obs}}^*$ = -0.37 (Figure SI 2.4).

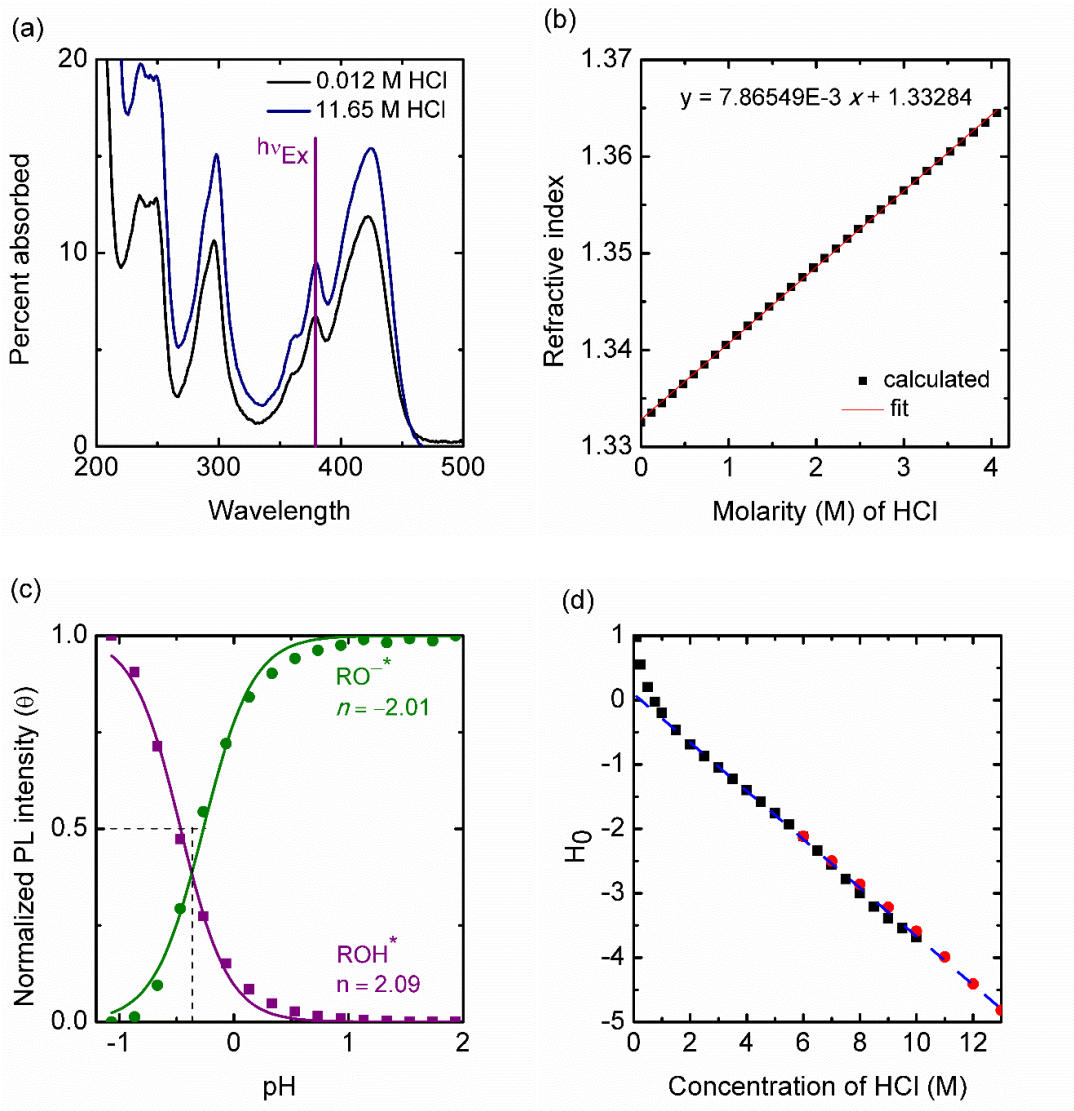

Figure SI 2.4. (a) Absorbance spectra of **2.1** in acidic HCl solutions at the two extremes of the photoluminescence titration. (b) Plot of refractive indices for various aqueous HCl solutions at 25 ^{0}C tabulated by Olsen and Washburn,[127] and displayed with a linear best-fit. (c) Plot of normalized photoluminescence (PL) intensity (θ) derived from relative peak heights (476 nm and 545 nm) as a function of pH. Displayed with non-linear least square best fits to the Hill equation (Equation 2.1)**.** (d) Plot of Hammett acidity values, H_0, for various aqueous HCl solutions reported by Paul and Long (black squares)[128] and by Bell and coworkers (red circles),[129] and displayed with a linear best-fit, Equation SI 2.6 (dashed blue line).

Chapter 2.6.5. Dyes located in an ensemble of nanopores.

Localization of **2.1** within PET pores was supported by data obtained using two-photon fluorescence microscopy of PET_8/**2.1** (Figure SI 2.5and Figure 2.3). The collective assortment of spectral features from the solution and film studies are presented in Table 2.1.

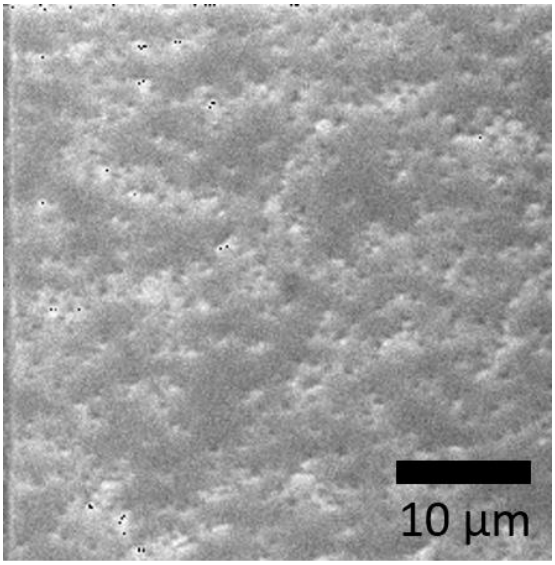

Figure SI 2.5. Optical microscopy reflection image of PET_8/**2.1** from Figure 2.3 of the main text; dark dots are openings on the large side of each conical nanopore.

Table SI 2.1 Spectral characteristics of **2.1** and PET_8/**2.1**.

Sample	2.1		**PET_8/2.1**	
Species	ROH	RO^-	ROH^*	RO^{-*}
$\lambda_{abs,\,max}$ (nm)	421	492	432	519
$\lambda_{em,\,max}$ (nm)	474	547	489	548
τ_{ES} (ns)	**3.9**	**5.8**	**1.0**	**1.2**

Chapter 2.6.6. Effects of surface charge on surface potentials and the concentration of protons at the surface.

The effects of surface charge, σ_D, on surface potential, Ψ_D, is described by the Debye-Hückel equation[130]:

$$\Psi_D = \frac{\lambda_D \sigma_D}{\varepsilon \varepsilon_0} \qquad \text{Equation SI 2.7}$$

where λ_D is the Debye length which is approximately 1.1×10^{-9} m for a nanopore immersed in 100 mM KCl, $\varepsilon_0$is the permittivity of vacuum ($8.85418717\times 10^{-12}$ F/m), and ε is dielectric constant of water at room temperature (80.1). The surface charges at the tip of nanopores with tip diameters of 10-100 nm has been reported to be 0.1-1 C m^{-2},[288,95,96] therefore the surface potential are 0.15-1.5 V.

Equation SI 2.8[130] is a Boltzmann relationship that approximates the surface concentration of protons ($c_{H^+}^{(0)}$) based on the effect of surface potential (Ψ_0) on the bulk concentration of protons (c_{H^+}).

$$c_{H^+}^{(0)} = c_{H^+} e^{-\frac{q\,\Psi_0}{\kappa T}}$$ Equation SI 2.8

where q is the elementary charge (1.60217662×10^{-19} C), κ is Boltzmann's constant (1.38064852×10^{-23} J K^{-1}), and T is temperature (293.15 K). The equation was solved for Ψ_0 with $c_{H^+}^{(0)}$ = 1.3×10^{-7} and c_{H^+} = 7.910^{-6} because the pK_a value of the hydroxyl group on **1** was 6.9 and 5.1 at the tip and bulk regions, respectively; then Ψ_0 was used in Equation SI 2.7 to solve for σ_D.

Chapter 2.6.7. Understanding electrochemical characterization of nanopores.

Functionalization of the inner surface of each nanopore tip with charged groups altered the ionic current–potential behavior, analogous to that reported previously.[68,89,98–100] Pore tips containing mostly fixed negative (positive) charges are thought to be cation-selective (anion-selective) and exhibit current rectification with low current resulting from applied positive (negative) voltages, i.e. anodic (cathodic) reactions occur at the electrode positioned on the side of the membrane with the large pore opening. The low current behavior is thought to be caused by an enhancement of electrostatic stabilization at the pore tip where the radius of the pore is comparable to the double-layer thickness. The electrostatic stabilization traps cations (anions) at the pore tip thereby preventing cation (anion) conduction from the large region to the small region of the pore.[61,66,131] Pores with mostly neutral tips exhibited ohmic, and more resistive, ionic currents due to ion exclusion resulting from hydophobicity.[61,89]

Chapter 2.6.8. Electrochemical characterization of PET$_n$/2.1 films.

Cyclic voltammetry of PET$_0$/**2.1** and PET$_8$/**2.1** as a function of solution pH was used to assess ion-selectivity, estimate modification efficiency, diagnose the number of amide bonds formed between **2.1** and PET, and approximate the pK_a values of protic groups inside nanopores (Figure 2.5). The cyclic voltammogram titration plots for the other **2.1**-modified nanopores and their unmodified control are presented in Figure SI 2.6 and Figure SI 2.7.

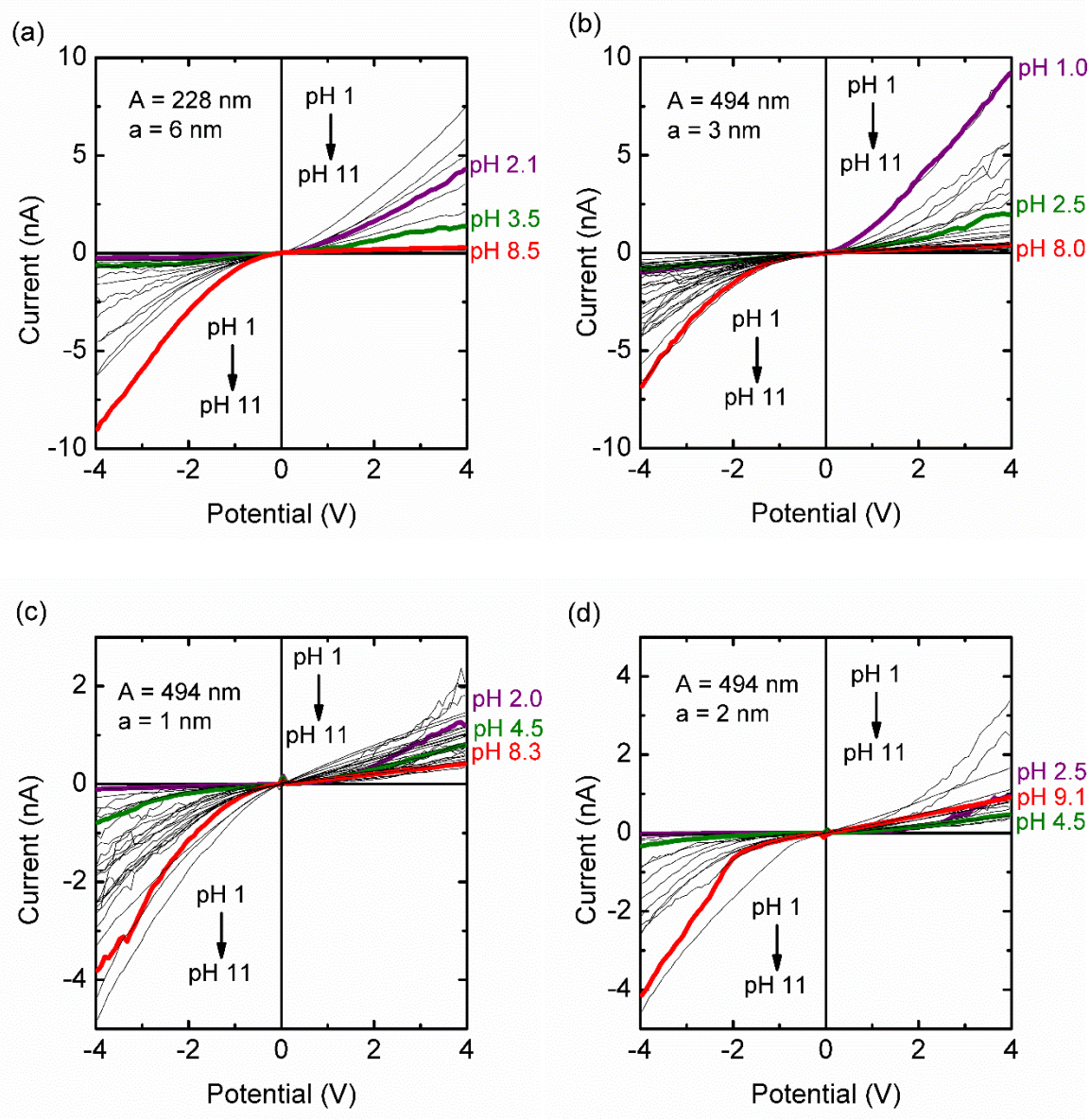
(a)
A = 228 nm
a = 6 nm
pH 1
pH 11
pH 2.1
pH 3.5
pH 8.5
pH 1
pH 11
Current (nA)
Potential (V)
(b)
A = 494 nm
a = 3 nm
pH 1
pH 11
pH 1.0
pH 2.5
pH 8.0
pH 1
pH 11
Current (nA)
Potential (V)
(c)
A = 494 nm
a = 1 nm
pH 1
pH 11
pH 2.0
pH 4.5
pH 8.3
pH 1
pH 11
Current (nA)
Potential (V)
(d)
A = 494 nm
a = 2 nm
pH 1
pH 11
pH 2.5
pH 9.1
pH 4.5
pH 1
pH 11
Current (nA)
Potential (V)

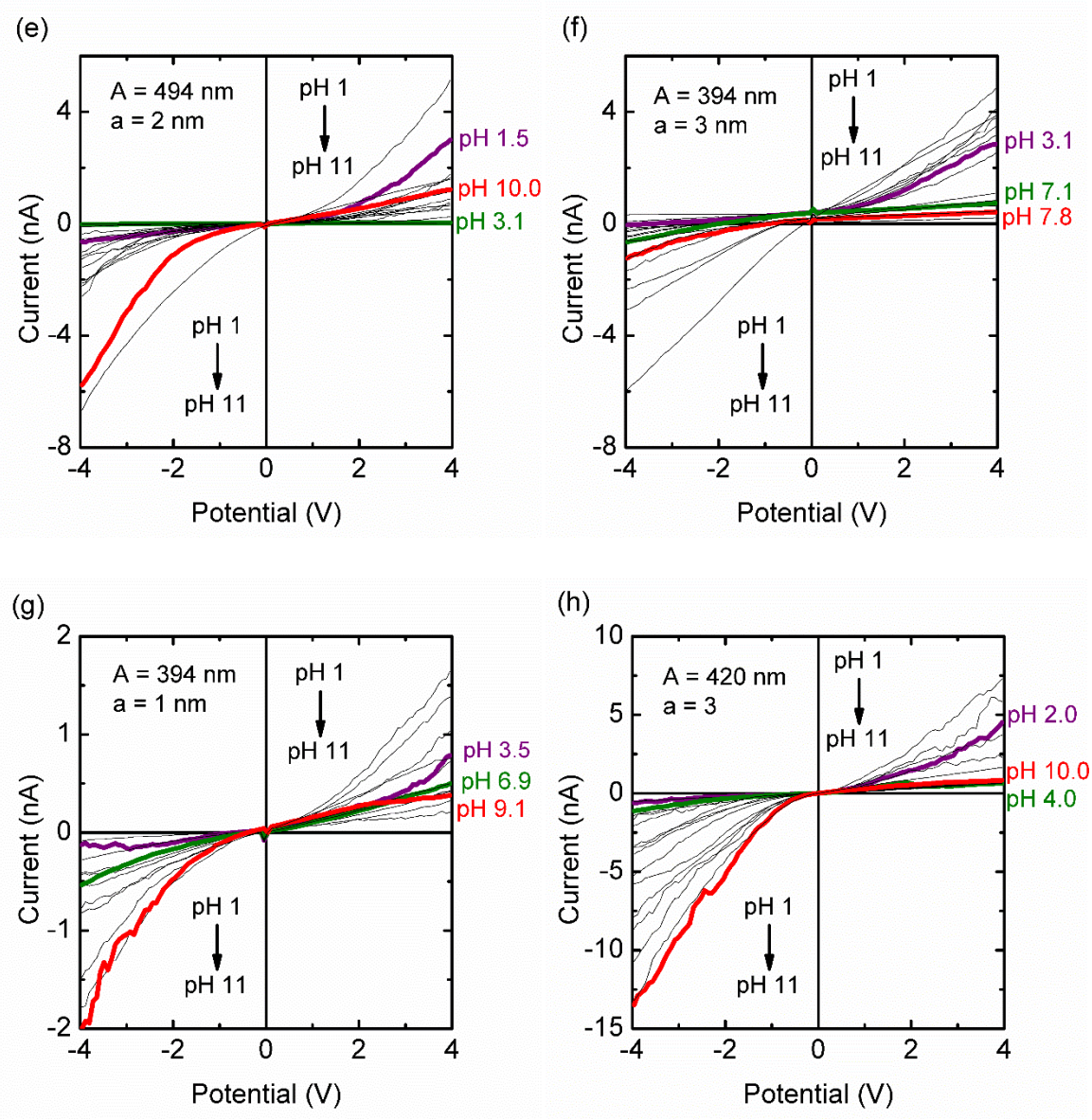
(e)
A = 494 nm
a = 2 nm
pH 1
pH 11
pH 1.5
pH 10.0
pH 3.1
pH 1
pH 11
Current (nA)
Potential (V)
(f)
A = 394 nm
a = 3 nm
pH 1
pH 11
pH 3.1
pH 7.1
pH 7.8
pH 1
pH 11
Current (nA)
Potential (V)
(g)
A = 394 nm
a = 1 nm
pH 1
pH 11
pH 3.5
pH 6.9
pH 9.1
pH 1
pH 11
Current (nA)
Potential (V)
(h)
A = 420 nm
a = 3
pH 1
pH 11
pH 2.0
pH 10.0
pH 4.0
pH 1
pH 11
Current (nA)
Potential (V)

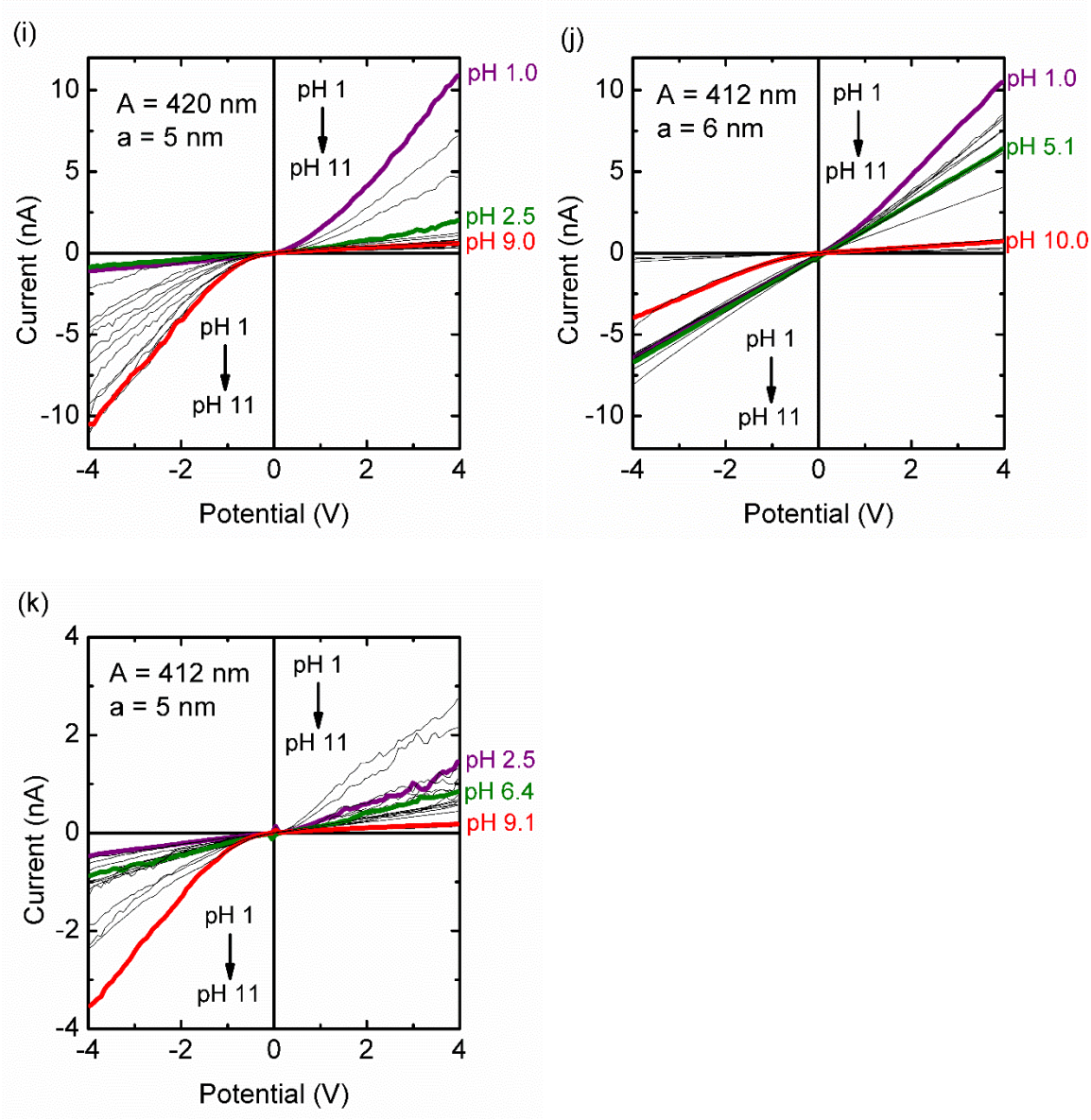

Figure SI 2.6. Cyclic voltammograms of PET_0/**2.1** samples immersed in aqueous 100 mM KCl. Also shown are the large (A) and small (a) diameters of the conical nanopore. Data presented here were used construct Figure SI 2.8and Figure 2.6a.

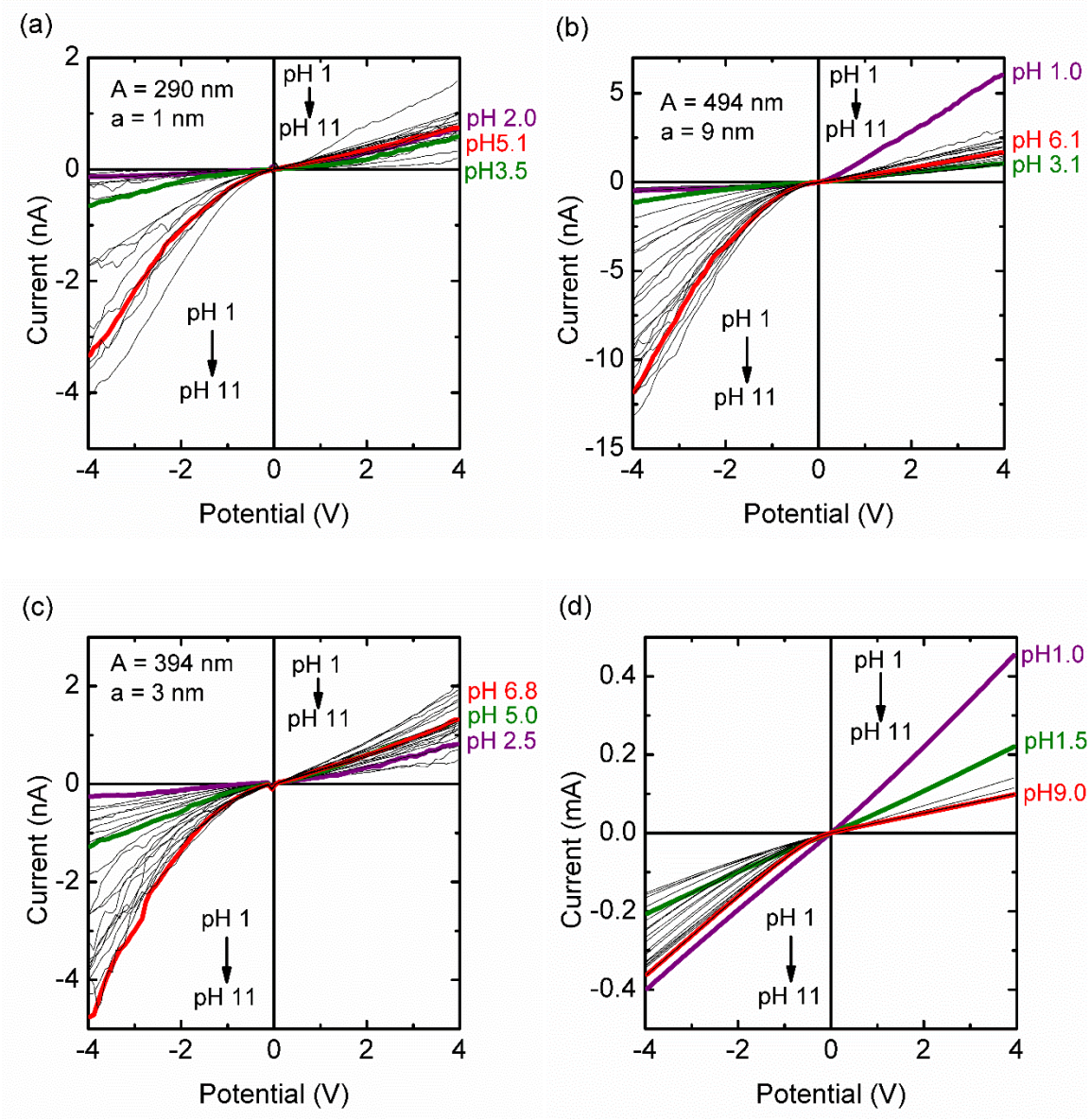

Figure SI 2.7. (a-c) Cyclic voltammograms of unmodified PET_0 samples immersed in aqueous 100 mM KCl. Also shown are the large (A) and small (a) diameters of the conical nanopore. (d) Cyclic voltammograms of unmodified PET_8 sample immersed in aqueous 100 mM KCl. Data presented here was used construct Figure SI 2.8and Figure 2.6a.

These cyclic voltammogram titration plots were used to plot the current values at ± 4 V versus pH (Figure SI 2.8). Rectification values were derived by taking the absolute current values of Figure SI 2.8, dividing the maximum current by minimum current at a given pH, and then normalizing the data. The minimum rectification value of each curve before normalization is ~1. PET_8/**2.1** has a maximum rectification value at pH 8.5. The rectification values of PET_0/unmodified, PET_8/unmodified, PET_0/**2.1**, and PET_8/**2.1** at pH 8.5 were 4.2, 7.6, 3.4, and 74.2, respectively. In the cyclic voltammogram plots (Figure 2.5 Figure SI 2.6Figure SI 2.7), violet curves correspond to the pH value at which a positive surface has the highest rectification value. Green curves correspond to the pH value at which the surface is neutral, that is, the pH at which rectification is lowest. Red curves correspond to the pH value at which a negative surface has the highest rectification value. Diameters were derived using the experimental equation, Equation 2.3.

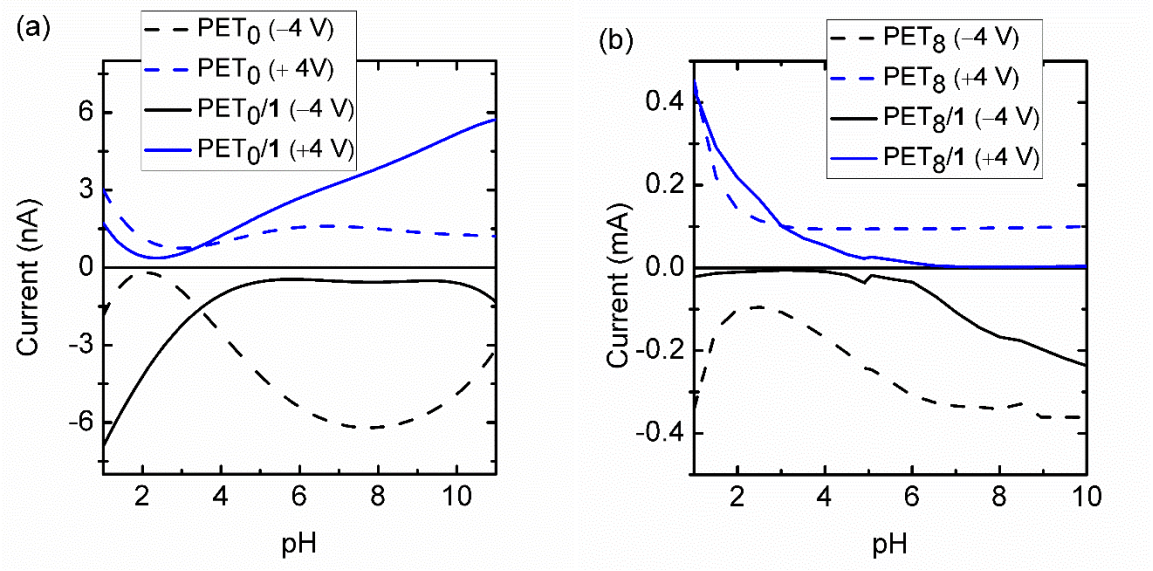

Figure SI 2.8. Averaged current values at ±4 V versus pH of unmodified and modified (a) single nanopores and (b) an ensemble of nanopores in 100 mM KCl. Plot constructed from Figure SI 2.6and Figure SI 2.7.

The plot of rectification as a function of pH for the PET$_8$/**2.1** is shown below (Figure SI 2.9). The plot was fitted to a linear combination of Hill equations, Equation SI 2.1, which accounts for changes in surface charge polarity such the fraction of positive charge imparted by ammonium groups is subtracted by the fraction of negative charge imparted by the alkoxide and carboxylate groups.

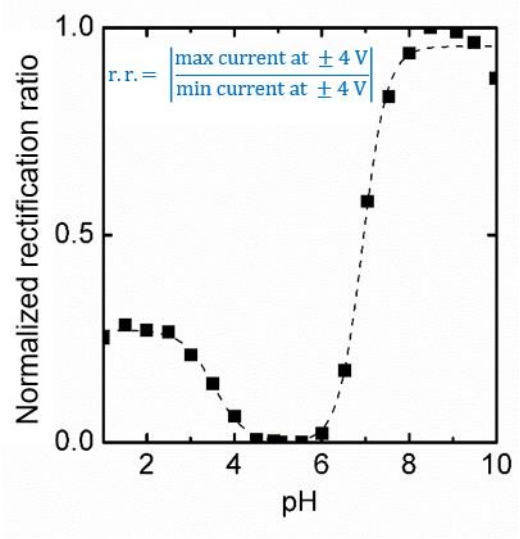

Figure SI 2.9. Rectification ratio as a function of pH displayed in a PET_8/**2.1** immersed in aqueous 100 mM KCl and displayed with a non-linear least square best fit to a linear combination of three Hill equations (Equation SI 2.1).

The obtained fitted-values of Figure SI 2.9 are shown in Table SI 2.2. The relatively large n_{NH3} value of 5 is due to lack of sufficient data at alkaline pH values, which could not be obtained without damaging PET. Meaning, this precluded us from obtaining a full titration event for the ammonium groups.

Table SI 2.2 Calculated fitted parameters of the fit displayed in Figure SI 2.9 (rectification ratio as a function of pH displayed in a PET_8/**1** immersed in aqueous 100 mM KCl) to Equation SI 2.1 (linear combination of three Hill equations).

Unbound functional group	A_{o_i}	n_i	pK_a of groups at nanopore tips
Ammonium of dye (NH3)	0.27	5	>10
Alkoxide of dye (OH)	0.96	-1.5	6.9
Carboxylate of PET (COOH)	0.27	1.2	3.5

The values in Table S2 were used to elucidate the surface environment of PET_8/**2.1** because the weights of the fits (A_{o_i}) are representative of the relative number of functional groups with respect to one another. Explanation for the approximation of binding coverage of the photoacid is presented here via Equation S7. The numerator in Equation S7 is the number of photoacids which is equal to $A_{o_{OH}}$ because an individual **2.1** molecule contains one hydroxyl. The denominator is the total number of binding sites, where the number of reacted sites is the three times the number of hydroxyls ($A_{o_{OH}}$ [because an individual **2.1** has three primary amines before binding]) minus the number of primary ammoniums unreacted ($A_{o_{NH3}}$), and the number of unreacted sites is the number of carboxylates ($A_{o_{COOH}}$). Multiplying that ratio by the preexisting coverage of carboxylate groups (C_{COOH}) results in the number of dyes per area.

$$C_{dye}^{Echem} = \frac{A_{o_{OH}}}{3A_{o_{OH}} - A_{o_{NH3}} + A_{o_{COOH}}} \times C_{\mathrm{COOH}} \qquad \text{Equation SI 2.9}$$

A native nanopore is reported to be adorned with one carboxylate group per nm^2, that is $C_{COOH} = 1$ group per nm^2.[105] With this and the inputs of Table SI 2.2, the C_{dye}^{Echem} = 0.33 dyes nm^{-2}.

Chapter 2.6.9. Electrochemical evidence of binding in nanopores.

Two-photon fluorescence microscopy measurements provided visual evidence suggesting pyrenol **2.1** molecules were bound to the inside of nanopores (Figure 2.3, Chapter 2.6.5). Further evidence of **2.1** bound to the inside of nanopores was provided by electrochemical measurements which depicted changes in the ion-selectivity and buffering capacity post dye modification. Figure 2.6a clearly shows that the isoelectric points of native PET_0 and PET_8 films were at pH 3.0, which is consistent with other reports.[89,132] Post modification, the average isoelectric point for PET_0/**2.1** was at pH 3.9, and the isoelectric region of the PET_8/**2.1** was at pH 4.5-6, with the midpoint at pH 5.3 (Figure 2.6a). This large isoelectric region likely resulted from the ensemble of differences in microenvironments or distribution of pore sizes. The changes in isoelectric points strongly suggest the surface of the nanopore was modified. The change in buffering capacities of covalently-modified PET nanopores has been extensively documented, some exemplary modifications include amino acids[100,133] and ionic polymers.[101,102,134]

Chapter 2.6.10. Estimation of binding coverage of 2.1 in nanopores.

As detailed in the experimental section, the carboxylate groups were converted into amide bonds via carbodiimide coupling chemistry. The binding surface coverage of **2.1** inside a nanopore was calculated using a two-step coupling/hydrolysis method with spectrophotometric detection and Equation SI 2.10.

$$C_{dye}^{Hydrolysis} = \frac{V N_A \left[\frac{\Delta A}{L\varepsilon}\right]}{\pi^2 r_f^2 p (r_b + r_t)\sqrt{L_f^2 + (r_b - r_t)^2}}$$

Equation SI 2.10

where $C_{dye}^{Hydrolysis}$ is the binding surface coverage of **2.1** inside a single nanopore determined from the two-step coupling/hydrolysis method; variables are explained in Table SI 2.3. The numerator in Equation SI 2.10 employs Beer's law to calculate the number of dyes inside the nanopores of PET_8/**2.1**. The dominator calculates the total surface area inside the nanopores of PET_8/**2.1** by approximating the number of nanopores on the film and multiplying it by the surface area of each pore, i.e. lateral area of a truncated cone.[135] Using the values in Table SI 2.3, $C_{dye}^{Hydrolysis}$ was calculated to be 0.33 dyes nm^{-2}.

Table SI 2.3 Explanation of variables used in Equation SI 2.10.

Variable	Explanation	Value (units)
ε	molar absorptivity at 463 nm of **1** in 1 M NaOH *(aq)*	30,090 M^{-1} cm^{-1} (Figure SI 2.10a-b)
L	pathlength of the cuvette	1 cm
ΔA	difference in the absorbance values at 463 nm of the hydrolysis solutions used to remove **2.1** from fully modified PET_0/**1** and PET_8/**2.1**	0.02309677 (Figure SI 2.10c)
V	volume of hydrolysis solution	5×10^{-3} L
r_f	radius of the film etched	1.3×10^7 nm
N_A	Avogadro's number	6.022×10^{23} mol^{-1}
p	pore coverage of PET_8/**2.1**	1×10^{-6} pores nm^{-2}
r_b	average radius of nanopore base opening	340 nm
r_t	average radius of nanopore tip opening	10 nm
l_f	Length of nanopore or thickness of film after etch: 1.2×10^4 nm – 2.13 nm min^{-1} × (etch time in min)	1.17×10^4 nm

* Note ΔA is the effective absorbance of dyes removed exclusively from the inside of the PET_8/**1** nanopores because the PET_8 film has a total of ~530 million pores in the modified film and thus the single pore on the PET_0 is inconsequential when calculating ΔA. Also, an accurate ΔA was calculated by ensuring that both PET films, PET_0/**1** and PET_8/**1**, underwent identical etching and modification chemistries.

The hydrolyzed dye was confirmed to be **1**; the absorbance, emission, and excitation spectra of the hydrolyzed dye matched those of the standard **1** dissolved in aqueous 1 M NaOH (Figure SI 2.10c-d).

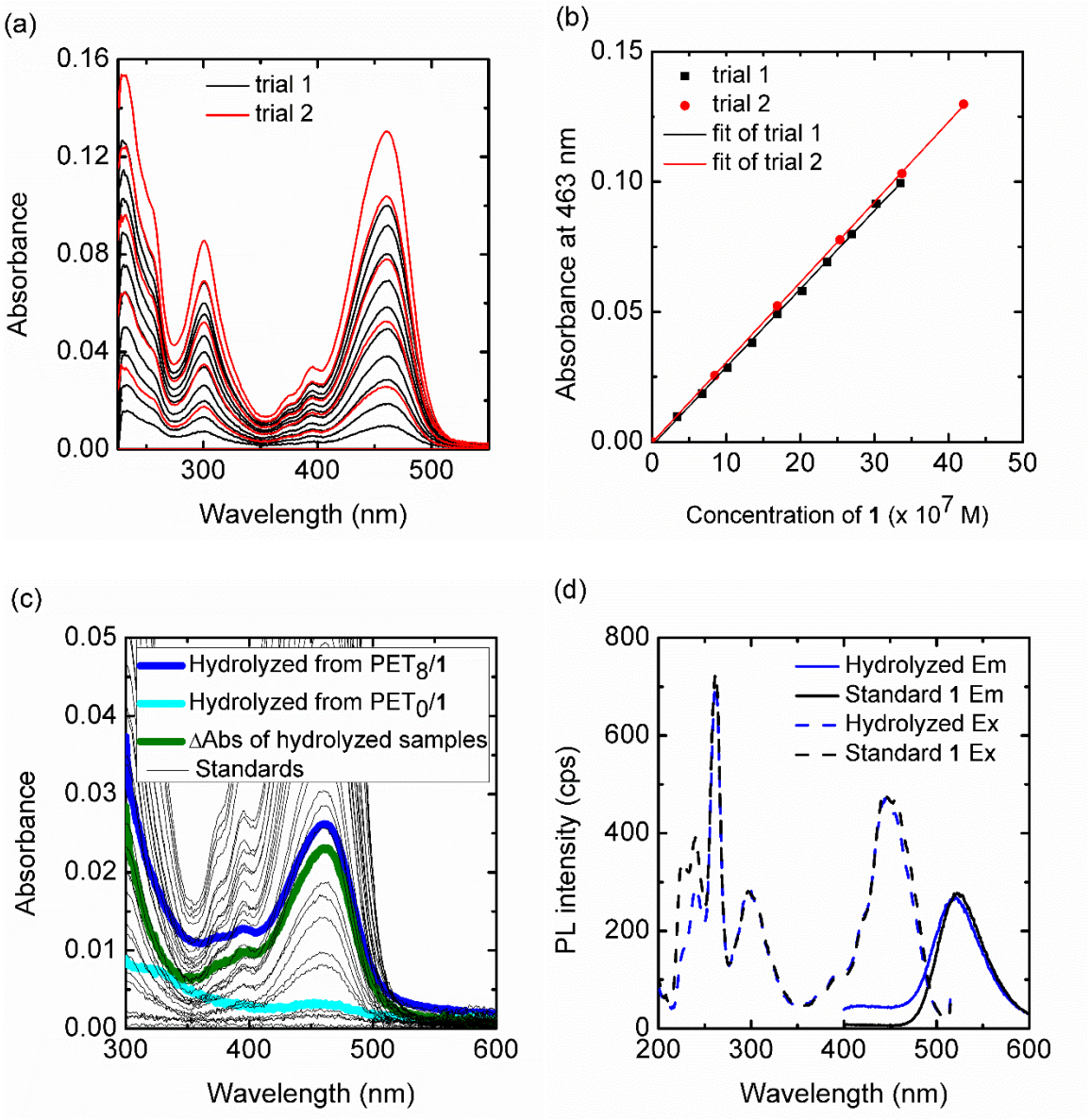

Figure SI 2.10. (a) Absorbance spectra of **2.1** dissolved in aqueous 1 M NaOH. (b) Molar absorptivity plot of **2.1** in aqueous 1 M NaOH; average $\varepsilon_{463\ nm}$ = 30,100 ± 900 M-1 cm-1. Fits have coefficients of determination, $R^2 \geq 0.999$. (c) Absorption spectra for **2.1** in aqueous 1 M NaOH after hydrolysis from fully modified PET_0/**2.1** and PET_8/**2.1**. Standards are of that of **2.1** dissolved in aqueous 1 M NaOH. (d) Emission and excitation spectra of **2.1** in aqueous 1 M NaOH after hydrolysis from fully modified PET_8/**2.1**, displayed with emission and excitation spectra of standard **2.1** in aqueous 1 M NaOH.

The conversion of carboxylates into amide bonds using carbodiimide chemistry on **1** and PET_n was calculated using Equation SI 2.11.

$$\% \, conversion = \frac{C_{dye}^{Hydrolysis} \frac{3A_{o_{OH}} - A_{o_{NH3}}}{A_{o_{OH}}}}{C_{\mathrm{COOH}}} \times 100 \qquad \text{Equation SI 2.11}$$

The numerator is the number of amides formed per nm^2 and was calculated from the results of Equation SI 2.10 ($C_{dye}^{Hydrolysis}$ = 0.33 dyes nm^{-2}) and the values from Table SI 2.2, and C_{COOH} is the surface coverage of a native PET film (one carboxylate group nm^{-2}).[105] Using these inputs, the percent conversation was determined to be 90%.

Chapter 2.6.11. Mimicking the binding of PET and 2.1 with model compound.

The ground-state pK_a of the hydroxyl group of **2.1** in aqueous buffered solution was 5.8. When bound to the bulk material of PET, the film wetted in the same solution displayed a pK_a of ~5.1. The model compound **2.2** was synthesized (Scheme SI 2.1) to help elucidate the reason for the change in pK_a, e.g. to discern between a confinement, electrostatic, or inductive effect. The coupling chemistry is identical to the coupling chemistry employed to bind **2.1** to PET_n films. An acid/base titration procedure of **2.2** in solution with spectrophotometric detection gave a pK_a of ~5.4 (Figure SI 2.11).

Scheme SI 2.1. Synthesis of dye 2.2 via carbodiimide activation of mono-methyl terephthalate.

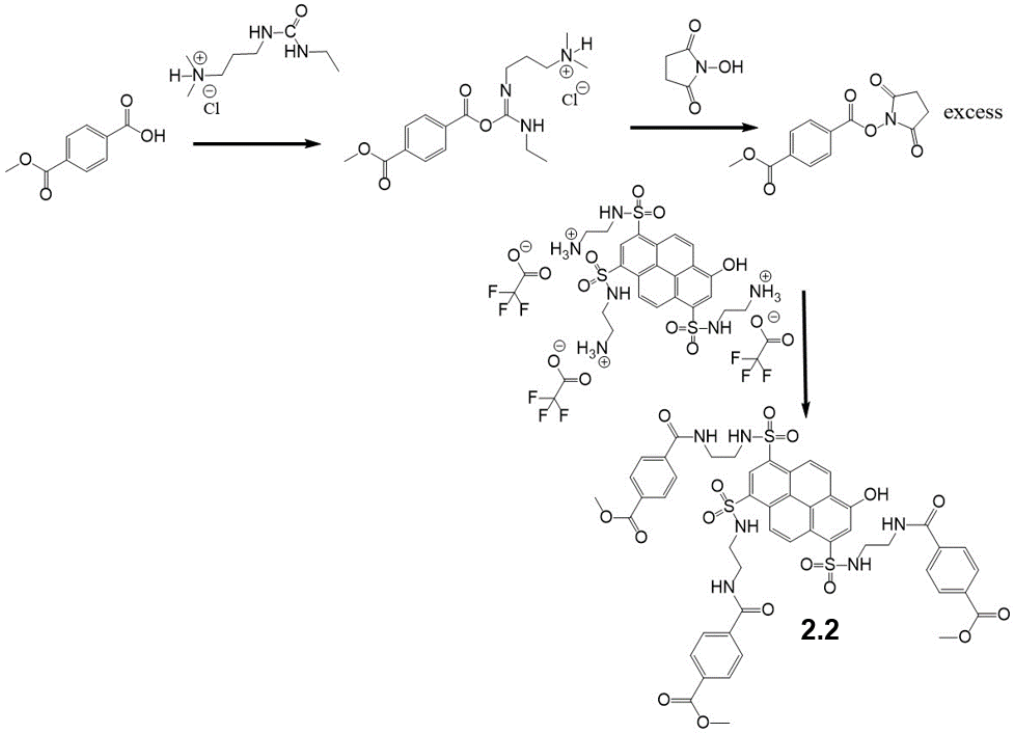

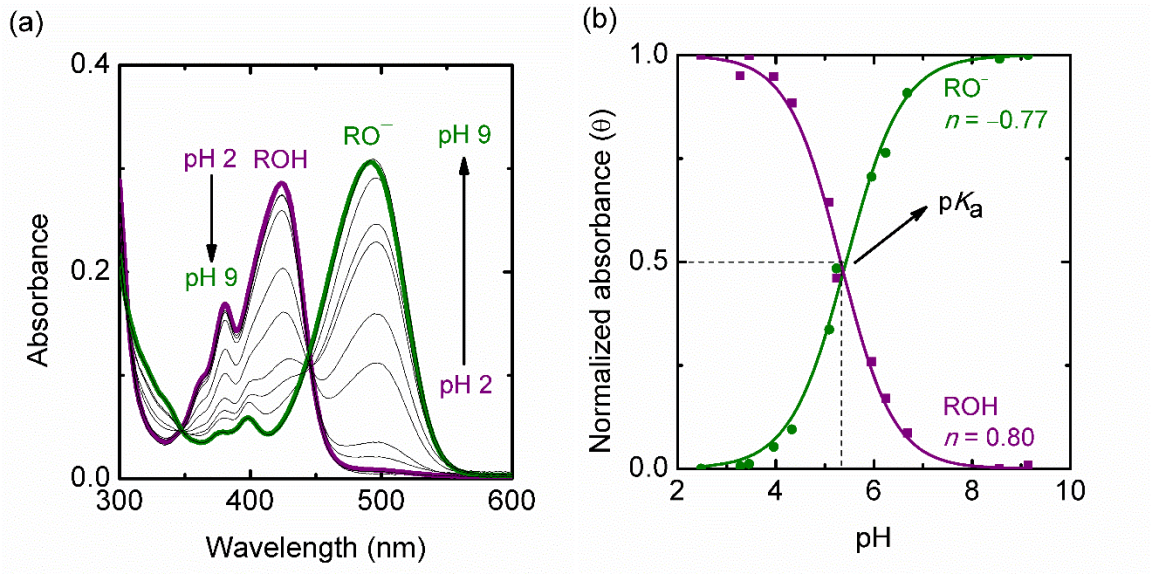

Figure SI 2.11. (a) Electronic absorption spectra of **2.2** in aqueous solution. (b) Plot of normalized absorbance (θ) at the λ_{max} for each species (425 nm and 500 nm) as a function of pH, and displayed with non-linear least square best fits to the Hill equation (Equation 2.1).

Chapter 2.6.12. Excited-state pK_a values in polymers.

One method used to determine the pK_a^* of **2.1** bound to PET was via the Förster cycle analysis, Equation 2.2. Values for v_{ROH} and v_{RO^-} were determined from Figure SI 2.12 and resulted in pK_a^* = -1.4.

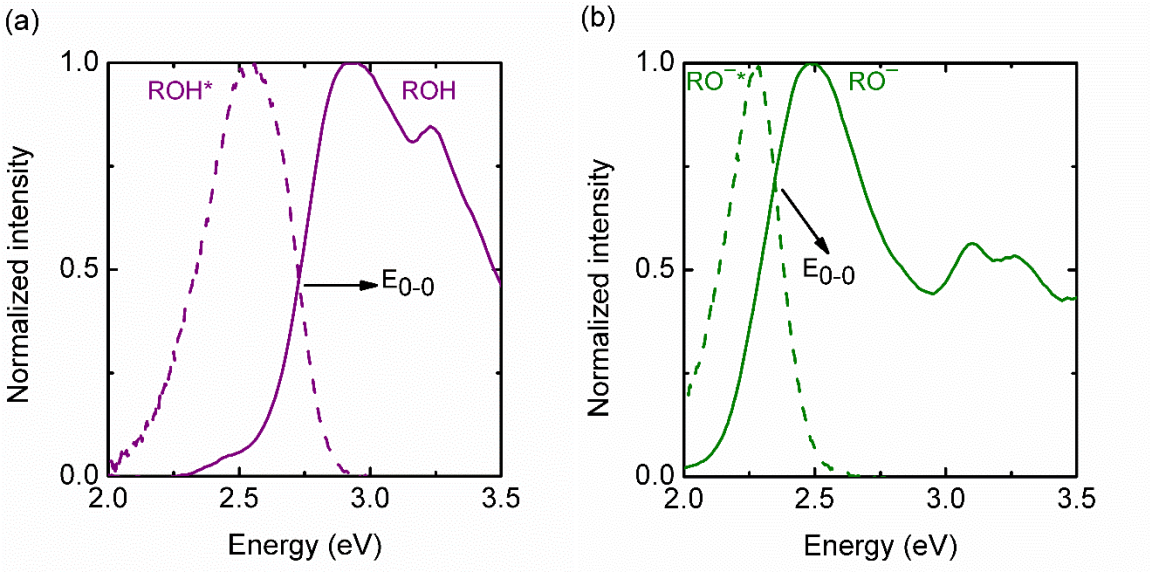

Figure SI 2.12. Normalized absorbance (solid) and photoluminescence intensity (dashed) spectra used to determine the energy of the 0-0 electronic transitions of PET_8/**2.1** for (a) the protonated photoacid (ROH and ROH*, 2.73 eV) and (b) deprotonated photoacid (RO^- and RO^{-*}, 2.35 eV).

An acid–base titration procedure equipped with two-photon fluorescence microscopy was also used to determine pK_a^* of **2.1** bound to PET. This photoluminescence technique provided the exclusive emission of **2.1** after the subtraction of PET emission which also ensured that isoemissive points were maintained for all pH values reported. Even though PET barely absorbed visible light, photoluminescence from PET was unavoidable; excitation wavelengths as red as 1000 nm still resulted in observable emission from PET (Table SI 2.4). Also, excitation-wavelength-dependent emission of PET polymer was observed (Table SI 2.4). A Raman scattering phenomenon was ruled out, because the difference in energy between the excitation wavelength and the corresponding emission

peak differed as a function of excitation wavelength (Table SI 2.4). The leading hypothesis for this observed behavior is that the polymer has a broad energetic distribution of isolated optically active states with limited capabilities to energy transfer to states with lower-energy optical transitions. With the excitation of PET inevitable, it was reasonable to excite the isosbestic point of PET_8/**2.1**, 450 nm (Figure 2.4), which avoids the need to scale the observed emission ratios of ROH^* and RO^{-*}.

Table SI 2.4 Excitation wavelength dependent emission of PET_8/T polymer.

λ_{ex} (nm)	800	900	1000
$\lambda_{em,\ max}$ (nm)	477	537	580
ΔE (cm^{-1})	4000	3600	2800

The effects of nanoconfinement on the pK_a^* of **2.1** bound to PET was observed by comparing the photoluminescence of PET_8/T+**2.1** to the PL of PET_8/**2.1**. PET_8/**2.1** contained cylindrical pores with openings of ~500 nm in radius (Figure SI 2.5). To readily observe the emission from **2.1**, the entire PET film was modified with **2.1**. Photoluminescence from the ROH^* and RO^{-*} species was observed in weakly acidic conditions. The ratio of emission from ROH^* and RO^{-*} in nanopores with tip diameters of ~500 nm was 0.3:1. However, for PET_8/T+**2.1**, which was only functionalized with **2.1** at the tip of the conical nanopores, the ratio of emission from ROH^* and RO^{-*} in nanopores was 0.7:1. The average radius of the conical nanopores in the PET_8/T+**2.1** was approximated to be ~20 nm based on the etching time of the film. Figure SI 2.13b represents a partial titration of PET_8/T+**2.1** that was fabricated via an identical procedure to that used to fabricate PET_8/T+**2.1** used to procure the data in Figure 8a, which suggests the pK_a^* of **2.1** in PET_8/T+**2.1** is again ~3 in the absence

of supporting electrolyte and highlights the reproducibility of this procedure and the observations.

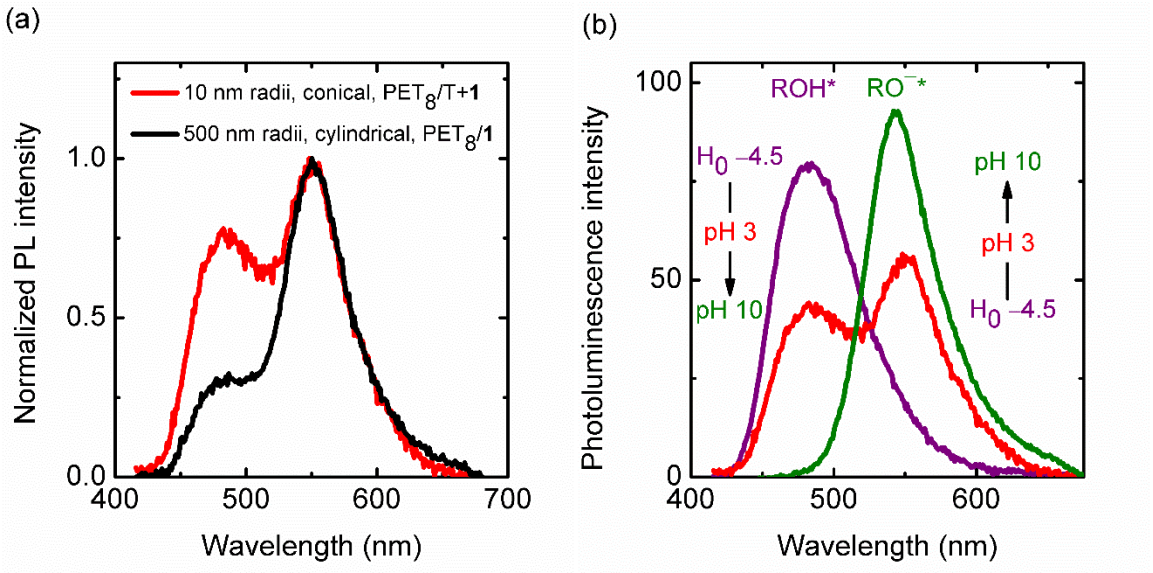

Figure SI 2.13. (a) Normalized photoluminescence (PL) spectra resulting from two-photon absorption (λ_{ex} = 900 nm) of nanoporous PET_8/T+**2.1** immersed in aqueous pH 3 solution. (b) Photoluminescence spectra of PET_8/T+**2.1** immersed in aqueous solutions without supporting electrolyte. Two-photon-absorption excitation wavelength (λ_{ex}) was 900 nm. Emission from the completely protonated and deprotonated excited-states are represented by ROH^* and RO^{-*}, respectively.

Transient changes in local acidity due to laser photoexcitation during microscopy studies did not seem to occur even at bulk pH values as large as ~3 (Figure SI 2.14). As Figure SI 2.14c reports, the ratio ROH^*:RO^{-*} changed only from 0.10:1 to 0.07:1 upon a 9-fold increase in excitation intensity. While this is a small shift in the ratio of ROH^*:RO^{-*}, a decrease in the ratio of ROH^* versus RO^{-*} is not expected if changes in local acidity due to laser

photoexcitation operates, i.e. an increase in laser intensity should increase emission from ROH^* versus RO^{-*}, not decrease it as observed.

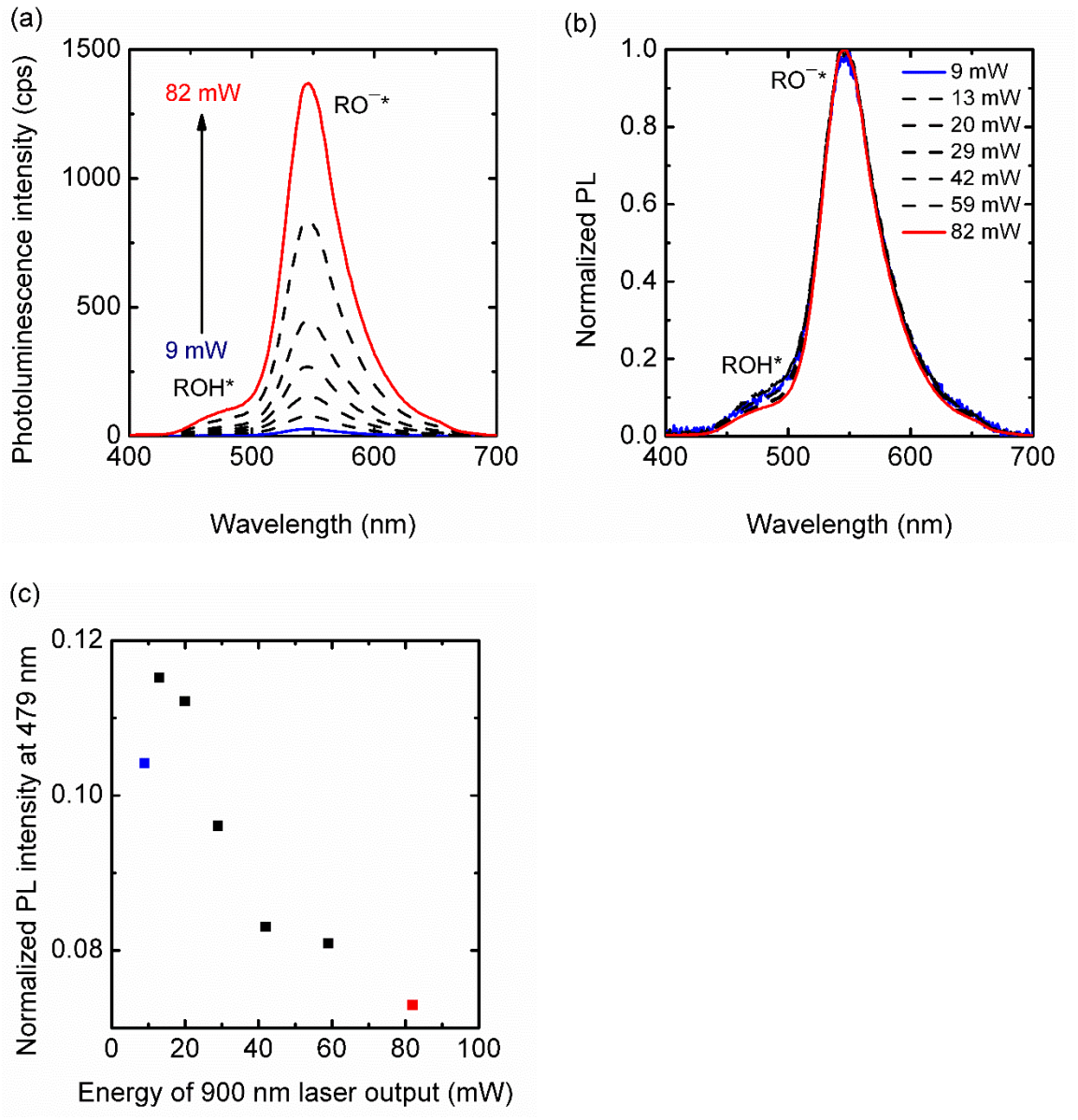

Figure SI 2.14. (a) Photoluminescence (PL) spectra of PET_8/T+**2.1** immersed in aqueous pH 3 solution without supporting electrolyte and excited with a two-photon-absorption wavelength (λ_{ex}) of 900 nm; the excitation intensity was varied from 9 mW to 82 mW. The data are (a) raw and (b) normalized to the RO^{-*} emission peak at 548 nm. Emission from the completely protonated and deprotonated excited-states are represented by ROH^* and RO^{-*}, respectively. (c) Ordinate values from the data in panel b at 479 nm are plotted versus the excitation intensity.

Chapter 2.7. Ancillary data.

Chapter 2.7.1. Calculation of expected protonic photocurrent from PET_0/1.

The generated photocurrent (PC) for a PET_0/**2.1** immersed in aqueous pH 3 solution under steady-state illumination with 405 nm, 5 mJ, was calculated to be 141 pA using Equation SI 2.12. The equation assumes that an impinging photon flux is absorbed by a fraction of photoacid that can perform an excited-state proton transfer, and that every excited-state proton transfer results in an observed photogenerated charge carrier.

$$PC = F\Phi\left(1 - 10^{\left(\varepsilon_{ex}(r_z\times10^{-7})\frac{N_{dye}}{N_A V_{pore}}\right)}\right)\left(\frac{\%_{RO^{-*}}\%_{ROH}}{100}\right)QY_{ESTP} \quad \text{Equation SI 2.12}$$

$$\Phi = \frac{E_{pulse}\lambda_{Ex}}{N_A \mathrm{h}c} f_{rep} \quad \text{Equation SI 2.13}$$

$$r_z = \frac{1.4\eta\lambda_{Ex}}{NA^2} \quad \text{Equation SI 2.14}$$

$$N_{dye} = C_{dye}\ \frac{\%_{ROH}}{100}\ \pi\ \left(\frac{A+a}{2}\right)\sqrt{{r_z}^2 + \left(\frac{A-a}{2}\right)^2} \quad \text{Equation SI 2.15}$$

$$V_{pore} = \frac{1}{3} r_z \left(\left(\frac{A}{2}\right)^2 + \left(\frac{a}{2}\right)^2 + \frac{Aa}{2}\right) \times 10^{-24} \quad \text{Equation SI 2.16}$$

Where Φ is the impinging photon flux, r_z is the penetration depth of light which is approximated using the axial optical resolution of a confocal microscope, N_{dye} is the number of dyes per pore, V_{pore} is the volume contained instead the nanopore, and QY_{ESTP} is the quantum yield of ESPT.

Table SI 2.5. Explanation of variables used in Equation SI 2.12− Equation SI 2.16.

Variable	Explanation	Value (units)
F	Faraday's constant	96485.33 A s mol^{-1}
N_A	Avogadro's number	6.022×10^{23} mol^{-1}
Φ	Photon flux	n/a mol of photons s^{-1}
E_{pulse}	Energy of laser pulse	0.005 J
λ_{Ex}	Excitation wavelength	4.05×10^{-7}m
h	Planck's constant	6.626×10^{-34} J s
c	Speed of light	2.998×10^{8} m s^{-1}
f_{rep}	Pulse repetition frequency	1 Hz
r_z	Penetration depth of light which was approximated using the axial optical resolution of a confocal microscope.	n/a nm
η	Refractive index of solution	1.33
NA	Numerical aperture	1.2
ε_{ex}	Molar absorptivity at the excitation wavelength. Shown earlier, $\lambda_{Ex} = 405$ nm. $\varepsilon_{405\ nm}$ determined using Figure S14.	15,739 L mol^{-1} cm^{-1}
N_{dye}	Number of dyes is a single conical nanopore	n/a dyes
C_{dye}	Binding surface coverage of **2.1** inside a single nanopore determined by Equation SI 2.10.	0.30 dyes nm^{-2}
$\%_{ROH}$	Percent of protonated dye in a PET$_0$/**2.1** film immersed in an aqueous pH 3 solution as determined from Figure 4.	98%
A	Diameter of larger opening of nanopore. Determined by 2.13 nm min^{-1} × (etch time in min).	1000 nm
a	Diameter of smaller opening of nanopore estimated based on Equation E1.	20 nm
$\%_{RO^{-*}}$	Percent of excited-state deprotonated emission resulting from the excitation of a PET$_0$/**2.1** film immersed in an aqueous 100 mM KCl pH 3 solution (Figure 2.7c).	96%
QY_{ESTP}	Quantum yield of ESPT	1*

Chapter 2.7.2. Ancillary data on 2.1 in solution.

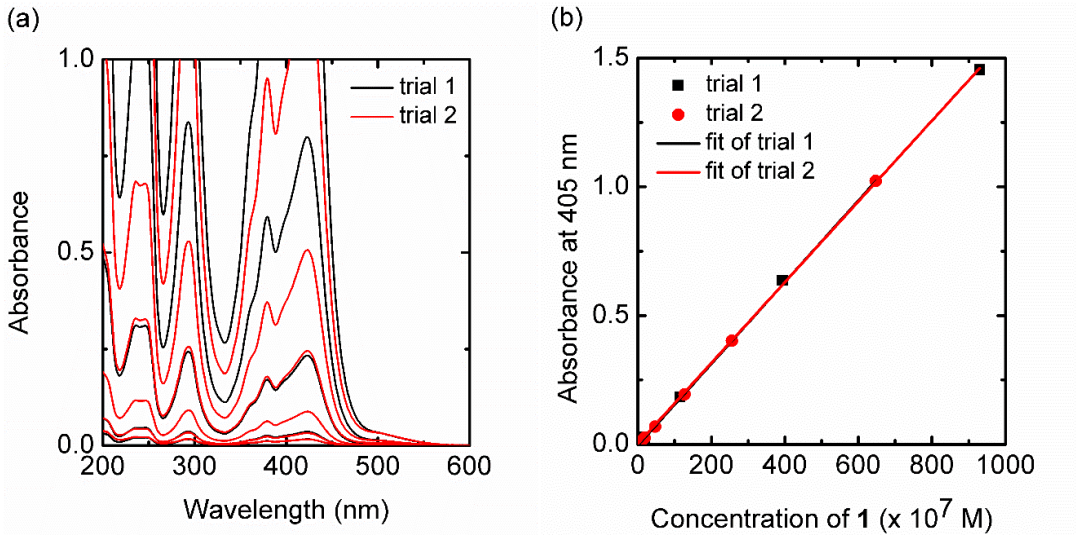

Figure SI 2.15. (a) Absorbance spectra of **2.1** dissolved in aqueous pH 3 solution. (b) Molar absorptivity plot of **2.1** in aqueous pH 3 solution; average $\varepsilon_{405\,nm}$ = 15,739 $\pm$ 33 L mol^{-1} cm^{-1}. Fits have coefficients of determination, $R^2 \geq 0.9998$.

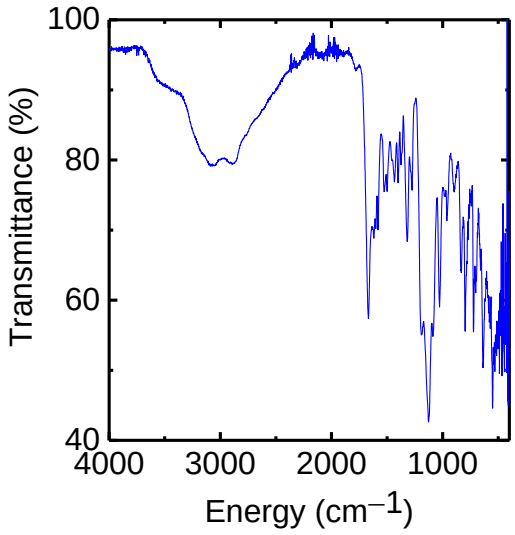

Figure SI 2.16. FTIR of **2.1**.

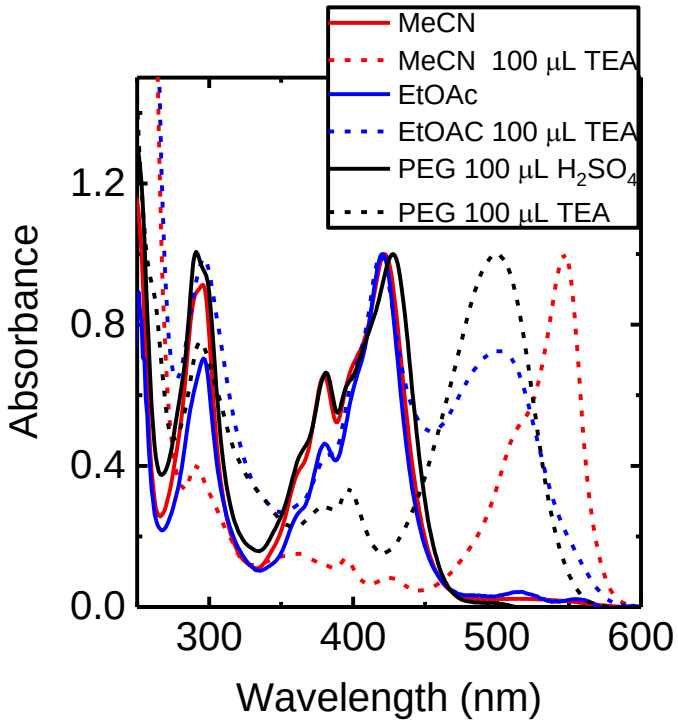

Figure SI 2.17. Protonated and deprotonated **2.1** non-aqueous solutions.

Isoemissive points were maintained during the titration of **2.1** and HPTS monitored with photoluminescence detection until acid concentrations became greater than approximately 7 M (Figure SI 2.18 and Figure SI 2.19). At concentrations greater than 7 M acid, the absorption maximum peaks broadened and isoemissive points were not maintained. For **2.1**, as the acid concentration increased from 0.04 M to 9.0 M, the absorbance of the photoacid increased without perturbing the isoemissive point. However, as the acid concentration reached 18 M, the absorbance and the photoluminescence decreased. This was strikingly different than HPTS, where the absorbance continuously decreased as the solution was acidified; however, the photoluminescence intensity became hyperchromic and bathochromic.

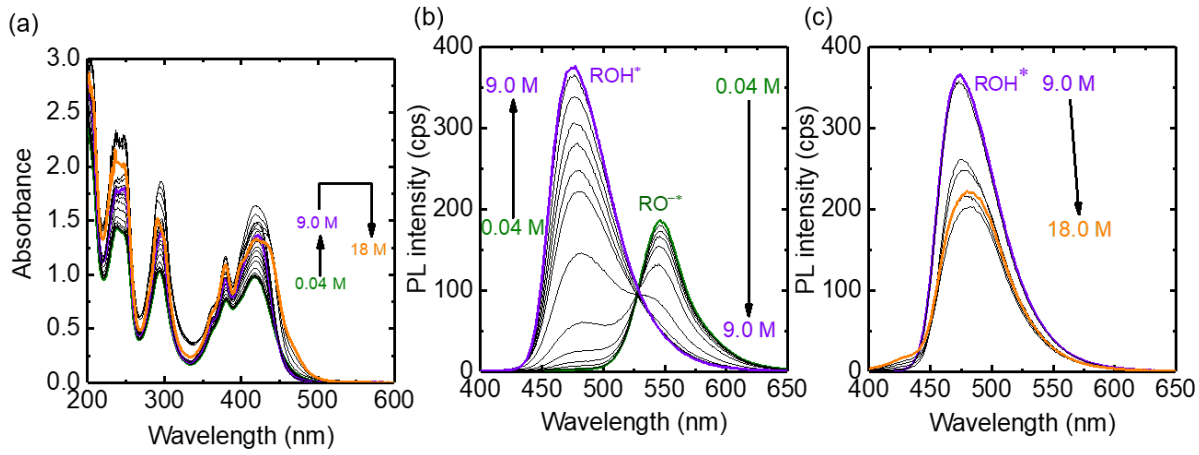

Figure SI 2.18. (a) Electronic absorption spectra and corresponding (b,c) photoluminescence of **2.1** in sulfuric acid (λ_{ex} = 375 nm).

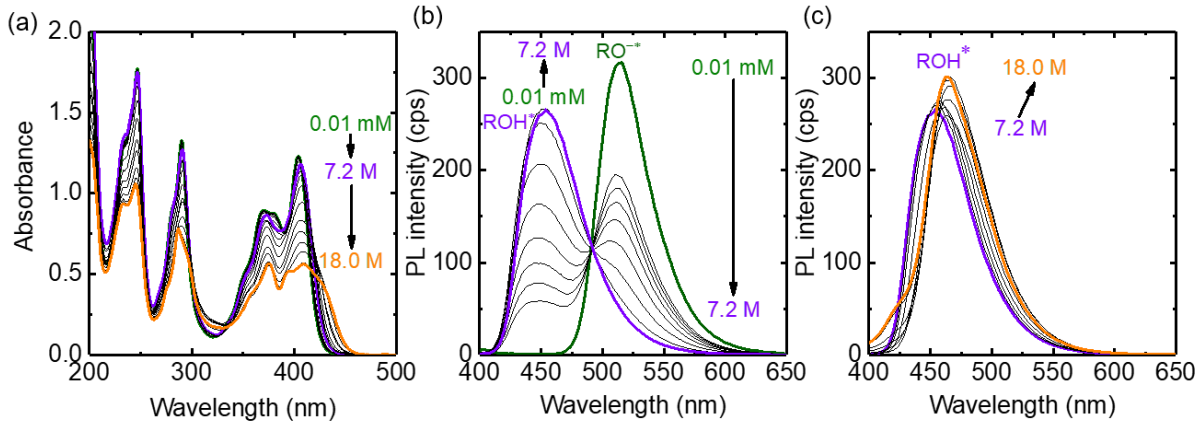

Figure SI 2.19. (a) Electronic absorption spectra and corresponding (b,c) photoluminescence of HPTS in sulfuric acid (λ_{ex} = 375 nm).

The thermodynamic quantities involving protonation and one electron reduction are related in their ground-states and electronic excited-states.[136] The changes in pK_a due to one electron reduction are well-described by the seminal work of Michaelis.[137] The pK_a change

due to the differences in the standard redox potentials (versus the standard hydrogen electrode [E_i]) of $ROH/ROH^{\cdot-}$ and $RO^{-}/RO^{\cdot 2-}$ at room temperature is equal to $16.92 \times (E_{ROH} - E_{RO-})$.[136] The one electron reduction event of **2.1**, $ROH/ROH^{\cdot-}$, in DMSO occurred at -1.28 V *versus* Fc/Fc^{+} (Figure SI 2.20) which is approximately equivalent to -0.6 *versus* the standard hydrogen electrode. Experiments to determine the reduction potential of $RO^{-}/RO^{\cdot 2-}$ and oxidation potentials of ROH/ROH^{+} and RO^{-}/RO are underway.

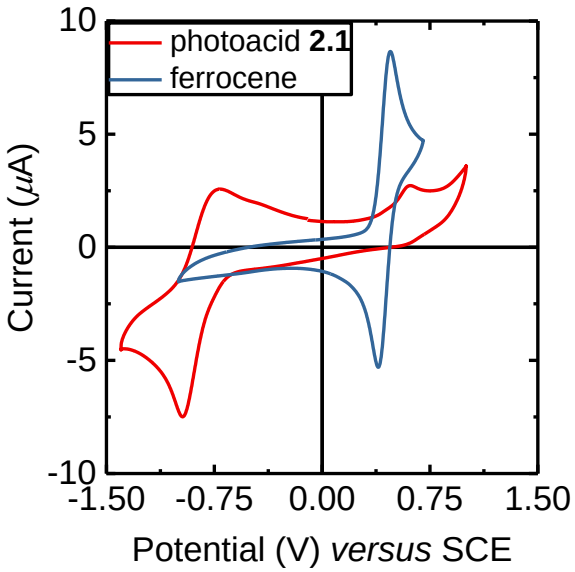

Figure SI 2.20. Cyclic voltammogram of **2.1** and ferrocene in DMSO.

Chapter 2.7.3. Exploring other alternatives to EDC chemistry on nanopores.

The surfaces of polyethylene terephthalate nanopores have pendant carboxylic acid groups and these groups can serve as functional handles for the attachment of photoacids. Figure SI 2.21 is visual representation of a native film from a lateral view. The film is not drawn to scale and the film is drawn with transparency to show the nanopore spanning the length of the film. The figure also displays reduced representations of the nanopore surface, where the trapezoid representation is used to indicate the surface functionalization throughout the length of a pore and the flat representation is used when surface modification is homogenous.

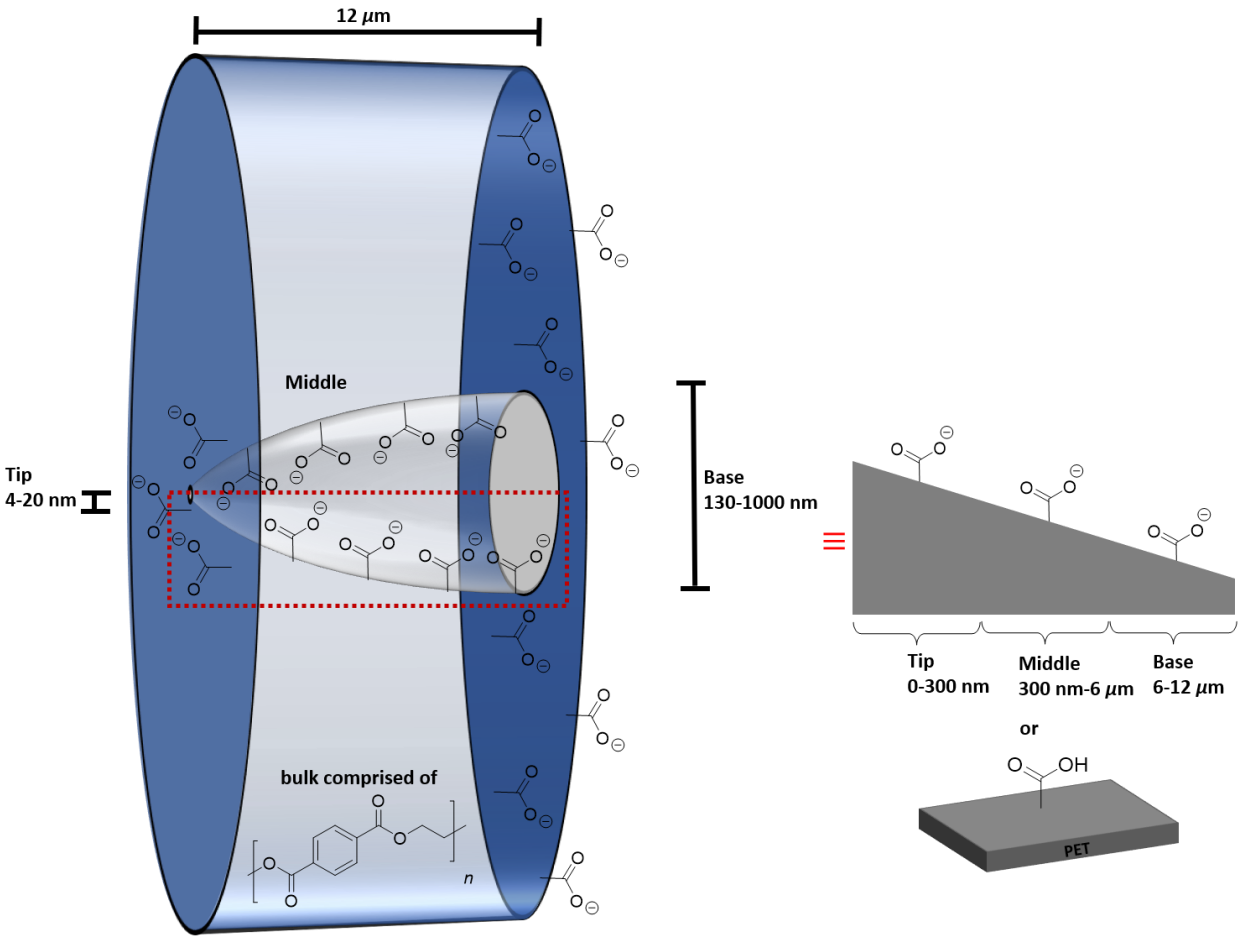

Figure SI 2.21. Lateral view of PET_0 and its reduced representation.

Two approaches were considered for photoacid attachment (Scheme SI 2.2). The first approach directly bonds the photoacid to the surface but requires the photoacid to possess primary amines. The second approach involves two steps where the carboxylic acids are converted into amides with pendant primary amines, and then the surface amines are reacted with an electrophile, such as a sulfonyl chloride, containing photoacid. The latter approach is synthetically appealing because it could eliminate protection/deprotection steps (red arrow) necessary to synthesize the photoacid with primary amines. The latter approach

was explored but results, which are presented below, suggest the former approach is necessary.

Scheme SI 2.2. Two routes of PET$_n$ modification.

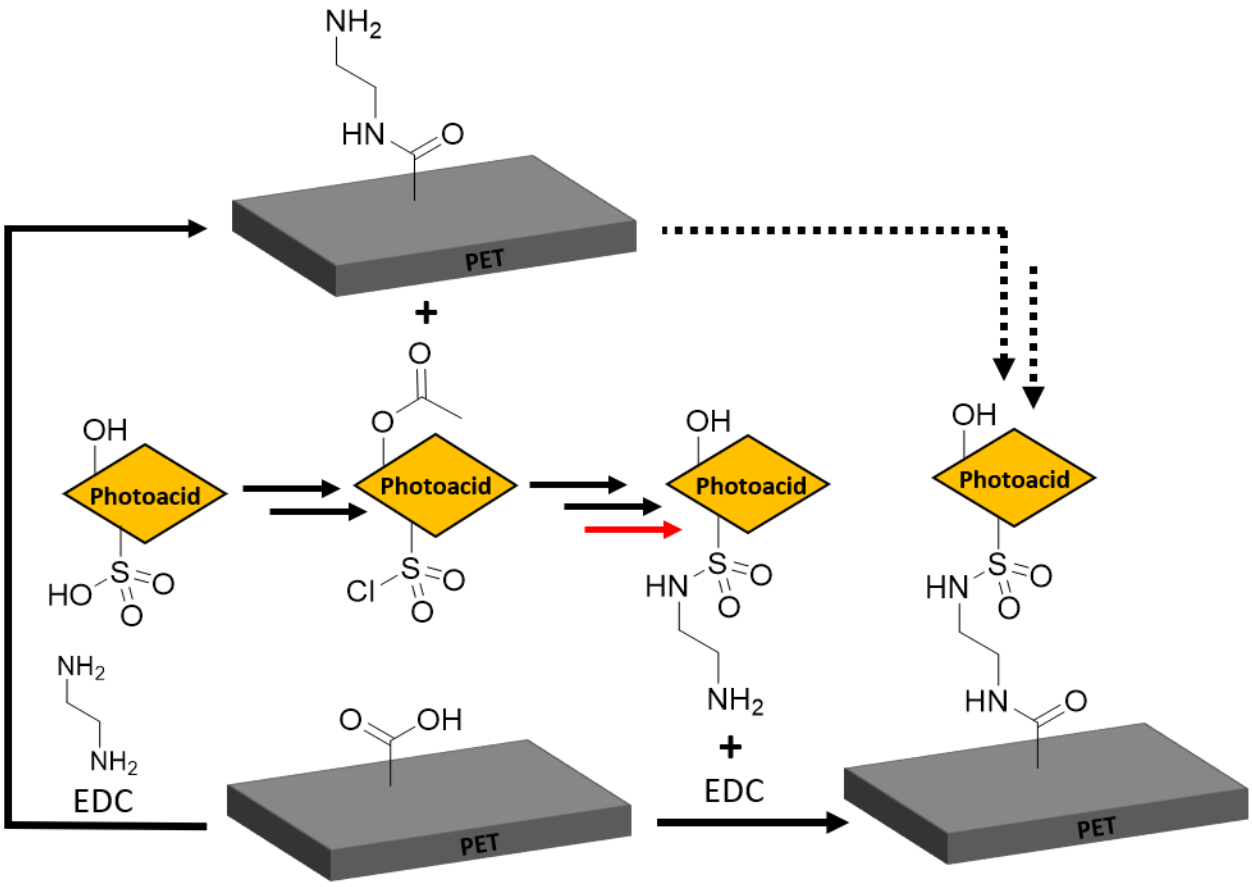

A primary concern using the sulfonyl chloride approach was the compatibility of the sulfonyl chloride and the media wetting the amine terminated surface. The modification of polyethylene terephthalate nanopores requires benign, polar protic conditions because the nonporous scaffold degrades or dissolves in an array of nonpolar organic, acidic, and alkaline media. Therefore, chemical transformations are confined to near-neutral water, methanol,

or ethanol media. This restricts the use of many electrophiles, specifically ones that have the propensity to undergo solvolysis.[138] Oae and Kadoma[139] noted that 4-toluenesulfonyl chloride was able to react cleanly with primary amines in basic ethanol conditions, suggesting that *i*) ethoxide anions did not produce the undesired 4-toluenesulfonic acid ester and *ii*) the formed amide bond is inert to solvolysis under these conditions. This was confirmed by synthesizing the *N,N*'-(ethane-1,2-diyl)bis(tolunesulfonamide) in ethanol with a modest yield of 74% (Scheme SI 2.3).

Scheme SI 2.3. Synthesizing of N,N'-(ethane-1,2-diyl)bis(tolunesulfonamide) via an activated sulfonyl chloride in ethanol.

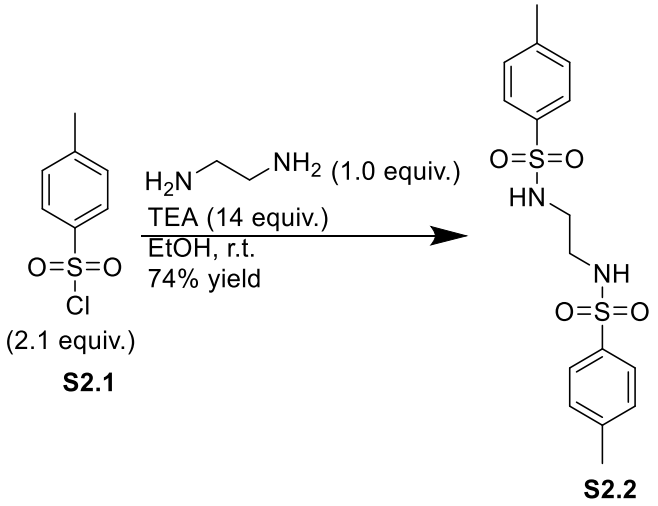

The basic ethanolic reactions conditions did not translate well to the modification of PET films. Specifically, the surface modification of PET_0/EDA was not detected via cyclic voltammetry when 4-toluenesulfonyl chloride was used in analogous ethanol conditions. Instead, the *current—voltage* response of the treated pore returned to its original state (Figure SI 2.22). This suggests that while coupling could have occurred, the surface was

slowly etched reverting the surface to its native form. The etching most likely occurred at the ester groups within the polymer chain rather than at the amides directly tethered to the terminal ammonium groups. This is because esters are the more prone to hydrolysis (hydrolytic E_a ~10-15 kcal mol^{-1}) than the amides (hydrolytic E_a ~20-30 kcal mol^{-1}).[140] In fact, most amides do not undergo hydrolysis at pH values greater than 12 unless heated to 100 °C.[140] Through this etching process, the dimensions of the pore changed and so the observed *current—voltage* response was not an exact replica of *current—voltage* response of the original nanopore. If future studies are warranted, it is advised to change the chemical modification procedure such that less triethylamine is used. Specifically, triethylamine should be ≤ 1 equivalent with respect to the moles of ammonium groups on the surface of PET_0/EDA.

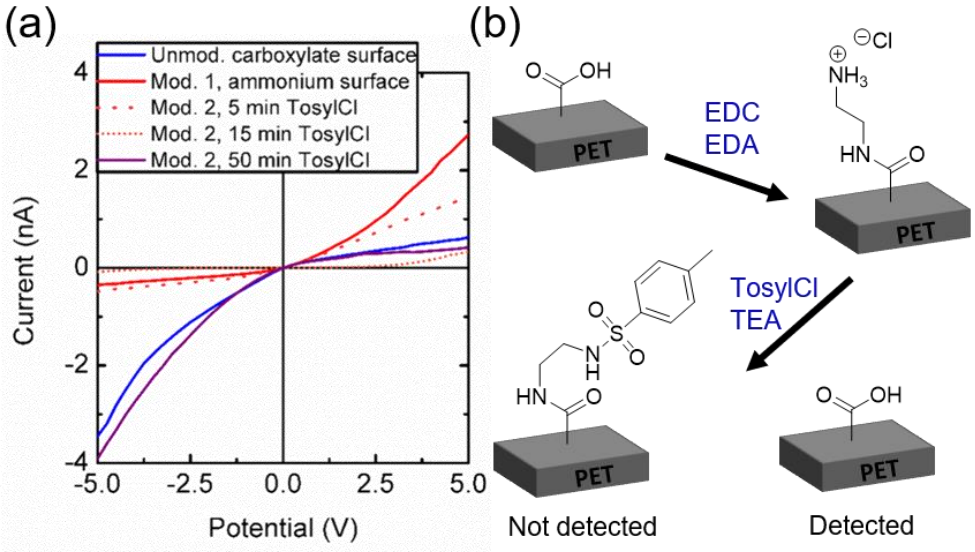

Figure SI 2.22. (a) Cyclic voltammograms of a native PET_0, PET_0/ethylenediamine (EDA) , and PET_0/EDA treated with 4-toluenesulfonyl chloride (TosylCl) in fresh aqueous 100 mM KCl. (b) Schematic of surface treatment measured in panel a.

Hydroxypyrene and its derivatives are ubiquitous to the understanding of excited-state proton transfer reactions. One of the most historically studied photoacid is 8-hydroxypyrene-1,3,6-trisulfonic acid (HPTS) and this molecule was chosen as the archetypal photoacid to bind to a nanopore. The photoacid HPTS has no amine groups and without chemical modification cannot make covalent bonds to the carboxylic acid surface of PET nanopores. Henceforth, the photoacid **2.1** was proposed as a molecular target which was ultimately synthesized from HPTS. A retrosynthetic disconnection approach (Scheme SI 2.4) shows that only three bonds need to be formed, all of which are sulfonamide bonds. Ideally, the three bonds can be formed in a one-step, one-pot procedure.

Scheme SI 2.4. Retrosynthetic analysis of pyrenol **2.1**.

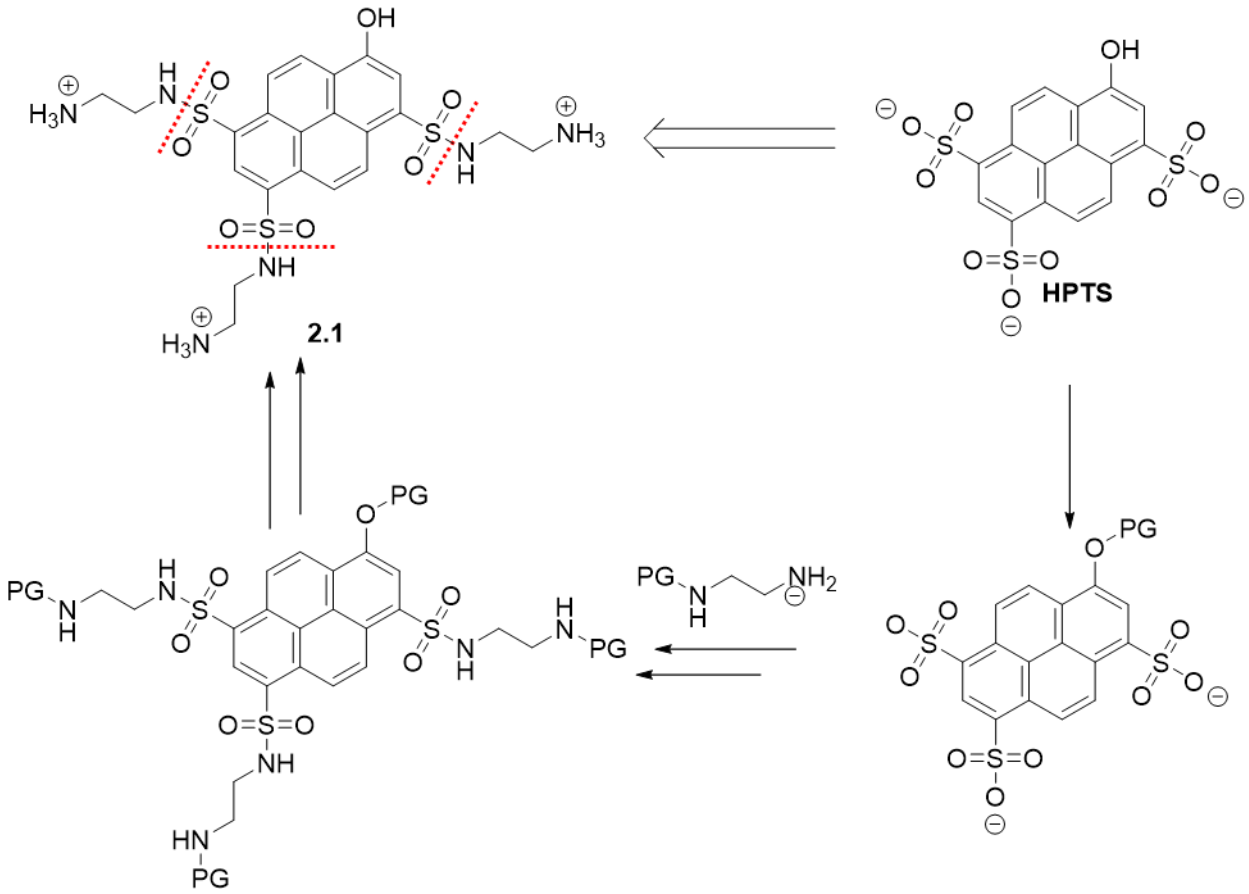

Practically this was not feasible because the activation of the sulfonate groups requires harsh conditions that were not compatible with unprotected hydroxyl group. Additionally, forming only one bond to a completely unprotected ethylene diamine linker is not straightforward. Viability was demonstrated using the model reagent, 4-toluenesulfonyl chloride, by which it was added dropwise to solution containing $>$ 30-fold equivalents of ethylenediamine. The large excess of ethylenediamine statistically ensured that out of all ethylenediamine groups which formed bonds, the majority would be bound to only one 4-toluenesulfonyl group (Scheme SI 2.5).

Scheme SI 2.5. Mono-functionalization of tosyl groups via unprotected ethylenediamine.

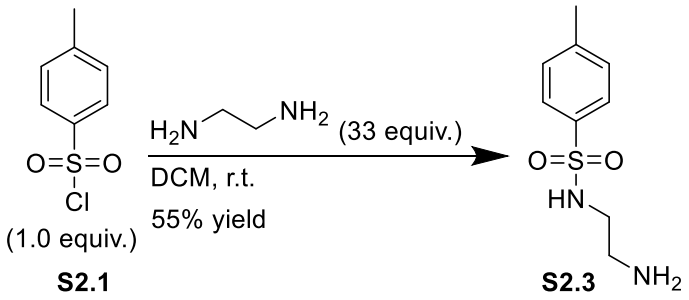

The model compound **S2.3** and ethylenediamine was used to test the applicability of patterning PET surfaces (Scheme SI 2.6). The first patterning step was monitored *in situ* via cyclic voltammetry and the normalized current values were plotted as a function of pH (Figure SI 2.23a). The currents at $\pm$5 V cease to change at $\sim$35 minutes suggesting that the carboxylates at the tip of the nanopore have been fully converted into amides tethered to **S2.3**. A second patterning step was used to couple ethylenediamine to the remaining, unreacted carboxylates. Cyclic voltammetry showed that the first modification neutralized

surface charge because the current-voltage response became more ohmic (less diode-like) in character. This is expected because anionic carboxylates were capped with non-ionic tosyl groups. The coupling of ethylenediamine reversed ion-selectivity with respect to the native film (Figure SI 2.23b). This is also expected neutral-positive patterned nanopores, which are known as unipolar diodes.[68]

Scheme SI 2.6. Patterning PET_0 films via step-wise EDC chemistry.

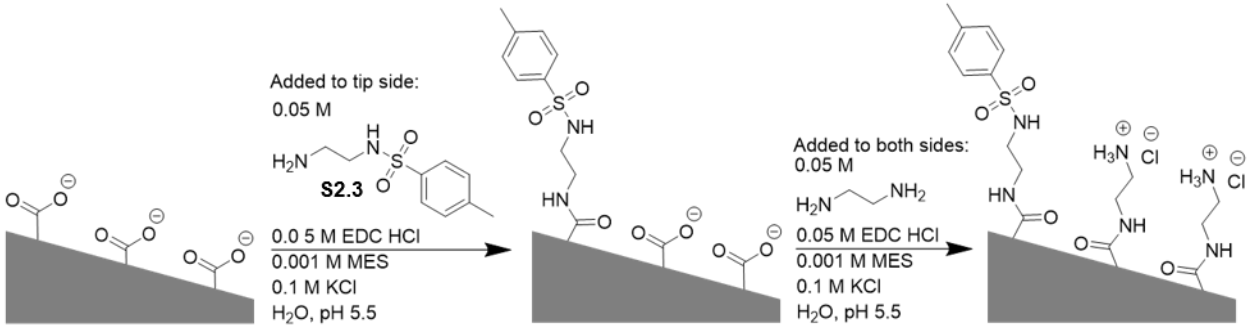

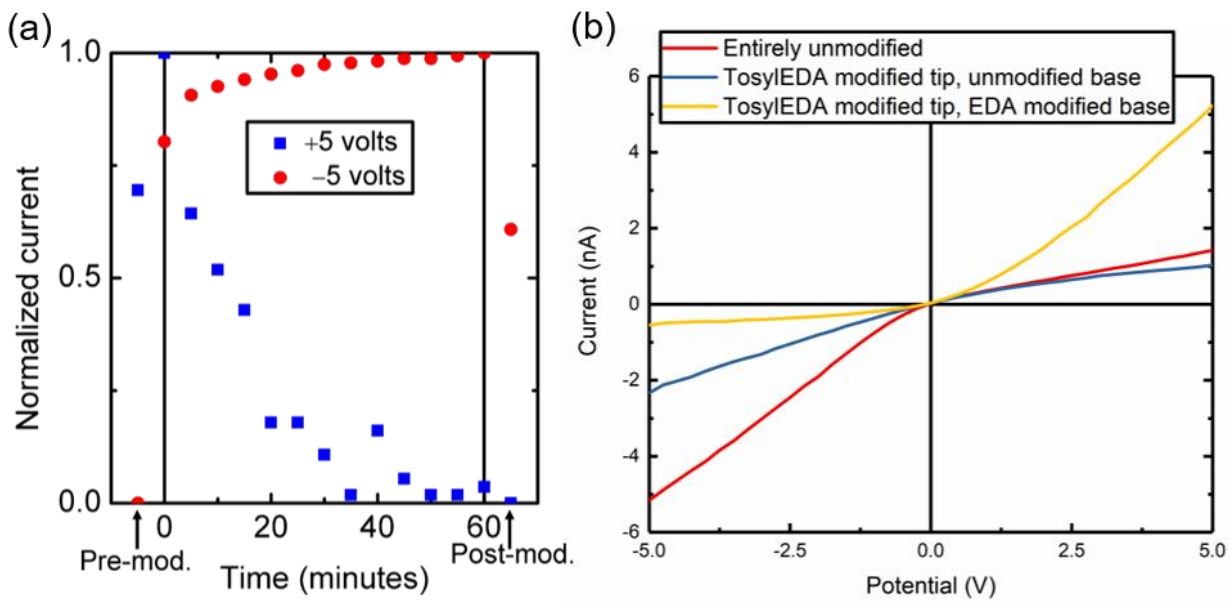

Figure SI 2.23. (a) *In situ* and *ex situ* currents measured during the amine **S2.3** modification procedure of PET_0. (b) PET_0 before and after modification with amine **S2.3** (TosylEDA) and ethylenediamine (EDA). *Ex situ* measurements are taken in pH 7, 100 mM KCl, 1 mM tris buffer.

The application of a forward bias on a unipolar diode allows ionic current to transverse the entire length of diode with little resistance; however, under reverse bias a depletion zone forms located primarily in the neutral region (Figure SI 2.24).[68] The depletion zone lacks a significant concentration of ions thereby increasing the resistance of the diode and limiting the amount of current flowing through the circuit. In Figure SI 2.23, positive voltages correspond to forward biases of the unipolar diode, conversely, negative voltages are reverse biases.

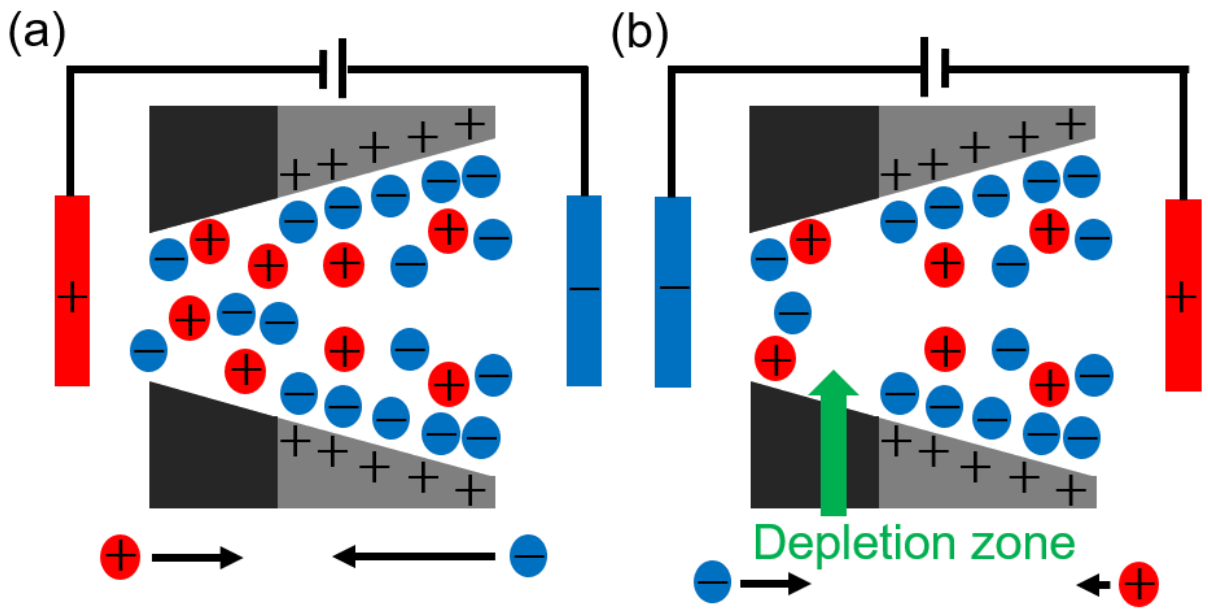

Figure SI 2.24. Operation of a unipolar diode under (a) forward bias and (b) reverse bias. [68]

The successful synthesis of **S2.3** and its application to patterning PET_0 surfaces prompted studies on the next model compound, 2-naphthol-6-sulfonic acid, which was in part to become familiar with a photoacid synthetically less complex than HPTS and to minimize expenditures (Scheme SI 2.7). Specifically, the photoacid has two less sulfonate groups and is marketed at ~\$1 g^{-1}, which is slightly more expensive than 4-toluenesulfonyl chloride (~\$0.05 g^{-1}) but much more economical than HPTS (>\$25 g^{-1}). The photoacid, 2-naphthol-6-sulfonic acid, **S2.4**, was treated with acetic anhydride under basic conditions to afford the acetoxy **S2.5** followed by refluxing in excess thionyl chloride with catalytic *N,N*-dimethylformamide to activate the sulfonate groups as sulfonyl chlorides (**S2.6**). Addition the sulfonyl chloride **S2.6** to a statistically large excess of ethylenediamine might have produced the desired product **S2.8** but isolation of the product was not achieved. Where the

difference in solubility of **S2.2** and ethylenediamine allowed easy separation, the product, **S2.8**, and the ethylenediamine have very similar solubility and thus were inseparable. The product **S2.8** was achieved in several extra steps. To the sulfonyl chloride **S2.6**, ~10 equivalents of *N*-Boc-ethylenediamine were added such that one equivalent formed the sulfonamide (**S2.7**) and HCl, which was neutralized by another equivalent, and the remaining equivalents assisted with the deacetylation. Lastly, the Boc protecting group was removed by heating the powder in acidic ethanol to yield **S2.8**.

Scheme SI 2.7. Synthesis of naphthol **S2.8** by sulfonate activation.

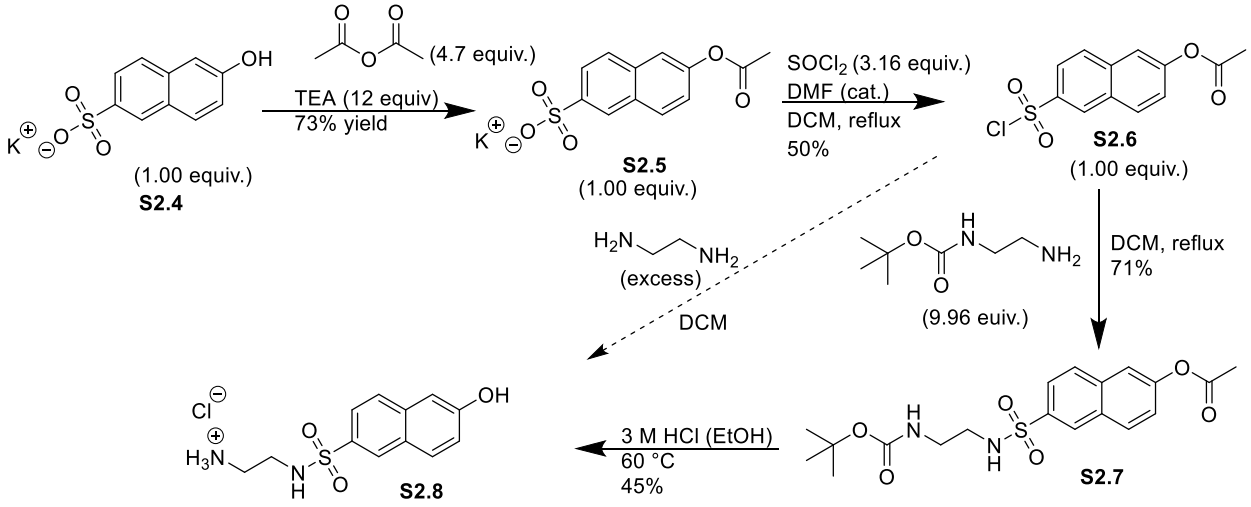

Chapter 2.7.4. Optimization of amide formation from nanopore PET surfaces, EDC, and amine terminated photoacid.

The coupling of amines to PET nanopores has been traditionally done in one step.[89,100,141,142] In the coupling process, the amine and carbodiimide were dissolved in a polar protic solvent. If the solvent is methanol or ethanol, the pH was not titrated.[100,141,142] With water as the solvent, the pH was titrated to a slightly acidic value (~5.5) [89] to ensure that the carbodiimide was protonated forming the activated electrophile.[143] The carbodiimide of choice was EDC in all scenarios because EDC is soluble in all three solvents and relatively stable to ambient bench-top conditions. However, EDC is sensitive to moisture and temperature, so the reagent was stored at -20 °C in a dry atmosphere to prevent degradation, and coupling solutions were made fresh. The fresh coupling solutions were added to the PET nanopores which converted the carboxylic acids into reactive *O*-acylisoureas (Scheme SI 2.8). The *O*-acylisourea is more selective towards amines than water under these conditions so the desired aminolysis presided over hydrolysis. Several procedures[100,141,142] also added acidic alcohols, such as pentafluorophenol (PFP, pK_a ~5.5)[144] and *N*-hydroxysuccinimide (NHS, pK_a ~6.0),[145] which reacted with the *O*-acylisourea to form a more stable ester intermediate. The increased stability resulted in increased coupling efficiencies because aminolysis becomes even more selective than hydrolysis. Note that the active ester intermediates are stable enough to be isolated but still labile enough to react with water if amines are absent. The NHS esters have half-lives of 5 hours, 1 hour, and 10 minutes in ~0 °C water with pH values of 7.0, 8.0, 8.6 respectively.[146–148] Also, if amines are absent or not nucleophilic enough to react with the intermediate, rearrangement from the *O*-acylisourea to the *N*-acylurea may also occur in solution.[149] Despite that two-step

carbodiimide modifications offer enhanced reaction efficiencies for the coupling of carboxylic acids and amines in solution, this author is unaware of any published works involving a PET nanopore which was modified using a two-step procedure.

A two-step procedure is as follows: in the first step, the carboxylic acid is reacted with EDC and the acidic alcohol, from which the active ester is isolated. In the second step, the active ester is treated with the amine. This allows the reaction conditions to be optimized. The first step is performed at pH values of 5-6 so that the EDC forms the protonated, reactive electrophile and a fraction of the acidic alcohol (~0.5) is deprotonated into the reactive, nucleophilic alkoxide.[150] The second step is performed at pH values of 7-7.5 which is basic enough that a fraction of amines (~0.01) remain in the reactive, nucleophilic free-base form (instead of the unreactive protonated, ammonium form), yet not basic enough to make hydrolysis of the intermediates a more favorable pathway than aminolysis.[150]

Scheme SI 2.8. Stepwise mechanism of amide formation on PET surfaces via EDC.

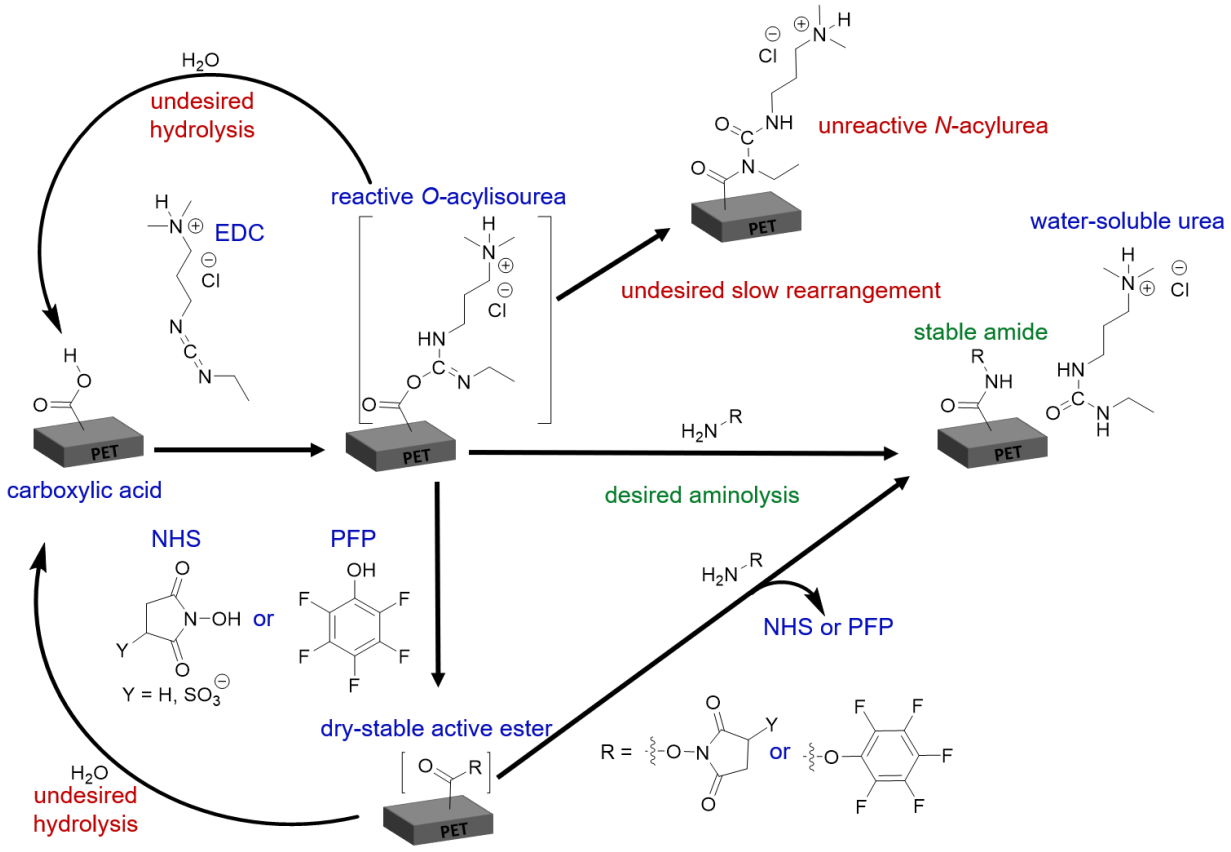

One-step procedures according to literature precedent[89,100,141,142] were performed in attempts to couple photoacid **2.1** to the surface of PET nanopores. Treated PET_0 showed no changes in ion-selectivity or buffering capacity as measured by cyclic voltammetry, which suggested the photoacid did not bind to PET, binding was too low to detect, or the bound photoacid does not change the electrostatics of the pore. The latter hypothesis seems unlikely because the isoelectric point of **2.1** at any possible binding orientation would be more basic than the isoelectric point of the PET carboxylates. And despite that **2.1** absorbs visible-light, common spectrophotometric techniques are not sensitive enough to detect a

monolayer of visible-light absorbing dyes on PET_0. Therefore, a more definitive experiment was devised by decreasing the sensitivity of the experiment by changing the sample from PET_0 to PET_8, and then using spectrophotometic detection.

A set of 20 PET_8 were cylindrically etched to opaqueness. The opaqueness was most likely caused by light scattering introduced by etching the diameter of the pores to micron-scale lengths.[149] Additionally, the etching process could have resulted in films with higher surfaces areas than films etched traditionally with conical nanopores. For instance, the surface area of PET_8 (2.6 cm^2 in diameter and 12 μm thick) consisting of cylindrical pores with diameters of 1 μm (~0.02 m^2) was approximated to be twice the surface area of PET_8 consisting of conical pores with diameters of 1 μm and 20 nm. The one-step coupling procedures[89,100,141,142] and a series of two-step procedures were used to bond photoacid **2.1** to a series of opaque PET_8. The photoacid **2.1** was hydrolyzed from the films and the concentration of **2.1** was quantified via spectrophotometric detection (Scheme SI 2.9).

Scheme SI 2.9. Two-step coupling/hydrolyzing with spectrophotometric detection.

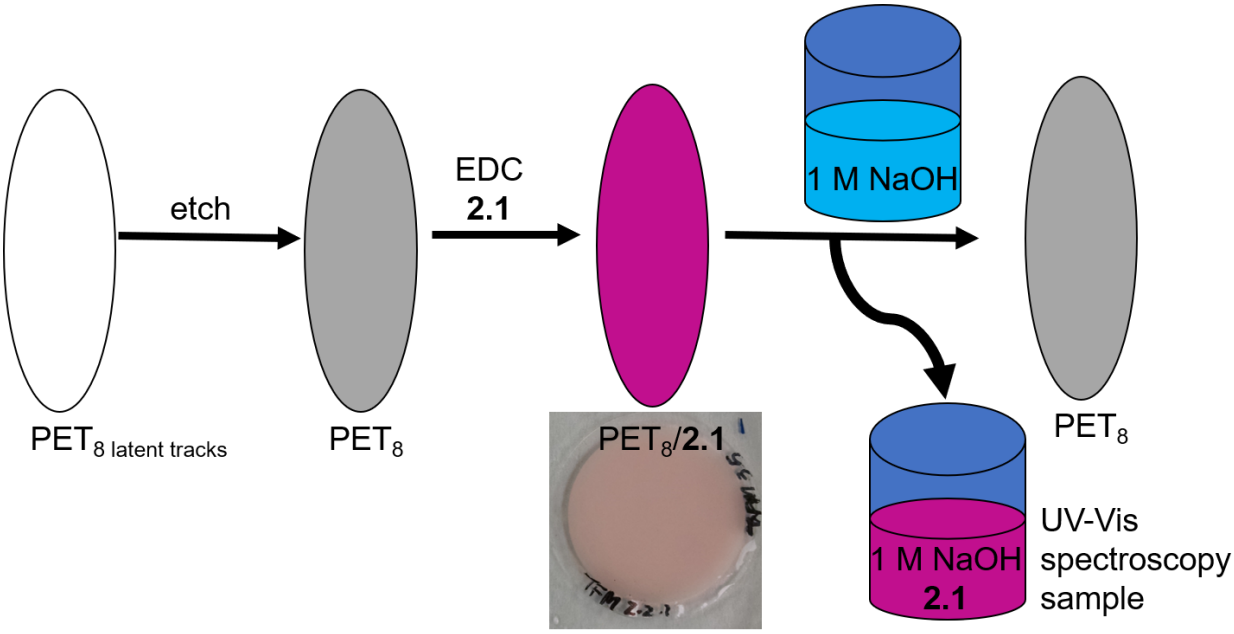

Table SI 2.6 shows the two-step coupling/hydrolyzing results of twenty different procedures. The blue rows are controls, and the green row highlights the best coupling procedure as indicated by the highest relative absorbance of hydrolyzed **2.1**. A slightly acidic pretreatment with supporting electrolyte was used to ensure the etchant was neutralized. In some cases, a nonreactive buffer (2-(*N*-morpholino)ethanesulfonic acid hemisodium salt [MES]) was added to stabilize the pH. Nonreactive buffers are those without primary amines, secondary amines, and carboxylates. On average, the addition of MES buffer or NHS in the first-step increased coupling efficiencies. On average, coupling efficiencies were greater for trials held at pH 7 or 9 than trials held at pH 3 or 6 in the second-step. These results are consistent with the mechanistic reasonings and literature aforementioned.[150]

Table SI 2.6. Optimization of two-step EDC chemistry.

Trial	Pretreatment	Step 1 pH	Step 1 additives	Step 2 pH	Relative absorbance of hydrolyzed **2.1**
1[89]	No	5.5	n/a	n/a	0.39
2[89]	Yes	5.5	n/a	n/a	0.56
3[100,141,142]	No	n/a (EtOH)	n/a	n/a	0.60
4[100,141,142]	Yes	n/a (EtOH)	n/a	n/a	0.23
5	Yes	4.0	n/a	3	0.39
6	Yes	4.0	n/a	6	0.29
7	Yes	4.0	n/a	7	0.41
8	Yes	4.0	n/a	9	0.45
9	Yes	5.0	n/a	3	0.27
10	Yes	5.0	n/a	6	0.33
11	Yes	5.0	n/a	7	0.35
12	Yes	5.0	n/a	9	0.49
13	Yes	4.0	MES	7	0.61
14	Yes	4.0	MES	9	0.53
15	Yes	4.0	MES, NHS	7	0.74
16	Yes	4.0	MES, NHS	9	0.77
17	Yes	5.0	MES	7	0.36
18	Yes	5.0	MES	9	0.82
19	Yes	5.0	MES, NHS	7	0.69
20	Yes	5.0	MES, NHS	9	1.00

Chapter 2.7.5. Electronic absorption spectra of pyrenol derivates.

The photoacid HPTS, and acetoxy HPTS (**2.1a**) have absorbance maximums (λ_{max}) at 404 nm and 371 nm, respectively (Figure SI 2.25). The 33 nm hypsochromic shift that follows protection is caused by the change in electron density of the hydroxyl group. The acetoxy lessens the electron-donating ability of the lone pairs on the aryl oxygen via resonance delocalization into the carbonyl. It can be reasoned that the electron-donating ability of the

acetoxy is similar to that of a sulfonate because **2.1a** and 1,3,6,8-pyrenetetrasulfonate (**S2.9**) compounds that only differ in chemical structure by that acetoxy group, have similar absorbance spectra. The λ_{max} of **S2.9** is at 376 nm, which is 5 nm bathochromic to the absorbance peak of **2.1a.** A 51 nm bathochromic shift was observed after **2.1a** was converted into the deprotected, tri(sulfonamide) **2.1**, which is consistent with reports of other 8-hydroxypyrene-1,3,6-tri(sulfonamide) photoacids.[84,151]

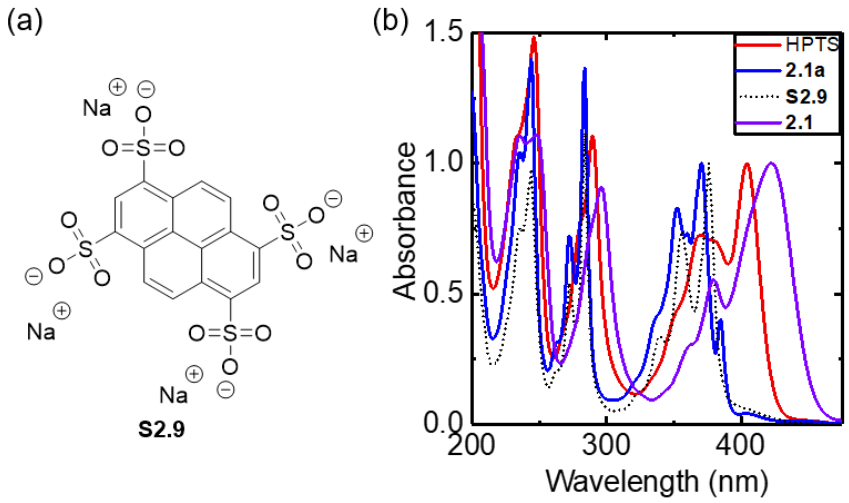

Figure SI 2.25. (a) Structure of pyrene **S2.9** and (b) electronic absorption spectrums of photoacids.

Chapter 2.7.6. Preferential binding of impurity.

Even without the use of RP-HPLC, the synthesis of **2.1** resulted in a pristine NMR spectrum that lacked evidence of impurities. However, use of **2.1** that was not purified by RP-HPLC in the surface modification of PET_8 did not result in the anticipated binding of photoacid **2.1**, and for all intents and purposes this film is called PET_8/impurity. The PET_8/impurity had a UV-Vis spectrum different than that of **2.1** dissolved in solution, but similar to an impurity isolated from the RP-HPLC of **2.1** (Figure SI 2.26). This suggests the impurity is mixed in the **2.1** sample, as opposed to the store-bought EDC, MES buffer, and NHS. Additionally, the impurity must bind preferentially with respect to **2.1** considering that it was not detected by NMR or by difference of difference spectra analysis of the UV-Vis spectrum (Chapter 2.7.7). The impurity was not isolated in a large enough quantity for NMR analysis and the true chemical structure remains elusive. Albeit, the PET_8/impurity was further characterized, and it was concluded that the impurity was also a pyrenol photoacid (discussed below).

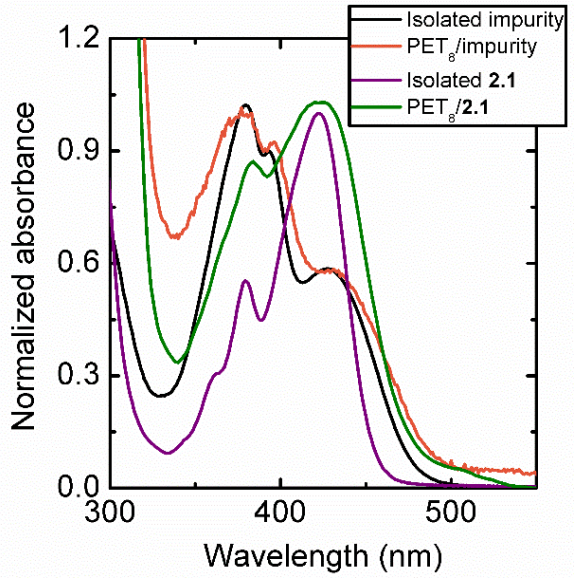

Figure SI 2.26. Electronic absorption spectra of photoacids dissolved in aqueous pH 2, and bound to PET immersed in aqueous pH 2.

The pK_a value of PET_8/impurity immersed in aqueous solution was determined to be 5.0 via acid/base titration procedure with spectrophotometric detection and non-linear least-squares fitting of the data to the Hill equation (Figure SI 2.27, Equation 2.1). This is approximately equivalent to the pK_a value of PET_8/**2.1** (~5.1). Also, the absorbance maximum of the hydroxyl protonation and deportation transition remained at the same wavelengths of 432 nm and 519 nm, respectively. However, unlike **2.1** a new absorption feature at 380 – 400 nm was present. The absorbance of the 380 – 400 nm feature was pH-independent and exhibited pH-dependent emission (Figure SI 2.28).

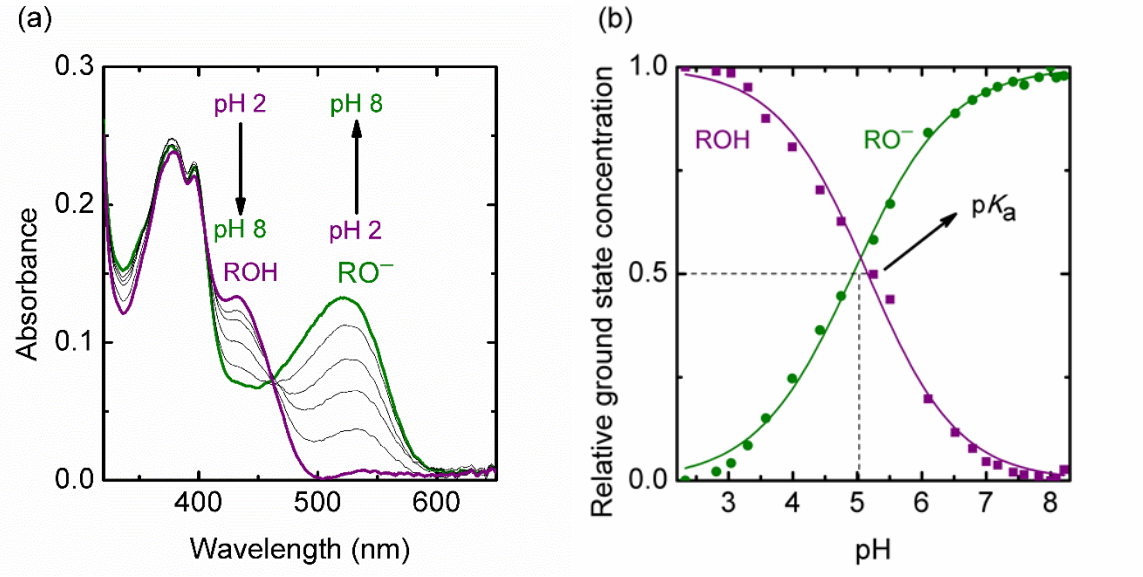

Figure SI 2.27. (a) Electronic absorption spectra of PET_8/impurity wetted with aqueous buffer. (b) Plot of normalized absorbance (θ) at the λ_{max} for each species (426 nm and 525 nm) as a function of pH, and overlaid with non-linear-least-squares best-fit curves to Equation 2.1.

Specifically, PET_8/impurity was excited while immersed in aqueous solutions at different pH values and the resulting emission was characteristic of protonated and deprotonated excited-state species with maxima at 476 nm to 522 nm. This is a slight hypsochromic shift with respect to the excited-state species of PET_8/**2.1** (489 nm and 548 nm). The intensities of these emission features were measured as a function of excitation wavelength (Figure SI 2.28a). The resulting excitation spectra presented the 380 – 400 nm feature at varying pH values and conditions. Collectively the data suggest that chemical structure resulting in this 380 – 400 nm feature is either from the pyrenol core or another entity covalently tethered to the pyrenol core (Figure SI 2.28b). If the latter scenario holds, the tethered moiety displayed energy transfer to the pyrenol dye. This is appealing for solar

conversion applications because it implies non-photoacid, light-absorbing molecules can be tethered to photoacids to increase light-harvesting, and consequently increase the external quantum efficiencies of the excited-state proton transfer.

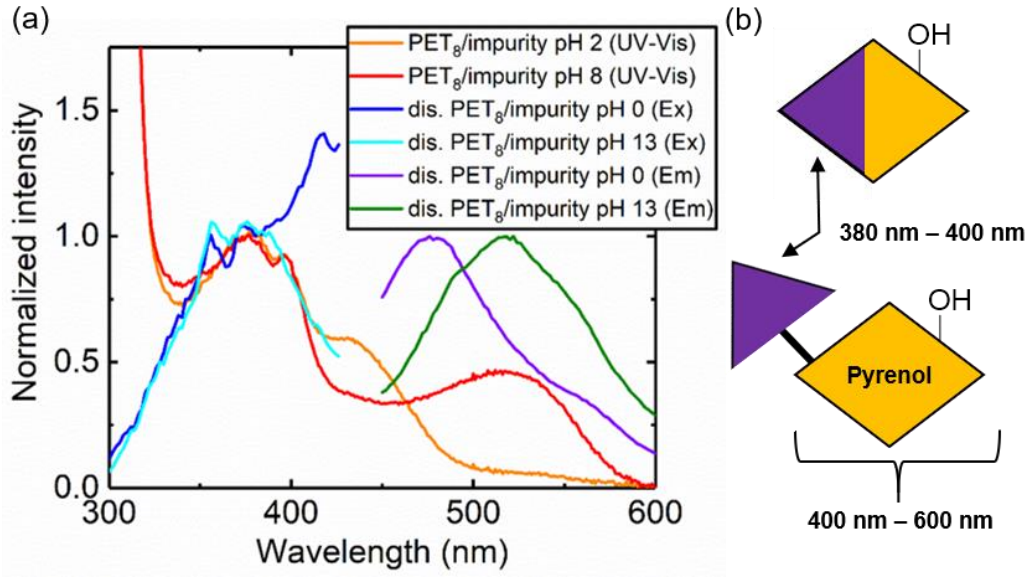

Figure SI 2.28. (a) Electronic absorption spectra PET_8/impurity and photoluminescence spectra of the film dissolved in solution. Excitation wavelength (λ_{ex}) was 420 nm and emission wavelength (λ_{em}) was 250 nm. (b) Hypothetical moieties of the impurity.

Lastly, the pK_a^* of PET_8/impurity was -1.3 as approximated using the Förster cycle analysis (Equation 2.2, Figure SI 2.29). This is similar to the pK_a^* of PET_8/**2.1** (-1.4) approximated by the Förster cycle analysis.

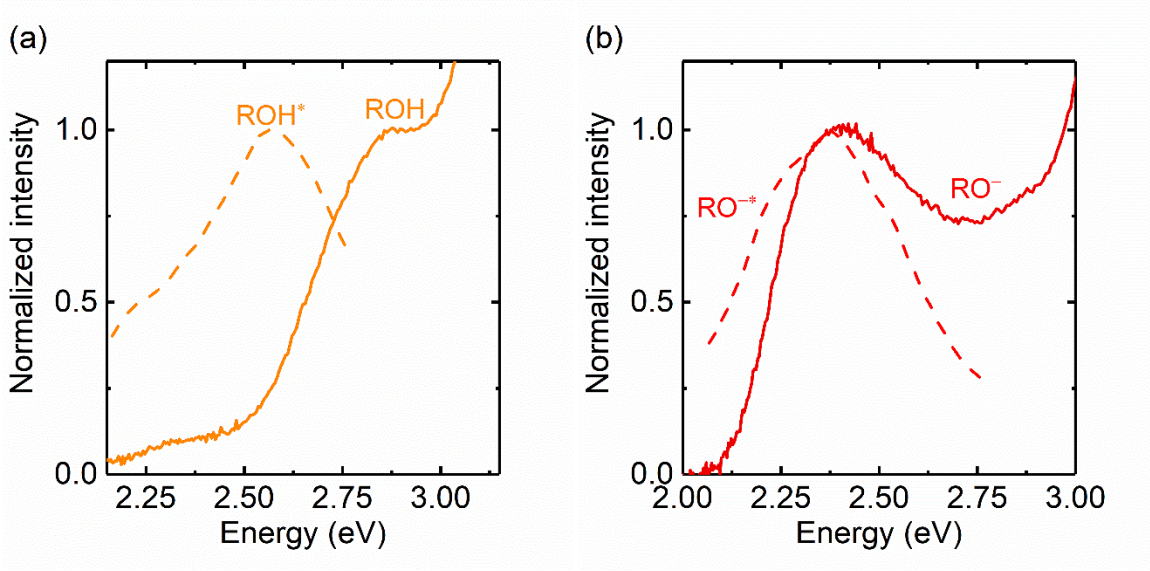

Figure SI 2.29. Normalized absorbance (solid) and photoluminescence intensity (dashed) spectra used to determine the energy of the 0-0 electronic transitions of PET_8/impurity wetted by solution for (a) the protonated photoacid (ROH and ROH^*, 2.73 eV) and (b) deprotonated photoacid (RO^- and RO^{-*}, 2.36 eV).

Chapter 2.7.7. Difference of difference spectra analysis

Difference of difference spectra analysis is used to assess the spectral changes associated with the titration of molecules from which, information about multiple titration events, side reactions, or impurities may be gathered. For demonstration purposes, 6-hydroxynaphthalene-sulfonic acid (**S2.4**) was added to HPTS to act as an impurity during its titration. Titration of the mixture from pH 2 to 12.5 is shown in Figure SI 2.30, left and the difference of difference spectra analysis is described below.

Initially the UV-Vis spectra at each pH were subtracted by the spectrum corresponding to the most alkaline solution. It was important to choose the spectrum taken

at the most alkaline pH because it ensured that all titration events were completed, that is, HPTS and HNS were fully deprotonated. The resulting difference absorption spectra (Figure SI 2.30b, left) show the growths and decays in absorbance as the pH is shifted from alkaline to acidic by the positive and negative ordinate values, respectively. Because HPTS absorbs at longer wavelengths than HNS, the growths and decays associated with the titration of HNS were isolated; this involved two steps. First, the difference absorption spectra were scaled to a wavelength which only HPTS absorbed (in the case, 460 nm) so that only the absorbance changes associated with the titration of HPTS coalesced (Figure SI 2.30c, left). Then scaled difference absorption spectra were subtracted by the scaled delta-spectrum at the second most basic pH; the scaled delta-spectra of the most alkaline pH is a horizontal line at y = 0 and cannot be usefully employed in the subtraction. Again, this result shows the growths and decays in absorbance of HNS as the pH is shifted from alkaline to acidic (Figure SI 2.30d, left). This was further supported by the titration of HNS in the absence of HPTS (Figure SI 2.30a, middle) and plotting the first difference absorption spectra (Figure SI 2.30b, middle), and noting that the spectra in Figure SI 2.30, middle and Figure SI 2.30, left are of identical shape.

Further, analysis provided an indication of the purity of the stock samples. Scaling the difference absorption spectra (Figure SI 2.30c, middle) and then plotting the difference of difference spectra (Figure SI 2.30d, middle) showed that the stock bottle of HNS has an impurity with a pH independent absorbance. A similar analysis (Figure SI 2.30b-d, right) on the titration plot of HPTS (Figure SI 2.30a, right) was performed and suggests that the stock bottle of HPTS does not contain impurities or the concentration of impurities is too low to detect because the difference of difference spectra (Figure SI 2.30d, right) are approximately

horizontal lines at Y = 0. Note that if impurities do not absorb light from >200 nm, then the analysis is not essential.

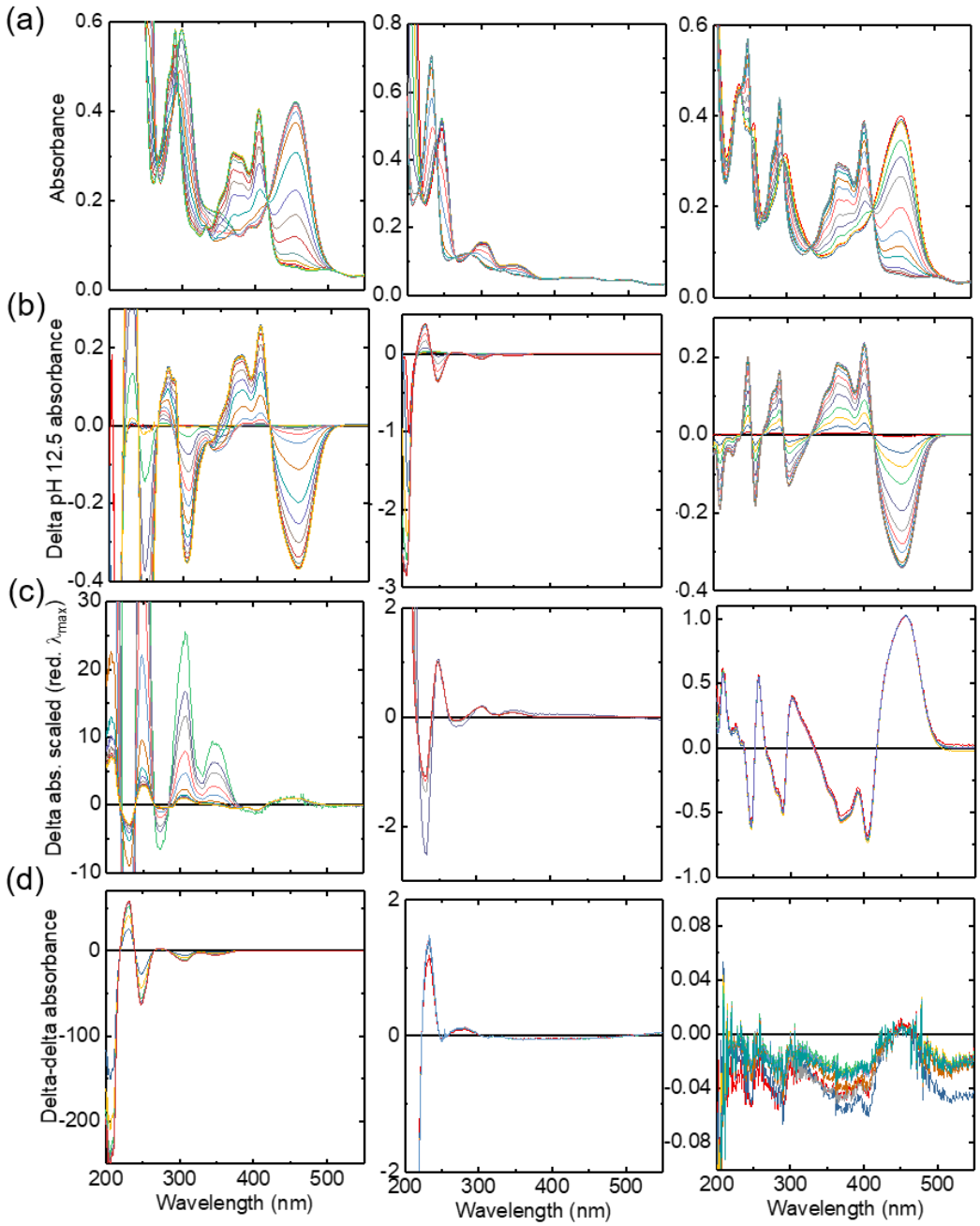

Figure SI 2.30. Difference of difference spectra analysis of (left) a mixture of HPTS and **S2.4**, (middle) HNS, and (right) HPTS. (a) Electronic absorption spectra of titrations from pH 2 to 12.5. (b) Spectra subtracted by the spectrum taken at pH 12.5. (c) Difference absorption spectra scaled to the reddest absorbance peak. (d) Difference absorption spectra subtracted by the difference absorption spectrum taken at the second most basic pH.

Chapter 2.7.8. Alternative synthesis of capped 2.2.

Scheme SI 2.10 was proposed as to isolate **2.2** without the need of RP-HPLC. Studies are ongoing.

Scheme SI 2.10. Alternative synthesis to capped **2.1**.

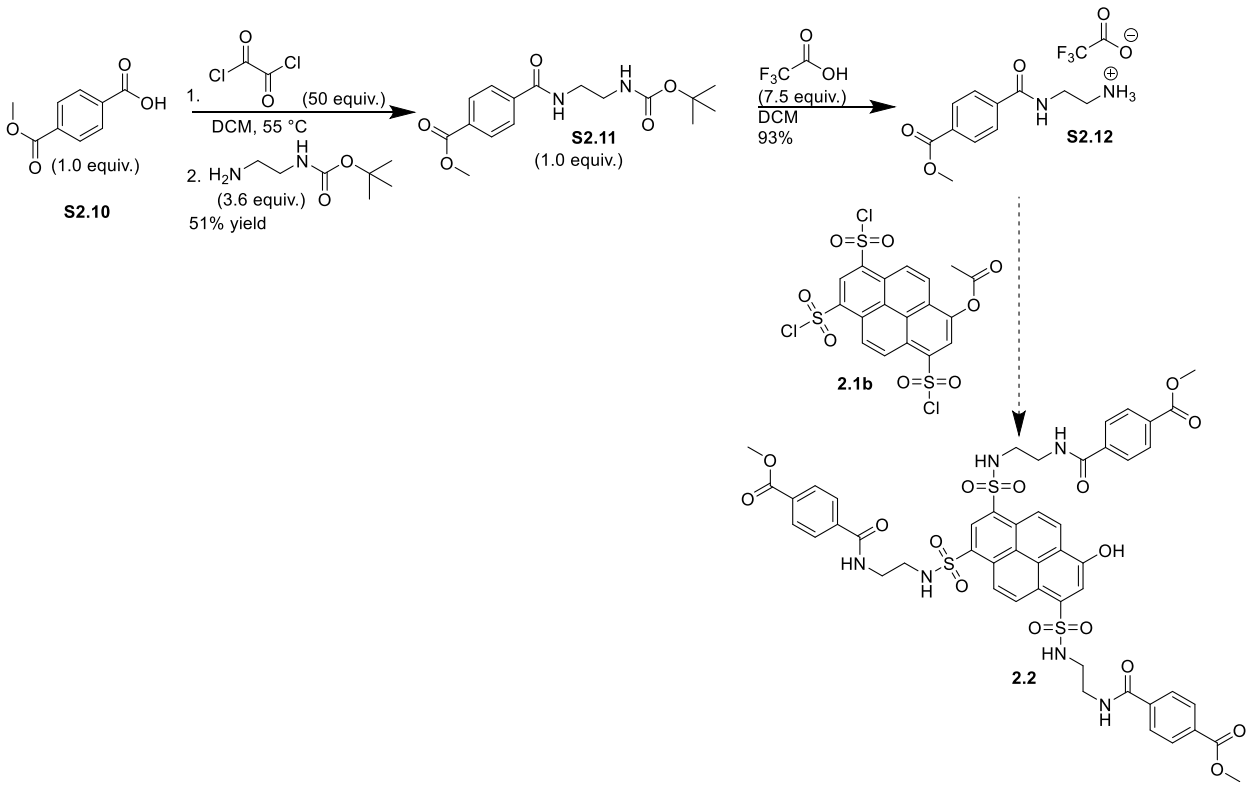

Chapter 2.7.9. Photo-responses from titanium dioxide nanoparticles covalently attached to nanopores.

This section is not related to photoacids but does involve photoelectrochemical measurements of nanoparticles in nanopores. These studies were to demonstrate proof of concept that a single nanoparticle or few nanoparticles can be characterized with photoelectrochemical measurements without the use of wires. It requires that the particle is trapped inside a nanopore and is the primary conduit for current flow. For semiconducting particles, it was envisioned that two-half redox reactions took place on either side of the trapped particle when illuminated.

Using a procedure similar to Abbasian and Aali, the surfaces of TiO_2 particles were modified with (3-aminopropyl)triethoxysilane (APTES [Figure SI 2.31]).[152] FTIR of white powder is similar to reports[153,154] of aminosilanized TiO_2 (Figure SI 2.32) suggesting that the functionalization was successful.

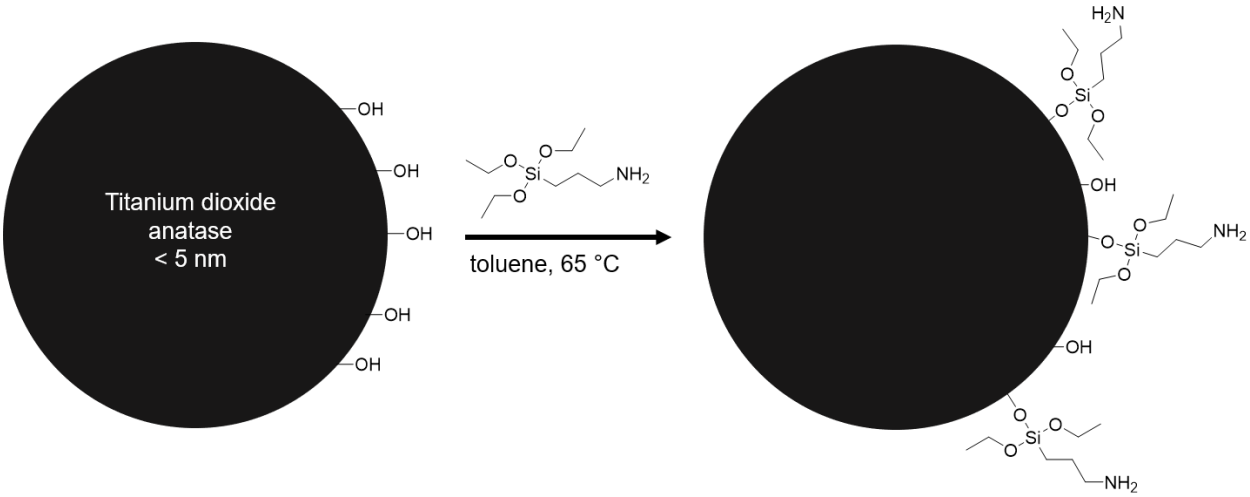

Figure SI 2.31. Partial representation of titanium dioxide surface modification with (3-aminopropyl)triethoxysilane.

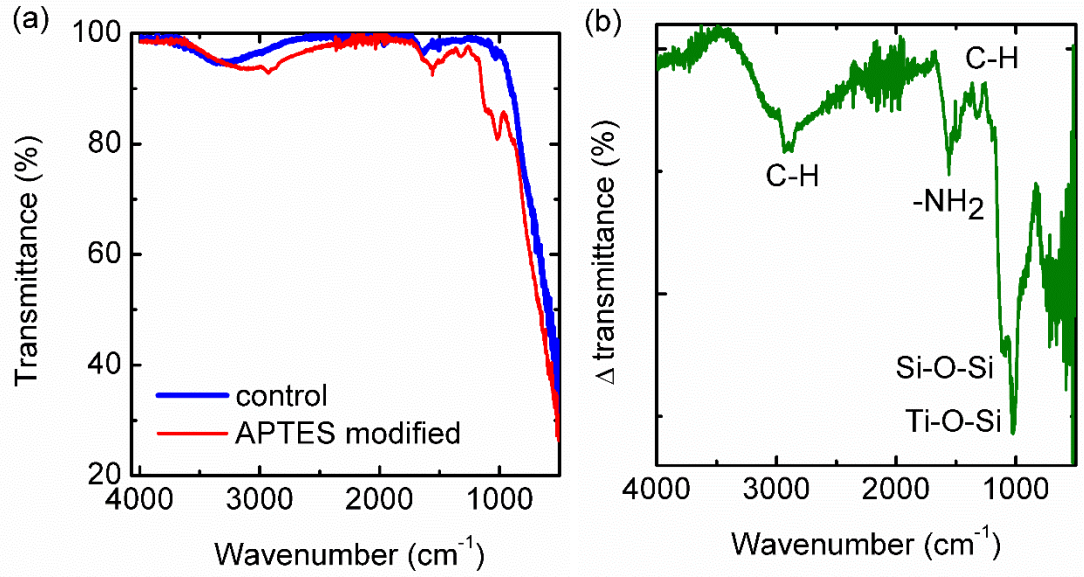

Figure SI 2.32. FTIR of TiO_2 nanopowder, (anatase, < 5 nm particle size, 99.5%) before and after aminosilanization. (b) Difference of before and after modification curves.

An hourglass nanopore was etched for a total of 61 minutes, with breakthrough occurring at 58 minutes (Figure SI 2.33). Figure SI 2.33b shows the resistance of the pore in 1 M KCl which was used to estimate the base and midpoint radii of the pore which were determined to be ~130 nm and ~1 nm respectively.

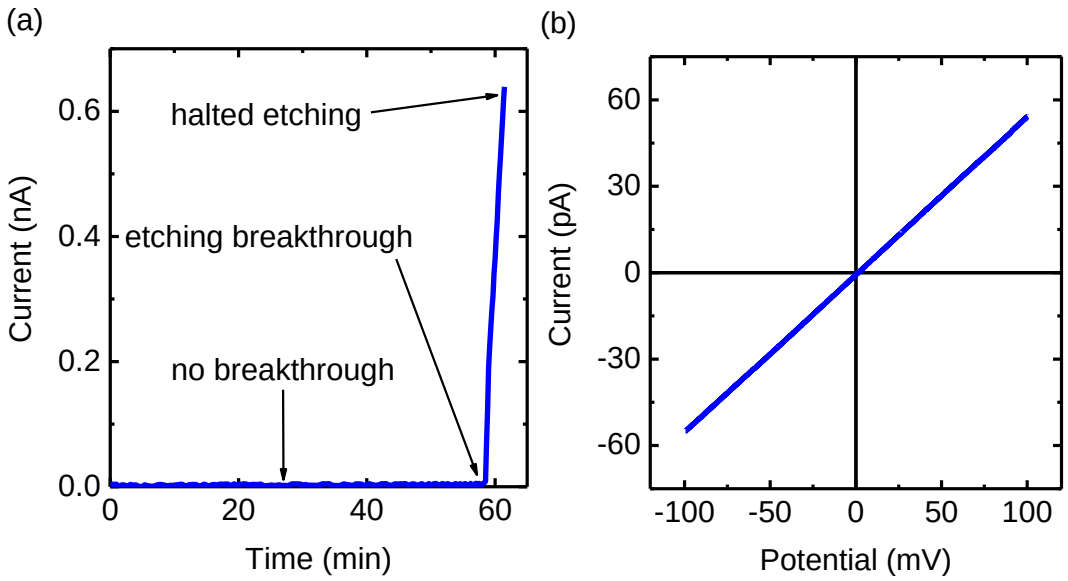

Figure SI 2.33. (a) Chronoamperometry is used to monitor etching process with Pt electrodes applying 1 V vs E_{oc}. (b) Cyclic voltammogram of hourglass nanopore immersed in 1 M KCl, 1 mM tris, pH 7.0 (aq). Slope of line is 550 pA/V.

The outer regions of the pore were capped with taurine groups using carbodiimide chemistry such that the terminal sulfonate would be unreactive to further modifications. The middle carboxylate region was converted into amide linking the titanium dioxide particles through the APTES linker (Figure SI 2.34).

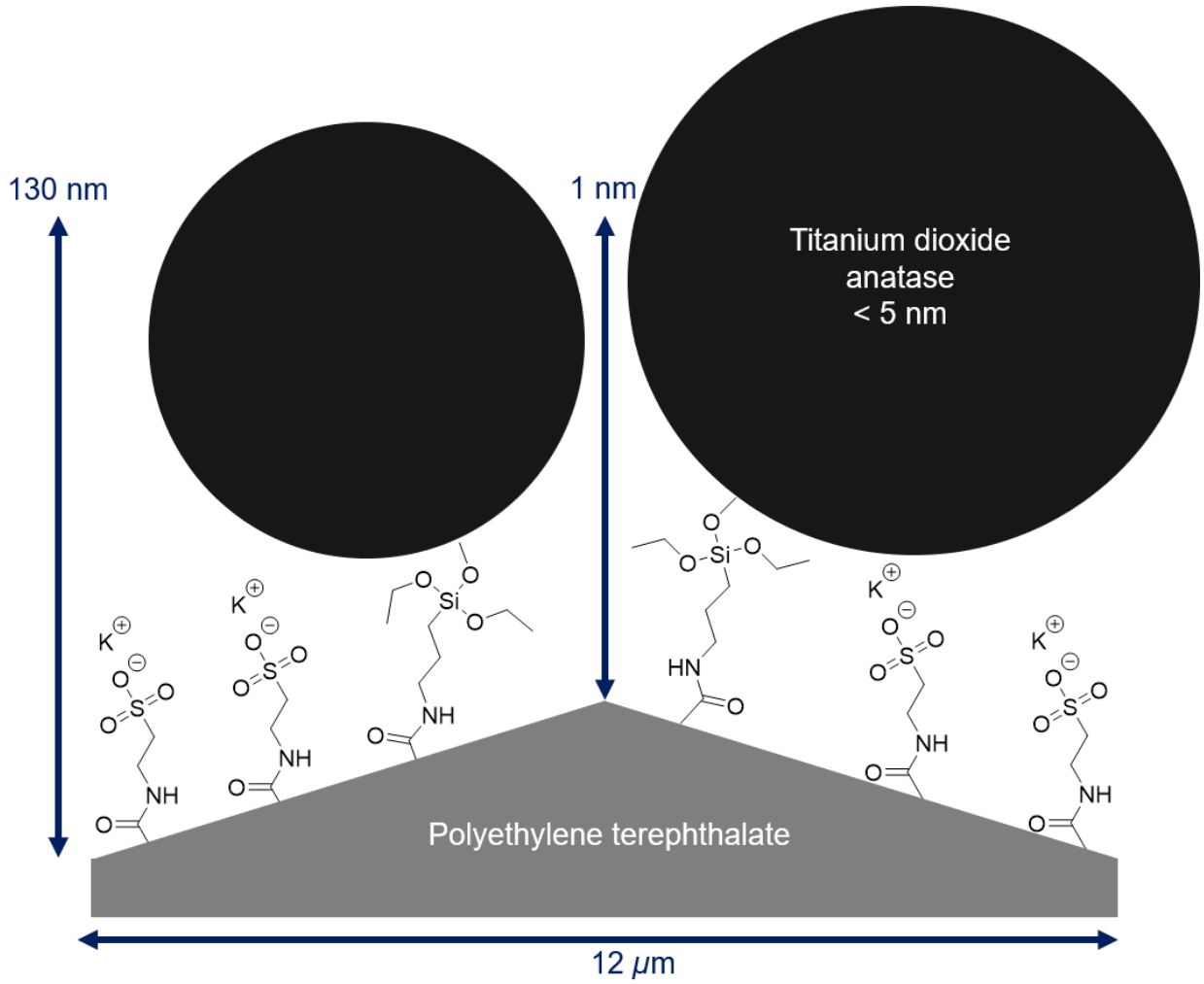

Figure SI 2.34. Half of a cross-section depicting possible surface arrangement of titanium dioxide modified hourglass nanopore.

nanopore by means of the surface charge on the channel walls. When the opening of the pore is similar to the thickness of the electrochemical double layer, the nanopore will be predominately filled with ion of opposite charge to the charge of the walls.[6] Unmodified hourglass nanopores have linear *IV*-curves due to the symmetry of the nanopore.[4] Both modification steps with taurine did not change the surface charge state of the nanopore

and thus the nature of the nanopore remained symmetric. Consequently, their *I*–*V* curves remained linear. However, the *I*–*V* curves of a nanopore coupled with APTES-TiO_2 were nonlinear with clear evidence for current rectification, likely due to the change of symmetry of the pore (Figure SI 2.35). However, the observed currents are not significantly lower than those of the pre-modified nanopore. This suggests that the covalently bound TiO_2 particles are likely not completely occluding ion transport through the nanopore. Notwithstanding, APTES-TiO_2 modified nanopores possessed a desirable photoresponse.

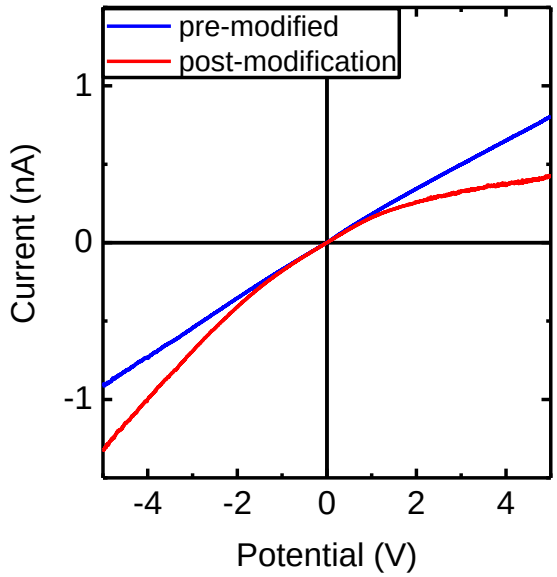

Figure SI 2.35. Cyclic voltammogram of pre-modified hourglass nanopore and post-modified hourglass nanopore. Modified nanopore had APTES-TiO_2 covalently bound to the middle surface of the hourglass and taurine covalently bound to the remainder of the surface. Electrolyte was aqueous pH 7, 100 mM KCl, 1 mM tris buffer.

An open-circuit voltage (OCV) of 0.4 mV was observed for APTES-TiO_2 modified nanopores immersed in aqueous pH 4 100 mM KCl electrolyte, and illuminated with an ELH lamp at 1.5 Suns intensity. A steady-state OCV of ~0.4 mV was observed after approximately 15 seconds of illumination (Figure SI 2.36a). When MeOH was added to one chamber of the cell, an increase in the OCV was observed to a value of 1.75 mV; however, the time to reach this condition nearly quadrupled, to 55 seconds (Figure SI 2.36b). The effect was reproducible; moreover, an OCV was not observed in control samples that did not contain APTES-TiO_2. A long pass 420 nm filter was introduced during OCV and short-circuit measurements (Figure SI 2.36c,d). The filter blocked the high energy electromagnetic radiation that would otherwise be absorbed by the titanium dioxide and allowed only longer wavelengths of electromagnetic radiation to pass. In doing so, the titanium dioxide particle was not able to partake in an excited-state reaction and photo-responses were not observed. This suggests that the observed photo-effects were not thermally induced. Shown in Figure SI 2.36e is capacitive charging and discharging of the particles in the absence of methanol upon initial illumination and discontinuing illumination. When the particle underwent the illumination sequence in the presence of methanol, an electron donor, the capacitive effects were not observed.

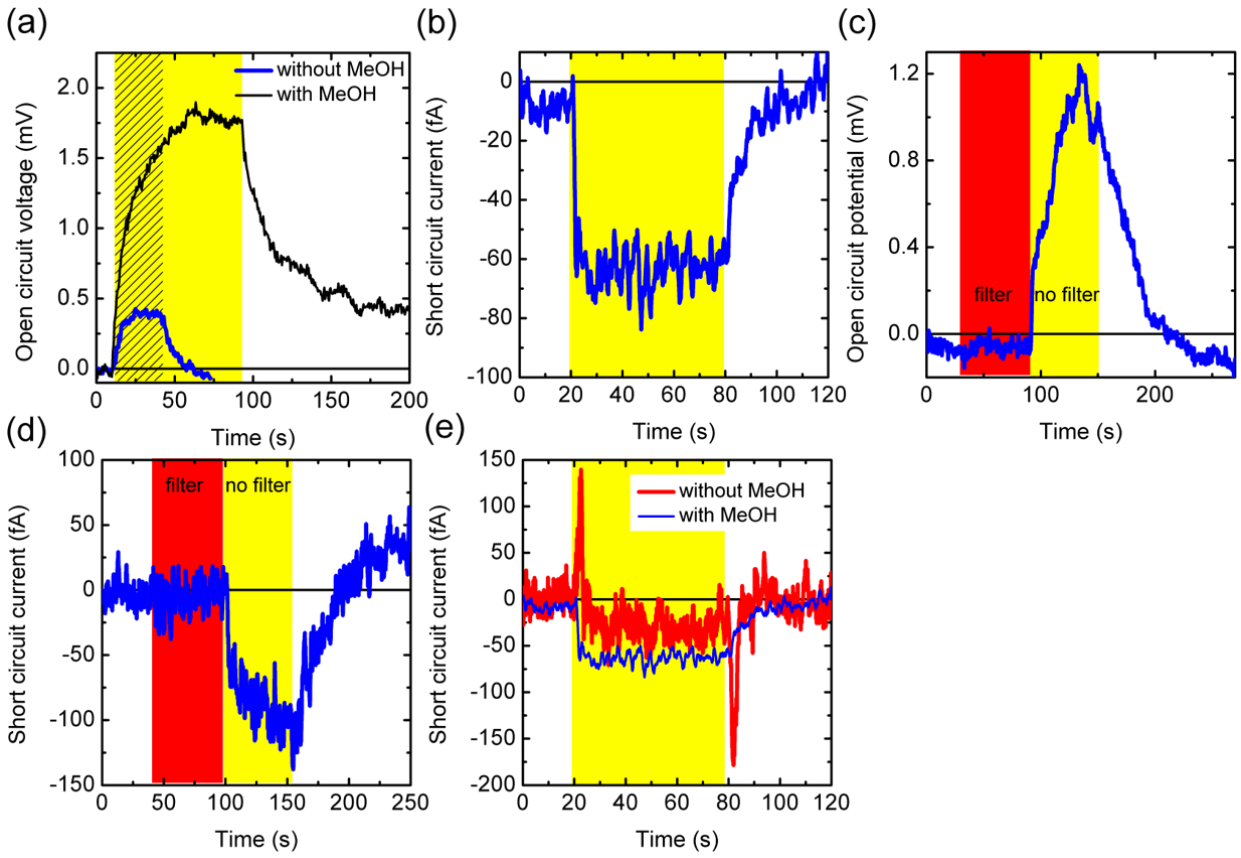

Figure SI 2.36. (a) Blue line is an OCV of sample in aqueous pH 4 100 mM KCl illuminated with an ELH lamp at 1.5 Suns intensity. Black line is an OCV of same sample in aqueous pH 4 100 mM KCl illuminated with an ELH lamp at 1.5 Suns intensity; sample contained 1:6, volume MeOH: volume of pH 4 100 mM KCl, in the chamber farthest from the window. (b) Short-circuit current of sample in aqueous pH 4 100 mM KCl illuminated with an ELH lamp at 1.5 Suns intensity; sample contained 1:6, volume MeOH: volume of pH 4 100 mM KCl, in the chamber farthest from the window. (c) OCV of sample illuminated with an ELH lamp at 1.5 Suns intensity with and without a long pass 420 nm filter to rule out thermal effects. (d) Short-circuit current of sample in aqueous pH 4 100 mM KCl illuminated with an ELH lamp at 1.5 Suns intensity with and without long pass 420 nm filter. (e) Short-circuit current of sample with and without methanol.

Chapter 2.8. Supplemental Experimental.

Synthesis of the N,N'-(ethane-1,2-diyl)bis(tolunesulfonamide) (S2.2). Reaction conditions were adopted from Oae and Kadoma[139]. 4-toluenesulfonyl chloride (0.203 g, 1.06 mmol, 2.12 equiv.) was added to a stirring solution of 10 mL, 200 proof ethanol. Subsequently, triethylamine (1 mL, 7 mmol, 14.0 equiv.) was added to the stirring solution. Ethylenediamine (33.4 µL, 0.500 mmol, 1.00 equiv.) was added which caused the solution to become an opaque white. Additional triethylamine (1 mL, 7 mmol, 14.0 equiv.) was added. Reaction was monitored by TLC; starting material was consumed within 30 minutes. The white powder was vacuum filtered and washed with ether (0.137 g, 0.371 mmol, 74% yield). ^{1}H NMR (400 MHz, $CDCl_3$) δ 7.72 (d, 4H), 7.32 (d, 4H), 4.94 (s, 2H), 3.07 (s, 4H), 2.44 (s, 6H).

N-(2-aminoethyl)-4-methylbenzenesulfonamide (S2.3). Synthesized according to Sheldon and coworkers.[155] 4-toluenesulfonyl chloride (0.870 g, 4.56 mmol, 1.00 equiv.) was dissolved in 10 mL of dichloromethane, which was then added dropwise over a period of 15 minutes to a rapidly stirring solution of ethylenediamine (10.0 mL, 150 mmol, 32.7 equiv.) and dichloromethane (10 mL). The solution was stirred for an additional 30 minutes, washed twice with water, and carefully dried over calcium hydride. The solvent was concentrated under vacuum to obtain a white powder (0.542 g, 2.53 mmol, 55% yield). ^{1}H NMR (400 MHz, $CDCl_3$) δ 7.77 (d, 2H), 7.31 (d, 4H), 2.98 (t, 2H), 2.82 (t, 2H), 2.59 (broad, 2H), 2.43 (s, 3H); ^{13}C NMR (600 MHz, $CDCl_3$) δ 129.88, 127.27, 45.36, 40.07, 21.66.

Utilization of sulfonyl chloride S2.1 in nanopores.

A polyethylene terephthalate nanofluidic diode was fabricated using the asymmetric etching procedures and the chemical modification (of pore surfaces with ethylenediamine) procedures outlined in the supplemental materials presented by Vlassiouk and Siwy.[89] The dimensions of the nanopore were approximated to be A = 716 nm and a = 10.6 nm by the bulk etch rate and the electrochemical resistance relation (Equation X). While still contained in the H-cell, the pore was rinsed with 200 proof ethanol and then a 200 proof ethanolic solution of 0.1 M 4-toluenesulfonyl chloride and 0.7 M triethylamine was added to both sides of the pore. The reaction solution sat for 50 minutes, and then was rinsed with 200 proof ethanol three times and then reverse osmosis water three times.

Unipolar diode fabrication. Two step S2.3 and ethylenediamine modification.

A conical nanopore was fabricated using the asymmetric etching procedures outlined in the supplemental materials presented by Vlassiouk and Siwy.[89] The dimensions of the nanopore were approximated to be A = 405 nm and a = 2.5 nm by the bulk etch rate and the electrochemical resistance relation (Equation X). A chemical modification process similar to Vlassiouk and Siwy was used to modify the surface.[89] An aqueous solution containing 1 mM 2-(*N*-morpholino)ethanesulfonic acid hemisodium salt and 100 mM KCl was titrated to pH 5.5 and used to wash a freshly prepared nanopore contained in a H-cell. After several rinses, the solution was placed on the base side of the nanopore. An aqueous solution containing 1 mM MES buffer, 0.05 M N-(2-aminoethyl)-4-methylbenzenesulfonamide, 0.05 M *N*-(3-dimethylaminopropyl)-*N*′-ethylcarbodiimide hydrochloride, and 100 mM KCl was titrated to pH 5.5 and placed on the tip side of the

nanopore. A silver/silver chloride electrode was placed on both sides of the membranes and used to probe the reaction progression every five minutes via a -5 volts to $+5$ volts cyclic voltammogram sweep. The reaction solution sat for 60 minutes and then the entire H-cell was rinsed out with reverse osmosis water twice, 200 proof ethanol twice, and reverse osmosis water three times.

The nanopore underwent electrochemical characterization measurements (Figure X and Xx) and then modified further with the Vlassiouk and Siwy procedure.[89] The H-cell containing the nanopore was rinsed with reverse osmosis water three times. An aqueous solution containing 1 mM 2-(*N*-morpholino)ethanesulfonic acid hemisodium salt and 100 mM KCl was titrated to pH 5.5 and used to the rinse the H-cell and film. An aqueous solution containing 1 mM MES buffer, 0.05 M ethylenediamine, 0.05 M *N*-(3-dimethylaminopropyl)-*N*′-ethylcarbodiimide hydrochloride, and 100 mM KCl was titrated to pH 5.5 and placed on both sides of the nanopore. The reaction solution sat for 60 minutes and then the entire H-cell was rinsed out with reverse osmosis water three times.

2-acetoxynaphthalene-6-sulfonic acid potassium salt (S2.5). The 2-naphthol-6-sulfonic acid potassium salt (1.073 g, 4.090 mmol, 1.000 equiv.) was suspended in a stirring solution of TEA (7.0 mL, 50 mmol, 12 equiv.) and acetic anhydride (1.8 mL, 19 mmol, 4.7 equiv.). The reaction was stirred for 24 hours at room temperature and a powder was collected by vacuum filtration. The tan powder was washed with acetone (0.912 g, 3.00 mmol, 73% yield). ^{1}H NMR (400 MHz, D_2O) δ 8.34 (s, 1H), 8.03 (d, 1H), 7.96 (d, 1H), 7.84 (d, 1H), 7.63 (s, 1H), 7.34 (d, 1H), 2.38 (s, 3H).

6-(chlorosulfonyl)naphthalen-2-yl acetate (S2.6). Thionyl chloride (0.17 mL, 2.34 mmol, 3.58 equiv.) was added to a stirring suspension of acetoxynaphthol **S2.5** (0.199 g, 0.654 mmol, 1.00 equiv.) in dichloromethane (10 mL) and three drops of dimethylformamide. The solution refluxed for four hours. The solution was cooled and concentrated under vacuum. After the first concentration, dichloromethane was added, and the solution was concentrated under vacuum again; this aided in the co-distillation of residual thionyl chloride. Compound was dissolved in dichloromethane and celite (0.1 g) was stirred in the solution for 20 minutes. The celite was removed via vacuum filtration, and the filtrate was concentrated under vacuum until only a small amount of residual solvent remained as a cluster of liquid drops. Yellow crystals were precipitated from the liquid drops by adding 3 mL of *n*-pentane (0.094 g, 0.30 mmol, 50% yield). ^{1}H NMR (400 MHz, $CDCl_3$) δ 8.58 (s, 1H), 8.04 (d, 1H), 8.00 (coalescing, 2H), 7.71 (d, 1H), 7.43 (dd, 1H), 2.37 (s, 3H).

***tert*-butyl (2-((6-hydroxynaphthalene)-2-sulfonamido)ethyl)carbamate (S2.7).** Sulfonyl chloride S**2.6** (0.502 g, 1.76 mmol, 1.00 equiv.) was dissolved in dichloromethane (5 mL) and added to a stirring solution of *N*-Boc-ethylenediamine (2.81 g, 17.6 mmol, 9.96 equiv.) diluted in dichloromethane (5 mL). The solution was refluxed for 19 hours and then allowed to cool. The solution was washed with 1 M hydrochloric acid (100 mL × 4). The product partially precipitated during the separation process and was collected via vacuum filtration and washed with chilled dichloromethane (0.116 g). From the separation process, the organic layer was cooled to coerce further precipitation of product which was collected via vacuum filtration (0.186 g). The organic filtrates were combined, washed with water,

and concentrated under vacuum. Chilled dichloromethane was added and used to wash the powder during collection via vacuum filtration (0.157 g). The white powdered products were combined (0.452 g, 1.25 mmol, 71% yield). ^{1}H NMR (400 MHz, $(CD_3)_2CO$) δ 9.14 (s, 1H), 8.34 (d, 1H), 7.99 (d, 1H), 7.85 (d, 1H), 7.76 (dd, 1H), 7.32 (d, 1H), 7.30 (dd, 1H), 6.58 (t, 1H), 6.04 (broad, 1H), 3.18 (q, 2H), 3.02 (q, 2H), 1.35 (s, 9H).

2-((6-hydroxynaphthalene)-2-sulfonamido)ethan-1-aminium chloride (S2.8). Carbamate **2.7** (0.117 g, 0.318 mmol) was added to 4 mL of 3 M hydrochloric acid (ethanolic) and stirred at 60 °C for 1 hour. The solution was concentrated under vacuum and scrapped into a scintillation vial for storage (0.056 g, 78% purity therefore 45% yield, 0.184 mmol). ^{1}H NMR (500 MHz, D_2O) δ 8.35 (s, 1H), 7.94 (d, 1H), 7.88 (d, 1H), 7.72 (dd, 1H), 7.27 (coalescing, 2H), 3.15 (coalescing, 4H).

4-methoxybenzoyl chloride (S2.11a). Thionyl chloride (10 mL, 1.46 mmol, 94.3 equiv.) was added to 4-methoxybenzoic acid (0.225 g, 1.45 mmol, 1.00 equiv.). Five drops of dimethylformamide was added while stirring. The reaction was refluxed for 48 hours. The solvent was removed under vacuum and a yellow oil was obtained (0.211 g, 1.23 mmol, 84% yield). ^{1}H NMR (500 MHz, DMSO-d_6) δ 8.06 (coalescing, 4H), 3.88 (s, 3H). ^{1}H NMR (500 MHz, $CDCl_3$) δ 8.19 (d, 2H), 8.16 (d, 2H), 3.97 (s, 3H).

***tert*-butyl (2-(4-methoxybenzamido)ethyl)carbamate (S2.11).** The powder, 4-methoxybenzoic acid (0.532 g, 3.49 mmol, 1.00 equiv.) was dried under reduced pressure and then oxalyl chloride (15.0 mL, 175 mmol, 50.1 equiv.) was added. The solution was

stirred for 6.5 hours at 55 °C, and then cooled to room temperature and concentrated under vacuum. A mixture of *N*-Boc-ethylenediamine (2.0 g, 12 mmol, 3.6 equiv.) in dichloromethane (20 mL) was added. The solution was stirred for 18 hours at room temperature and then ether was added to coerce precipitation of the unreacted *N*-Boc-ethylenediamine salt. The precipitate was removed via vacuum filtration and the filtrate was concentrated under vacuum to a white powder. The white powder was rinsed with slightly acidic water (pH 2) and dried under vacuum (0.527 g, 1.79 mmol, 51% yield). ^{1}H NMR (500 MHz, DMSO-d_6) δ 8.63 (s, 1H), 8.03 (d, 2H), 7.95 (d, 2H), 6.91 (s, 1H), 3.88 (s, 3H), 3.30 (q, 2H), 3.11 (q, 2H), 1.36 (s, 9H). ^{1}H NMR (500 MHz, DMSO-d_6) δ 8.63 (s, 1H), 8.03 (d, 2H), 7.95 (d, 2H), 6.91 (s, 1H), 3.88 (s, 3H), 3.30 (q, 2H), 3.11 (q, 2H), 1.36 (s, 9H).

2-(4-methoxybenzamido)ethan-1-aminium trifluoroacetate (S2.12). Trifluoroacetic acid (1.0 mL, 13 mmol, 7.5 equiv.) was added to a stirring solution of carbamate **5.1** (0.512 g, 1.73 mmol, 1.00 equiv.) in dichloromethane (25 mL). The solution was stirred for 30 minutes and then concentrated under vacuum to an oil. The oil was co-distilled with dichloromethane under vacuum which resulted in the removal of residual acid and the formation of a white powder (0.501 g, 1.63 mmol, 93% yield). ^{1}H NMR (500 MHz, DMSO-d_6) δ 8.84 (s, 1H), 8.05 (d, 2H), 7.99 (d, 2H), 7.95 (broad, 3H), 3.88 (s, 3H), 3.52 (q, 2H), 3.01 (t, 2H).

Cyclic voltammetry of 2.1. A cyclic voltammetry experiment was performed on a VSP-300 (BioLogic Science) using a 2 mm diameter platinum disk working electrode, a saturated calomel reference electrode, and a platinum wire counter electrode. Measurements were

recorded in an argon purged vessel at ambient temperature and a scan rate of 100 mV s^{-1}. The sample concentration of **2.1** was 0.9 mM in DMSO containing 100 mM [*N*-Bu_4N][PF_6] as the supporting electrolyte. Potential was referenced to the Fc^+/Fc couple at 433 mV.

Titanium dioxide particle modification.

Titanium dioxide nanopowder (TiO_2, anatase <5 nm particle size, 99.5%) was purchased from US Research Nanomaterials, Inc. (3-aminopropyl)triethoxysilane (98%) was purchased from Sigma-Aldrich. Using a procedure similar to Abbasian and Aali, the surfaces of TiO_2 particles were modified with (3-aminopropyl)triethoxysilane (APTES).[152] Briefly, TiO_2 (1.068 g, 13.37 mmol) was suspended in anhydrous toluene under nitrogen. Then APTES (2.290 g, 12.77 mmol) was added. The solution was heated to 65 ^{0}C and stirred for 24 hours. The suspension was filtered under vacuum, washed with dichloromethane, and dried under vacuum to obtain a white powder (1.009 g).

Hourglass nanopore fabrication.

Single hourglass-pore polyethylene terephthalate (PET) films were prepared by bombarding 12 μm PET films with a single heavy ion, specifically uranium, bismuth, or gold ions of energy of 11.4 MeV per nucleon, to generate a latent track that spanned the thickness of the film (UNILAC, GSI Darmstadt, Germany). The hourglass nanopore was then produced by a chemical track etching procedure. For better etching results, the films were irradiated with near-UV light on both sides, rinsed with isopropanol, methanol, followed by a RO water rinse. The film was then placed in a clean H-cell for subsequent etching; 9 M

NaOH was placed on both sides of the film to etch the latent track.[4] The latent track etches faster than the bulk PET. A bias of 1 V was applied across the film, a decrease in the resistance (passing 650 pA) across the film signified pore breakthrough and complete synthesis of an hourglass nanopore. The reaction was usually halted when a current of ≅650 pA was observed. Breakthrough occurred at 58 minutes and the reaction was halted at 61 minutes. The resulting nanopore has a large pore opening with a radius A which was approximated based on the bulk etch rate (for the described etching scenario[5]) of 2.13 nm/min. The middle of the hourglass pore has a radius of a and is approximated by the equation, $R = \frac{L}{\pi g A a}$, where R is the resistance of a nanopore, L is the full length of the pore, and g is the specific conductivity of the electrolyte (10 S/m). Between -0.1 V and 0.1 V, the *IV*-curves of hourglass nanopores at 1 M KCl are linear; the slope of the line is the electrical conductance, and thus R is equal to its recipricol.[5] For pores presented herein, a ≈ 2 nm and A ≈ 130 nm.

Chemical modification of pore surfaces.

1. A nanoporous film was placed in an H-cell. The film acts as a divider and separated the two-chambers.
2. The cell was rinsed with a pH 3.9, 100 mM KCl aqueous solution.
3. An aqueous 0.1 M 1-ethyl-3-(3-dimethylaminoproypl)carbodiimide (EDC) solution was titrated to pH 3.9 with aqueous HCl.
4. An aqueous 0.1 M 1 M phosphate buffer solution was titrated to pH 10.5 with aqueous NaOH.

5. The EDC solution and phosphate solution were put on opposite sides of the film. The EDC solution activated the PET surface whereas the phosphate solution prevented activation. The solutions were allowed to stand for 1 hour. The solutions were removed, and the cell was rinsed out with RO water.
6. To both sides of the film, a 0.1 M taurine solution, pH 6.9, was added and allowed to stand for 4 hours. Taurine reacts with the activated surface.
7. Steps 2-6 were repeated with the exception that the EDC solution and phosphate solution were placed in the opposite chambers. By doing so, the PET surface is modified with taurine everywhere except in the middle of the hourglass. The linked taurine is not reactive towards EDC modification.

1. The middle of the nanopore was then covalently modified with TiO_2 (Figure 5b).

1. The cell was rinsed with a pH 3.9, 100 mM KCl aqueous solution.
2. An aqueous 0.1 M 1-ethyl-3-(3-dimethylaminoproypl)carbodiimide (EDC) solution was titrated to pH 3.9 with aqueous HCl.
3. The EDC solution was placed on both sides of the film and the solution was allowed to stand for 1 hour.
4. The EDC solution was removed and the cell was rinsed out with RO water.
5. The APTES treated TiO_2 (0.1 g) was sonicated in methanol (20 mL) for 10 minutes.
6. The methanolic suspension of APTES treated TiO_2 was placed on both sides of the film and allowed to stand for 18 hours.
7. The solutions were removed and the film was thoroughly rinsed with RO water.

Electrochemical characterization of hourglass nanopore surface.

Experiments were carried out on the potentiostat, VSP-300 (BioLogic Science), equipped with low-current cables using Pt, SCE, SCE, Pt electrodes as the working, reference #1, reference #2, and counter electrode, respectively. The nanoporous film was placed in an H-cell; the film acted as a divider and separated the two chambers. The film which was immersed in pH 4 100 mM KCl electrolyte. Each side of the cell had both Pt and SCE electrodes immersed in the electrolyte. The cells were illuminated with an ELH lamp at 1.5 Suns intensity.

Ancillary data and data processing methods of photoelectrochemical measurements. (a) Blue line is an OCV of sample in aqueous pH 4 100 mM KCl illuminated with an ELH lamp at 1.5 Suns intensity. Black line is an OCV of same sample in aqueous pH 4 100 mM KCl illuminated with an ELH lamp at 1.5 Suns intensity; sample contained 1:6, volume MeOH: volume of pH 4 100 mM KCl, in the chamber farthest from the window. Blue line represents the average of 5 individual illumination sequences after baselining the dark potential to 0 V. Black line is single illumination event after baselining the dark potential to 0 V. Before baselining, the average dark potential was ~0.4 mV; raw data was subtracted by ~0.4 mV to obtain baseline. During entire OCV measurements, no drifting occurred; no other math was applied to data. (b) Short-circuit current of sample in aqueous pH 4 100 mM KCl illuminated with an ELH lamp at 1.5 Suns intensity; sample contained 1:6, volume MeOH: volume of pH 4 100 mM KCl, in the chamber farthest from the window. First an OCV was performed until OCV remained steady at ~0 V. Then CA measurement was performed in which 0 V vs E_{oc} was applied. The data represents the average of 5 individual

illumination sequences after baselining the dark current to 0 A. Before baselining, the average dark current was ~0.1 nA; raw data was subtracted by ~0.1 nA to obtain baseline. (c) OCV of sample illuminated with an ELH lamp at 1.5 Suns intensity with and without a long pass 420 nm filter to rule out thermal effects. Only one illumination sequence, not an average of 5. Baselined data with simple subtraction. (d) Short-circuit current of sample in aqueous pH 4 100 mM KCl illuminated with an ELH lamp at 1.5 Suns intensity with and without long pass 420 nm filter to rule out thermal effects. Only one illumination sequence, not an average of 5. Baselined data with simple subtraction. (e) Short-circuit current of sample with and without methanol. First an OCV was performed until OCV remained steady at ~0 V. Then CA measurement was performed in which 0 V vs E_{oc} was applied. The data represents the average of 5 individual illumination sequences after baselining the dark current to 0 A. Before baselining, the average dark current was ~0.1 nA; raw data was subtracted by ~0.1 nA to obtain baseline.

Chapter 2.9. Acknowledgments

The authors are grateful for financial support from the Department of Chemistry and the School of Physical Sciences at the University of California Irvine and the Gordon and Betty Moore Foundation under a Moore Inventor Fellowship for S.A. We thank the UCI Laser Spectroscopy Facility (LSF) for photoluminescence spectroscopy instrumentation, the NMR Facility for NMR measurements, and the Mass Spectrometry Facility for ESI-MS measurements. We also thank Eugenia Toimil-Molares for supplying the heavy-ion irradiated PET films, Zuzanna Siwy and Steven Buchsbaum for training and guidance in nanopore etching and functionalization, Enrico Gratton and Michelle Digman for use of their Laboratory of Fluorescence Dynamics (LFD), Jonathan Lam for general synthetic advice, and Alan Heyduk for use of his laboratory space and his group members for support and guidance.

Chapter 3. Observation of photovoltaic action from photoacid-modified Nafion due to light-driven ion transport.[76]

Chapter 3.1. Overview.

Replacing passive ion-exchange membranes, like Nafion, with membranes that use light to drive ion transport would allow membranes in photoelectrochemical technologies to serve in an active role. Toward this, we modified perfluorosulfonic acid ionomer membranes with organic pyrenol-based photoacid dyes to sensitize the membranes to visible light and initiate proton transport. Covalent modification of the membranes was achieved by reacting Nafion sulfonyl fluoride poly-(perfluorosulfonyl fluoride) membranes with the photoacid 8-hydroxypyrene-1,3,6-tris(2-aminoethylsulfonamide). The modified membranes were strongly colored and maintained a high selectivity for cations over anions. Fourier transform infrared spectroscopy, X-ray photoelectron spectroscopy, and ion-exchange measurements together provided strong evidence of covalent bond formation between the photoacids and the polymer membranes. Visible-light illumination of the photoacid-modified membranes resulted in a maximum power-producing ionic photoresponse of ~100 μA cm^{-2} and ~1 mV under 40 Suns equivalent excitation with 405 nm light. In comparison, membranes that did not contain photoacids and instead contained ionically associated Ru^{II}–polypyridyl coordination compound dyes, which are not photoacids, exhibited little-to-no photoeffects (~1 μA cm^{-2}). These disparate photocurrents, yet similar yields for nonradiative excited-state decay from the photoacids and the Ru^{II} dyes, suggest temperature gradients were not likely the cause of

the observed photovoltaic action from photoacid-modified membranes. Moreover, spectral response measurements supported that light absorption by the covalently bound photoacids was required in order to observe photoeffects. These results represent the first demonstration of photovoltaic action from an ion-exchange membrane and offer promise for supplementing the power demands of electrochemical processes with renewable sunlight-driven ion transport.

Chapter 3.2. Introduction.

Proton pumps are ubiquitous in biology, where light or adenosine triphosphate drives the proton-pumping process to generate a difference in proton activity across a lipid bilayer. [156,157] When these nonequilibrium conditions are generated using light, the photoconversion process can be termed "photo-voltaic" because light is responsible for the generation of a voltage across the membrane. [158–165] When proton transport is accompanied by the transport of other ions to maintain charge neutrality, the energy storage process is chemical like that in batteries, whereas when protons are the only species that are transported, the energy storage process is mostly electric like that in capacitors. [156,157] The most efficient and well-studied solar cells utilize semiconductors with pn-junctions and exhibit photovoltaic action by a capacitive mechanism. We aimed to develop an artificial light-driven proton pump that operated by the same mechanism but with protons and hydroxides serving as the charge-separated species instead of electrons and holes.[165]

Several demonstrations of artificial light-driven proton pumps have been reported. [39,46,74,166,167] Most reports utilized a nanometers-thick lipid bilayer membrane containing

molecular dyes, which initiated the proton pumping process by a photoinduced proton-coupled electron-transfer reaction.[4–6,8,9] The report by Bakker and colleagues was unique, because it used a 30 μm thick microporous polyethylene membrane impregnated with merocyanine photoacid dye molecules to sensitize the light-to-ionic energy conversion process.[46] The authors observed a ~210 mV photovoltage using bidirectional excitation from a Xe arc lamp. This consisted of visible-light illumination from one side of the membrane and ultraviolet-light illumination from the other side of the membrane. Although this proton-pumping process utilized an external optical asymmetry, and not an internal asymmetry like that present in many semiconductors, the magnitude of the photovoltage was independent of the bulk pH, suggesting that the voltage was capacitive, like that observed in state-of-the-art electronic solar cells.

Light absorption by a dye molecule ultimately results in a thermally equilibrated excited state whose electronic and nuclear configurations differ from those of the ground state. In typical dye-sensitized light-to-electrical energy-conversion devices, electron transfer is driven by a change in the redox potential of a dye when it is electronically excited.[168] In our design, proton transfer is driven by a change in the strength of a protic bond of a photoacid dye, and thus its Brønsted acidity, when it is electronically excited (Figure 3.1a).[151] In aqueous electrolytes at moderate pH, thermodynamically a proton dissociates from the protic group of an excited-state photoacid dye and therefore the concentration of free (or solvated) protons increases, via the reaction PA-OH + photon → PA-O^- + H^+, where PA-OH is the protonated photoacid molecule. For successful photoacidic dye sensitization, the free proton must cage escape from the conjugate base of the photoacid. Then, in its ground state, the conjugate base of the photoacid is reprotonated by a proton donor, e.g.,

water, to regenerate the initial state of the photoacid with concomitant formation of the conjugate base of the proton donor, e.g., OH^-.[169–171]

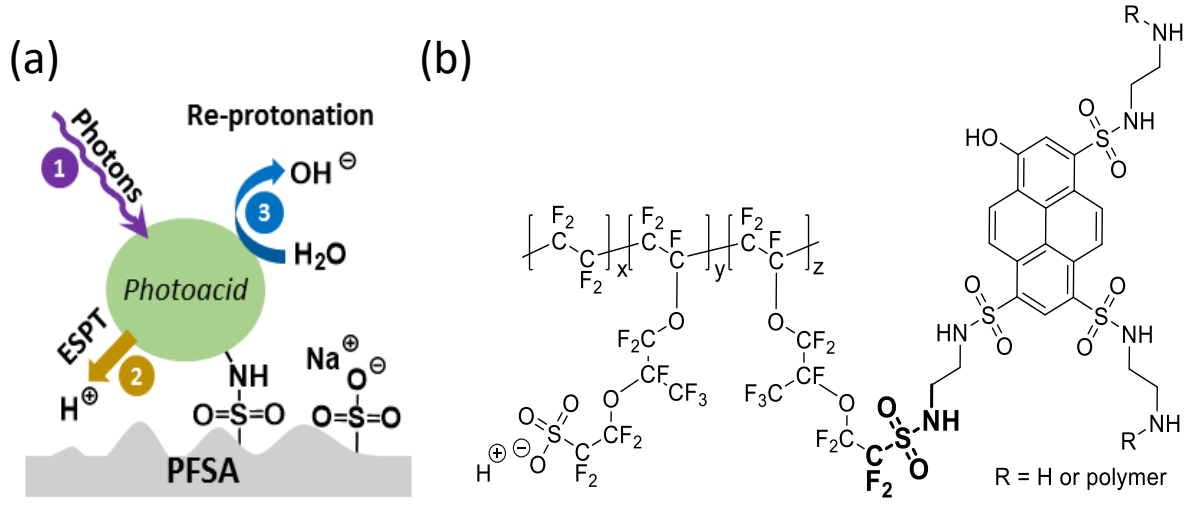

Figure 3.1 (a) Scheme showing the proposed sensitization cycle of perfluorosulfonic acid ionomer membrane (**PFSA**) modified with 8-hydroxypyrene-1,3,6-tris(2-aminoethylsulfonamide) photoacids, including excited-state proton transfer (ESPT). (b) Proposed structure of the membrane, where R = $-SO_2R'$ or $-H$. In the case of R = $-H$, the amine is protonated to form a positively charged ammonium group.

Using this as motivation, we incorporated photoacid dye molecules into Nafion, a perfluorosulfonic acid ionomer membrane (**PFSA**) that is a copolymer with a poly-(tetrafluoroethylene) backbone and pendant sulfonate groups attached via perfluorovinyl ether groups.[82] Nafion is the state-of-the-art cation-exchange membrane used in most electrochemical technologies, is completely transparent to visible light, and is a permselective polymer with superb cationic conductivity.[81,172] We intended for Nafion to serve as an optically transparent contact to selectively collect transiently generated protons

at the Nafion–solution interface and therefore facilitate photovoltaic action.[165,173] Sensitization of Nafion to visible light was achieved through covalent modification using photoacid dye molecules, 8-hydroxypyr-ene-1,3,6-tris(2-aminoethylsulfonamide) (Figure 3.1b), or ionic incorporation of Ru^{II}–polypyridyl coordination compounds. While cationic dye molecules have been incorporated ionically into Nafion for over several decades, covalent modification of Nafion with dye molecules has not been previously reported.[174–177]

Chapter 3.3. Experimental.

Reagents and Chemicals. All chemicals were reagent grade and were used without further purification unless stated otherwise. The following reagents were used as received from the indicated suppliers: sulfuric acid (95%, Fisher Scientific), sodium hydroxide (>95%, Macron Fine Chemicals), Nafion NR-212 poly(perfluorosulfonic acid) membrane (2 mil (50.8 μm) thick, equivalent weight (EW) = 1100, Ion Power), Nafion sulfonyl fluoride poly(perfluorosulfonyl fluoride) membrane (2 mil (50.8 μm) thick, EW = 1100, C.G. Processing), dimethyl sulfoxide (>99.9%, EMD Millipore Corporation), tris(2,2′-bipyridyl)ruthenium(II) chloride hexahydrate (98% Acros Organics), and triethylamine (>99.5%, EMD Millipore Corporation). Purified 8-hydroxypyrene-1,3,6-tris(2-aminoethylsulfonamide), **2.1**, synthesized according to experimental in Chapter 2.5.

Covalent Modification of Nafion Sulfonyl Fluoride Poly-(perfluorosulfonyl fluoride) with Hydroxypyrene-Based Photoacid Molecules. First, 3 mg of the trifluoroacetate salt of 8-hydroxypyrene-1,3,6-tris(2-aminoethylsulfonamide) was dissolved in 20 mL of

isopropyl alcohol. Then to this solution, 75 μL of 1 M NaOH (aq), 45 μL of triethylamine, and a 2 cm × 2 cm piece of precast Nafion sulfonyl fluoride poly(perfluorosulfonyl fluoride) membrane were added and the reaction was stirred for 7 days at 90 °C, resulting in yellow coloration of the membrane. Inclusion of NaOH ensured that after the synthesis no sulfonyl fluoride groups remained. The membrane was subsequently and serially immersed in 10 mL of the following, for 20 min each: deionized water, 1 M H_2SO_4 (aq), 1 M NaOH (aq), deionized water. The membrane was then stored in 1 M NaCl (aq) until use. FTIR–ATR: 627, 981, 1095, 1144, 1200, 1299, 1632, 2857, 2924, 3513, and 3663 cm^{-1}.

Ionic Association of Dye Molecules in Nafion. Freshly cut Nafion membrane (2 cm × 2 cm) was pretreated by stirring in 1 M H_2SO_4 (aq) for 1 h. A stock solution of the photoacid dye 8-hydroxypyrene-1,3,6-tris(2-aminoethylsulfonamide) was prepared by dissolving 20 mg of photoacid in 10 mL of 1 M H_2SO_4 (aq) to a final concentration of 3.4 mM. A stock solution of the dye $[Ru(bpy)_3]Cl_2$ was prepared by dissolving 25 mg of $[Ru(bpy)_3]Cl_2 \cdot 6H_2O$ in 20 mL of 1 M H_2SO_4 (aq) to a final concentration of 1.6 mM, where bpy is 2,2′-bipyridine. For each dye, 5 mL of dye stock solution was added to a scintillation vial along with a 2 cm × 2 cm piece of precast Nafion and stirred for 36 h at 80 °C.

Ion Exchange Capacity. Membranes were dried for 24 h at 80 °C under reduced pressure, and a dry weight was measured gravimetrically. The membranes were then rinsed with copious amounts of deionized water and then immersed in 20 mL of 1 M HCl (aq) and stirred for 24 h at room temperature. The protonated films were then rinsed with copious amounts of deionized water, immersed in 1 M NaCl (aq), and stirred for 24 h at room temperature.

The membranes were then removed, and the soaking solution was titrated to pH 7 using 10 mM NaOH (aq). Ion exchange capacity (mmol g^{-1}) was calculated as the volume (L) of 10 mM NaOH (aq) used to titrate the solution to pH 7 multiplied by its concentration (10 mM) and divided by the dry mass of each membrane (g).[178,179]

Ultraviolet–Visible (UV–Vis) Electronic Absorption Spectroscopy. Electronic absorption spectra were acquired at room temperature using a UV–Vis spectrophotometer (Cary 60, Agilent Technologies) with a resolution of 1 nm. UV–Vis absorption spectra were measured by mounting membranes in the beam path, and spectra are reported versus a baseline spectrum taken on ambient air and after correction for the nonzero absorption at 750 nm due to scattering by subtracting the observed absorbance value at 750 nm from all data points in the spectrum.

Infrared Spectroscopy. Membranes were dried for >24 h at 105 °C and under reduced pressure prior to measurements. Fourier transform infrared spectroscopy in attenuated total reflectance (ATR) detection mode was performed on a Jasco FTIR-4700 spectrophotometer equipped with a monolithic diamond ATR crystal. Spectra were acquired with a resolution of 1 cm^{-1} and an acquisition time of 74 seconds, and spectra are reported versus a baseline spectrum taken on ambient air.

X-ray Photoelectron Spectroscopy. Membranes were dried for >2 h at room temperature and under reduced pressure prior to measurements. X-ray photoelectron spectroscopy was performed using an AXIS Supra by Kratos Analytical with an Al Kα X-ray source (1486.8 eV).

Survey scans were taken first, followed by high-resolution scans of each element region. The raw data was shifted to higher binding energies so that the C 1s binding energy for an sp^3 hybridized R–CF_2–R′ group corresponded to the literature value of 292.2 eV.[180]

Fluorescence Microscopy. A custom-built two-photon excitation microscope based on an Olympus FV1000 microscope (Olympus Corporation, Tokyo, Japan) was used for solution lifetime measurements. Photoacid dye was dissolved in either concentrated 12 M HCl (aq) or dissolved in aqueous buffered solution and titrated to pH 8. The microscope was equipped with an Olympus 60X UPlanAPO objective (numerical aperture of 1.2, water immersion) (Olympus Corporation, Tokyo, Japan). Multiphoton excitation was achieved using a mode-locked 80 MHz Ti:sapphire laser (Chameleon Ultra, Coherent Inc., Santa Clara, CA) tunable from 690 to 1040 nm. The laser power was controlled by an acoustic optical modulator, and the signal was detected using a two-channel detection unit with two photosensor modules (H7422P-40, Hamamatsu Photonics KK). The fluorescence signal collected by the detectors was externally amplified and fed to a constant fraction discriminator (model 6915, Phillips Scientific, Mahwah, NJ) to produce TTL signals. These TTL pulses were counted using a Fast FLIM box (A320, ISS, Champaign, IL) and registered based on the arrival time and phase with respect to the excitation laser pulse. The channels were separated with a dichroic unit: channel 1, 460/50 nm, and channel 2, 525/50 nm. All data was obtained and analyzed using Sim-FCS software (Laboratory for Fluorescence Dynamics, UCI, http://www.lfd.uci.edu/globals/, Irvine, CA).

For cross-sectional fluorescence imaging, membranes were freshly cut using a razor blade, placed between two glass microscope slide supports, and oriented with their large

areas parallel to the direction of propagation of the incident light output from a user-modified Olympus FV1000 microscope (Olympus Corporation, Tokyo, Japan). Electrolyte (10 mM HCl (aq)) was introduced to the membrane via capillary action by placing a drop between the edges of the microscope slides. An Ar-ion laser (LASOS Lasertechnik GmbH, Jena, Germany) with an acoustic optic tunable filter enabled 488 nm excitation. Cross sections were imaged at 1024 × 1024 pixels with a pixel dwell time of 10 μs and a pixel size of 210 nm. The data was processed using ImageJ to plot mean cross-sectional intensity profiles across the film thickness.

Photoelectrochemical Procedures. Platinum electrodes were fabricated by soldering a platinum wire (1 cm long, 300 μm diameter) to a piece of insulated tinned Cu wire and inserting and sealing this into a glass tube using two-part epoxy (Loctite Hysol 1C). Platinum electrodes were used as the power/current-carrying electrodes and were placed on opposite sides of the membrane, with the working electrode (WE) in the acidic chamber and the counter electrode (CE) in the basic chamber. Nominally identical saturated calomel electrodes (SCEs, KCl saturated) (CH Instruments, Inc.) served as the reference electrodes (REs) and were placed on opposite sides of the membrane to measure the potential difference across it. The electrochemical cell (Figure 3.2a) consisted of two poly(chlorotrifluoroethylene) blocks, each containing a horizontal cylindrical channel with a diameter of 1.54 cm and three vertical cylindrical holes on the top of each block, each 0.5 cm in diameter and spaced 1 cm apart center-to-center. The electrochemical cell was connected to a potentiostat (VSP-300, Bio-Logic), with the two current-carrying leads attached to the platinum electrodes and the two potential-sensing leads attached to the

reference electrodes. Reported current densities were calculated by dividing the external current passed through the potentiostat by the geometric area of the membrane exposed to the aqueous electrolyte solution (1.86 cm^2). A negative external current meant that net electrons moved from the Pt wire CE through the external circuit to the Pt wire WE and therefore that there was a positive membrane current, where cations in the electrolyte moved toward the Pt wire WE from the basic chamber to the acidic chamber and/or that anions moved in the opposite direction, as shown in Figure 3.2b. In the dark, this process occurred under reverse-bias conditions when the applied bias was less than the so-called open-circuit potential (E_{oc}). Open-circuit potentials were measured using galvanostatic chronopotentiometry performed at 0 μA. Current densities (J) at each potential (E) were measured using potentiostatic chronoamperometry. Rate constants were determined by fitting the rise and the fall for each of the photovoltage and photocurrent transients to a single exponential function ($y = A \exp[-t/\tau] + B$, with fitted parameters of A, τ, and B).

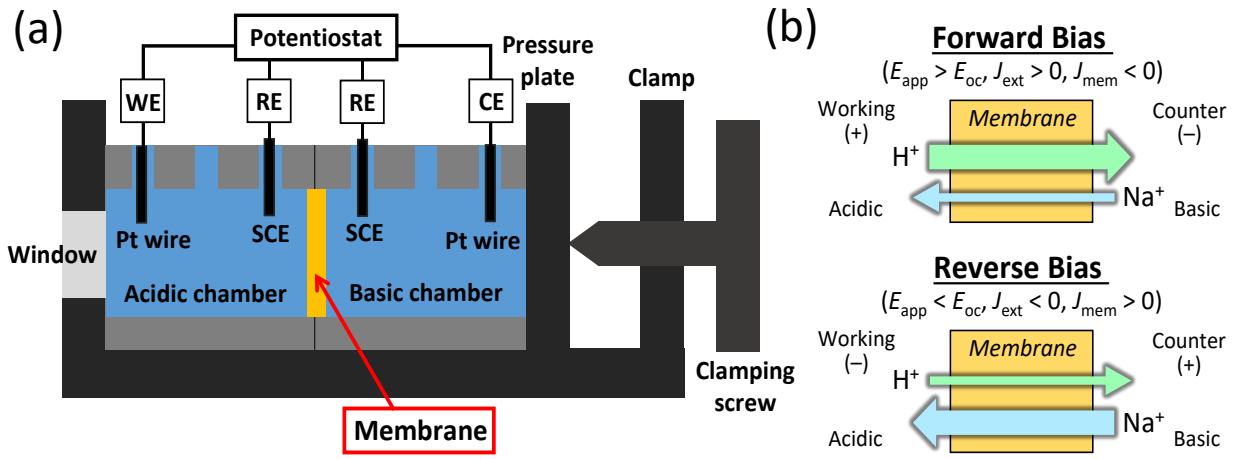

Figure 3.2. (a) Electrochemical cell used to conduct photoelectrochemical experiments indicating the locations of the working electrode (WE), counter electrode (CE), and reference electrodes (REs) with respect to the locations of the ion-exchange membrane, the acidic and basic electrolytes, and the borosilicate glass window. (b) Conditions during forward bias (top) and reverse bias (bottom) of the electrochemical cell including the polarization of the working/acidic compartment versus the counter/basic compartment, the sign of the applied bias (E_{app}) versus the open-circuit potential in the dark (E_{oc}), the sign of the current density at the WE through the potentiostat (J_{ext}) and through the membrane (J_{mem}) (and where all current densities reported herein are J_{ext} values), and the predominant ions responsible for current in the electrolyte, with arrow sizes that are qualitatively proportional to expected transport numbers.

All electrochemical data was corrected for baseline drift using a linear−exponential combination fit ($y = at + b \exp[ct + d]$, with fitted parameters of a, b, c, and d) of the data in the dark before illumination started and after illumination ceased. This baseline correction was performed in order to deconvolute the photoresponse from the background drift

because E_{oc} changed slightly over the course of the experiment due to reduction of the junction potential through exchange of Na^+ and H^+ across the cation-exchange membrane. Optical excitation was achieved using continuous-wave light from laser pointers that emitted at 405 ± 10 nm (fwhm = 1.96 mm; (1 ± 0.2) × 10^{18} photon cm^{-2} s^{-1}), 532 ± 10 nm (fwhm = 0.96 mm; (6.472) × 10^{18} photon cm^{-2} s^{-1}), or 650 ± 10 nm (fwhm = 1.91 mm; (1.1 ± 0.4) × 10^{19} photon cm^{-2} s^{-1}). Each was calibrated using a knife-edge measurement and a silicon photodiode detector (FDS100, Thorlabs). Briefly, a razor blade was affixed to a micrometer stage, and photocurrent was measured on the silicon detector as a function of the transverse position of the blade; the absence of a blade was used to calculate the total photon flux. The derivative of the resulting sigmoidal best-fit functions to the light intensity versus blade position were Gaussian functions whose maximum value was used to determine the full width at half-maximum of the collimated illumination, which was used as the dimension in calculating the approximate square illumination area. The absorbed photon fluence rate at 405 nm was calculated by multiplying the photon fluence rate at 405 nm by the absorptance of the sample at the 405 nm excitation wavelength ($1 - 10^{-\mathrm{Abs}_{405\,\mathrm{nm}}}$). This absorbed photon fluence rate was then converted into an equivalent number of Suns excitation by dividing it by the absorbed photon fluence rate expected under conditions of excitation by 1 Sun of Air Mass 1.5 Global solar illumination. Using the absorption spectrum of **PFSA** containing covalently bound photoacids (**cPFSA**) at wavelengths less than 550 nm, the equivalent number of Suns excitation was determined to be 40.

Turnover numbers were calculated from light-generated current density (J_{ph}) values measured from 177 consecutive cycles of 30 min of illumination using 405 nm light followed by 30 min of darkness. For these measurements, the photoactive area was reduced to 0.237

cm^2 using a Viton sheet to cover the majority of the membrane from being wetted by electrolyte. Electrolyte was refreshed every 24 h.

Chapter 3.4. Results and Discussion.

Chapter 3.4.1. Polymer Materials Synthesis and characterization.

Covalently modified **PFSA** (**cPFSA**) was synthesized by immersing precast Nafion sulfonyl fluoride poly-(perfluorosulfonyl fluoride) membrane (**PFSF**) in an isopropyl alcohol and water mixture containing the photoacid, triethylamine, and NaOH (Figure SI 3.1a,b). Electronic absorption spectra of **cPFSA** in both the protonated and deprotonated forms (Figure 3.3a) are consistent with spectra of the photoacids dissolved in aqueous solution (Chapter 3.6.1, Figure SI 3.1). Deprotonation resulted in a 0.35 eV bathochromic shift of the lowest-energy absorption transition. Cross-sectional photoluminescence microscopy images of **cPFSA** indicated that photoacids were present throughout the ~50 μm thickness of the membrane and that the near-surface regions contained fewer photoacids than in the bulk (Figure 3.3b).

Covalent bonding of photoacids in **cPFSA** were supported by data shown in Figure 3.4, which contains the Fourier transform infrared (FTIR) spectra and X-ray photoelectron spectroscopy (XPS) spectra for Nafion, **PFSF**, **cPFSA**, and ionomer membranes containing ionically associated photoacids (**iPFSA**). The characteristic sulfonyl fluoride peaks at 795, 823, and 1467 cm^{-1} present in FTIR spectra of **PFSF** were undetectable in spectra of **cPFSA**, which was synthesized from **PFSF**.[181–184] This suggests that most sulfonyl fluoride groups

were modified to sulfonates/sulfonic acids or covalently bound dyes in **cPFSA**.[184–189] Two small peaks were also present in the 2800–2950 cm^{-1} range for **iPFSA** and **cPFSA**, which based on previous literature reports are consistent with assignment to C–H stretches in the pyrene core of the photoacids (Chapter 3.6.1, Figure SI 3.2 and Figure SI 3.3). Partial hydration of the membranes precluded accurate identification of sulfonate and sulfonamide vibrational modes due to overlap with strong and broad vibrational peaks at 1625 and 3530 cm^{-1}, which are characteristic of water in hydrated Nafion.[184,186,189]

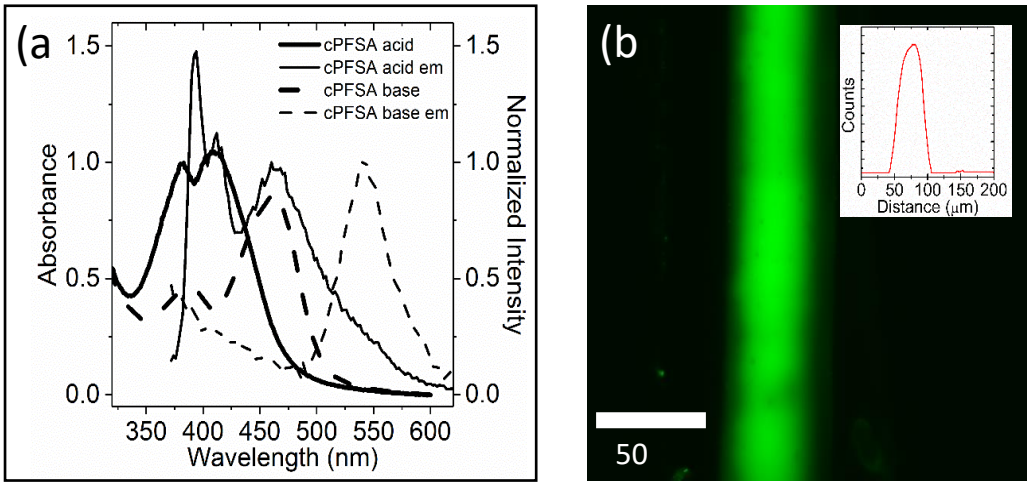

Figure 3.3. (a) Electronic absorption (solid lines) and emission (dashed lines) spectra of **cPFSA** after protonation by strong acid (1 M H_2SO_4 (aq); bold lines) or deprotonation by strong base (1 M NaOH (aq); thin lines). (b) Cross sectional fluorescence microscopy image of **cPFSA** with the inset depicting the fluorescence intensity versus position.

To learn more about the binding of the photoacids in **PSFA**, the four samples were analyzed using XPS over the range of energies for core emission from O (Figure 3.4b) and C, N, F, and S (Chapter 3.6.1, Figure SI 3.4). The O 1s core region spectra are diagnostic of the

substitution of sulfonyl fluoride and clearly show a difference in binding energy between the mixed sulfonamide/sulfonate-containing membranes (**cPFSA** and **iPFSA**) and the sulfonate-only-containing membrane, Nafion. Prior literature supports that the higher binding energy peak at >535 eV is attributed to the ether oxygen atoms in the polymer and that the lower binding energy peak at 531–534 eV is attributed to the sulfonyl oxygen atoms.[180,186,190,191] The binding energies of oxygen bound to sulfur exhibit a logical trend, SO_3^- > SO_2NR, based on the convolution of electronegativity and electron donating strength of the substituents.[191] This trend is observed between **cPFSA** and **iPFSA**, where the smaller binding energy observed for **cPFSA** is consistent with it having a greater proportion of sulfonamides, due to the formation of covalent membrane–photoacid sulfonamide bonds, as compared to **iPFSA**, which only has sulfonamide bonds in the photoacid structure itself.

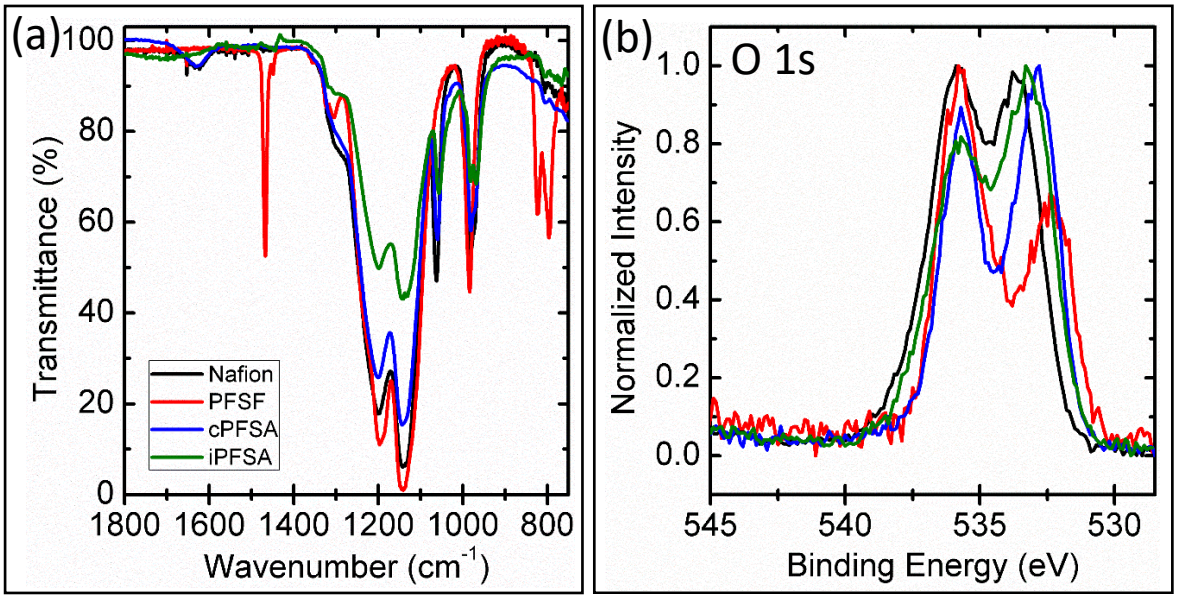

Figure 3.4. (a) Low-energy FTIR–ATR transmission spectra and (b) O 1s XPS spectra for Nafion (black), **PFSF** (red), **cPFSA** (blue), and **iPFSA** (green), with each spectrum normalized to its largest intensity peak. The key in (a) is also accurate for the data in (b).

When **cPFSA** was immersed in 1 M NaOH (aq) for 2 h, there was no visual evidence for leaching of dyes into solution. Conversely, when **iPFSA** was submerged in the same electrolyte, desorption of dyes was immediately apparent. Together, the FTIR and XPS spectroscopy results and alkaline ion-exchange studies suggest that photoacids reacted with the sulfonyl fluoride groups in **PFSF** and resulted in covalent modification as **cPFSA**.

The membranes were also found to be mechanically robust and chemically stable. Submerging **cPFSA** in water, *N*,*N*-dimethylformamide, or dimethyl sulfoxide for 7 days at 100 °C resulted in no apparent dissolution of the membrane suggesting that the polymer may be cross-linked. The average ion-exchange capacity for **cPFSA** was determined to be 0.66 ± 0.06 mequiv/g, while Nafion was measured to have an ion-exchange capacity of 0.83 ± 0.07 mequiv/g,[192] indicating that the ion-exchange capacity changed by > ~5%, as 1 − ((0.66 + 0.06)/ (0.83 − 0.07)). Synthesis of **cPFSA** used 60 mg of **PFSF** (~55 μmol of sulfonyl fluoride groups) and 3.2 μmol of photoacid. Given that the ion-exchange capacity technique identifies protons associated with sulfonates and protons present in the alcohol group of the photoacids, bonding each photoacid molecule to the polymer via one sulfonamide does not change the measured ion-exchange capacity. The most likely scenario is that each photoacid molecule bonded to the polymer via two sulfonamides, therefore replacing two sulfonate protons with one alcohol proton in the ion-exchange capacity measurement and decreasing the ion-exchange capacity by ~6%, as (3.2/55). However, this assumes no cross-linking of **cPFSA** by the photoacids, which may render some of the sulfonates inaccessible to electrolyte. The FTIR spectra of **cPFSA** and **iPSFA** do not exhibit clear peaks that are characteristic of the photoacid as a powder, making it difficult to assign the binding mode of the photoacid (Chapter 3.6.1, Figure SI 3.3).

Chapter 3.4.2. Assessment of Photoelectrochemical Performance.

For **cPFSA** to exhibit photovoltaic action, i.e., a photovoltage and power production when illuminated, it must absorb light, separate charge, and collect charge.[165] Electronic absorption spectra suggest that protonated photoacids in **cPFSA** absorb visible light. Photoluminescence data exhibiting a shoulder at ~550 nm indicate some radiative decay from specifically *deprotonated* excited-state photoacids in **cPFSA** (Figure 3.3), supporting the assignment of this process to charge separation by excited-state proton transfer. A measurable photovoltage response under open-circuit conditions suggests that both charge separation *and* cage escape of photoliberated protons from the solvation environment of the photoacids occurred (Figure 3.5a). Charge collection was verified by measurements of the photocurrent densities (Figure 3.5b). Observation of a nearly constant steady-state photocurrent from electronically insulating **cPFSA** supported that illumination resulted in an increase in the rate of ion transport to the current-carrying electrodes of the potentiostat.[193]

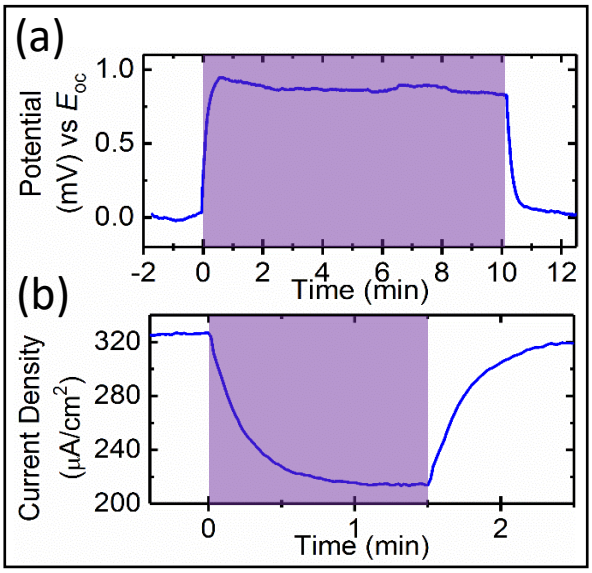

Figure 3.5. (a) Open-circuit photovoltage and (b) photocurrent at a small positive bias for **cPFSA** wetted by 1 M H_2SO_4 (aq) on one side of the membrane and 1 M NaOH (aq) on the other side of the membrane. Regions highlighted in purple indicate illumination with 405 nm laser light at 40 Suns equivalent excitation.

The steady-state open-circuit potential across the membrane *in the dark*, E_{oc}, was measured to be approximately -30 mV. This is ascribed to a liquid-junction electric potential generated by the difference in the concentration of protons and Na^+ across the membrane.[194] The negative sign of E_{oc} is consistent with proton diffusion from the acidic to the alkaline electrolyte that is faster than Na^+ diffusion in the opposite direction.[195] The open-circuit photovoltage *in the light* versus E_{oc} was measured to be approximately +1 mV. The positive sign of the photovoltage means that illumination decreased the magnitude of the electric potential across the membrane, behavior that is consistent with the conclusion that the membrane exhibited photovoltaic action. The *steady-state* liquid-junction electric potential in the dark and observation of photovoltaic action are analogous to conditions in traditional

semiconductor pn-junction and Schottky-junction solar cells, except that *equilibration* in the dark generates the built-in electric potential in a traditional semiconductor. In the presence of inert or acidic electrolyte at the same concentration on both sides of Nafion, an electric potential difference was not measured and photovoltaic action was not observed.

While the photovoltaic properties observed for **cPFSA** are poor, pathways to larger efficiencies do exist. For example, assuming that the concentration of photoacids in **cPFSA** was increased to the concentration of sulfonate groups in Nafion, the photocurrent observed herein would be expected under conditions of ~10 times less intense illumination. Moreover, use of a bipolar membrane structure instead of a single monopolar ion-exchange membrane would likely slow ion leakage and generate much larger built-in potentials.[194] This would conceivably result in larger photovoltages and therefore larger light-to-ionic energy conversion efficiencies.

The rise and decay of the photocurrent (τ_{rise} = 16 s and τ_{fall} = 14 s) and the photovoltage (τ_{rise} = 10 s and τ_{fall} = 10 s) signals were each well described by an exponential process (Chapter 3.6.1, Figure SI 3.5). The similarity of the rates of all four processes suggests that the current transients were due to capacitive charging and/or attaining a steady-state mass-transport regime.[195] To further assess the photophysical and photochemical properties of the photoacid, the quantum yield of emission, ϕ_{em} (~0.29), and rate constants for excited-state deactivation, k_r and k_{nr}, were calculated for photoacids dissolved in acidic aqueous solution (Chapter 3.6.1, Table SI 3.2). Increasing ϕ_{em} for photoacids bound to **cPFSA** may be important for attaining large photovoltages because the ultimate efficiency limit for photovoltaic devices occurs when the rate-determining recombination process is radiative decay of the excited state, and therefore ϕ_{em} = 1.[196]

Measurements of the power-producing region of J–E behavior in the light were imperfect due to the weak photoresponses and difficulties in generating a stable short-circuit condition, i.e., applying a bias precisely equal to E_{oc}. However, additional chronoamperometry measurements sup-ported the conclusion that **cPFSA** exhibited photovoltaic action because the sign of J_{ph}, calculated as the difference in the light versus dark current densities, was independent of the sign of the applied potential (Figure 3.5b and Figure 3.6). For a solar cell, J_{ph} is the contribution to the current that results from optical excitation, and in the ideal case it is a constant value irrespective of potential bias.[165,173] In practice, this value is at least single-signed over the power-producing region, behavior that was observed for **cPFSA** in this region and beyond (Supporting Information, Figure S3.6).

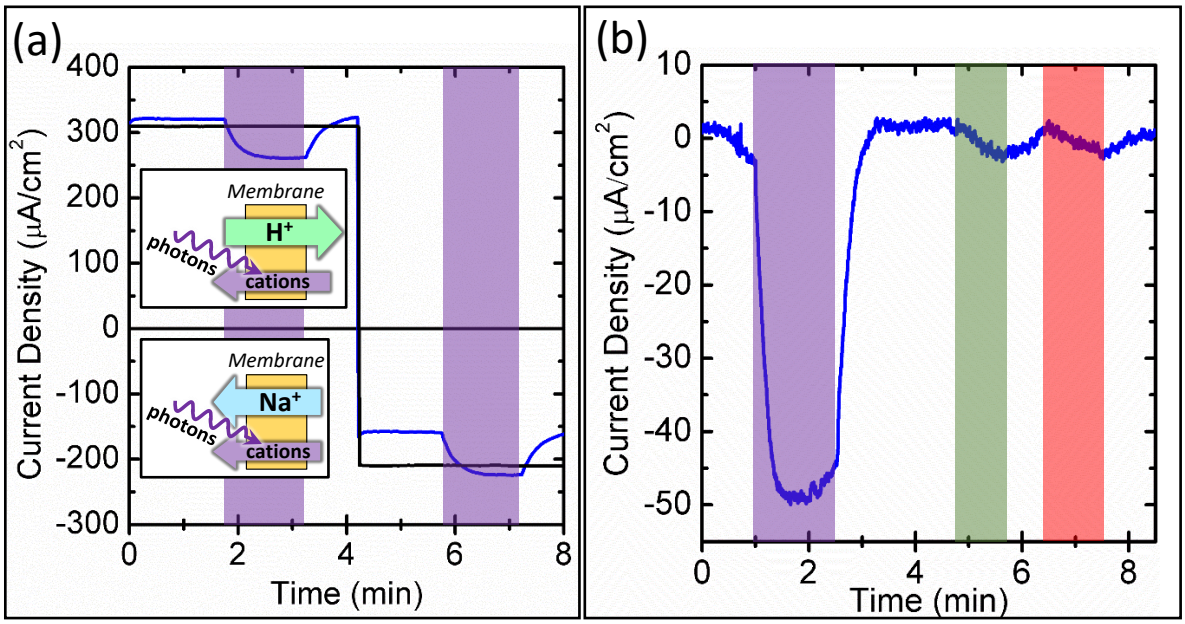

Figure 3.6. Chronoamperometry data in the dark and under illumination (highlighted regions) for **cPFSA** (blue) wetted by 1 M H_2SO_4 (aq) on one side and 1 M NaOH (aq) on the other side of the membrane. (a) Data measured under forward bias (left, and top inset) and reverse bias (right, and bottom inset) and for Nafion impregnated with $Ru(bpy)_3^{2+}$ (black), under the same conditions. (b) Spectral response, reported as J_{ph} values after correction for a dark current density of 1.4 ± 0.6 $\mu A/cm^2$, when illuminated with laser light at 405 nm (purple), 532 nm (green), and 650 nm (red), colored, respectively.

Diagrams of the membrane under forward bias or reverse bias conditions are shown as insets to Figure 3.6a, with clear indication of the expected type and direction of majority cation flux. While these fluxes have not been measured directly, precedent from related Nafion membranes supports that these processes are likely occurring. Given the experimental setup, a negative value for J_{ph} is consistent with light driving net *cation* transport into the compartment with a large concentration of protons. Because the dyes are

photoacids, our hypothesis is that the observed behavior is specifically due to light-driven *proton* transport against a pH gradient, behavior that is consistent with photovoltaic action. The previous data do not preclude that thermal effects from local heating were at least in part responsible for the observed behavior. Nafion has been shown to have a Seebeck coefficient that depends on the relative humidity, bias, and/or temperature.[197] For relative humidities >50%, the Seebeck coefficient was observed to be negative, with a reported maximum magnitude value of -2 mV/K. This implies that increasing the local temperature could result in behavior consistent with photovoltaic action. Therefore, a comparison was made between **cPFSA** and Nafion containing ionically associated $Ru(bpy)_3^{2+}$ dyes, **iPFSA-Ru** (Figure 3.6a). $Ru(bpy)_3^{2+}$ dissolved in aqueous solution exhibits a large nonradiative rate constant and a quantum yield of emission that is smaller than that observed for the photoacids dissolved in aqueous solution ($\phi_{em} < 0.07$ for $Ru(bpy)_3^{2+}$ and $\phi_{em} \approx 0.29$ for the photoacid [Chapter 3.6.2]).[198] Notwithstanding, J_{ph} values for **cPFSA** were observed to be orders-of-magnitude larger than for **iPFSA-Ru**, which implies that the observed photovoltaic action for **cPFSA** was not due to local heating caused by nonradiative decay of the excited-state photoacids or electron-transfer/energy-transfer to dissolved O_2 in the aqueous electrolyte.

The photocurrent response of **cPFSA** was over an order-of-magnitude larger when illuminated with 405 nm light in comparison to illumination with 532 or 650 nm light, whose photon fluxes were each more than six times larger (Figure 3.6b). This further supports the conclusion that photovoltaic action was due to optical excitation of the photoacids and not due to other optical effects. Also, over the course of a 177-hr experiment, the total number of charges passed was calculated to be 3.55 μmol. Given that the maximum concentration of

dyes within the entire 4 cm^2 film was 3.2 μmol, and that the membrane area in direct contact with the electrolyte and illuminated was 0.237 cm^2, the photoacids exhibited a turnover number of >18 and the photocurrent response was stable over the course of the experiment, meaning the sensitization process was regenerative/photocatalytic and not stoichiometric.

Chapter 3.5. Conclusions.

Using **PFSA** modified with photoacid dye molecules, 8-hydroxypyrene-1,3,6-tris(2-aminoethylsulfonamide), a first-of-its-kind synthetic polymer membrane light-driven proton pump was demonstrated. Bonding of photoacids to the polymer was supported by results obtained using FTIR–ATR spectroscopy and XPS, and clear differences in the transport of ionically associated dyes when in contact with strongly alkaline aqueous electrolyte. **cPFSA** was shown to undergo excited-state proton transfer and exhibited photovoltaic action with a turnover number of >18. Maximum photoresponses were $J_{ph} \approx 100\ \mu A/\ cm^2$ and ~1 mV open-circuit photovoltage under 40 Suns equivalent excitation with 405 nm light. This behavior was clearly different (at least an order-of-magnitude larger J_{ph}) than that observed for Nafion that contained ionically associated $Ru(bpy)_3^{2+}$ dyes or **cPFSA** illuminated with 532 or 650 nm light. This new class of dye-sensitized ion-exchange materials is capable of alleviating power demands from electrochemical processes such as electrodialysis and electrolytic generation of acid and base.

Chapter 3.6. Supplemental Information.

Chapter 3.6.1. Material characterization

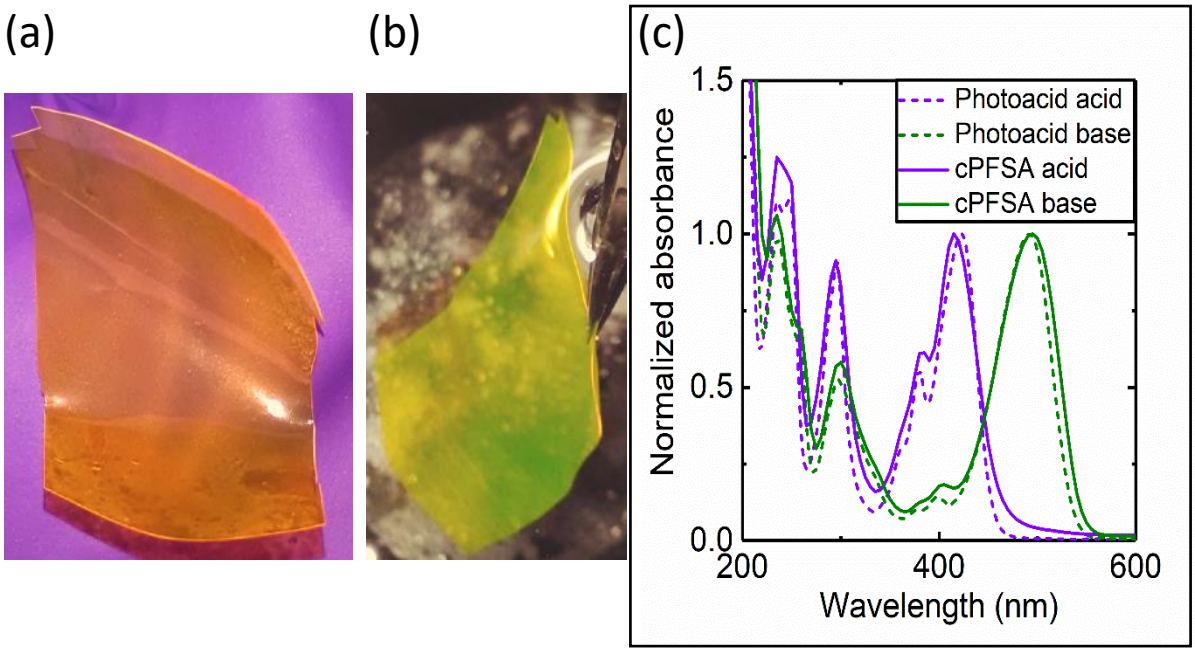

Figure SI 3.1. Digital photographs of **cPFSA** (a) immediately after synthesis and (b) immersion in water. (c) Electronic absorption spectra of photoacids in solution (dashed lines) and incorporated into **cPFSA** (solid lines) after protonation by strong acid (1 M H_2SO_4(aq); bold lines) or deprotonation by strong base (1 M NaOH(aq); thin lines).

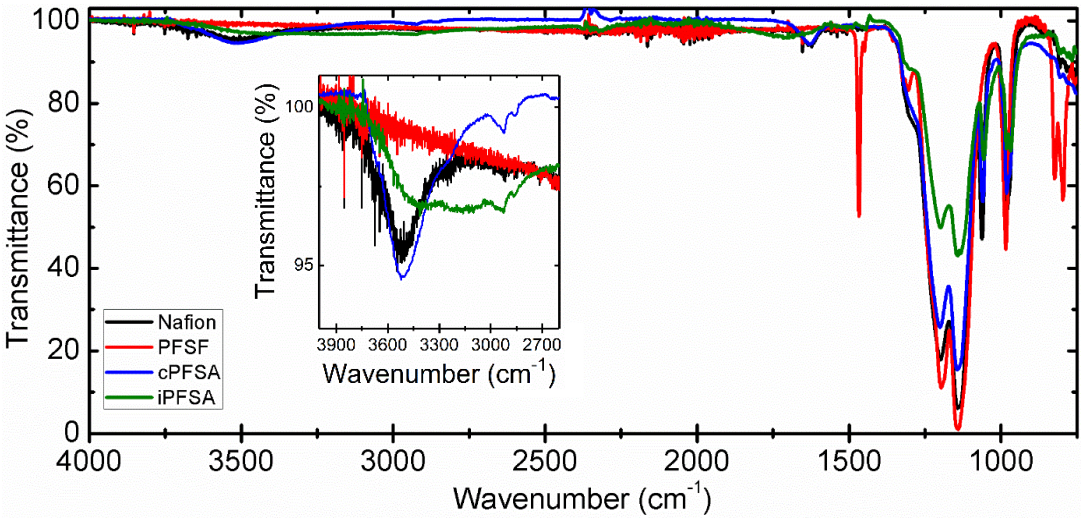

Figure SI 3.2. FTIR–ATR spectra of Nafion, **PFSF**, **cPFSA**, and **iPFSA** with an inset highlighting the 2600 – 3800 cm^{-1} region.

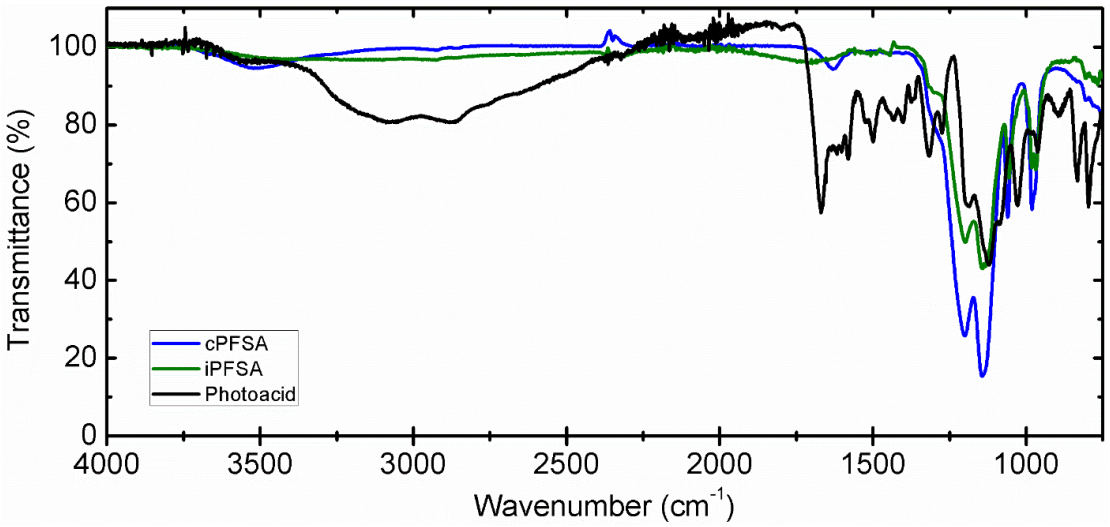

Figure SI 3.3. FTIR–ATR spectra of **cPFSA**, **iPFSA**, and photoacid powder.

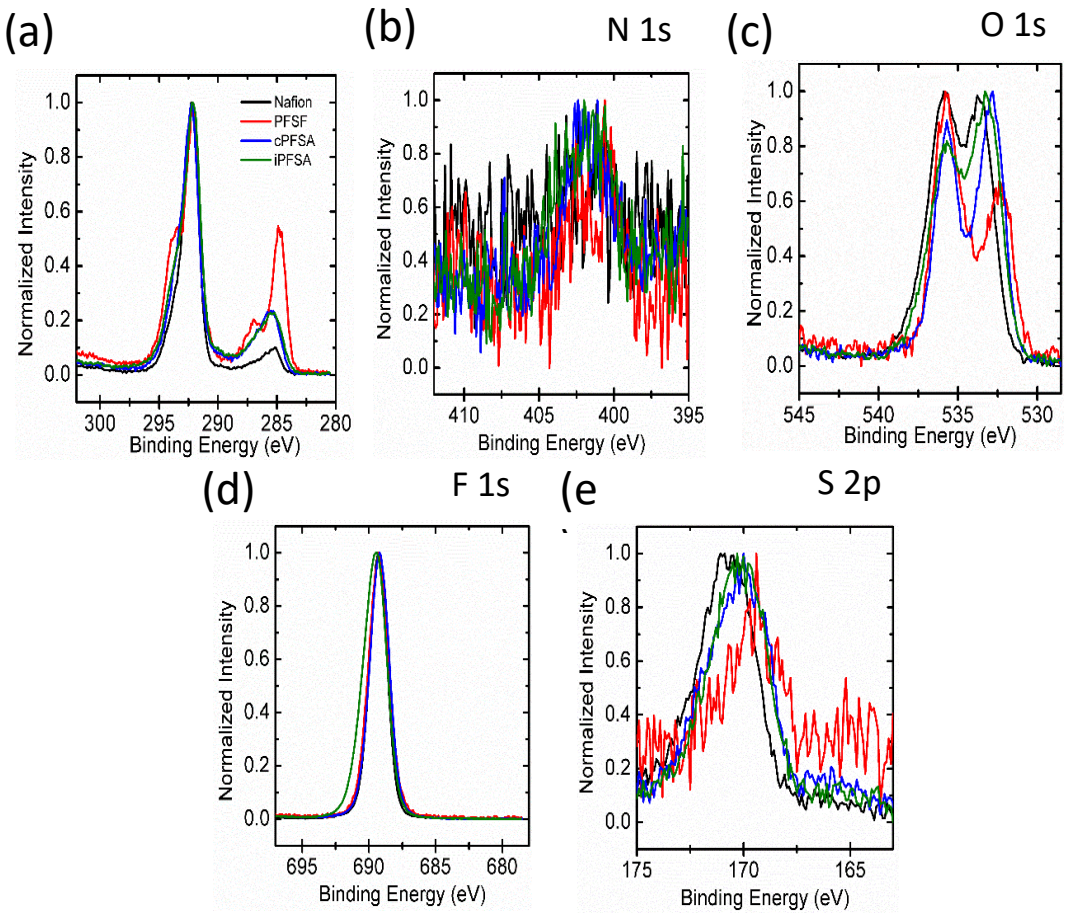

Figure SI 3.4. XPS core emission spectra of C, N, O, F, and S from Nafion (black), **PFSF** (red), **cPFSA** (blue), and **iPFSA** (green).

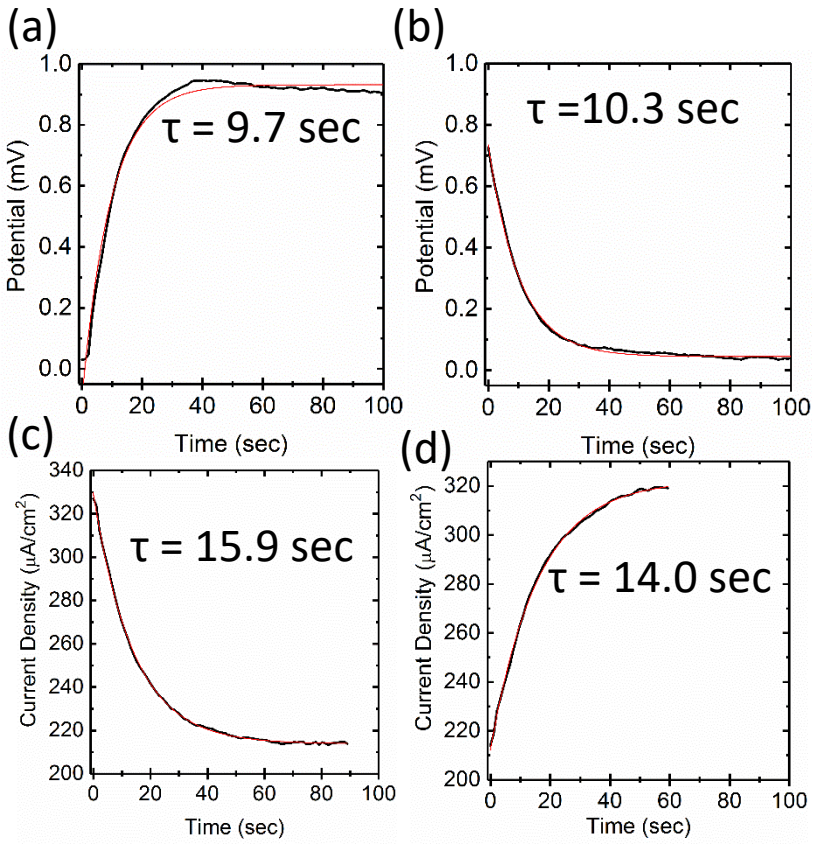

Figure SI 3.5. Kinetics for the growth and decay of the (a, b) open-circuit photovoltage and (c, d) photocurrent at a small positive bias, each overlaid in red with a non-linear least-squares best fit to an exponential function.

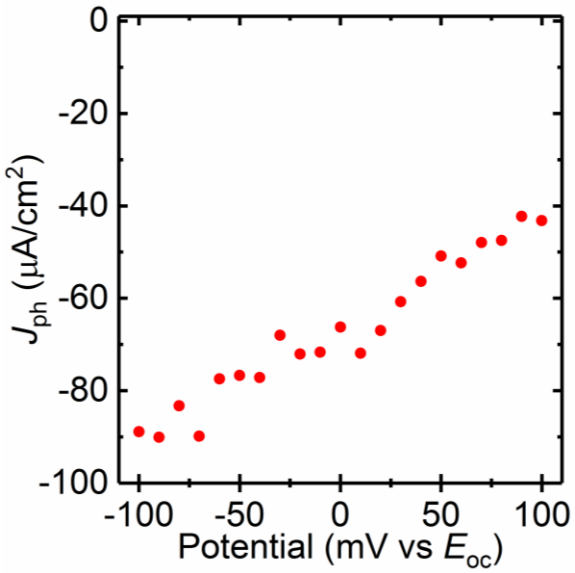

Figure SI 3.6. J_{ph}–E behavior of **cPFSA** wetted by 1 M H_2SO_4(aq) on one side of the membrane and 1 M NaOH(aq) on the other side of the membrane, showing that the J_{ph} is negative over the entire 200 mV range.

Chapter 3.6.2. Determination of the quantum yield of emission

The quantum yield of emission from the photoacid dissolved in aqueous solution was determined using protocols listed in the IUPAC technical report on the determination of the quantum yield of emission from dilute dye solutions.[199] Briefly, three optically dilute solutions each containing reference molecules, norharmane and quinine sulfate, or the photoacid were characterized at various concentrations (Figure SI 3.7 and Figure SI 3.8). Photoluminescence (PL) spectra were recorded using an excitation wavelength of 350 nm and a slit width of 5 nm, and the PL intensities were corrected for the wavelength-dependent response of the detector and optics reflectance, as well as inner-filter effects using the following equation:[114]

$$\mathrm{PLI_{corr}} = \mathrm{PLI_{obs}}\ 10^{\left(\frac{A_{\lambda_{ex}} + A_{\lambda_{em}}}{2}\right)}$$ Equation SI 3.1

where $A_{\lambda_{ex}}$ is the absorbance at the excitation wavelength and $A_{\lambda_{em}}$ is the absorbance at the emission wavelength. Values for the quantum yield of emission are shown in Table SI 3.1 and Table SI 3.2, and were calculated using the following equation:

$$\Phi_{em} = \Phi_{\mathrm{Ref}} \left(\frac{m}{m_{\mathrm{Ref}}}\right)\left(\frac{n^2}{n^2_{\mathrm{Ref}}}\right)$$ Equation SI 3.2

where Φ_{em}, m, and n stand for the quantum yield of emission, the slope of the trend line of integrated photoluminescence intensity *versus* absorbance at the excitation wavelength (cps), and the refractive index of the solvent, respectively, and the subscript Ref stands for the reference molecule. The reference molecules were cross-calibrated against each other to validate the experimental technique and assess reproducibility (Table SI 3.1).

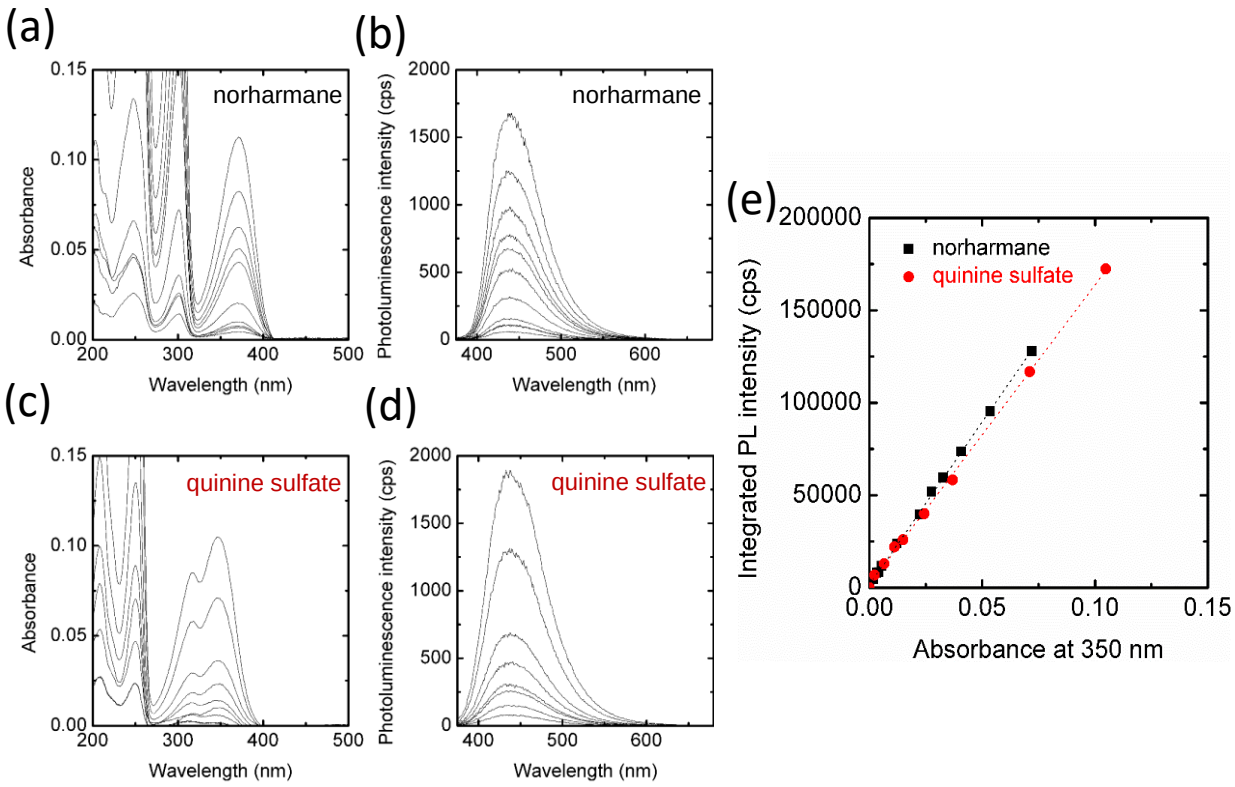

Figure SI 3.7. (a, c) Absorbance and (b, d) photoluminescence (λ_{ex} = 350 nm) spectra at varying concentrations of (a, b) norharmane and (c, d) quinine sulfate, each dissolved in aqueous 0.1 M H_2SO_4. (e) Integrated photoluminescence (PL) intensity as a function of absorbance at 350 nm for both reference molecules.

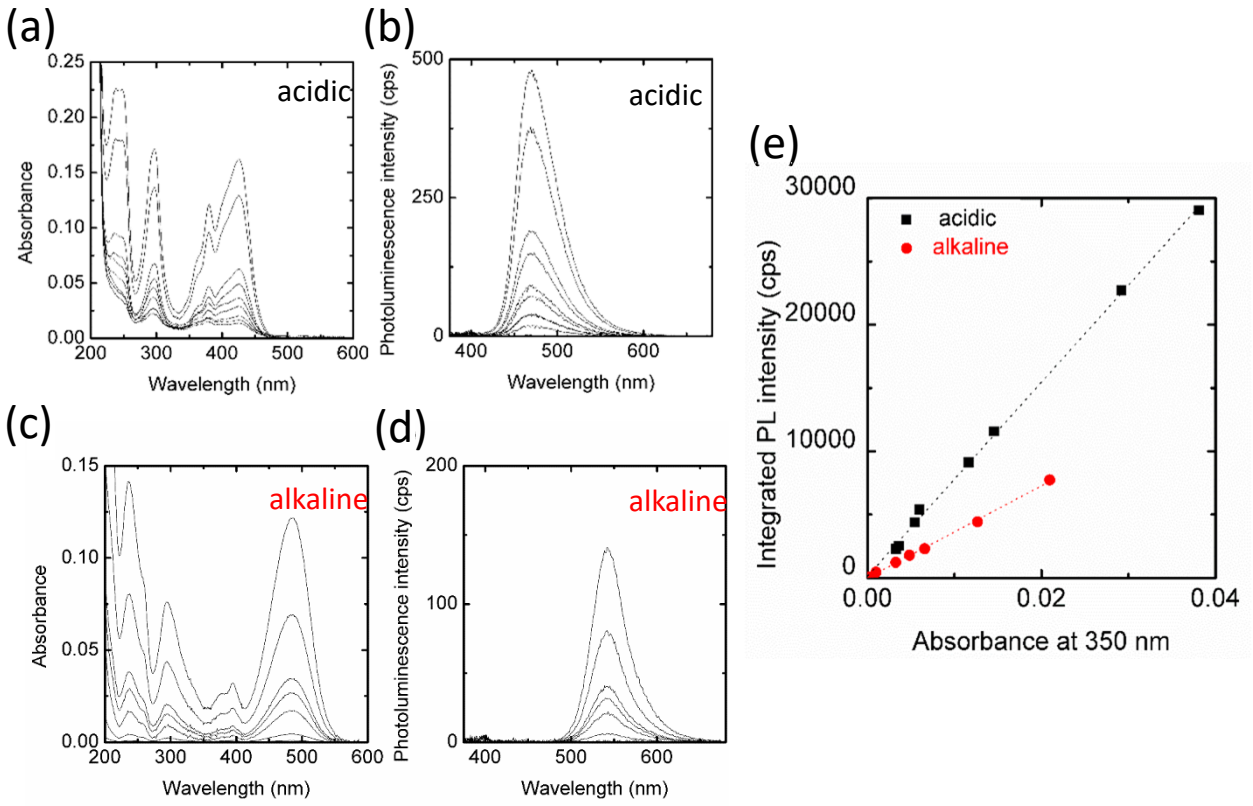

Figure SI 3.8. (a, c) Absorbance and (b, d) photoluminescence (λ_{ex} = 350 nm) spectra at varying concentrations of the photoacid in (a, b) highly acidic aqueous solution (12 M HCl) and (c, d) basic aqueous solution (pH 8). (e) Integrated photoluminescence (PL) intensity as a function of absorbance at 350 nm at these two extreme pH values. See Table S3.2 for conditions.

Table SI 3.1. Cross-calibration of reference molecules in aqueous 0.1 M H_2SO_4.

Compound	Calculated Φ_{em}	Literature value for Φ_{em}
Norharmane	0.59	0.58 [200]
Quinine Sulfate	0.53	0.54 [201]

Table SI 3.2 Photophysical properties of the photoacid in solution in its protonated and deprotonated states.

Solution	Predominant species	Refractive index	Φ_{em} [a, c]	τ [d] (ns)	k_r (s^{-1})	k_{nr} (s^{-1})
Aqueous concentrated HCl (12 M)	ROH/ROH*	1.42 [b]	0.286 ± 0.004	3.9	7×10^7	18×10^7
Aqueous 0.001 M tris buffer, pH 8	RO^-/RO^{-*}	1.33 [202]	0.118 ± 0.002	6.0	2×10^7	15×10^7

[a] Average ± standard deviation from two calculations, one using each reference.

[b] Calculated by plotting, fitting, and extrapolating refractive index *versus* HCl concentration data from the work of Olsen and Washburn.[127]

[c] Determined from fluorescence spectroscopy, λ_{ex} = 350 nm.

[d] Determined using two-photon fluorescence-lifetime imaging microscopy, λ_{ex} = 900 nm.

Chapter 3.7. Acknowledgements.

Chapter 3 has been reproduced with permission from:

White, W.; Sanborn, C. D.; Reiter, R. S.; Fabian, D. M.; Ardo, S. *J. Am. Chem. Soc.* **2017**, 139 (34), 11726−11733.

We are grateful for financial support from the Department of Chemistry and the School of Physical Sciences at the University of California Irvine and the Gordon and Betty Moore Foundation via a Moore Inventor Fellowship under Grant #5641. R.S.R. was supported by a UC Irvine Chancellor's Fellowship. D.M.F. is supported by a National Science Foundation Graduate Research Fellowship under Grant No. DGE-1321846. We thank Lee Moritz from the UC Irvine Machine Shop and Rick P. Gerhart from the Caltech Glassblowing Shop for fabricating custom electrochemical cells, Prof. Enrico Gratton and Prof. Michelle Digman for use of their Laboratory of Fluorescence Dynamics (LFD) and Dr. Jenu Varghese Chacko for training and assistance with the laser microscopy instruments in the LFD, and Dr. Walter Grot for advice and for generously supplying Nafion sulfonyl fluoride poly(perfluorosulfonyl fluoride) membrane and ionic dyes for use in permselectivity experiments. FTIR and photoluminescence experiments were performed at the UCI Laser Spectroscopy Facility under the supervision of the Facility Director, Dr. Dima Fishman. XPS experiments were performed at the UC Irvine Materials Research Institute (IMRI) using instrumentation funded in part by the National Science Foundation Major Research Instrumentation Program under grant no. CHE-1338173. We thank Dr. Ich Tran for guidance in XPS data analysis.

Chapter 4. Conversion of Visible Light into Ionic Power Using Photoacid-Dye-Sensitized Bipolar Ion-Exchange Membranes.[203]

Chapter 4.1. Overview.

For over half a century, it has been recognized that the classical physics that dictates the behavior of hydrated ion-exchange membranes, such as Nafion, and semiconductors, such as doped silicon, are similar. However, no demonstrations of photovoltaic action from ion-exchange materials existed. We recently reported a synthetic light-driven proton pump derived from an ion-exchange membrane. Absorption of light by covalently bound photoacid molecules resulted in photovoltaic action. This design lacked a second permselective membrane contact, which limited its performance. Here, we report an ~60-fold increase in the photovoltage through use of a bipolar membrane structure consisting of a cation-exchange membrane affixed to an anion-exchange membrane. The junction between the layers was characterized in detail using electrochemistry, scanning electron microscopy, spectroscopy, and thermal gravimetric analysis. Our results represent considerable progress toward a device that directly converts sunlight into ionic electricity, which has implications for direct solar desalination of salt water.

Chapter 4.2. Context and scale.

Access to clean and potable water is one of the top issues facing humanity and is expected to become even more pressing in the next several decades. While efficient and renewable energy technologies could supply the power needed to generate potable water, advances are slow and are in general incremental from prior demonstrations. Moreover, the developing world cannot afford current clean water solutions, yet the majority of the four billion people expected to be under water stress in approximately the next decade will live in the developing world. In the long term, it is expected that newly developed nations with large gross domestic product and an established grid or micro-grid infrastructure will utilize state-of-the-art cost-effective plant-scale technologies for clean water generation, such as those based on osmosis, distillation, or electrodialysis. In the immediate near term, an inexpensive technology to desalinate water could support economic development.

Chapter 4.3. Introduction.

It has been over three-quarters of a century since the discovery of the semiconductor pn-junction diode, which later led to the advent of other functional circuit elements, such as the transistor and the integrated circuit.[204] These circuit elements enable many of today's advanced technological capabilities, including the digital camera, computer, cell phone, and solar cell. Less than 15 years after the discovery of the semiconductor pn junction, a publication by Fuller compared water to a semiconductor,[205] indicating that the equations that approximate equilibrium carrier concentrations in non-degenerate semiconductors are

the same as those that dictate the concentration of protons and hydroxides in water. Several years later, the first electronic pn-junction solar cells were developed and within just 2 years after their discovery, a sunlight-to-electricity power conversion efficiency of > 6% was demonstrated.[206,207] Around this time, work by Bockris and colleagues showed that water, with the proper permselective membrane contacts for protons and hydroxides, could behave like traditional diodes and exhibit ionic current rectification.[208] Although the analogy of water to an electronic semiconductor had been clearly articulated,[209] there was little evidence to suggest that researchers attempted to fabricate solar cells based on water as the ''protonic semiconductor,'' most likely because the properties of water result in rates of ion transport and ion lifetimes that are much smaller than rates of electron transport and electron lifetimes in high-quality electronic semiconductors. It was not until 20 years later, in 1978, that Prof. George Murphy briefly outlined several possible means to convert light into ionic power through photodriven transport of protons and hydroxides;[210] however, there are no publications that report experiments related to Murphy's purely ion-transporting concepts in the absence of Faradaic charge transfer. Today, 40 years later, no one has demonstrated experimentally or theoretically that an ionic analog to the electronic pn-junction solar cell can be made for sunlight-to-ionic-electricity power conversion. Here, we describe the fabrication and photoelectrochemical evaluation of such a device and also include a perspective on outlooks for its practical use.

To further support the notion that water is a ''protonic semiconductor,'' we compare the fundamental concepts of doped electronic semiconductors with water-containing ion-exchange membranes. Standard physical equations that describe properties of traditional electronic pn-junction semiconductors are introduced along with analogous concepts for

water-containing ion-exchange membranes. One rationale to support that water is a ‘‘protonic semiconductor’’ is based on its conductivity: it is insulating until doped or heated.[211] For example, the room temperature conductivity of electrons and holes in undoped crystalline silicon (~5 μS cm 1)[205,212] is only several orders of magnitude larger than that of protons and hydroxides in deionized water (~5×10^{-2} μS cm^{-1}),[195,213] because in each there exists a small concentration of free charge carriers. Moreover, the number of charge carriers in each system increases as the temperature increases or through doping, both indicative of semiconducting behavior.[211]

The device physics of an electronic pn-junction diode are well described by Poisson’s equation, the Fermi function, and the continuity equations, which include generation and recombination of free charge carriers and drift and diffusion transport processes.[214] Fixed dopant distributions, equilibration between regions of differing electrochemical potential, and Poisson’s equation are used to predict properties of the electrostatic space-charge region that results from equilibration across a junction formed between two different phases. These same processes and phenomena can occur using water that is doped differently across a junction. Addition of small amounts of strong acid or strong base dopes water; however, fixing the location of these dopants so that a space-charge region can form between these two different aqueous phases requires an ion-impermeable separator or a scaffold for the acidic and basic functionalities. An example of the latter is the ion-exchange membrane, which contains large concentrations of hydrated acidic or basic dopants covalently bound to a polymer scaffold. When the counterions of these dopants are mobile protons and/or hydroxides, equilibration occurs with aqueous contacting phases resulting in charged groups covalently bound to the polymer that do not have nearby mobile

counterions. These separated unscreened fixed charges have associated electric fields, which generate space-charge regions and an electric potential difference between them that is termed a Donnan potential.[215] The only fundamental difference in the electronic *versus* ionic processes is that the thermodynamics and resulting free carrier concentrations are determined by Fermi-Dirac statistics for traditional electronic semiconductors and by Maxwell-Boltzmann statistics for water.[216] The differences in statistical approximations are insignificant, because in most cases the physics of electronic semiconductor devices are calculated with sufficient accuracy when Maxwell-Boltzmann statistics are used to describe the concentrations of free charge carriers.[216]

In addition to Poisson's equation and statistical thermodynamics that are used to determine properties at thermal equilibrium, the continuity equations describe transient non-equilibrium processes, including those at steady state. These equations include those that describe the rates of free carrier generation and recombination, which in the dark satisfy a straightforward equilibrium process: $2A \leftrightharpoons A^- + A^+$. The equilibrium constants for this reaction are the square of the intrinsic carrier concentration (n_i^2) for electronic semiconductors and the autoprotolysis constant for water (K_w) and other solvents (K_{ap}). By the law of mass action, each of these equilibrium constants equals the product of the activities, and approximated by concentrations, of the free anionic charge carriers (a_{A-}) and free cationic charge carriers (a_{A+}).[217] This relation does not contain a_A because it is often assumed that A has standard-state activity. Under illumination, both a_{A-} and a_{A+} increase, and therefore the system is no longer in thermodynamic equilibrium. While generation and recombination dictate the steady-state concentration of free charge carriers during illumination, drift and diffusion are the predominant processes that dictate transport in

electronic semiconductors.[214] These same processes are responsible for ionic transport in quiescent solutions as dictated by the Nernst-Planck equation.[215] These conditions set the stage for an ionic diode based on water, or other solvent, that transports ions (protons and hydroxides) instead of electrons and holes.

Most highly efficient solar cells contain a semiconductor pn junction, and therefore they rely on internal electric fields to generate the asymmetry required for photovoltaic action.[214] These internal electric fields assist in charge separation and result in selective contacts for electrons and holes.[173,214,218] This means that electron transport is asymmetric, such that the rate of transport from the conduction band into states that form the low-resistance electron-selective contact is faster than the rate of trans-port from the low-resistance electron-selective contact to the valence band. Analogous processes occur for holes. A pn junction based on water has been previously demonstrated by Bockris and colleagues over 50 years ago using ion-exchange membranes and water as the semiconductor.[208] They used a bipolar ion-exchange membrane architecture, which consisted of a cation-selective layer containing fixed sulfonate groups and mobile proton counterions as p-type dopants in intimate contact with an anion-selective layer containing fixed quaternary ammonium groups and mobile hydroxide counterions as n-type dopants. This is the architecture that we employ here.

The most efficient single-junction solar cells absorb light using a crystalline semiconductor with an electronic bandgap energy (E_g) of 1.1–1.4 eV.[196] This bandgap range represents an ideal balance of beneficial sunlight absorption and wasteful energy loss due to thermalization of electrons and holes to the semiconductor band edges.[196] The bandgap energy of an electronic semiconductor is defined as the difference in the minimum energy

(E_c) of the effective electronic states near the bottom of the conduction band (N_c) and the maximum energy (E_v) of the effective electronic states near the top of the valence band (N_v), by the following equation:[219]

$$E_g = E_c - E_v = k_B T \ln\left(\frac{N_c}{n_i}\right) - k_B T \ln\left(\frac{n_i}{N_v}\right) \qquad \text{Equation 4.1}$$

$$= -k_B T \ln\left(\frac{n_i^2}{N_c N_v}\right)$$

where k_B is the Boltzmann constant (1.381×10^{-23} J K^{-1}), T is the temperature (in units of K), n_i^2 is the equilibrium constant (in units of M^2), and E_c and E_v are referenced to the condition when N_c = N_v = n_i. The N_c and N_v terms correct the equilibrium constant for non-unity maximum concentration of charge carriers near the band edges. Solvents have analogous energy gaps, which we term ‘‘protonic energy gaps.’’ As examples, we approximate the protonic energy gap at 298.15 K, E_g, of water to be 1.03 eV and the protonic energy gap of ethanol to be 1.28 eV, both generally in the optimal range of energy gaps for solar-cell applications. (See Supplemental Derivation SI 4.1 in Chapter 4.10 for calculations of these E_g values.) The phrase protonic energy gap is not meant to imply that either of these solvents have bands of electronic states like those in crystalline electronic semiconductors. Rather, by analogy to electronic semiconductors and shown in Figure 4.1, we define the protonic energy gap as the difference in the energy for deprotonation of all solvent molecules and the energy for protonation of all solvent molecules. Therefore, for water we set N_c = N_v = [H_2O] = 55.5 M and n_i^2 = K_w = K_{ap} = $10^{-14.0}$ M^2 at room temperature and for ethanol we set N_c = N_v = [CH_3CH_2OH] = 17.1 M and n_i^2 = K_{ap} = $10^{-19.15}$ M^2 at room temperature.[213] While these energies

form the approximate extremes of the pH scale and are analogous to standard-state conditions, intermediate pH values, which are related to the chemical potential of protons, are possible based on the equilibrated distribution of protonated and deprotonated solvent molecules. Also by analogy to an electronic semiconductor where absorption of light results in reduction of a state in the conduction band and oxidation of a state in the valence band to form an electron-hole pair, light-driven dissociation of solvent molecules (e.g., for water, $2H_2O$ + light → $H_3O^+ + OH^-$) results in two charged species with energies that differ by E_g. This, however, does not mean that the open-circuit photovoltage (V_{oc}) in either case equals E_g/q, where q is the elementary charge (1.602×10^{-19} C). In electronic semiconductors, light-driven quasi-Fermi-level splitting dictates the maximum observed photovoltage of a solar cell fabricated using that semiconductor.[214,218] For water, light-driven dissociation of water molecules results in two quasi-electrochemical potentials whose difference (divided by q) is the maximum possible photovoltage (Figure 4.1), and is equivalent to the following equation:

$$V_{oc} = \frac{2.303 k_B T}{q} (pK_w - pH - pOH) \qquad \text{Equation 4.2}$$

where pM = –log(M). (See Supplemental Derivation SI 4.2 in Chapter 4.10 for derivation of Equation 4.2.) Qualitatively, pK_w encompasses the concentrations of charge carriers at thermal equilibrium, while pH and pOH represent the concentrations of charge carriers under any condition, e.g., at thermal equilibrium, under illumination.

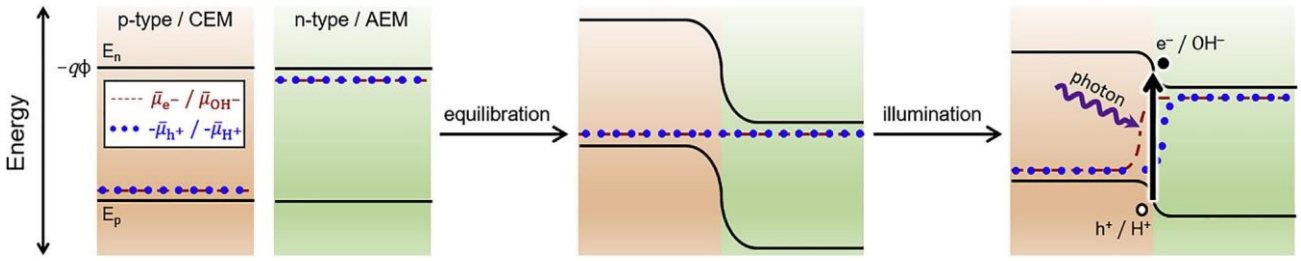

Figure 4.1. Semiconductor and Bipolar Ion-Exchange Membrane Energy-Level Diagrams. Energy-level diagrams, focusing on the junction region, for an electronic (e^-,h^+) pn-junction semiconductor or an ideal aqueous protonic (H^+,OH^-) bipolar ion-exchange membrane consisting of a homogeneous cation-exchange membrane (CEM; p-type) and a homogeneous anion-exchange membrane (AEM; n-type): before the two phases are in physical contact (left), after contact and at thermal equilibrium (middle), and after contact and during light-driven generation of charge carriers (right). Electronic energies for the semiconductor are reported before ''protonic energies'' for the bipolar membrane and are separated by a slash (/). Shown are relative energies of the two charge-carrier states, $E_{\mathrm{n}}\left(k_B T \ln\left(\frac{N_{\mathrm{c}}}{n_{\mathrm{i}}}\right) = E_{\mathrm{c}}/k_B\, T \ln\left(\frac{[\mathrm{H_2O}]}{\sqrt{K_{\mathrm{w}}}}\right)\right)$ and $E_{\mathrm{p}}\left(k_B T \ln\left(\frac{n_{\mathrm{i}}}{N_{\mathrm{v}}}\right) = E_{\mathrm{v}}/k_B\, T \ln\left(\frac{\sqrt{K_{\mathrm{w}}}}{[\mathrm{H_2O}]}\right)\right)$ (black lines), relative spatial distributions of the electric potential for negative charge carriers (as an energy), $-q\Phi$ (same black lines), and relative energies of the (quasi-)electrochemical potentials for each charge carrier (see key), $-\bar{\mu}_{\mathrm{h^+}} = E_{\mathrm{F,h^+}}/-\bar{\mu}_{\mathrm{H^+}}$ (blue), where E_{F} is the Fermi level and the standard Gibbs free energy of formation of H_2 and O_2 were each chosen so that $\mu^{\mathrm{o}}_{\mathrm{H_2O}} = 0$.

An important distinction between water and an electronic semiconductor is the number of possible charge-carrier types.[209] In most electronic semiconductors, the only charge carriers are electrons and holes, whereas in membranes wetted by aqueous

electrolytes, in addition to OH^- and H^+, mobile counterions and other inert salt species may also be present. This arises due to imperfect exclusion of ions from ion-exchange membranes. Including all of these charge carriers in analyses of the drift-diffusion semiconductor device physics equations are necessary to determine the actual processes expected to occur in water-containing ion-exchange mem-branes. However, inclusion of other ions will not likely affect the resulting physical properties of water-containing ion-exchange membranes to a large extent, because at moderate concentrations of acid or base, low concentrations of counterions are expected to be present in the ion-exchange membranes.[215] Other differences between water and an electronic semiconductor are the mechanisms for thermal generation and recombination of charge carriers. However, this is not unique, because even among solar cells based on electronic semiconductors, a variety of possible mechanisms and elementary reaction steps for recombination are possible.[214] And so while differences in mechanisms and rate constants result in various overall properties, each can result in electronic semiconductors or ‘‘protonic semiconductors’’ that exhibit current rectification and enable photovoltaic action. While the aforementioned facts support that water is a protonic semiconductor, the challenge that remained for realizing a solar cell based on water was a means by which to convert the energy in light into spontaneous dissociation of water into protons and hydroxides.

This work follows up on our recent report of a photoacid-dye-modified monopolar Nafion cation-exchange membrane that generated a photocurrent and photovoltage consistent with protons being transported against a pH gradient, and opposite to the thermodynamically favored direction.[76] The photoacid dye molecules converted light into an increase in chemical potential of protons (decrease in pK_a), which leads to deprotonation in

the excited state and generation of free protons. Upon relaxation of the photoacid molecules to their ground states, reprotonation was favored thermodynamically. Therefore, it was hypothesized that the ground-state photoacid molecules were protonated through deprotonation of water, resulting in formation of hydroxides. In that report, no net power was generated because of rapid and continuous ion crossover across the membrane due to use of a single monopolar ion-exchange membrane with a large pH gradient across it. Here we report a bipolar ion-exchange membrane structure, to prevent most of the ionic crossover, functionalized with the same photoacid dye molecules. A first-of-its-kind stable membrane system was developed that converts visible light into net ionic power and generates a photovoltage that is ~60 times larger than that reported previously for photoacid-dye-modified monopolar Nafion cation-exchange membranes.

Chapter 4.4. Results and discussion.

Chapter 4.4.1. Fabrication and Characterization of Dye-Sensitized Bipolar Ion-Exchange Membranes.

Photoacid-sensitized bipolar membranes (**PSBMs**) were fabricated by laminating and annealing a dye-sensitized monopolar cation-exchange membrane with covalently bound photoacid dyes, **cPFSA**, to a commercial monopolar anion-exchange membrane, AHA (Figure 4.2). The resulting **PSBM** was deeply colored and preserved the absorbance peaks of the original **cPFSA** membrane in its protonated form (Figure 4.3A and Figure SI 4.1). After soaking **PSBM** in 1 M NaOH (aq), its visible-light-absorbing peak exhibited a bathochromic shift, consistent with the behavior in **cPFSA** only, but the peak also broadened considerably

(Figure 4.3A and Figure SI 4.1). Peak broadening could be due to formation of aggregates[220] or an electro-absorption Stark effect caused by local electrostatic fields at the interface of **cPFSA** and AHA, **cPFSA**|AHA, a phenomenon that is commonly observed in analogous electronic dye-sensitized solar cells and organic photovoltaics.[221–223] Photoluminescence spectra indicate that both protonation states of the photoacids in **PSBM** emit predominantly from their deprotonated excited states, which is desired for the in-tended light-driven proton release (Figure 4.3B). However, the acidic form of **PSBM** also exhibited significant emission from the protonated excited state of the photoacids where net proton transfer did not occur. This inefficient charge separation process limits the photocurrent of **PSBM**. To overcome this, photoacids that are more acidic in their thermally equilibrated excited states are needed.

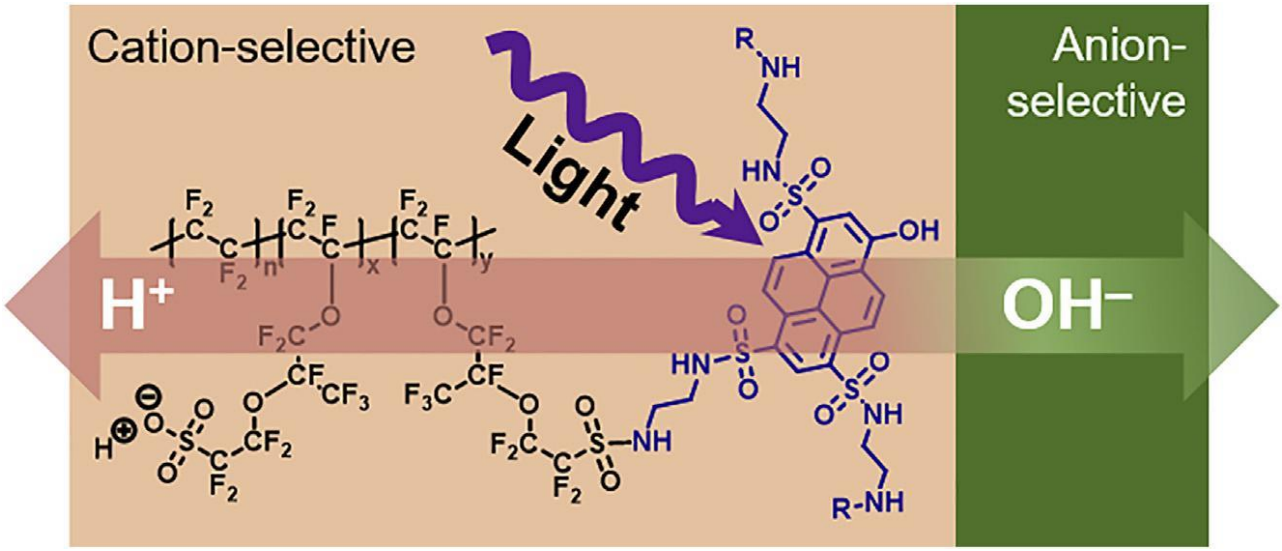

Figure 4.2. Dye-Sensitized Bipolar Ion-Exchange Membrane. Arrangement and chemical compositions of structures in photoacid-dye-sensitized bipolar ion-exchange membrane, **PSBM**, and proposed transport processes. Photoexcitation of a covalently bound 8-hydroxypyrene-1,3,6-tris(2-aminoethylsulfonamide) photoacid molecule (blue) results in a decrease of its pK_a followed by deprotonation and proton transport in the cation-selective layer. Subsequent protonation of the photoacid molecule in its ground state is followed by hydroxide transport in the anion-selective layer. Initial charge separation is proposed to be driven by local electric fields at the interface of the two layers.

Thermal gravimetric analysis was performed on **cPFSA** and AHA to evaluate the thermal stability of the polymers relevant to the membrane annealing process required for fabrication of **PSBM**. At temperatures below 135 °C and under a flow of argon gas, there was a loss of < 8% mass in **cPFSA** and AHA, which was attributed to loss of water (Figure 4.3C and Figure SI 4.2). The AHA membrane showed significant decomposition at temperatures above 200 °C. Although the thermal stability of AHA has not been thoroughly reported in the literature, many quaternary-ammonium-based anion-exchange membranes undergo three

decomposition events.[224–227] The first decomposition event is typically loss of absorbed water, which occurs at temperatures below 100 °C; the second decomposition event is decomposition of the ammonium groups, which occurs at temperatures ranging from 140 °C to 200 °C; and the third decomposition event is degradation of the main chain of the polymer at temperatures greater than 250 °C (Figure 4.3C and Figure SI 4.2).[224–227] Additional stability tests performed on AHA showed the expected ~4.5% weight loss over the first ~4 min due to dehydration, followed by only a 0.5% weight loss with prolonged heating at 120 °C for 4 hr (Figure SI 4.3). This suggests that little degradation of AHA occurred during the fabrication of **PSBM**, which was annealed at 120 °C for 4 hr during fabrication.

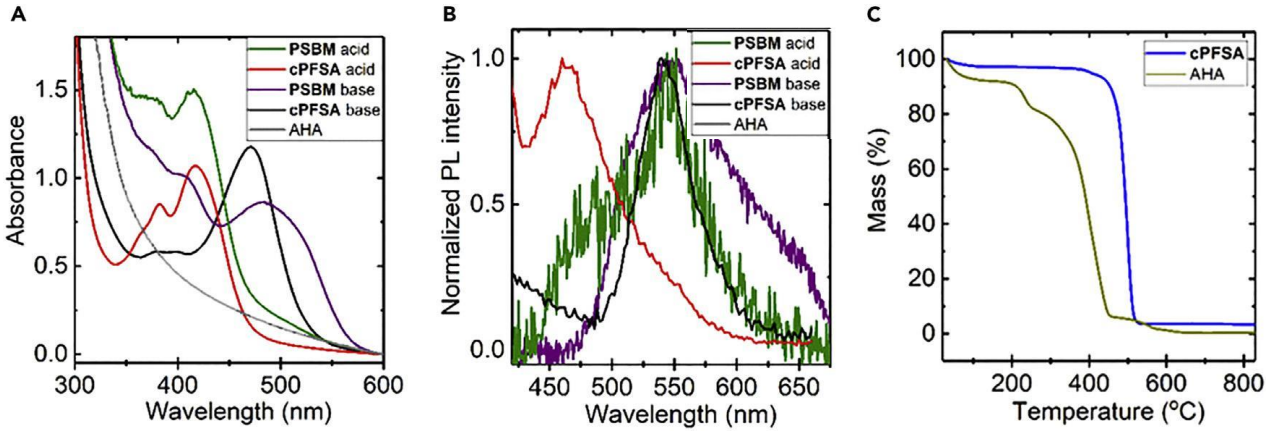

Figure 4.3. Spectroscopic and Gravimetric Characterization of Dye-Sensitized Bipolar Ion-Exchange Membranes. (A and B) Transmission-mode electronic absorption spectra (A) and photoluminescence (PL) spectra (B) of **cPFSA** after soaking it in 1 M HCl (aq) (red) and in 1 M NaOH (aq) (black), **PSBM** after soaking it in 1 M HCl (aq) (green) and in 1 M NaOH (aq) (purple), and native AHA (gray). (C) Thermal gravimetric analysis data during a temperature ramp for the sodium form of **cPFSA** (blue) and chloride form of AHA (dark yellow). See also Figure SI 4.1Figure SI 4.3 andFigure SI 4.8.

Cross-sectional scanning electron micrographs of a typical section of **PSBM** were used to assess the physical properties of **PSBM**. The **cPFSA** layer was observed to range from ~30 to 50 μm thick (Figure 4.4 and Figure SI 4.4), which was significantly thinner than before annealing (~51 μm). The AHA layer was observed to be 210 $\pm$ 20 μm thick (Figure 4.4 and Figure SI 4.4), consistent with reported thicknesses from AHA data sheets.[228] The **cPFSA**|AHA interface was smooth with no large voids and no evidence of delamination (Figure 4.4A and Figure 4.4B), and these membranes exhibited the best photoelectrochemical performance. Some **PSBMs** exhibited the opposite sign of the photovoltage, but with a magnitude that was more than ten times smaller. Cross-sectional

scanning electron micrographs of these membranes showed noticeable defects and regions of poor adhesion at the **cPFSA**|AHA interface (Figure SI 4.4). **PSBM** had been soaked in 1 M KCl (aq) prior to measurements and elemental maps are consistent with this, showing predominant localization of potassium in the **cPFSA** layer and chlorine in the AHA layer, and where **cPFSA** is apparent by the large number of counts for fluorine and sulfur (Figure 4.4C–Figure 4.4F). Significant exclusion of co-ions from each membrane further corroborates that each membrane layer remained highly selective for cations or anions after annealing them together. Additional elemental maps are shown in Figure SI 4.5.

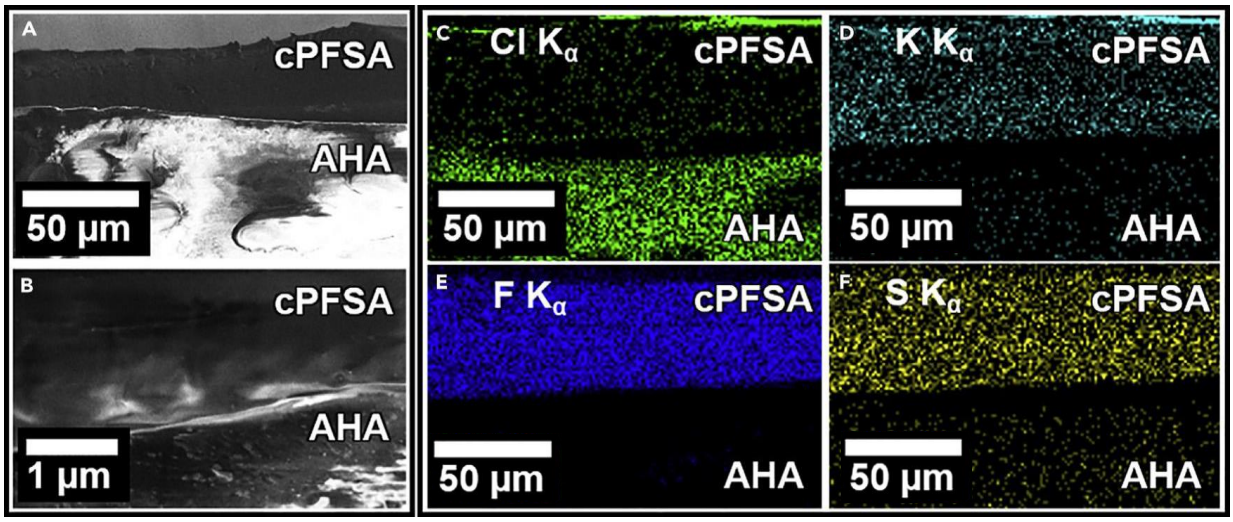

Figure 4.4. **Electron Microscopy of Dye-Sensitized Bipolar Ion-Exchange Membrane.** (A–F) Representative scanning electron micrographs of the interface of **cPFSA** and AHA layers in **PSBM** as a (A) wide view and (B) zoomed in view. Energy-dispersive X-ray spectroscopy elemental maps for (C) chlorine, (D) potassium, (E) fluorine, and (F) sulfur. See also Figure SI 4.4 and Figure SI 4.5.

Chapter 4.4.2. Photovoltaic Action Requires Light Absorption by Dyes.

The photoelectrochemical properties of **PSBM** were assessed when it separated aqueous electrolytes consisting of 10 mM $HClO_4$ (aq) and 10 mM KOH (aq), and therefore roughly pH 2 and pH 12, in part to prevent strongly alkaline conditions that are known to rapidly degrade most anion-exchange membranes.[229] Figure 4.7 is a schematic of the electrochemical cell and Figure 4.8 is a schematic of the processes that occur during bias polarization. Under this condition, the initial value of the open-circuit potential in the dark (E_{oc}) across **PSBM** was measured to be -400 ± 200 mV (Table SI 4.1), which decreased in magnitude slowly over time at a rate of 0.17 mV/min for a **PSBM** with E_{oc} = –535 mV (Figure SI 4.6). If **PSBM** behaved as a perfectly ion-selective bipolar membrane, then wetting it by aqueous acid on the **cPFSA** cation-exchange-membrane side and aqueous base on the AHA anion-exchange-membrane side should generate a net built-in electric potential difference across the membrane consistent with the following formula:[230]

$$E_{\mathrm{oc}} = \frac{k_B T}{q} \ln\left(\frac{[\mathrm{H}^+]_{\mathrm{eq}}^{\mathrm{base}}}{[\mathrm{H}^+]_{\mathrm{eq}}^{\mathrm{acid}}}\right) \qquad \text{Equation 4.3}$$

where $[\mathrm{H}^+]_{\mathrm{eq}}^{\mathrm{phase}}$ is the bulk concentration of protons in each electrolyte in the dark (in units of M). Equation 4.3 predicts that E_{oc} = –592 mV at 298.15 K; however, the extreme concentrations of protons and hydroxides in each chamber imply that even small imperfections and/or incorporation of co-ions could alter this value significantly.[230] This expected value for E_{oc} is due to formation of three built-in electric potential differences, one

across each interface: acid solution|**cPFSA**, **cPFSA**|AHA, and AHA|base solution. The value of the Donnan potential across each membrane-solution interface is dictated by the difference in concentrations of ions on either side of the interface and these Donnan potentials oppose the built-in potential of the space-charge region across the **cPFSA**|AHA interface. However, the net sign and magnitude of E_{oc} are dominated by the potential across the space-charge region at the **cPFSA**|AHA interface.

PSBM exhibited a photocurrent measured at a small applied bias versus E_{oc} ($J_{ph\text{-}sc}$) of $-5 \pm 4\ \mu A/cm^2$ and an open-circuit photovoltage versus E_{oc} (V_{oc}) of $+60 \pm 50$ mV, and with a best-performing cell V_{oc} = 121 mV (Table SI 4.1 and Figure SI 4.7). E_{oc} and V_{oc} were also measured using a high-impedance digital multimeter, instead of a potentiostat, to monitor the potential between the two nominally identical reference electrodes, and very similar behavior was observed. Previously, for **cPFSA** alone we reported E_{oc} = –30 mV, V_{oc} = 1 mV, and $J_{ph\text{-}sc}$ = $-100\ \mu A/cm^2$. [76] These data indicate that incorporation of a second membrane contact for OH^- in the form of AHA increased the magnitude of E_{oc} by a factor of ~10 and increased V_{oc} by a factor of ~60, but decreased the magnitude of $J_{ph\text{-}sc}$ to ~5% of that observed for state-of-the-art **cPFSA** alone.[76] The increase in the magnitude of the potentials when AHA was introduced is reasonable because this second membrane layer attenuated cation leakage across the membrane therefore increasing the magnitude of E_{oc}. Assuming E_{oc} is dictated solely by the potential drop across the space-charge region, the value of V_{oc} is less than the magnitude of E_{oc},[214] and therefore, a larger magnitude E_{oc} also translated to larger V_{oc} values. The decrease in the magnitude of the photocurrent for **PSBM** could be due to formation of a well-defined and stable space-charge region that is expected to be on the order of several nanometers thick,[231,232] beyond which **cPFSA** is strongly acidic. Most

photogenerated carriers in the space-charge region will charge separate and be collected if the drift length is larger than the width of the space-charge region. The drift length is often much larger than the width of the space-charge region in traditional pn-junction solar cells. This may not be true for photoacid-sensitized bipolar ion-exchange membranes, but unfortunately the drift length cannot easily be calculated for conditions where the electric field is not constant and recombination is a second-order process.[214] Carriers photogenerated outside of the space-charge region must first diffuse to the space-charge region located across the **cPFSA**|AHA interface to charge separate and be collected. The maximum distance that minority charge-carrier hydroxides can diffuse to the space-charge region prior to recombination, l_{diff}, is calculated using the one-dimensional diffusion equation for the root-mean-square displacement,

$$l_{\text{diff}} = \sqrt{D\tau} \qquad \text{Equation 4.4}$$

where D is the diffusion coefficient ($cm^2\ s^{-1}$) and τ is the lifetime (s). The room temperature diffusion coefficient of hydroxides in water is $D_{OH^-} = 5.26 \times 10^{-5}\ cm^2\ s^{-1}$.[195] Recombination likely occurs by diffusion-limited association of protons and hydroxides with a second-order rate constant of $1.3 \times 10^{11}\ M^{-1}\ s^{-1}$,[233,234] and given 0.54 M protons in protonated Nafion,[107] the pseudo-first-order rate constant is $7.0 \times 10^{10}\ s^{-1}$, and thus, $\tau = 1.4 \times 10^{-11}$ s. This results in l_{diff} = 0.3 nm and suggests that efficient collection of photogenerated charges occurs on the scale of several nanometers across the **cPFSA**|AHA interface, even though each monopolar membrane is >50 μm thick. Based on the equivalent number of Suns excitation in **cPFSA** of 0.65 and the measured percent transmittance of **cPFSA** at 405 nm, which was

~6% based on the –log(% transmittance [T]) value of ~1.2 (Figure SI 4.8), an equivalent of ~0.04 Suns of light reached the junction formed across the **cPFSA**|AHA interface. This value was determined by calculating the percent of incident light that was transmitted through **cPFSA**, %T × (incident Suns) = %T × (Suns/[1 – % T]). This ~15-fold decrease in illumination intensity may explain the similar decrease in $J_{ph\text{-}sc}$ between **cPFSA** and **PSBM**, because the previous photoelectrochemical results for **cPFSA** used 40 Suns equivalent excitation and with a junction responsible for charge separation that likely consisted of a potential drop across the entire **cPFSA**.[76]

PSBM exhibited photovoltaic action as demonstrated by a shift in the *J*–*E* data into quadrant IV which is consistent with cations being transported against a pH gradient to the more acidic compartment (Figure 4.5A). Assuming that the photoacid is liberating protons when illuminated, this suggests that protons are being transported opposite to their favorable direction of diffusion in the dark and therefore that visible-light illumination results in net photovoltaic action. The substantial increase in hysteresis between **PSBM** under illumination versus in the dark is explained by an increase in the number and distribution of mobile charge carriers at the **cPFSA**|AHA interface (Figure 4.5A). Hysteresis is a common phenomenon in many electrochemical systems, and notably in the hybrid organic-inorganic perovskite solar cells where ions are weakly mobile.[235–237] The sluggish transport kinetics in ion-exchange membranes support that hysteresis is likely due to transient changes in ion distributions even at very slow scan rates, although E_{oc} returns to its original value after the electrolyte is refreshed. Spectral response measurements using **PSBM** showed a photocurrent response with 405 nm laser light excitation, but not with 532 nm laser light excitation that delivered > 5 times as many photons per second (Figure 4.5B).

A Nafion|AHA bipolar membrane that did not contain photoacid dye molecules showed zero photoresponse when illuminated with the same laser light sources (Figure 4.5B). To rule out ionic current resulting from photoinduced electron transfer between photoacid molecules and dissolved O_2, measurements were performed that carefully excluded O_2 from the cell and electrolyte. Use of deoxygenated electrolyte resulted in very similar photoelectrochemical performance to ambient electrolyte (Figure SI 4.9). These data support that sensitization of **PSBM** to visible light by photoacid dye molecules enables its photovoltaic action.

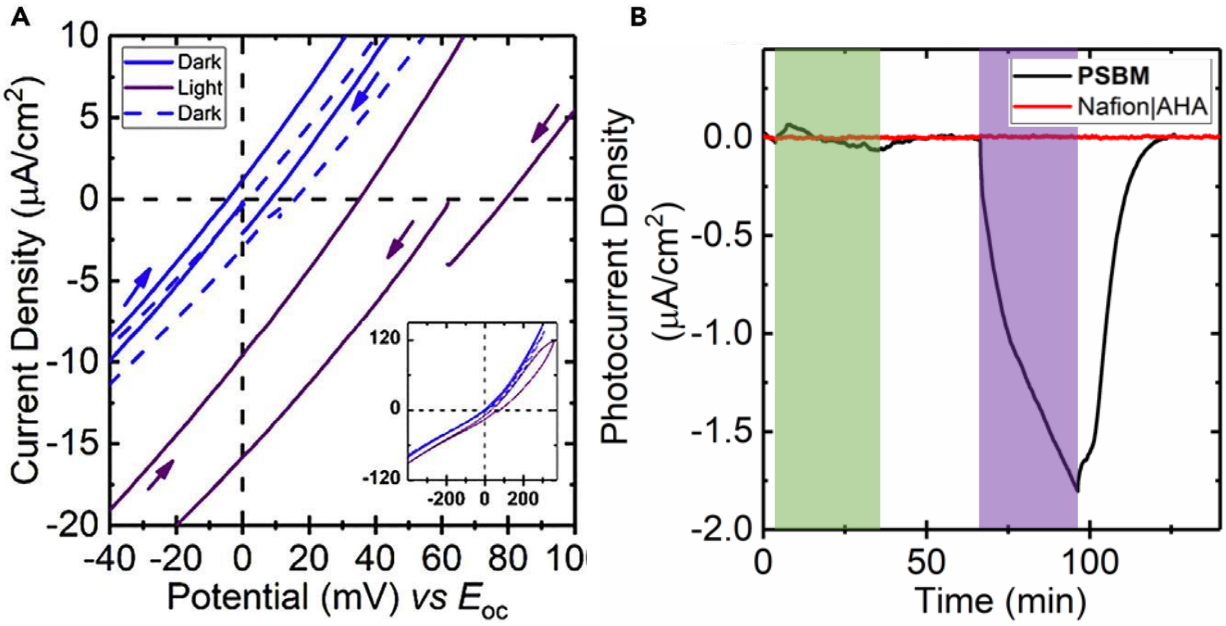

Figure 4.5. Photovoltaic Action from Dye-Sensitized Bipolar Ion-Exchange Membrane. (A) Cyclic voltammograms in the dark (blue), under illumination with 405 nm laser light (purple), and in the dark again after introducing fresh electrolyte (dashed blue) for **PSBM** wetted by 10 mM $HClO_4$ (aq) on one side of the membrane and 10 mM KOH (aq) on the other side of the membrane. The direction of each linear potential sweep is indicated by the arrows. (B) Spectral response of **PSBM** (black) and Nafion|AHA (red), reported as $J_{ph\text{-}sc}$ values after correction for a small dark current, when illuminated intermittently with 532 nm laser light (green) followed by 405 nm laser light (purple), highlighted by these respective colors. See also Figure SI 4.6 Figure SI 4.7, Figure SI 4.9, and Table SI 4.1.

Chapter 4.5. Conclusions.

An arrangement for a light-driven proton pump was reported that mimicked the structure of a traditional electronic pn-junction diode used in efficient solar cells. Photoacid-sensitized bipolar ion-exchange membranes were fabricated and their physical, optical, and photoelectrochemical properties were compared with those of a monopolar cation-exchange membrane modified with photoacid dyes reported previously. Good adherence at the interface of the polymer layers of the photoacid-sensitized bipolar membrane was found to be crucial for efficient photovoltaic action. Use of a strongly adhering anion-exchange membrane with near-conformal contact with the dye-sensitized cation-exchange membrane resulted in an increase in the magnitude of the built-in potential by a factor of ~10, a ~60-fold increase in the photovoltage, and a ~20-fold decrease in the magnitude of the photocurrent over analogous monopolar membranes. These observations are consistent with the formation of a stable and thin space-charge region at the interface of the two polymer layers. Photovoltaic action occurred when the incident light was absorbed by the protonated version of the photoacid even in the absence of O_2.

Chapter 4.6. Outlook.

Access to clean and potable water is one of the top issues facing humanity and is expected to become even more pressing in the next several decades.[238,239] While efficient and renewable energy technologies could supply the power needed to generate potable water, advances are slow and are in general incremental from prior demonstrations. Moreover, the

developing world cannot afford current clean water solutions, yet the majority of the four billion people expected to be under water stress in approximately the next decade will live in the developing world.[238] Therefore, in the absence of enormous altruism from governments, companies, and philanthropic organizations, people in developing nations will suffer and many will die, especially children. In the long-term, it is expected that newly developed nations with large gross domestic product and an established grid or micro-grid infrastructure will utilize state-of-the-art cost-effective plant-scale technologies for clean water generation, such as those based on osmosis, distillation, or electro-dialysis. In the immediate near term, an inexpensive technology to desalinate water could support economic development.[238] Presented here is the first step toward an inexpensive, yet rapid, solar-powered water desalination device that mimics a traditional pn-junction solar cell and is powered by a solar cell based on water as the semiconductor. We expect a water solar cell to be well-suited to drive processes that only require ion motion, such as desalination. Toward this, we report a design for direct solar desalination of salt water by an integrated photodialysis process where at no time during operation is electronic current generated.[240] Visible light drives charge separation of protons and hydroxides, which in turn drive anions (Cl^-) and cations (Na^+) out of a secondary compartment, forming aqueous HCl, NaOH, and less salty water (Figure 4.6).[210,39] This is a delineation from electrodialysis, a leading technique to generate potable water from saltwater sources, where electronic current must be converted into ionic current via Faradaic interfacial electron transfer reactions. The Faradaic reactions are often water electrolysis, a process that requires >1.23 V, which is wasted as heat during the con-version of electronic current into ionic current. (See Supplemental Derivation SI 4.3 in Chapter 4.10 for a thermodynamic comparison of [solar-

driven] electrodialysis and integrated solar photodialysis.) Integrated solar photodialysis only requires relatively simple and inexpensive plastic ion-exchange membranes, like those based on polyethylene terephthalate, polyacrylamide, or polystyrene, and does not require relatively expensive electronic semiconductors such as silicon. Also, the proposed mechanism for the photoacid dye molecules does not include electron transfer and therefore, exquisite chemical stability of the polymer membranes is not required. This differs from most electrochemical technologies where expensive and robust membranes such as Nafion are required to maintain membrane integrity even in the presence of reactive and/or free-radical intermediates. While still far from practical, the largest photovoltage that we reported here is more than half that needed to desalinate NaCl in sea water (~600 mM NaCl) to potable water (~10 mM NaCl) and all that is needed to convert moderately saline brackish water (~100 mM NaCl) to potable water.[241,242] A pathway exists for further development of this concept and of the functional materials required for this behavior.

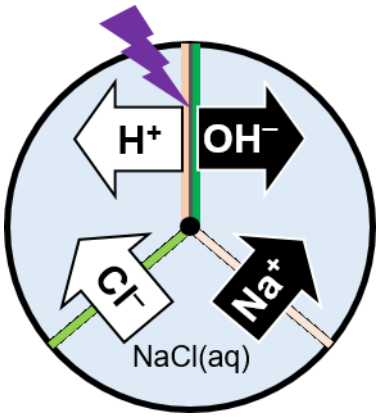

Figure 4.6. Proposed Dialysis Processes. Schematic representation of the major charge-transport processes that occur during electrodialysis or photodialysis. During electrodialysis, the lightning bolt represents an electric bias between the anode (left) and the cathode (right) (top vertical lines) to drive water electrolysis ($1.5H_2O \rightarrow 0.25O_2$ (left) + H^+ (left) + $0.5H_2$ (right) + OH^- (right)). During solar photodialysis, the lightning bolt represents visible light that is absorbed in **PSBM** (top vertical lines) to drive water dissociation ($H_2O \rightarrow H^+$ (left) + OH^- (right)). See also Supplemental Derivation SI 4.3 in Chapter 4.10.

Chapter 4.7. Experimental Procedures.

Reagents.

Purified 8-hydroxypyrene-1,3,6-tris(2-aminoethylsulfonamide) (**2.1**) was synthesized according to Chapter 2.5 experimental. **cPFSA** membranes were prepared as previously reported[76] (and presented in Chapter 3.3). The following materials were used without purification: sulfuric acid (95%, Fisher Scientific), sodium hydroxide (> 95%, Macron Fine Chemicals), potassium hydroxide (88%, Fischer Scientific), perchloric acid (70%, Alfa Aesar), Nafion sulfonyl fluoride EW = 1,100 (C.G. Processing), and Neosepta® AHA anion-exchange membrane (Astom Corporation).

Fabrication of Photoacid-Sensitized Bipolar Membrane.

Bipolar (ion-exchange) membranes sensitized with photoacid dye molecules, **PSBMs**, were constructed by laminating a monopolar **cPFSA** cation-exchange membrane to a monopolar Neosepta® AHA anion-exchange membrane and annealing them. To facilitate adhesion between the two monopolar membranes, the two-layer membrane assembly was placed between two silica glass slides and pressed mechanically together using two strong neodymium magnets. This membrane assembly was then immersed in 5 mL of deionized water in a 50 mL Teflon sleeve and in a stainless-steel autoclave that was sealed and heated in a muffle furnace for 4 hr at 120 °C after a heating ramp of 5 °C/min.

UV-Visible Electronic Absorption Spectroscopy.

Electronic absorption spectra were acquired at room temperature using a transmission-mode UV-visible spectrophotometer (Cary 60, Agilent Technologies) with a resolution of 1 nm. Membranes were placed in the beam path, and the reported spectra were baselined on a spectrum of ambient air and corrected for the non-zero signal at 600 nm due to scattering by subtracting the signal at 600 nm from all data points in the spectrum. Membranes were soaked in either 1 M HCl (aq) or 1 M NaOH (aq) prior to measurements to mimic conditions of **PSBM** under photoelectrochemical evaluation.

Photoluminescence Spectroscopy.

Photoluminescence spectra were acquired at room temperature using a fluorescence spectrophotometer (Cary Eclipse, Agilent Technologies) with excitation light at 350 nm, matched slit widths of 5 nm, and detection in a right-angle geometry. Data were corrected for the wavelength-dependent response of the detection system. Membranes were soaked for 3 days in either 1 M HCl (aq) or 1 M NaOH (aq) prior to measurements being taken with fresh solution, to mimic conditions of **PSBM** under photoelectrochemical evaluation.

Thermal Gravimetric Analysis.

Thermal gravimetric analysis was performed under an atmosphere of argon gas using a platinum pan with a heating ramp of 10 °C/min and a maximum temperature of 850 °C (TGA Q500, TA Instruments). Membranes were soaked in 1 M NaCl (aq) for 1 day prior to evaluation.

Scanning Electron Microscopy and Energy-Dispersive X-Ray Spectroscopy.

Cross-sectional scanning electron micrographs were acquired at a 1 kV bias and 0.1 nA beam current (Magellan 400L XHR, FEI). Energy-dispersive X-ray spectroscopy maps were performed at a 15 kV bias and 0.8 nA beam current using an 80 mm^2 silicon drift detector (INCA software, Oxford Instruments). Membranes were soaked in 1 M KCl (aq), rinsed with copious amounts of deionized water, dried in ambient air for 3 days, and dried under reduced pressure for 4 hr immediately prior to imaging.

Electrochemical Experiments.

All electrochemical experiments were performed using a potentiostat (VSP-300, Biologic Science) in four-electrode measurement mode with a setup and protocol similar to those reported previously,[20,31] but with minor modifications as noted here. **PSBM** separated the two compartments of an H-cell that was made of poly(chlorotrifluoroethylene) with three 0.5 cm holes drilled through the top of each cell and a 1.54 cm diameter bore hole through the center of the poly(chlorotrifluoroethylene) block. Two saturated calomel electrodes (SCEs) were used as the potential-sensing reference electrodes and two platinum mesh electrodes were used as the power-supplying working and counter electrodes, with one of each placed on either side of **PSBM** (Figure 4.7). Each electrochemical experiment used 10 mM $HClO_4$ (aq) in the acidic chamber and 10 mM KOH (aq) in the alkaline chamber. All electrochemical data shown in Figure 4.5, Figure SI 4.6, andFigure SI 4.7 were from the best-performing **PSBMs**, whereas values reported in the text are from four functional **PSBMs** and are reported as the mean $\pm$ SD.

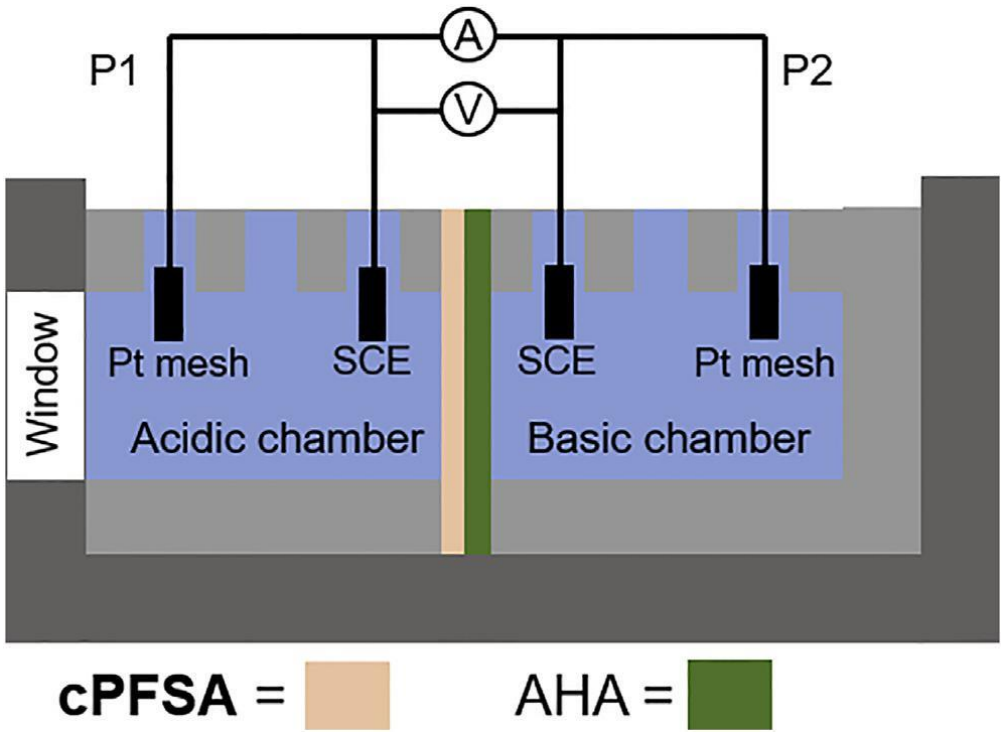

Figure 4.7. Electrochemical Cell for Assessing Dye-Sensitized Bipolar Ion-Exchange Membranes. Electrochemical cell and simplified circuit diagram for the photoelectrochemical experiments. Light was shone through the borosilicate glass window and into the acidic chamber where the incident beam contacted the dye-sensitized layer. The electric potential was measured across the membrane using two nominally identical saturated calomel (reference) electrodes (SCE). The ionic current was measured as the electronic current that passed through the potentiostat and between the Pt mesh electrodes (P1 and P2).

Reported current densities were calculated by dividing the external current passed through the potentiostat by the geometric area of the membrane exposed to the aqueous electrolyte solution (1.86 cm^2). To follow the *J–E* convention used in our previous publication[76] and prior literature reports of *J–E* behavior of bipolar membranes where the working electrode is on the acidic side of the bipolar membrane, and therefore P1 is the

working electrode in Figure 4.7,[57,232,243,244] current and voltage data that were measured with P2 as the working electrode were multiplied by –1. This correction was applied to the data reported in Figure 4.5, Figure SI 4.6, andFigure SI 4.7, and the data from mem2S0 and mem7S1 in Table SI 4.1. After applying the correction, or for the data where P1 was the working electrode (Figure SI 4.9 and the other entries in Table SI 4.1), forward (reverse) bias is the condition where a positive (negative) potential was applied to the P1 working electrode, as shown in Figure 4.8. Open-circuit potential (E_{oc}) was measured immediately prior to cyclic voltammetry measurements using galvanostatic chronopotentiometry performed at 0 μA and was found to be +535 mV. Then, cyclic voltammetry was performed versus E_{oc} by scanning from 0 V to –1 V (under reverse bias) to +0.3 V (under forward bias) at a scan rate of 20 mV s^{-1}.

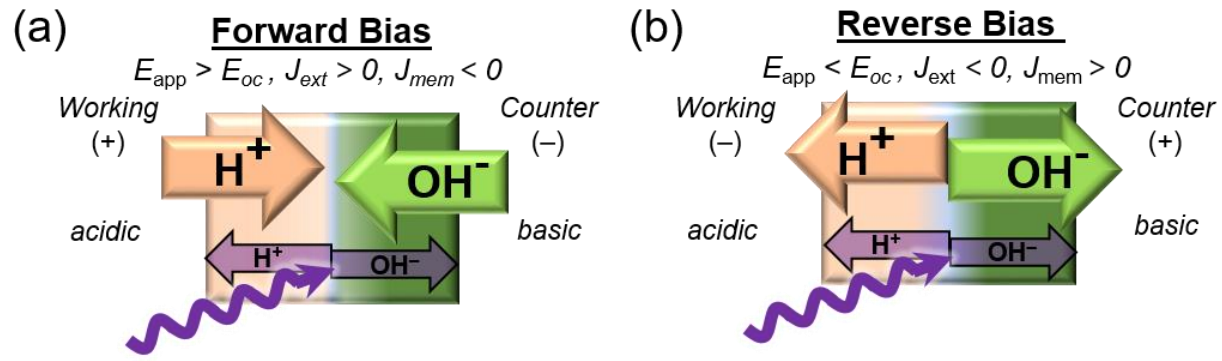

Figure 4.8. Electrochemical Terms for Dye-Sensitized Bipolar Ion-Exchange Membranes. (A and B) Schematic representations of the electrochemical response of PSBM under (A) forward bias or (B) reverse bias polarization. Shown are the regions of the dye-sensitized cation-selective layer (cPFSA, yellow), the proposed interfacial space-charge region (light blue), and the anion-selective layer (AHA, green) as well as the proposed majority processes that occur during each condition and the effect that illumination has on ion transport. Except for the light-driven processes indicated at the bottom, these same processes occur in the dark. E_{app} is the external applied potential, E_{oc} is the open-circuit potential measured in the dark, J_{ext} is the net electronic current density flowing through the potentiostat, and J_{mem} is J_{ext} but with respect to the membrane.

All light experiments were performed using a visible-light-emitting laser pointer with wavelength of 405 $\pm$ 10 nm (full width at half maximum [fwhm] = 1.96 mm; [1 $\pm$ 0.2] $\times$ 10^{18} photon cm^{-2} s^{-1}) or 532 $\pm$ 10 nm (fwhm = 0.96 mm; [6.47 $\pm$ 2] $\times$ 10^{18} photon cm^{-2} s^{-1}). Lasers were calibrated using a previously reported procedure (also discussed in Chapter 3.3).[76] An

upper bound for the equivalent number of Suns from the 405 nm light source over the area of excitation was calculated to be 40 times the absorbed photon flux rate expected from 1 Sun of air mass 1.5-global solar illumination. This was calculated using the previously reported procedure[76] (also discussed in Chapter 3.3) and the absorption spectrum of protonated **PSBM**. Assuming that charge carriers delocalized across the entire membrane area, the equivalent number of Sun excitation was more accurately 0.65. This value was determined by correcting 40 Suns for the ratio of the area of the collimated excitation beam and the area of the membrane wetted by the aqueous electrolyte solution ([$\pi \times$ (0.5 3 0.196 cm)^2]/[1.86 cm^2]). This is a reasonable assumption given that the observed photoresponse was similar when the excitation light was expanded to the size of **PSBM** wetted by the aqueous electrolyte solution. Light was incident from the acidic **cPFSA** side of **PSBM** because AHA is opaque and highly scattering. To deconvolute the photoresponse from the dark current, the photocurrent values at near-zero applied bias, $J_{ph\text{-}sc}$, reported in the spectral response (Figure 4.5B), deoxygenated experiments (Figure SI 4.9), and membranes (Table SI 4.1) were each corrected for background drift by subtracting an exponential linear combination fit of the dark regions before and after illumination ($y = at + b\exp[ct] + d$, with fitted parameters of a, b, c, and d).

Effect of O_2 on the Photoelectrochemical Performance.

To evaluate the effect that O_2 had on the observed photoelectrochemical behavior, several experiments were conducted using **PSBM** under an argon atmosphere. The electrochemical cell containing **PSBM** was placed in a large plastic bag and sealed, the electrolyte was sparged

with argon gas for 30 min prior to running the experiment, and the head space was continuously purged with argon gas during the measurements.

Chapter 4.8. Author contributions.

S.A. proposed the research, helped design experiments, and discussed results. W.W. fabricated membranes, performed most electrochemical, absorption spectroscopy, and thermal gravimetric analysis measurements, and analyzed data with advice from S.A. C.D.S. synthesized photoacid dye molecules, performed all photoluminescence measurements, performed some electrochemical measurements, and analyzed data. D.M.F. performed all electron microscopy and spectroscopy measurements and analyzed data with advice from S.A. S.A. and W.W. prepared the majority of the manuscript and all authors contributed to editing it.

Chapter 4.9. Supplemental Information.

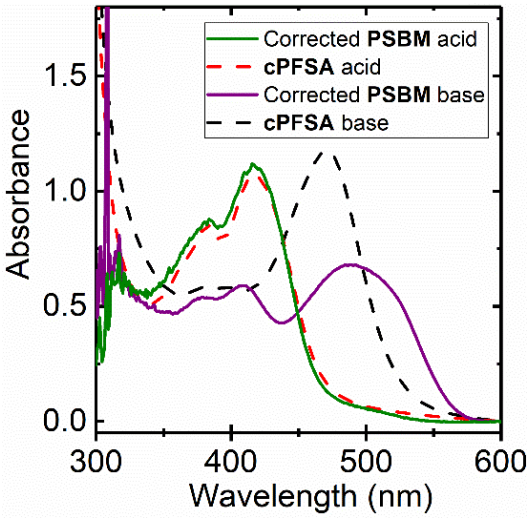

Figure SI 4.1. Related to Figure 4.3. Transmission-mode electronic absorption spectra of **PSBM** after soaking it in 1 M HCl(aq) (green) and in 1 M NaOH(aq) (purple), corrected for the spectrum of AHA only, and compared to **cPFSA** after soaking it in 1 M HCl(aq) (dashed red) and in 1 M NaOH(aq) (dashed black). Each spectrum is corrected for scattering by subtracting its value at 600 nm from all data points in the spectrum.

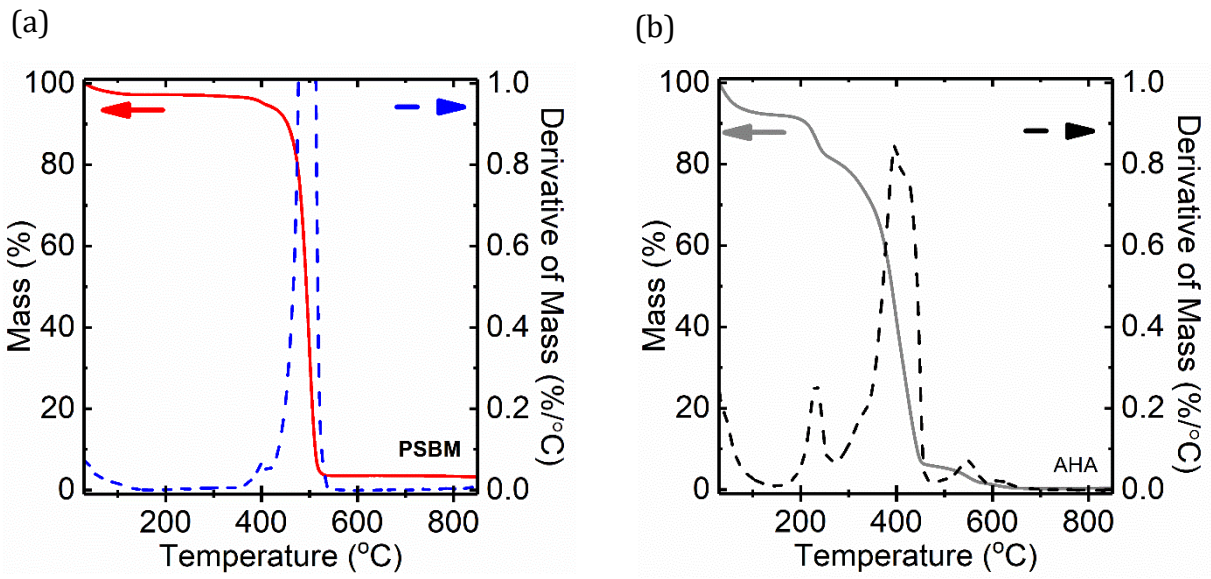

Figure SI 4.2. Related to Figure 4.3. Thermal gravimetric analysis data and its derivative during a temperature ramp for (a) **cPFSA** (red; derivative is dashed blue) and (b) AHA (grey; derivative is dashed black).

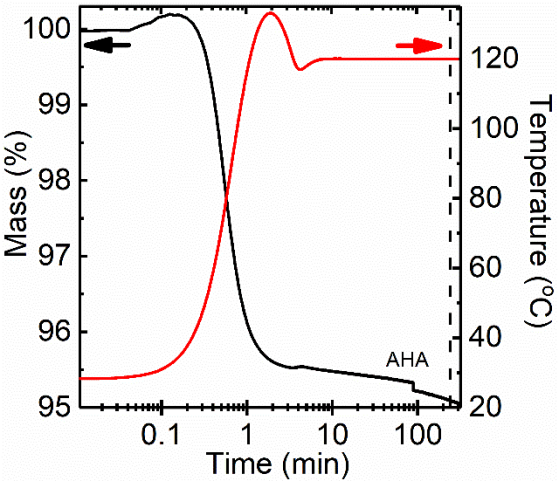

Figure SI 4.3. Related to Figure 4.3. Semi-logarithmic plot of thermal gravimetric analysis data over time for AHA after a quick temperature ramp to 120°C, the temperature used to anneal **cPFSA** to AHA for fabrication of **PSBM**. Four hours is the time used to anneal **cPFSA** to AHA for fabrication of **PSBM** and is indicated by the vertical dashed line.

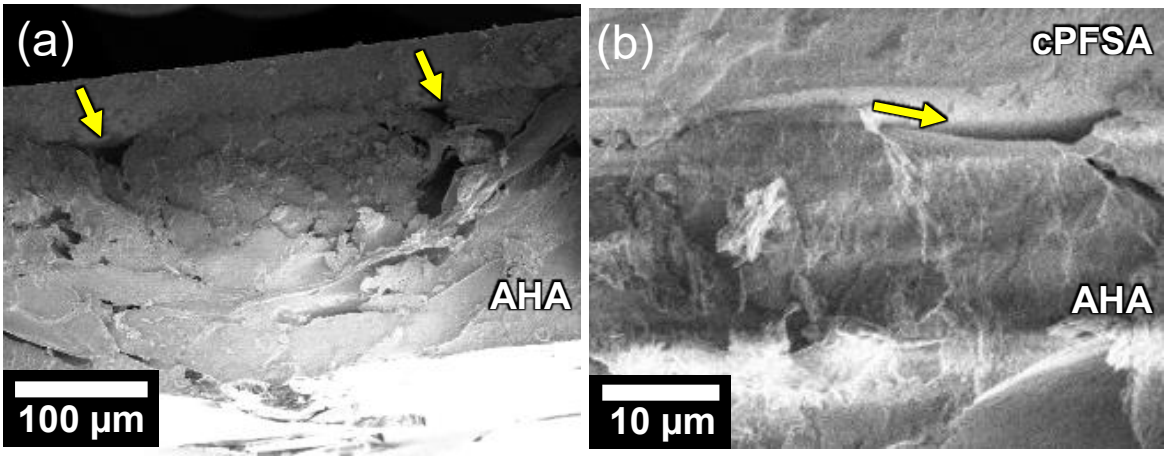

Figure SI 4.4. Related to Figure 4.4. Representative scanning electron micrographs of **PSBM** that exhibited poor photovoltaic action and poor adhesion of the **cPFSA** and AHA layers as evidenced by the presence of several ~20 µm voids (yellow arrows) as a (a) wide view and (b) zoomed in view.

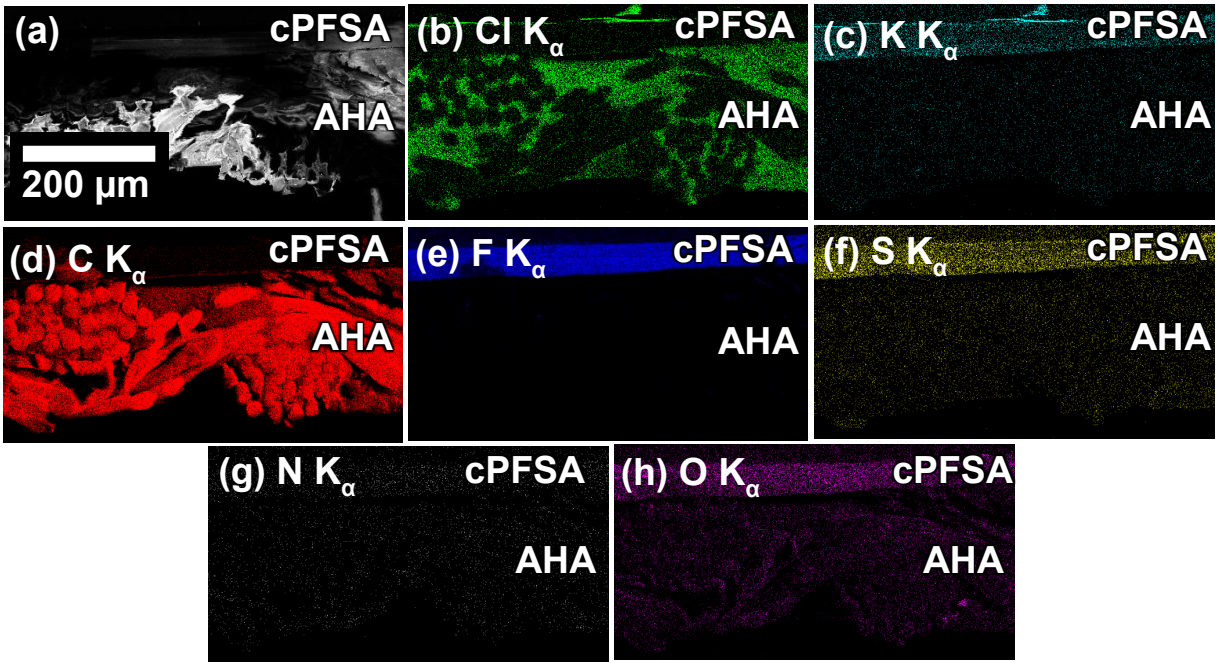

Figure SI 4.5. Related to Figure 4.4. (a) Representative scanning electron micrograph of **PSBM** and (b – h) energy-dispersive X-ray spectroscopy elemental maps for each element with a significant signal. The scale bar in panel a is also valid for the data in panels b – h.

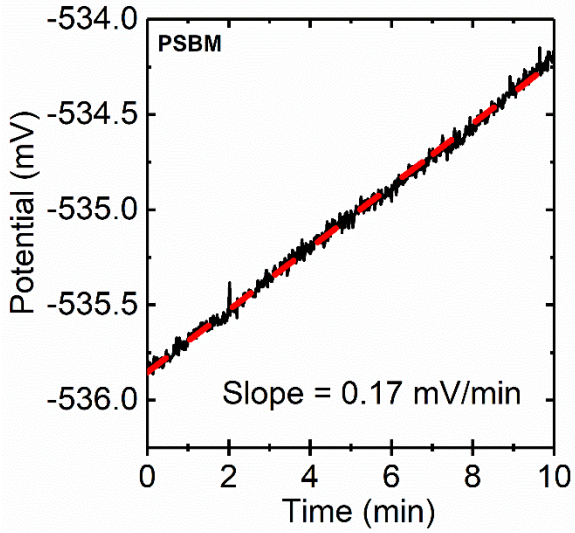

Figure SI 4.6. Related to Figure 4.5. Open-circuit potential chronopotentiometry data for **PSBM** wetted by 10 mM $HClO_4$(aq) on one side of the membrane and 10 mM KOH(aq) on the other side of the membrane in the dark showing the loss of the open-circuit potential and its rate.

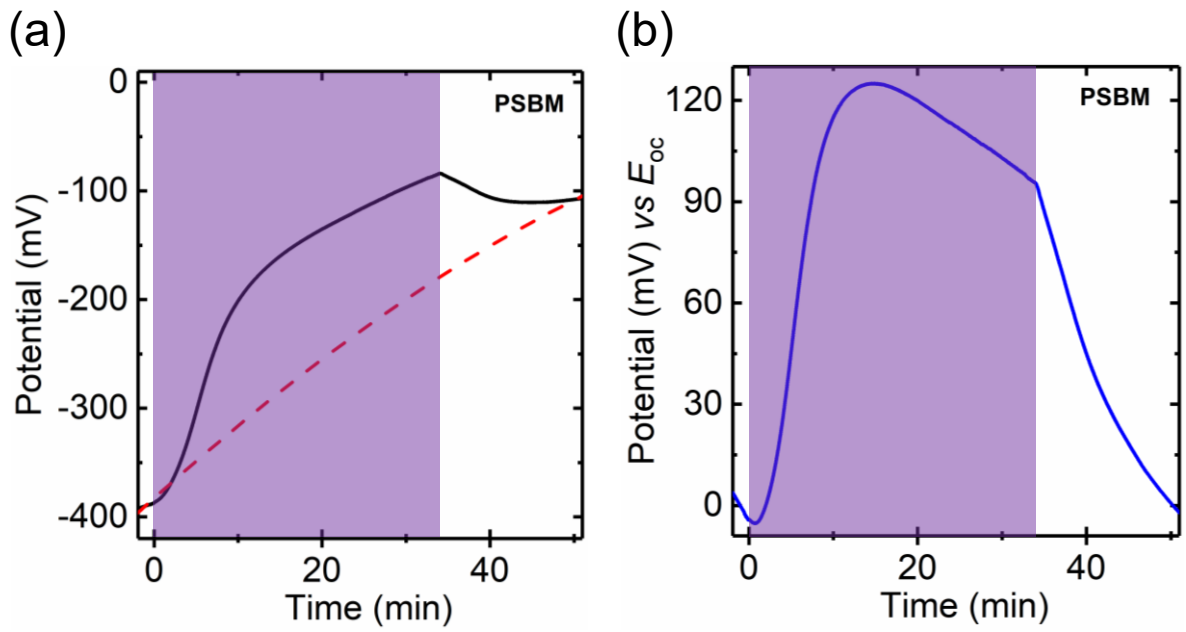

Figure SI 4.7. Related to Figure 4.5. Open-circuit potential chronopotentiometry data in the dark and under illumination with 405 nm laser light (highlighted regions) for the best-performing **PSBM** wetted by 10 mM $HClO_4$(aq) on one side of the membrane and 10 mM KOH(aq) on the other side of the membrane (a) before correction for baseline drift (black; best-fit baseline drift (dashed red)) and (b) after correction for baseline drift.

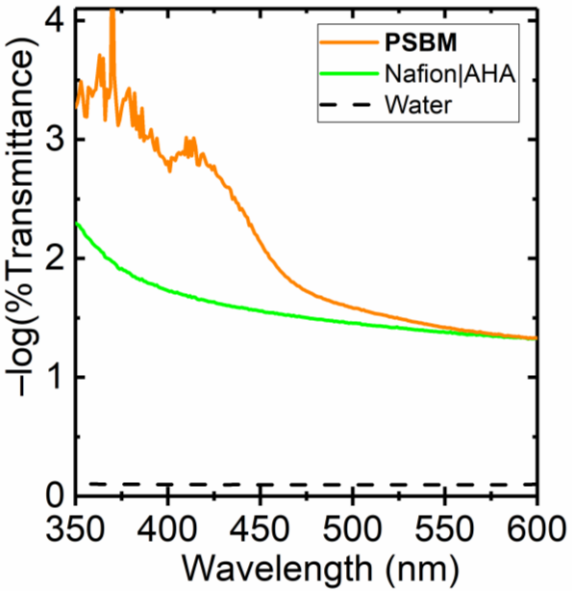

Figure SI 4.8. Related to Figure 4.3. Absorption + Scattering spectra reported as –log(%Transmittance) of **PSBM** wetted by 10 mM $HClO_4$(aq) on one side of the membrane and 10 mM KOH(aq) on the other side of the membrane (orange), an undyed bipolar membrane consisting of Nafion and AHA wetted by the same electrolytes (green), and water (black) measured *in situ* in a modified electrochemical cell that contained two borosilicate glass windows.

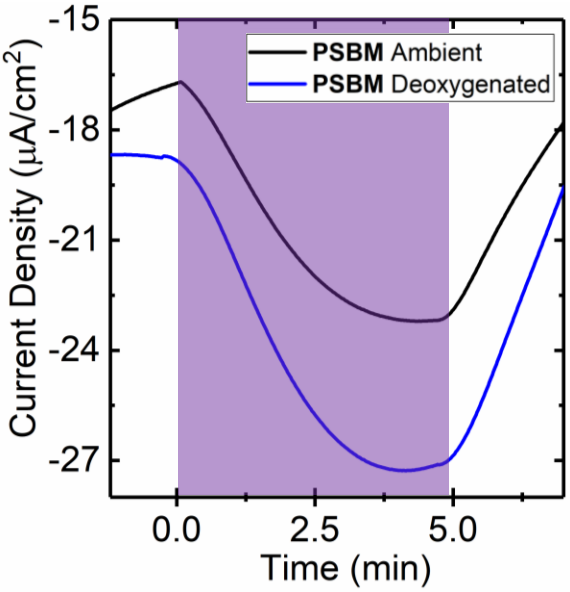

Figure SI 4.9. Related to Figure 4.5. Baseline-corrected chronoamperometry data measured at a small applied reverse bias in the dark and under illumination with 405 nm laser light (highlighted region) for **PSBM** wetted by ambient 10 mM $HClO_4$(aq) on one side of the membrane and 10 mM KOH(aq) on the other side of the membrane (black) and the same electrolyte after being thoroughly deoxygenated (blue).

Table SI 4.1. Related to Figure 4.5. Dark open-circuit potentials, open-circuit photovoltages under illumination, and dark-corrected photocurrent densities under illumination for **PSBM**.

Membrane	**Open-Circuit Potential, E_{oc} (mV)**	**Photovoltage, V_{oc} *vs* E_{oc} (mV)**	**Photocurrent Density, $J_{ph\text{-}sc}$ (μA cm^{-2})**
Mem1S0	-350	25	-7.0
Mem2S0	-524	58	-0.5
Mem7S1	-535	121	-9.5
Mem7S2	-106	19	-2.5
Mean	**-400**	**60**	**-5**
Standard Deviation	**200**	**50**	**4**

Chapter 4.10. Supplemental Derivations

Derivation SI 4.1. Calculation of the "protonic energy gap" of water and ethanol. Related to Equation 4.1.

Using Equation 4.1,

$$E_{\mathrm{g-water}} = -\frac{2.303 k_B T}{q} \log\left(\frac{K_{\mathrm{w}}}{N_{\mathrm{c}} N_{\mathrm{v}}}\right) = -\frac{2.303 k_B T}{q} \log\left(\frac{10^{-14.0}\ \mathrm{M}^2}{(55.5\ \mathrm{M})(55.5\ \mathrm{M})}\right) = -\frac{2.303 k_B T}{q}(-17.49) =$$

1.035 eV

$$E_{\mathrm{g-ethanol}} = -\frac{2.303 k_B T}{q} \log\left(\frac{K_{\mathrm{s}}}{N_{\mathrm{c}} N_{\mathrm{v}}}\right) = -\frac{2.303 k_B T}{q} \log\left(\frac{10^{-19.15}\ \mathrm{M}^2}{(17.1\ \mathrm{M})(17.1\ \mathrm{M})}\right) = -\frac{2.303 k_B T}{q}(-21.62) =$$

1.279 eV

Derivation SI 4.2. Derivation of Equation 4.2.

Using the definition of the open-circuit photovoltage,[16]

$$|V_{\mathrm{oc}}| = \frac{1}{q}\left(\Delta\bar{\mu}_{\mathrm{p}} + \Delta\bar{\mu}_{\mathrm{n}}\right)$$

$$= \frac{1}{q}\left(\left(\bar{\mu}_{\mathrm{p}} - \bar{\mu}_{\mathrm{p}}^{\mathrm{eq}}\right) + \left(\bar{\mu}_{\mathrm{n}} - \bar{\mu}_{\mathrm{n}}^{\mathrm{eq}}\right)\right)$$

$$= \frac{1}{q}\left(\left(\bar{\mu}_{\mathrm{H^+}} - \bar{\mu}_{\mathrm{H^+}}^{\mathrm{eq}}\right) + \left(\bar{\mu}_{\mathrm{OH^-}} - \bar{\mu}_{\mathrm{OH^-}}^{\mathrm{eq}}\right)\right) \qquad \text{Equation SI 4.1}$$

where

$$\bar{\mu}_{\mathrm{H^+}} = \bar{\mu}^{\mathrm{eq}}_{\mathrm{H^+}} + k_B T \ln\left(\frac{a_{\mathrm{H^+}}}{a^{\mathrm{eq}}_{\mathrm{H^+}}}\right)$$

$$\bar{\mu}_{\mathrm{OH^-}} = \bar{\mu}^{\mathrm{eq}}_{\mathrm{OH^-}} + k_B T \ln\left(\frac{a_{\mathrm{OH^-}}}{a^{\mathrm{eq}}_{\mathrm{OH^-}}}\right) \qquad \text{Equation SI 4.2}$$

and $\bar{\mu}_i$ and a_i are the electrochemical potential and activity, respectively, of species i, and eq stands for equilibrium.

Substituting Equation SI 4.2 into Equation SI 4.1 one obtains,

$$|V_{\mathrm{oc}}| = \frac{1}{q}\left(k_B T \ln\left(\frac{a_{\mathrm{H^+}}}{a^{\mathrm{eq}}_{\mathrm{H^+}}}\right) + k_B T \ln\left(\frac{a_{\mathrm{OH^-}}}{a^{\mathrm{eq}}_{\mathrm{OH^-}}}\right)\right)$$

$$= \frac{k_B T}{q} \ln\left(\frac{a_{\mathrm{H^+}} a_{\mathrm{OH^-}}}{a^{\mathrm{eq}}_{\mathrm{H^+}} a^{\mathrm{eq}}_{\mathrm{OH^-}}}\right) \qquad \text{Equation SI 4.3}$$

Recalling that $K_{\mathrm{w}} = a^{\mathrm{eq}}_{\mathrm{H^+}} a^{\mathrm{eq}}_{\mathrm{OH^-}}$ and substituting it into Equation SI 4.3 one obtains,

$$|V_{\mathrm{oc}}| = \frac{k_B T}{q} \ln\left(\frac{a_{\mathrm{H^+}} a_{\mathrm{OH^-}}}{K_{\mathrm{w}}}\right)$$

$$= -\frac{2.303 k_B T}{q} \log\left(\frac{K_{\mathrm{w}}}{a_{\mathrm{H^+}} a_{\mathrm{OH^-}}}\right)$$

$$= \frac{2.303 k_B T}{q} (\mathrm{p}K_\mathrm{w} - \mathrm{pH} - \mathrm{pOH})$$ Equation SI 4.4

Notably, the middle expression resembles that of Equation 4.1, but with N_c and N_v replaced by the concentration-dependent activities of OH^- and H^+, respectively.

Derivation SI 4.3. Calculation of the minimum thermodynamic potential required for dialysis of sea water to potable water. Related to Figure 4.6.

The potential required to transport NaCl from nearly potable water (~10 mM) to sea water (~600 mM) can be calculated using the Nernst equation,[44,45] and is proposed to be the minimum potential required for integrated solar photodialysis (ISPD),

$$E_{\mathrm{ISPD}} = E^{\mathrm{o}} - \frac{2.303 k_B T}{q} \log\left(\frac{a_{\mathrm{Na}^+}^{\mathrm{out}} a_{\mathrm{Cl}^-}^{\mathrm{in}}}{a_{\mathrm{Na}^+}^{\mathrm{in}} a_{\mathrm{Cl}^-}^{\mathrm{out}}}\right) \approx E^{\mathrm{o}} - \frac{2.303 k_B T}{q} \log\left(\frac{[\mathrm{Na}^+]^{\mathrm{out}}[\mathrm{Cl}^-]^{\mathrm{in}}}{[\mathrm{Na}^+]^{\mathrm{in}}[\mathrm{Cl}^-]^{\mathrm{out}}}\right)$$

$$E_{\mathrm{ISPD}} = -\frac{2.303 k_B T}{q} \log\left(\frac{(0.6\ \mathrm{M})(0.6\ \mathrm{M})}{(0.01\ \mathrm{M})(0.01\ \mathrm{M})}\right) = -\frac{2.303 k_B T}{q} \log(3600) = -0.21\ \mathrm{V}$$

The potential to perform the same process by (solar-powered) electrodialysis requires additional energy to drive Faradaic electron-transfer reactions,[7] which often constitute water electrolysis,

$$E_{\mathrm{ED}} = E_{\mathrm{ISPD}} + E^{\mathrm{o}}_{\text{water electrolysis}} = (-0.21\ \mathrm{V}) + (-1.23\ \mathrm{V}) = -1.44\ \mathrm{V}.$$

Chapter 4.11. Acknowledgments.

Chapter 4 has been reproduced with permission from:

White, W.; Sanborn, C. D.; Fabian, D. M.; Ardo, S *.Joule.* **2017**, 139 (34), 11726−11733. © 2017 Elsevier Inc.

We are grateful for financial support from the Department of Chemistry and the School of Physical Sciences at the University of California, Irvine and the Gordon and Betty Moore Foundation via a Moore Inventor Fellowship under grant no. 5641. D.M.F. is supported by a National Science Foundation Graduate Research Fellowship under grant no. DGE-1321846. We thank Daniel Bar from Ameridia, Division of Eurodia Industrie, for constructive conversations about Neosepta AHA, Mark Steinborn from the UC Irvine Machine Shop and Kevin Tkacz for fabrication of custom spectroelectrochemical cells, Dmitry Fishman for assistance and guidance with the instrumentation in the Laser Spectroscopy Facility (LSF), Enrico Gratton and Michelle Digman for use of their Laboratory of Fluorescence Dynamics (LFD) and Jenu Varghese Chacko for training and assistance with the laser microscopy instruments in the LFD, and Walter Grot for advice and for generously supplying Nafion sulfonyl fluoride poly(perfluorosulfonyl fluoride) membrane. Scanning electron micrographs and energy-dispersive X-ray spectroscopy measurements were performed at the UC Irvine Materials Research Institute (IMRI) using instrumentation funded in part by the National Science Foundation Major Research Instrumentation Program under grant no. CHE1338173. We also thank Adam Nielander, Matt Shaner, Juan Bisquert, Yogi

Surendranath, Shannon Boettcher, Sebastian Oener, and Kyle Grew for helpful and thought-provoking conversations related to this work.

Chapter 5. Improving the efficiencies of solar-energy conversion in photoacid-sensitized bipolar membranes via photoacid modifications.

Chapter 5.1. Introduction.

Short-circuit photocurrents, open-circuit photovoltages, and solar-energy conversion efficiencies are functions of light absorption which are directly correlated to photogenerated current densities. In **PSBM** the photocurrent is produced by excited-state proton transfer reactions from photoacid **2.1** (Figure 5.1). A photoacid absorbs photon-energy and performs excited-state proton transfer such that a proton is donated to a nearby water molecule to form a hydronium ion. The hydronium ion is then transported through the cation-exchange membrane against a proton gradient. A nearby water molecule is able to reprotonate the ground-state conjugate base, from which a hydroxide is formed and is transported through the anion-exchange membrane against a hydroxide gradient. In Chapter 2 photoluminescence studies suggested that the covalent attachment of photoacid **2.1** to the inside of nanopores shifted the pK_a^* to more basic pH values and decreased the excited-state lifetime of the photoacid. In our light-driven proton pumps (**cPFSA** and **PBSM**) this correlates to lower yields of excited-state proton transfer efficiencies, fewer photogenerated carriers, and lower solar-energy conversion efficiencies.

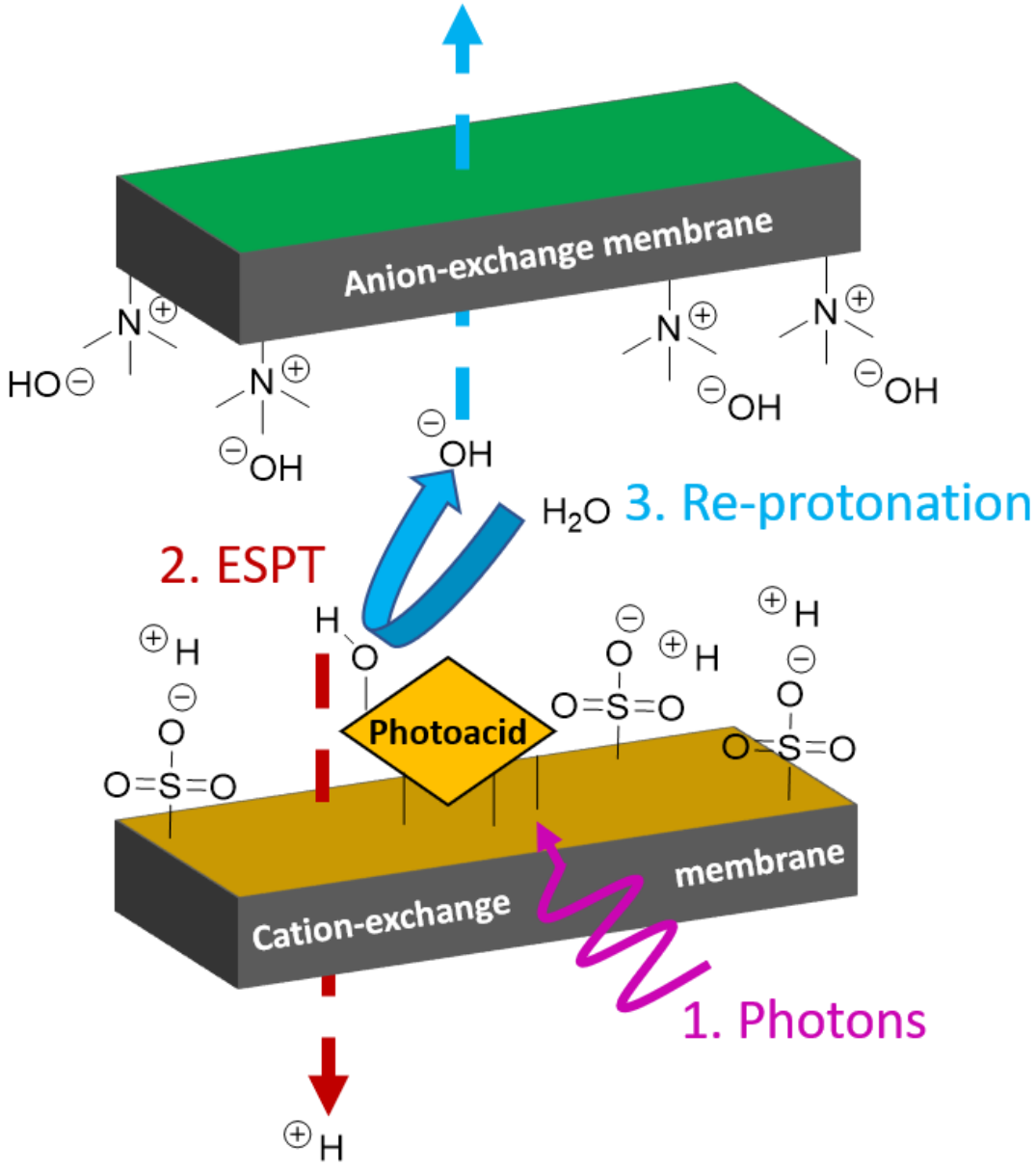

Figure 5.1. Proposed photo-current generation in a **PBSM**.

Preliminary photoluminescence studies presented in Chapter 3 and 4 already suggested that **2.1** becomes a weaker photoacid when bound to the insides of Nafion channels. This was confirmed by measuring excited-state lifetimes of **cPFSA** with

fluorescence-lifetime imaging microscopy and emission profiles at varying pH values. The excited-state lifetimes ranged from ~1 to 2 ns for films wetted in aqueous solution ranging from pH 1 to 13. Similarly, **cPFSA** was dissolved in DMSO and then diluted in the aqueous electrolyte and showed no deviation in lifetime, which implies that the solvent interactions likely do not completely explain the observed changes in the pK_a or the excited-state lifetime. Furthermore, **PSBM** was cross-sectioned and the junction of the membranes was characterized by two-photon fluorescence microscopy (Figure 5.2). The **PSBM** immersed in pH 12 displayed the emission of RO^{-*} from **2.1** across the entire width of the **cPFSA**. This is expected because the photoacid should be fully deprotonated in the ground state under these conditions. This claim is supported with a titration curve of **cPFSA** (Figure 5.3) which shows that the pK_a of the photoacid shifted from 5.8 when dissolved in solution to 8.1. The direction of the shift is consistent with the pK_a shift of **2.1** bound in the tips of nanopores, which was measured to be 6.9 (Chapter 2). This implies that **2.1** might be affected by the electrostatics of PFSA. Albeit, the photoacids at the edges of the solution and junction of the film emitted from ROH^*. This suggests that there was a fraction of protonated **2.1** remaining in the film. It is hypothesized that **2.1** managed to intercalate away from the water nano-pools of the Nafion channels and into the backbone of the film,[107] or the sample was ionically insulating and prevented sufficient wetting of the channels. This is a possibility because the **cPFSA** precursor is more hydrophobic and ionically insulating than Nafion or **cPFSA**. **PSBM** immersed in pH 2 aqueous solution showed more than 50% emission from ROH^*. The experiment was repeated, (Figure 5.2, lower left panels) and the emission occurring at the junction of **PSBM** in 10 mM $HClO_4$ was fit to a linear combination of emissions from the protonated and deprotonated excited-state from which it was found

that ~60% of the emission was from the protonated excited-state. This implies the pK_a^* is greater than 2, which is similar to PET$_8$/**2.1** immersed in water without supporting electrolyte (pK_a^* ~1.6). Collectively the data suggests that alternative membranes or photoacids should be used to increase the quantum yield of excited-state proton transfer. The enhancements in quantum yield of excited-state proton transfer may correlate to enhancements in photogenerated current densities and consequently, enhancements in short-circuit photocurrents, open-circuit photovoltages, and solar-energy conversion efficiencies.

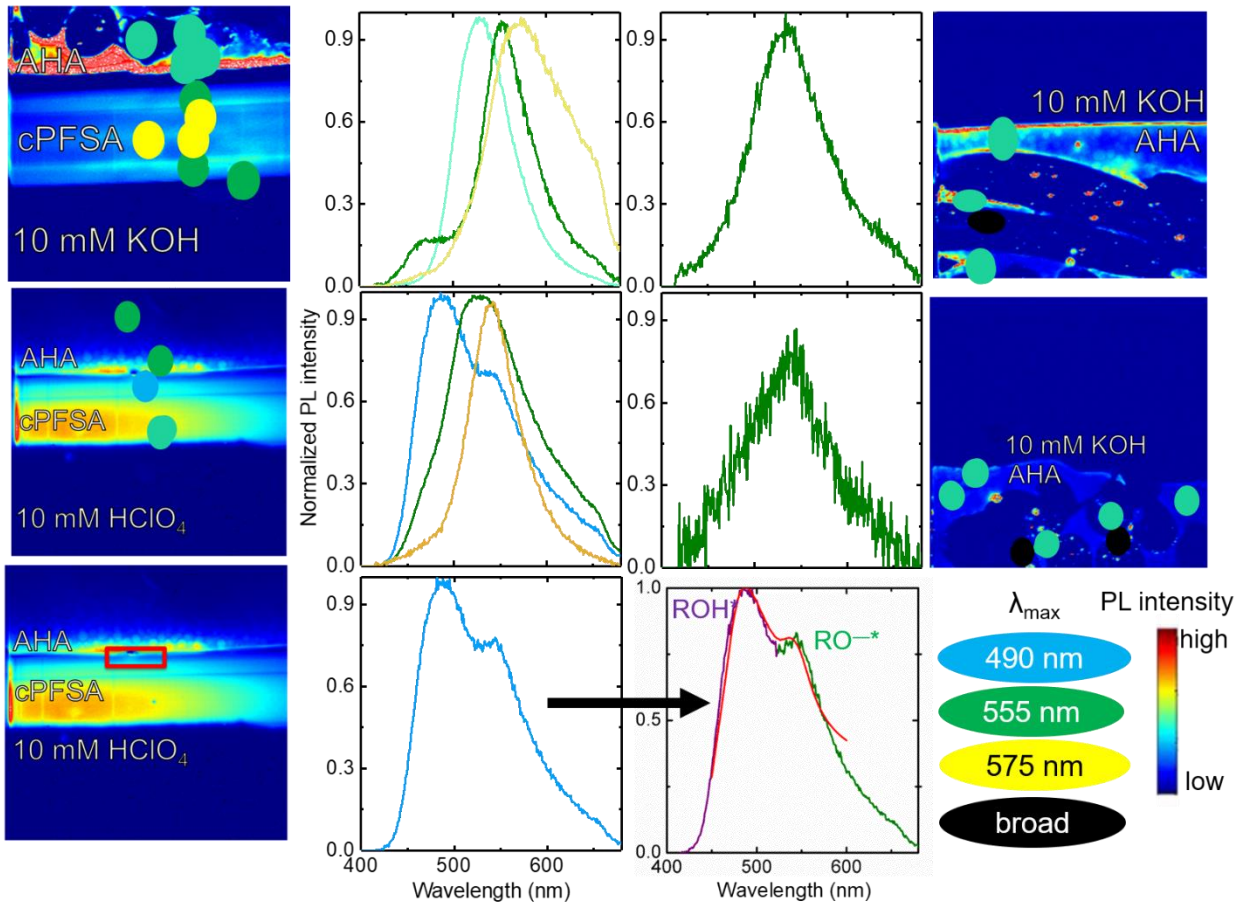

Figure 5.2. Cross-sectional fluorescence microscopy of **PSBM** (far left) and AHA controls (far right). Colored dots indicate the λ_{max} of the emission peak. Colored foreground indicates emission intensity. (Middle two columns) Emission spectra occurring at the location of colored dots. (λ_{max} = 876 nm). (Red line) Emission at the junction of **PSBM** in 10 mM $HClO_4$ was fit to a linear combination of emissions from the protonated and deprotonated excited-state.

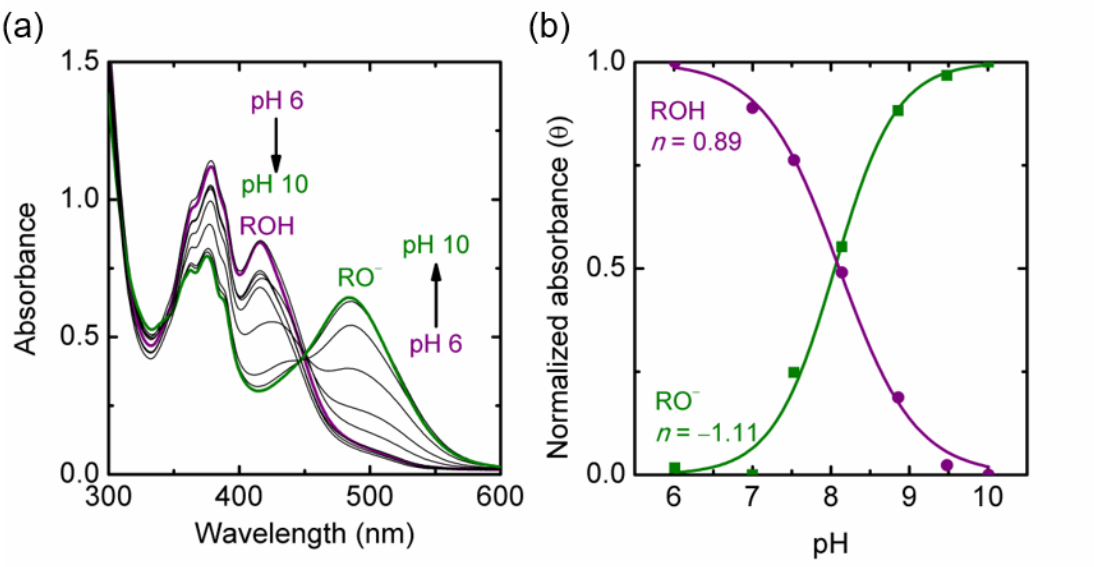

Figure 5.3. (a) Electronic absorption spectra of **cPFSA** wetted by an aqueous buffer solution. The completely protonated and deprotonated ground-state spectra are bolded, colored, and are labeled with ROH and RO^-, respectively. (b) Plot of normalized absorbance (θ) at the λ_{max} (418 nm and 488 nm) for each species as a function of pH, and displayed with non-linear least square best fits to the Hill equation (Equation 2.1).

Chapter 5.2. Photoacids with longer linkers.

The photoacid HPTS is able to perform unhindered excited-state proton transfer when dissolved into the channels of fully hydrated Nafion even though it is a weaker photoacid than **2.1**.[106] The reorientation dynamics of HPTS in Nafion remain the same as its values in bulk water unless the film is dehydrated, which suggests that the HTPS molecules are located in the water nano-pools instead of the reverse micelle wall.[106] This is expected because the HPTS has three negatives charges that would repel away from the negative

pendant sulfonates lining the Nafion channels while also making the photoacid polar so that it would not intercalate into the backbone as likely. It is possible that the excited-state proton transfer efficiency of the covalently bound photoacid could be increased if a longer tethering group was used so that the bound photoacid would be suspended further into the middle of the channels, where the water environment is more bulk-like.

The linker length of **2.1** was increased by four methylene units by reacting the activated tris(sulfonyl chloride) **2.1b** with two equivalents of *N*-Boc-ethylenediamine per sulfonyl chloride such that one equivalent formed the sulfonamide and HCl, which was neutralized by the other equivalent. The product was then deacetylated via addition of NaOH (aq) and the Boc protecting group was removed via trifluoroacetic acid treatment to yield **5.1** (Scheme 5.1). Additional purification was achieved with RP-HPLC. Purified **5.1** was bound to Nafion sulfonyl fluoride membranes and is currently under investigation.

Scheme 5.1. Synthesis of **5.1** by sulfonate activation from pyranine.

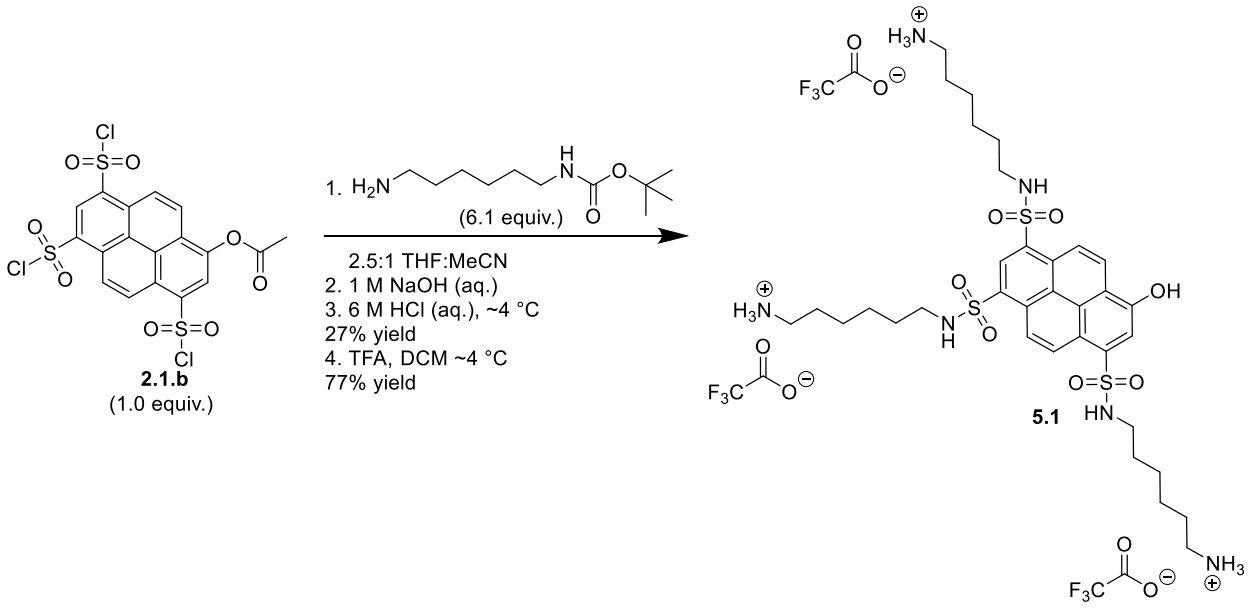

Chapter 5.3. Excited-state proton transfer described by Marcus theory.

An enhancement in the quantum yield of excited-state proton transfer in a **PSBM** may correlate to enhancements in photogenerated current densities and consequently, enhancements in short-circuit photocurrents, open-circuit photovoltages, and solar-energy conversion efficiencies. It is hypothesized that the efficiency of the excited-state proton transfer of a photoacid bound to the interior of an ion-exchange membrane channel can be enhanced if the photoacid is positioned away from the channel walls and into the center of the channels to ensure that the solvation environment is similar to that of bulk water, or that the photoacid is modified such that the photoacidity is enhanced. This is because the pK_a^* correlates to the rate of excited-state proton transfer; as the pK_a^* becomes more acidic, the rate of excited-state proton transfer becomes faster. If the back reaction (geminate recombination) is negligible, the quantum yield of excited-state proton transfer increases as the rate of proton transfer becomes faster than the summation of decay rates associated with the photoacid in its protonated excited-state without a means to partake in an excited-state proton transfer.[114] Therefore, in general, photoacids that are more acidic in the excited-state tend to have more efficient quantum yields of excited-state proton transfer.

The rate of excited-state proton transfer in a polar protic media has been modeled as an adiabatic process by which there exists a strong coupling between the reactant and product energy wells that lowers the activation energy of proton transfer. The solvent sets the reaction barrier, and upon the solvent reaching an orientation where the barrier

vanishes, excited-state proton transfer can occur The rate of proton transfer (K_{PT}) can be described via the Eyring transition-state-theory equation[245]:

$$K_{PT} = \frac{w_s}{2\pi} exp^{\left(-\frac{\Delta G^{\#}}{RT}\right)} \qquad \text{Equation 5.1}$$

where R, T, w_s, and $\Delta G^{\#}$ are the gas constant (8.314 J mol^{-1} K^{-1}), temperature (300 K), frequency factor (1×10^{13} s^{-1}), and activation free-energy of the proton transfer in units of J mol^{-1} (Equation 5.2), respectively. The frequency factor is the relaxation timescale of the solvent structure.

Kiefer and Hynes showed[246] that excited-state proton transfers can also be described by Marcus theory,[247,248] which was originally conceived to calculate the rates of electron transfer in outer-sphere reactions. Equation 5.2 relates the activation free-energy ($\Delta G^{\#}$) the thermodynamic free-energy change (ΔG_0) and the intrinsic activation energy of a symmetric transfer where the total free-energy change ($\Delta G^0 = \mathrm{RT}\log(10)\,\mathrm{p}K$) following the proton transfer is equal to zero($\Delta G_0^{\#}$).[245]

$$\Delta G^{\#} = \left(1 + \frac{\Delta G_0}{4\Delta G_0^{\#}}\right)^2 \Delta G_0^{\#} \qquad \text{Equation 5.2}$$

The intrinsic activation energy for a proton transfer reaction in water ($\Delta G_0^{\#}$) equals 10,500 J mol^{-1}.[245] The thermodynamic free-energy change (ΔG_0) for a proton transfer to water is proportional to the pK_a^* by Equation 5.3. [245]

$$\Delta G_0 = RTln(10) \times pK_a^* \qquad \text{Equation 5.3}$$

Marcus also proposed a bond energy-bond order (BEBO) relationship,[249] which lacks and inverted region but provides similar results to Equation 5.2 in the non-inverted region (Equation 5.3).[245]

$$\Delta G^{\#} = \frac{\Delta G_0}{2} + \Delta G_0^{\#} + \frac{\Delta G_0^{\#}}{\ln(2)} \ln\left(\cosh\left(\frac{\Delta G_0 \ln(2)}{2\Delta G_0^{\#}}\right)\right) \qquad \text{Equation 5.4}$$

Through Equation 5.2 and Equation 5.4 the rates of excited-state proton transfer were calculated as a function of pK_a^* and plotted in Figure 5.4. Figure 5.4 also shows experimentally measured rates of excited-state proton transfer of visible-light absorbing photoacids from literature sources.[245,250–254] The chemical structures and photophysical properties of these photoacids are shown in Figure 5.5 and Table 5.1, respectively. Collectively, the it is hypothesized that improvements to the solar-energy conversion efficiencies of **PSBM** can be made by incorporating photoacids with more negative pK_a^* values.

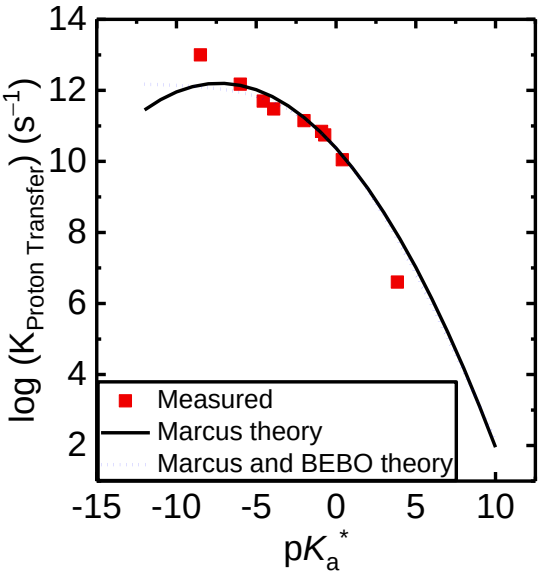

Figure 5.4. Calculated rates of excited-state proton transfer via Marcus theory and bond energy-bond order (BEBO [Equation 5.1-Equation 5.4]),[245] that is, the parabolas are not fits. Measured rates pertain to photoacids reported in literature and are shown below in Figure 5.5 for convenience. [245,250–254]

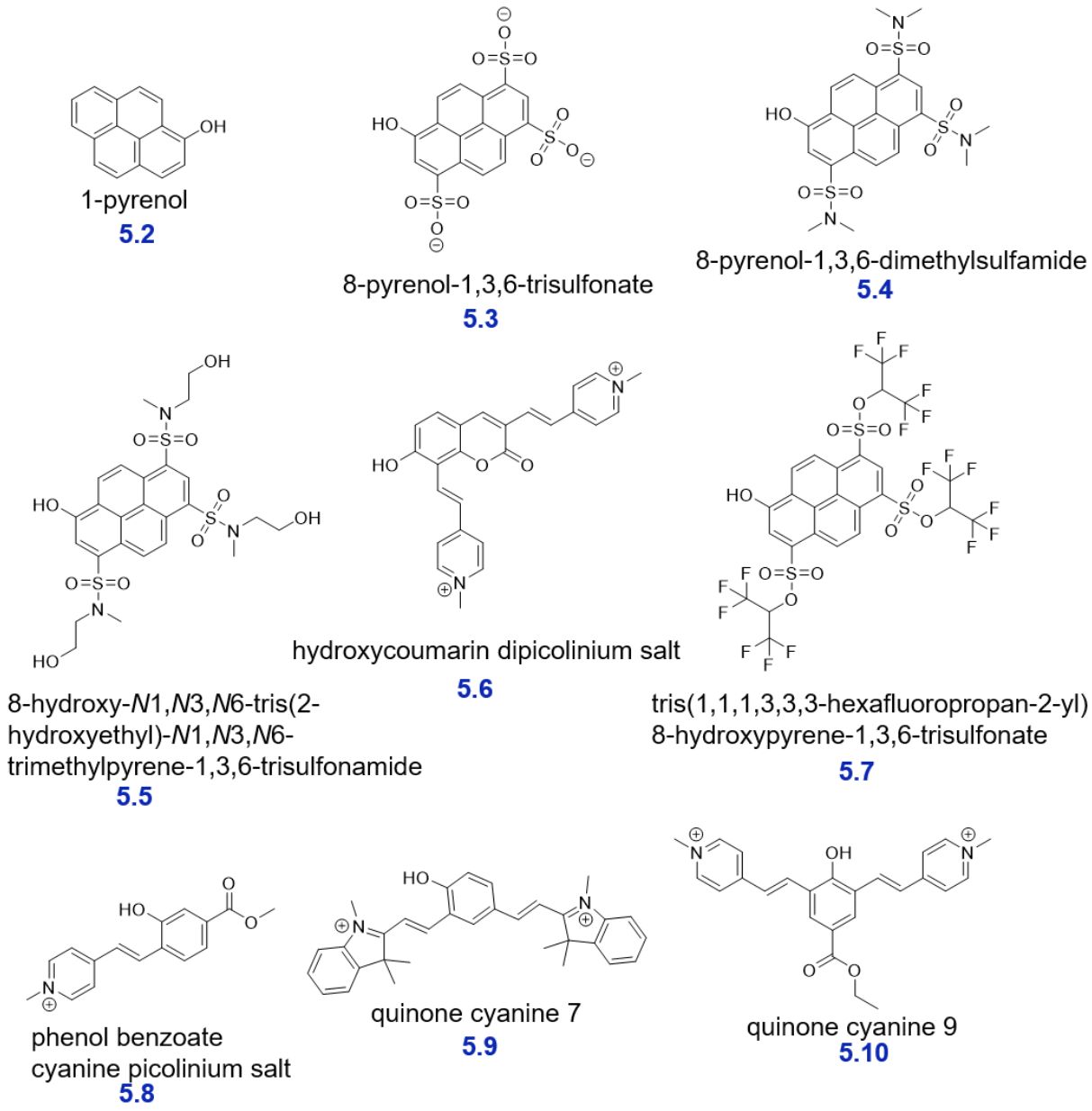

Figure 5.5. Visible-light absorbing photoacids reported in literature.[245,250–254] Photophysical properties of the compounds are listed in Table 5.1.

Table 5.1. Photophysical characteristics of visible-light absorbing photoacids.

Photoacid	pK_a	pK_a^*	τ_{PT} (ps)	reddest λ_{max} (nm)	reference
5.2	8.8	3.85	250000	378	[250]
5.3	7.7	0.4	90	403	[245]
5.4	5.7	-0.7	18	425	[245]
5.5	5.7	-0.9	14	422	[245]
5.6	5.4	-2	7	399	[251]
5.7	4.4	-3.9	3	441	[245]
5.8	6.5	-4.56	2	369	[252]
5.9	4.5	-6	0.7	594	[253]
5.10	5.5	-8.5	0.1	493	[254]

Chapter 5.4. The synthesis of super photoacids.

Photoacids with pK_a^* values less than 0 are ideal for photovoltaic applications because the acidity ensures ESPT is more likely to result in photo-generated carriers. Below is the synthesis of photoacids with pK_a^* values ranging from -12 to -3.

The amine variant of HPTS (**5.11**) has been noted to have a pK_a of ~2 and a Δ pK_a of approximately -10.[255] The photoacid **5.11** was synthesized from 1-aminopyrene (**5.2**) with fuming sulfuric acid in quantitative yield. The tris(sulfonate) **5.11** was isolated after the careful neutralization of the oleum and subsequent extraction with methanol. Further purification was achieved via RP-HPLC. The amine photoacid **5.11** was bound to Nafion sulfonyl fluoride membranes and is currently under investigation.

Scheme 5.2. Sulfonation of 1-aminopyrene.

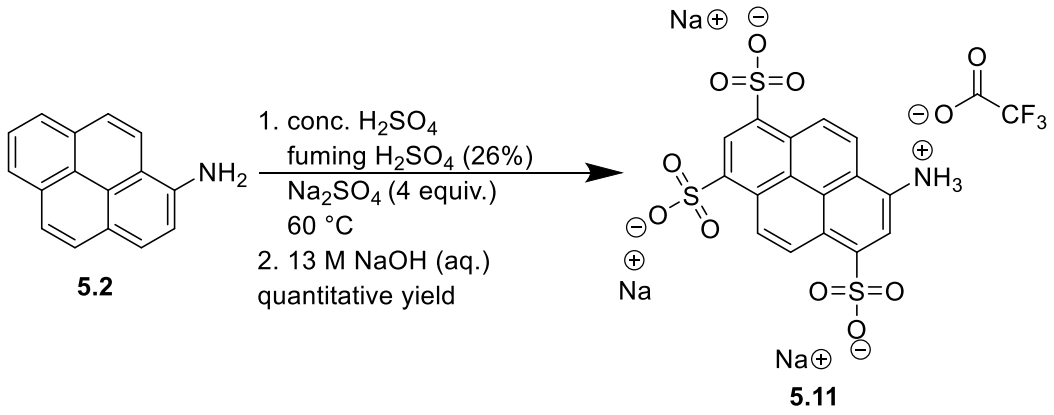

The quinone cyanine, **5.10**, is the strongest photoacid known to date with a pK_a^*equal to -8.5,[254] and thus the moiety was targeted to bind to photovoltaic proton pumps (Scheme 5.3). A simple change from the ester group to a carboxylic acid allowed the coupling of a tethering group. First the Duff reaction was performed on phenol **5.12**. The reaction requires at least three days of stirring to form the di(formyl) **5.13**. Picolinium acceptor groups **5.15** and **5.17** were synthesized from the picoline derivatives **5.14** and **5.16**, respectively. The reaction conditions were tailored to account for differences in the solubility of the two picolines. The nonpolar **5.14** reacted with methyl iodide in refluxing toluene. The same reaction conditions did not convert **5.16** to the desired product, as it remained suspended and inert in the toluene solution. However, the ionic **5.16** dissolved in DMF and reacted with the methyl iodide with gentle heating. The two equivalents of picolinium **5.15** or **5.17** were condensed with the aid of two equivalents of piperidine catalyst to the di(formyl) **5.13** according to literature precedent.[256] The workup procedure was modified which allowed *i*) quantitative yields, *ii*) multi-gram scale up, and *iii*) avoided the use of RP-HPLC. By acidifying the reaction solution, the alkoxide and carboxylate become protonated and **5.18** precipitates from solution allowing for facile isolation. Amide

formation of **5.18** is synthetically challenging. The picolinium groups withdrawal electron density from the carboxylic acid, thereby making an already relatively unreactive group more inert. A reported coupling procedure[257] used to synthesize **5.19** was implement but without success because the reaction conditions resulted in less than 5% product formation. The procedure required the supplementation of reagents to excess. Only with ~12 mole equivalents of excess coupling reagents (BocEDA, HBTU, TEA) did the reaction proceed. Albeit, the reaction was only performed successfully several times. The resulting reaction solution becomes impractical to purify as the surplus of reagents creates a solution too viscous to handle and purify via RP-HPLC.

Scheme 5.3. Synthesis of quinone cyanine 9 derivative.

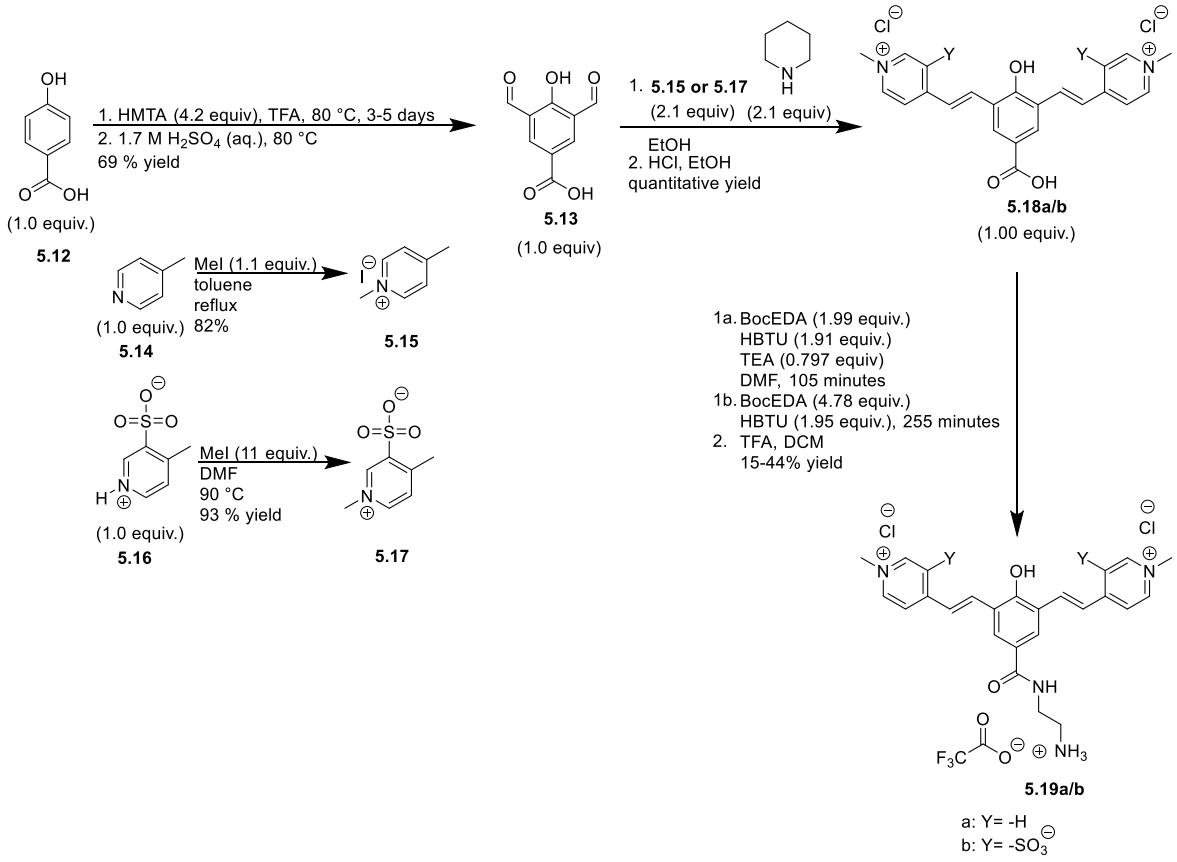

The synthesis of **5.19a** was approached using more reactive coupling reagents, specifically oxalyl chloride (Scheme 5.4). First, the alcohol **5.18a** was treated with acetic anhydride under basic conditions to afford the acetyl-protected hydroxyl group, **5.20**, followed by one-pot amide bond formation through an acid chloride intermediate to yield **5.21.** If this route were to be implemented again, it is recommended that oxalyl chloride should be used as the solvent because the photoacid was not soluble when DCM was used as the solvent.

Scheme 5.4. Amide bond formation via acid chloride.

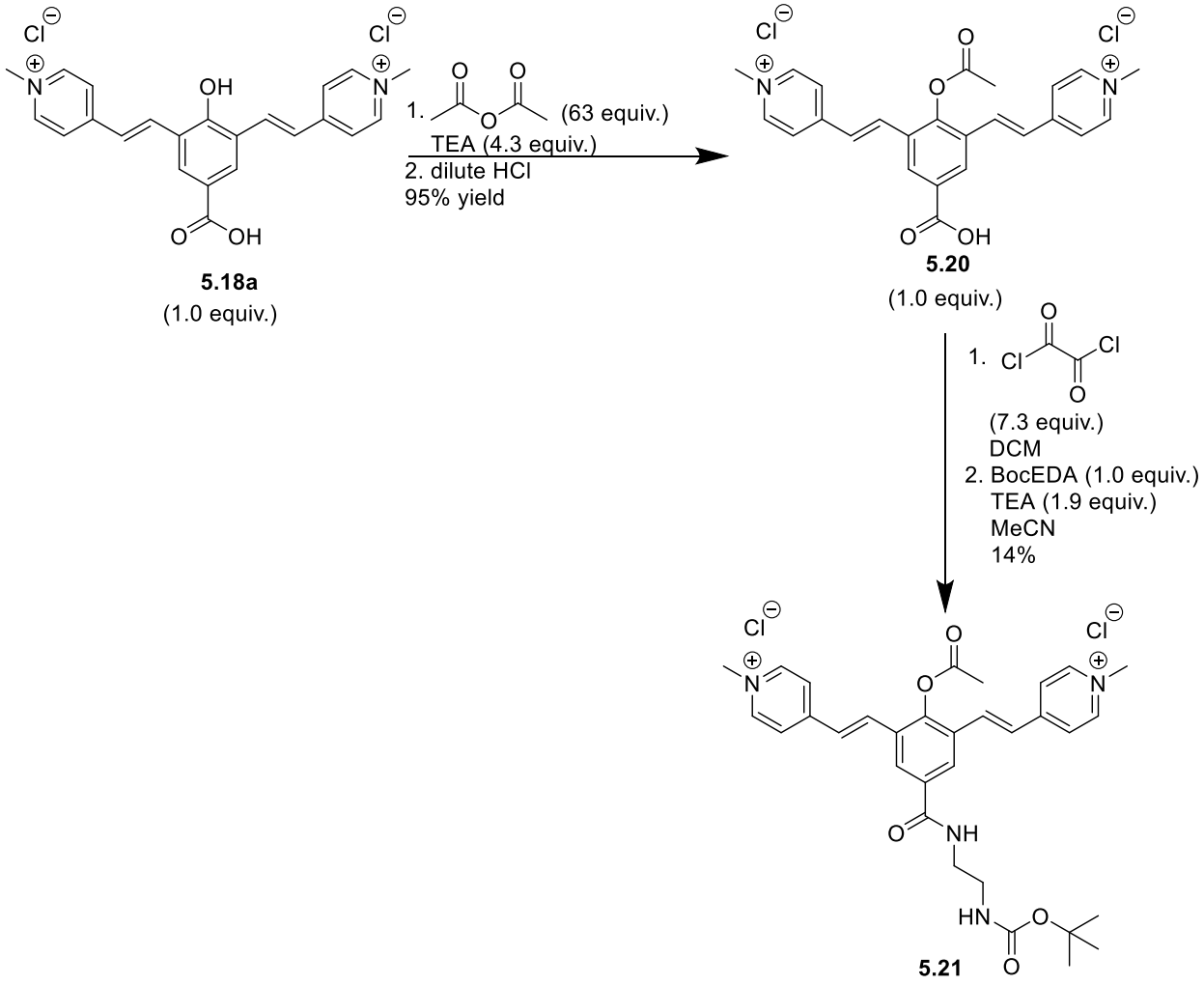

The acetoxy group on **5.20** conceals the absorption band that results from the deprotonation of the hydroxyl on **5.18a** (Figure 5.6a,c). Moreover, the titration of acetoxy **5.20** in concentrated hydrochloric acid solutions suggests that the carboxylic acid ground-state pK_a is -0.68 or perhaps even more negative because a titration end-point was not reached at the acidic regime where a hydrochloric acid concentration of 10 M was reached. However, it is feasible that the acetoxy group was hydrolyzed during the titration due to the extremely acidic conditions; studies to conclude the stability of the acetoxy group during the titration remain ongoing. The carboxylic acid on **5.20** is more acidic than that of trifluoroacetic acid (pK_a -0.25), which reflects the electron-withdrawing nature of the conjugated picolinium moieties and further supports that the idea that this carboxylic acid is very deactivated and unreactive towards standard coupling chemistries.

The electronic absorption spectrum of free hydroxyl photoacid, **5.18a**, was monitored during the titration of aqueous solution from pH 2 to 10 and the data (Figure 5.6b,d) suggests the hydroxyl ground-state pK_a is 5.2, which similar to the ester variant, **5.10**, that was reported to have a hydroxyl ground-state pK_a of 5.5.[254] Little to no change in the hydroxyl pK_a of **5.18a** and **5.10** was expected because esters and carboxylic acid have very similar electron withdrawing ability. An isosbestic point was not maintained due to changes in the solubility of the photoacid; slight precipitation occurred at pH values less than 5.

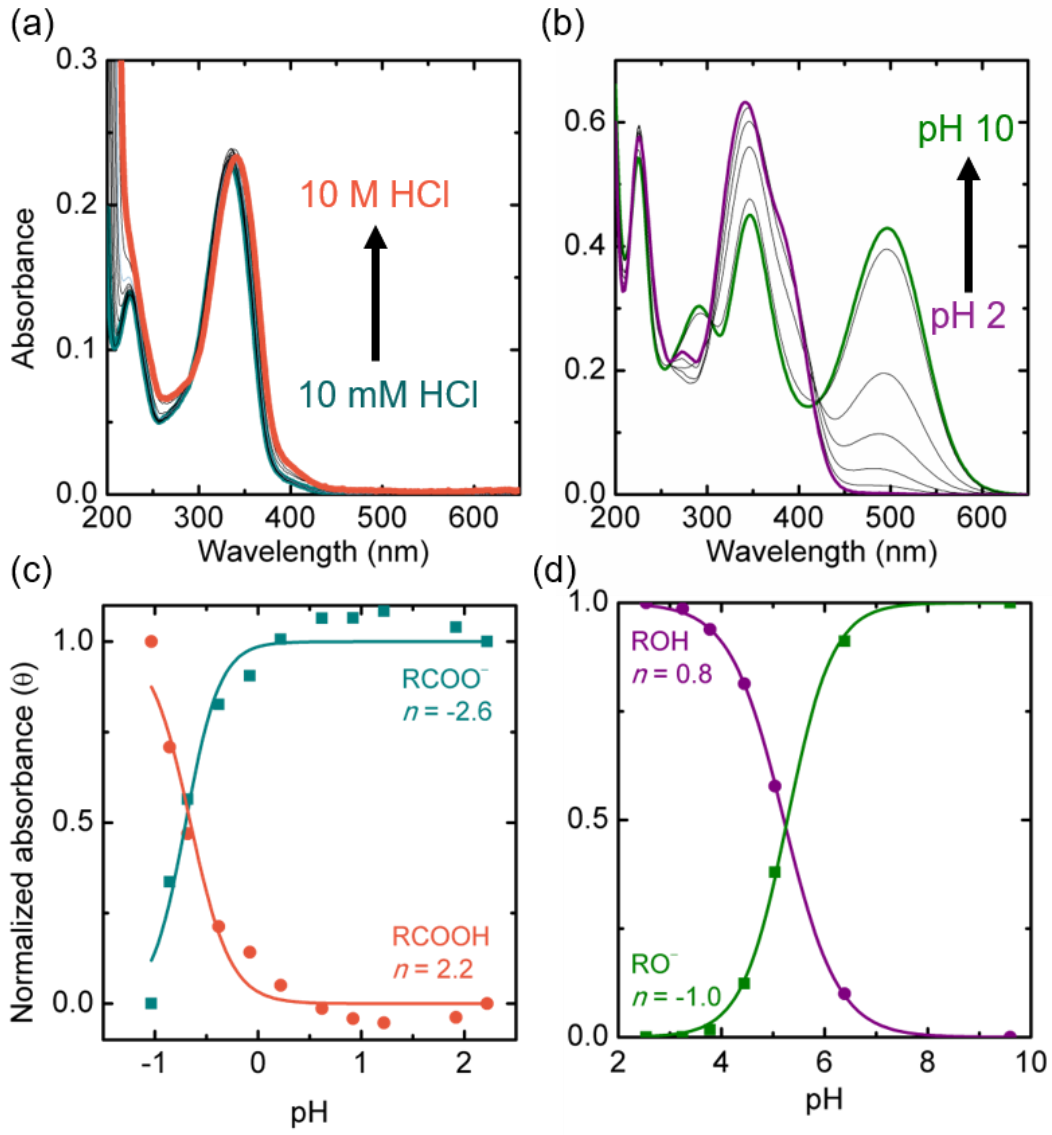

Figure 5.6. Electronic absorption spectra of quinone cyanine 9 derivatives titrated in solution. Panel a and c correspond to **5.20** and panel b and d correspond to **5.18a**.

Primary amine, quinone cyanine 9 derivative, **5.19a**, was bound to Nafion sulfonyl fluoride membranes. The Förster cycle analysis (Equation 2.2) was employed to approximate the ΔpK_a of **5.19a** bound to the film. Because the unbound ester variant **5.10** was reported to have a pK_a^* of -8.5,[254] it was hypothesized that evoking emission from only

ROH* (necessary for the calculation of v_{ROH}) would require stock solutions of concentrated acids. Therefore, ROH* emission was recorded from the film being immersed in 12 M hydrochloric acid and 18 M sulfuric acid; however, the emission spectra were different in the two stock solutions of acid, thus using these two different emission plots, two v_{ROH} numbers were calculated, and consequently, two ΔpK_a were calculated (Figure 5.7). When the film was immersed in 12 M hydrochloric acid and 18 M sulfuric acid, the ΔpK_a of **5.19a** bound to the film was determined to be -9.8 and -12.2, respectively (Equation 2.2, Figure 5.7). If the photoacid retains a hydroxyl ground-state pK_a that is similar to quinone cyanine 9 derivatives dissolved in solution ($pK_a \sim 5$) then the pK_a^* would be approximately -5 to -7. Further characterization studies of the quinone cyanine photoacid in solution and quinone cyanine photoacid modified ion-exchange films are underway.

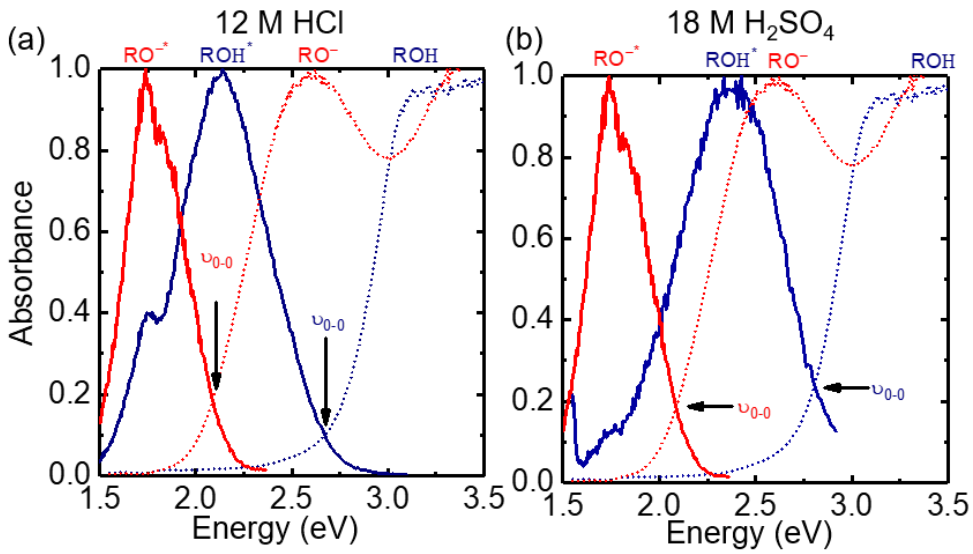

Figure 5.7. Normalized absorbance (dotted) and photoluminescence intensity (solid) spectra used to determine the energy of the 0-0 electronic transitions of **5.19a** bound to **PMSB** (a) immersed in 12 M HCl (2.09 eV and 2.67 eV) and (b) immersed in 18 M H_2SO_4 (2.09 eV and 2.81 eV).

Chapter 5.5. Ancillary dyes capable of photo-induced proton dissociation or association.

The following two sections include the synthesis of long-lived photoacids and photobases. These dye molecules are inspired by related work by Bakker[46] and have the ability to generate charge carriers from absorbing sunlight energy.

Chapter 5.5.1. The synthesis of long-lived photoacids.

Long-lived photoacids undergo cis-trans isomerization in their excited-state. In the process the photoacid changes from a weak acid to a strong acid. Using conjugated indolinium-phenol moieties, the photoacid not only releases a proton, but an intramolecular bond is formed from the alcohol and nitrogen. These closed rings have a half-life of ~70 seconds and lose their visible-light absorption bands due to the disruption of the conjugation (Figure 5.8).

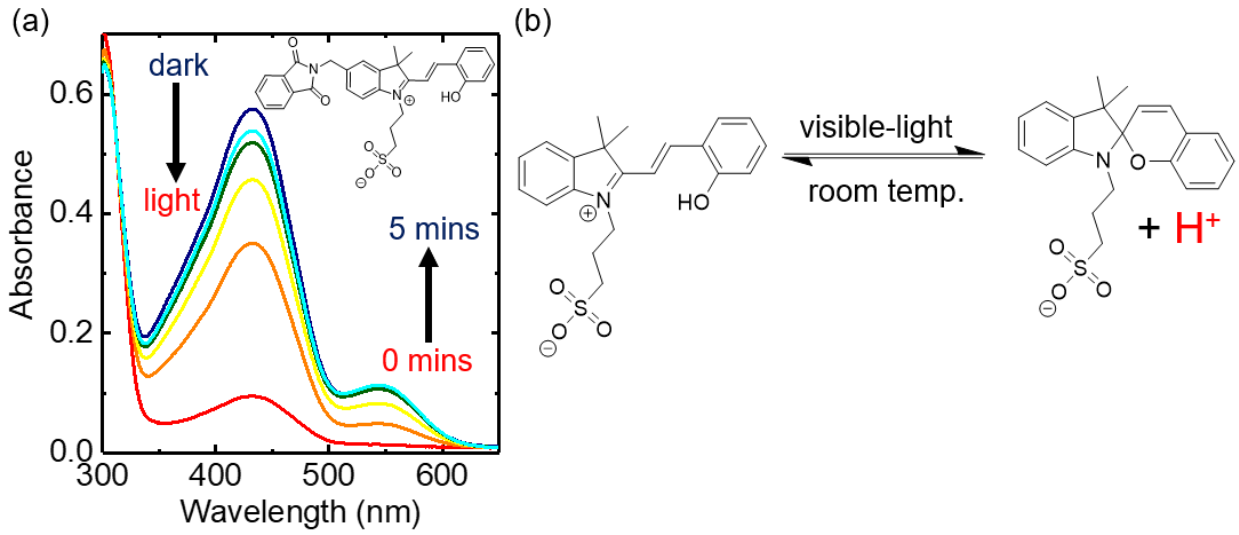

Figure 5.8. (a) Electronic absorption spectra of long-lived photoacid fist in the dark, and then illuminated, and monitored for five minutes. (b) Reversibility of long-lived photoacids.

The synthesis of the long-lived photoacid **5.24** was achieved by treating indoline **5.**22 with sultone and then condensing the indolinium **5.23** with commercially bought salicylaldehyde (Scheme 5.5).[258]

Scheme 5.5. Long-lived photoacid synthesis via condensation.

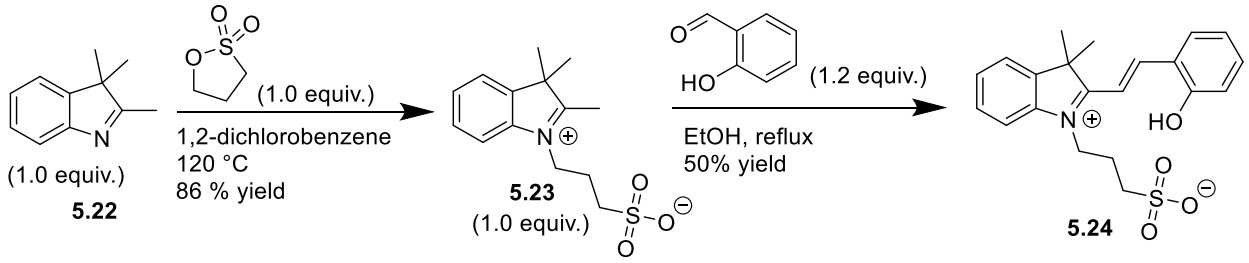

The indolinium **5.28** was the first long-lived photoacid target with a pendant amine. Indolenine **5.22** was stirred with the amine precursor, *N*-(hydroxymethyl)-phthalimide in concentrated sulfuric acid. The product **5.25** was isolated via basification and then treated

with sultone to form the zwitterion, **5.26.** The salicylaldehyde was condensed with the indolinium to the phthalimide photoacid **5.27**. Removal of the phthalimide protecting group was not trivial. It was found that **5.27** degrades in the conditions needed to remove the phthalimide group. Returning to the more inert **5.25**, the phthalimide group was removed to form the primary amine **5.29**. Studies suggest that **5.29** can be treated with the aldehyde under high heat to selectively bind through the activated carbon instead of the primary amine. However, success was not found with that route. Using the same strategy, **5.22** can be nitrated into **5.30**, then reduced to form the primary amine, and the aldehyde selectively condensed with the carbon at high heat. This route was avoided because a method to the asymmetrically formylated phenol **5.11** was realized.

Scheme 5.6. Initial attempts to fasten linker to long-lived photoacid.

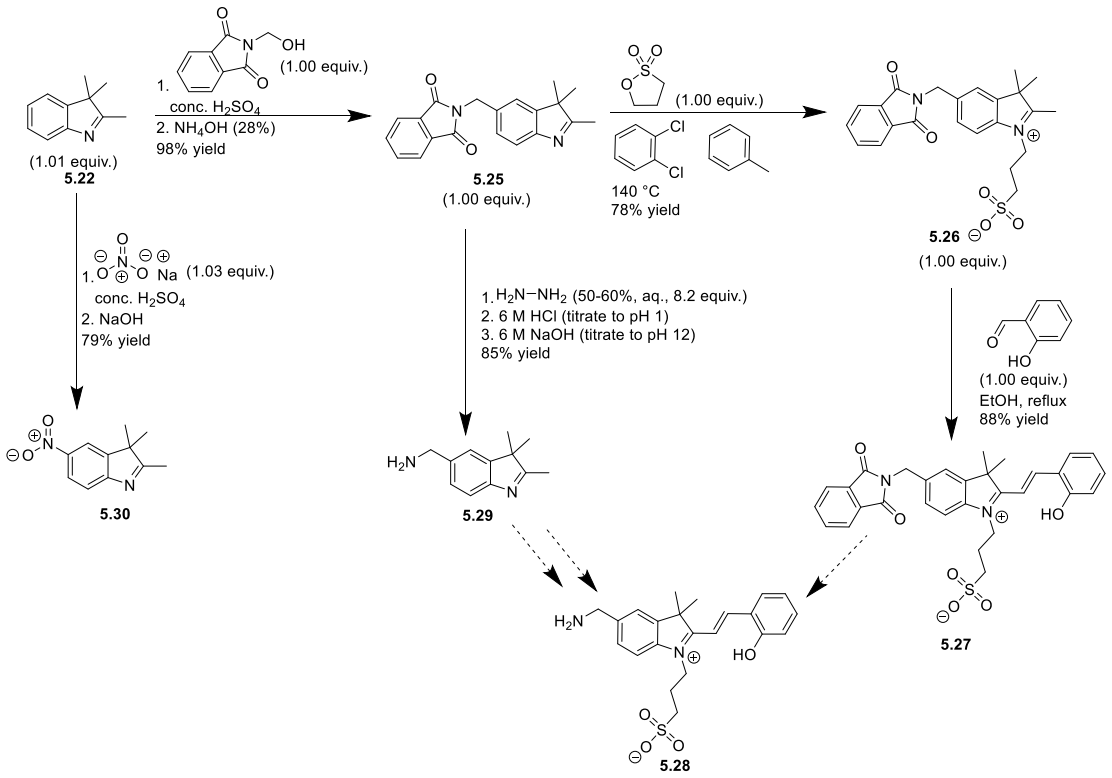

The Duff reaction needed three days to convert the **5.12** to the bis(formyl) **5.13** when the reaction was stirred less than one day, the exclusive mono(formyl) **5.31** was isolated. The mono(formyl) **5.31** was condensed with indolinium **5.23** in the typical fashion to isolate photoacid **5.32**. The studies to form **5.33** are ongoing. The carboxylic acid is slightly deactivated by the conjugated indolinium, but not as drastically as the two-acceptor **5.19** photoacid. Therefore, standard coupling reactions are being implemented to form the amide. The mono(formyl) **5.31** could also be condensed with a picolinium such as **5.15** to form the super photoacid, phenol benzoate cyanine picolinium salt **5.34**; these studies are also ongoing.

Scheme 5.7. Route of choice synthesizing asymmetric photoacids.

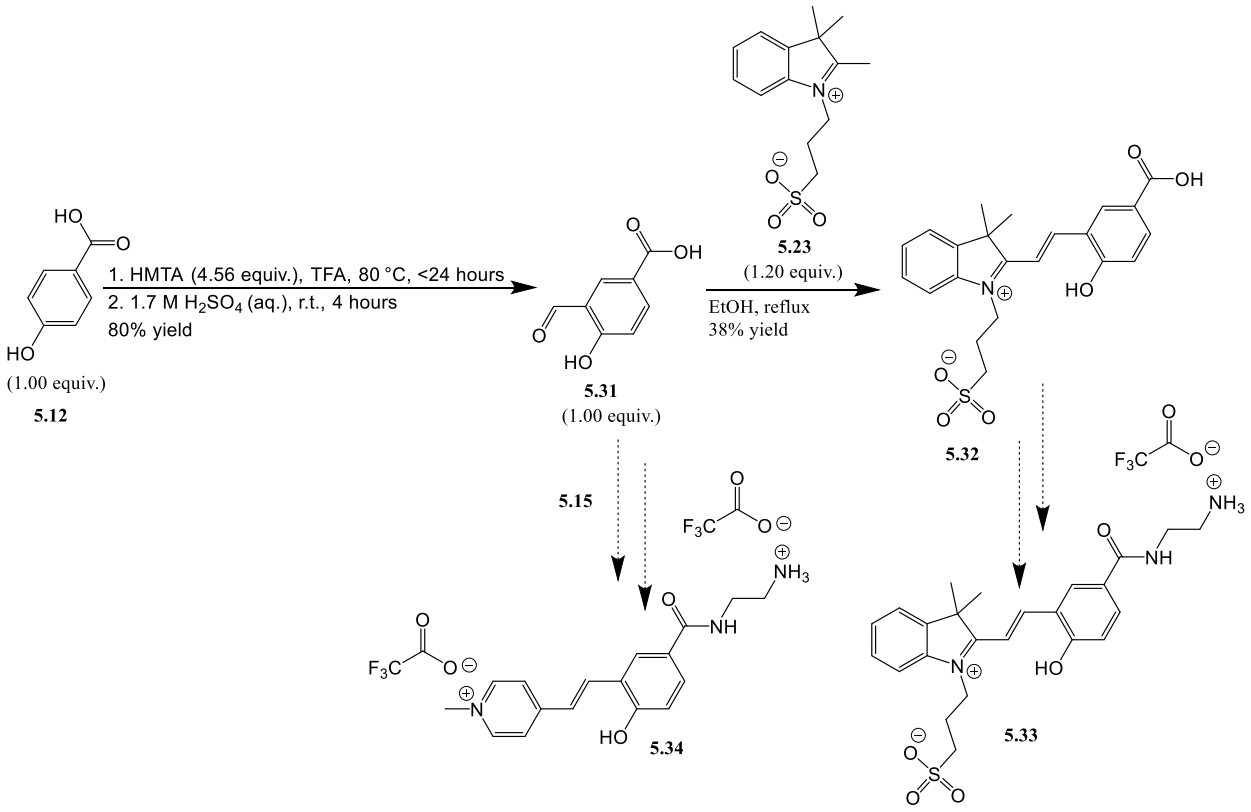

Chapter 5.5.2. The synthesis of photobases.

Photobases become more basic in their excited-state. The pK_a of unsubstituted acridine is 5.4 but photoexcitation results in a pK_a^* of 10.6.[114] The presented synthesis of the tri-substituted acridine **5.39** begins with the extremely slow addition of bis(aryl)amine **5.35** to a refluxing solution of oxalyl chloride. The slow addition ensures that the acid chloride intermediate of **5.35** do not crosslink with another molecule of **5.35.** The addition of aluminum trichloride catalyzes ring closure to the dione **5.37**. The dione was treated with alkaline conditions to aromatize the rings to the acridine core. Then the carboxylic acid **5.38** was activated with thionyl chloride and coupled to *N*-Boc-1,2,-diaminoethane. The Boc protecting group of **5.39** was removed to yield the primary ammonium group. Characterization of the photobase in solution and incorporated into ion-exchange membranes is ongoing.

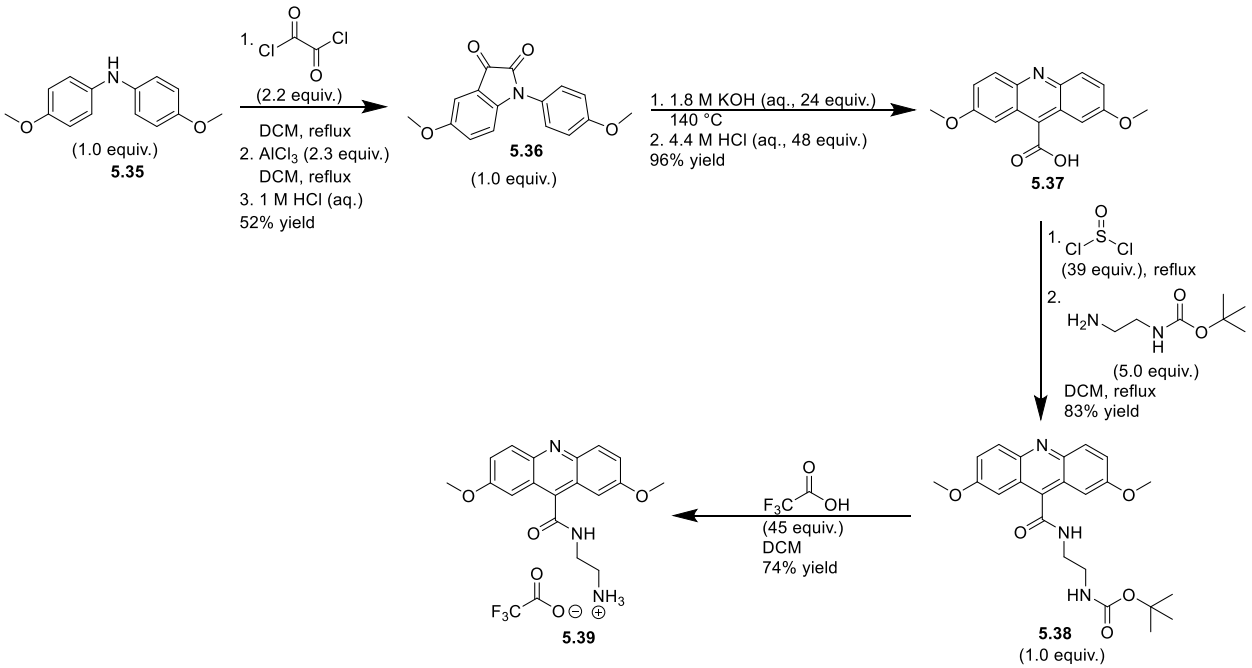

Chapter 5.6. Experimental.

***tert*-butyl (6-((3,6-bis(N-(6-((tert-butoxycarbonyl)amino)hexyl)sulfamoyl)-8-hydroxypyrene)-1-sulfonamido)hexyl)carbamate (5.1a).** *N*-boc-1,6-hexanediamine (1.05 g, 4.855 mmol, 6.15 equiv.) was added to a solution of tetrahydrofuran (25 mL), acetonitrile (10 mL), and *N*,*N*-diisopropylethylamine (870 μL, 4.99 mmol, 6.34 equiv.). While stirring, pyrene sulfonyl chloride **2.1b** (2.184 g, 3.938 mmol) was added. The resulting red solution was stirred for 64 hours at room temperature. Consequently, 1 M NaOH (30 mL) was added to the flask and shook vigorously, and stirred for 30 minutes. The dye was washed with dichloromethane (150 mL × 4), hexanes (100 mL × 3), and chloroform (100 mL × 3). The separated aqueous solution was added to a beaker containing ice water and a stir bar. Concentrated hydrochloric acid was added to ice (50%:50% volume), and used to titrate the aqueous dye solution to pH 1. The dye was extracted with ethyl acetate and the solution was concentrated under vacuum to obtain a yellow powder (0.227 g, 0.216 mmol, 27% yield). ^{1}H NMR (500 MHz, CD_3CN) δ 9.81 (broad, 1H), 9.20 (coalescing, 2H), 9.02 (d, 1H), 8.97 (d, 1H), 8.74 (d, 1H), 8.42 (s, 1H), 6.38 (t, 1H), 6.33 (t, 1H), 6.29 (b, 1H), 5.26 (t, 1H), 5.21 (t, 1H), 5.18 (t, 1H), 2.86 (m, 6H), 2.73 (m, 6H), 1.33 (coalescing, 27H), 1.22 (m, 6H), 1.06 (m, 6H), 0.97 (m, 6H), 0.90 (m, 6H).

6,6',6''-((8-hydroxypyrene-1,3,6-trisulfonyl)tris(azanediyl))tris(hexan-1-aminium) tris(trifluoroacetate) (5.1). Carbamate **5.1a** (0.227 g, 0.216 mmol) was dissolved in dichloromethane (10 mL) and added to a stirring solution of trifluoroacetic acid (10 mL)

and dichloromethane (10 mL) chilled on ice. The solution was stirred for 1.5 hours and then concentrated under vacuum. Dichloromethane was added and used to co-distill (under vacuum) the residual trifluoroacetic acid which remained until a yellow powder formed. the powder was purified via RP-HPLC. For injection purposes, the powder was dissolved in 3 mL of 20% acetonitrile in water (0.1% trifluoracetic acid). The eluent was ramped from % 5 acetonitrile in water (0.1% trifluoracetic acid) to 90% acetonitrile in water (0.1% trifluoracetic acid) over 30 minutes, and pumped at a rate of 15 mL per minute. The dye was collected from 34% to 41% acetonitrile in water (0.1% trifluoracetic acid). The combined fractions were concentrated under vacuum, and a yellow powder was obtained (0.182 g, 0.167 mmol, 77% yield). ^{1}H NMR (500 MHz, DMSO-d_6) δ 9.17 (d, 1H), 9.10 (s, 1H), 9.02 (d, 1H), 8.91 (d, 1H), 8.78 (d, 1H), 8.32 (coalescing, 4H), 7.64 (broad, 9H), 2.84 (m, 6H), 2.67 (m, 6H), 1.36 (coalescing, 12H), 1.15 (coalescing, 12H).

8-aminopyrene-1,3,6-trisulfonate (5.11). Procedures from Singaram were slightly modified.[259] Sodium sulfate (2.60 g, 18.3 mmol, 3.90 equiv.) and concentrated sulfuric acid (12 mL) were added to a dry RBF. The green fluffy buds of 1-aminopyrene (1.02 g, 4.70 mmol, 1.00 equiv.) were stirred into the solution, and then fuming sulfuric acid (26%, 13 mL) was added. The RBF was then equipped with a drying tube charged with Drierite and sodium hydroxide. The solution was brought to 60 °C and stirred for 30 hours. The mixture was carefully poured into ice (100 g) and neutralized with a chilled solution of sodium hydroxide (31.0 g) in water (30 mL) to pH 7. The solution was concentrated under vacuum and extracted with methanol; sonication was used to assist the extraction process. The methanol was concentrated under vacuum to yield a brown powder. The powder was

purified via RP-HPLC. For injection purposes, the brown powder was dissolved in water (12 mL, 0.1% trifluoracetic acid), and divided into 3 equal parts for 3 separate RP-HPLC runs. The eluent was kept at 5% acetonitrile in water (0.1% trifluoracetic acid) for 20 minutes, allowing the dye to be isolated. Impurities were flushed out of the RP-HPLC by ramping the eluent to 90% acetonitrile in water (0.1% trifluoracetic acid) for 20 minutes. ^{1}H NMR (400 MHz, CH_3OD, freebase) δ 9.08 (s,1H), 8.95 (d, 1H), 8.84 (d, 1H), 8.72 (d, 1H), 8.20 (d, 1H), 7.97 (s, 1H).

1 3,5-diformyl-4-hydroxybenzoic acid (5.13). The general procedure developed by Shabat and coworkers was modified.[256] Hexamethylenetetramine (65.0 g, 464 mmol, 4.23 equiv.) and 4-hydroxybenzoic acid (15.1 g, 110 mmol, 1.00 equiv.) were dissolved in trifluoroacetic acid (120 mL, 500 mL RBF). The solution was stirred for 96 hours at 80 °C. An aqueous acid solution (10 mL of concentrated sulfuric acid added to 100 mL of water) was added to flask. The reaction was kept at 80 °C and stirred for 4 hours. A yellow powder was collected by vacuum filtration, rinsed with methanol (75 mL × 3), and dried under reduced pressure (14.7 g, 75.5 mmol, 69% yield). ^{1}H NMR (500 MHz, DMSO-d_6) δ 10.29 (s, 2H), 8.54 (s,2H).

1,4-dimethylpyridin-1-ium iodide (5.15). Iodomethane (3.5 mL, 56 mmol, 1.1 equiv.) was added to a stirring solution of 4-picoline (4.9 mL, 50 mmol, 1.0 equiv.) in toluene (40 mL). The reaction temperature was set to 120 °C and refluxed for 18 hours. The solution was cooled to room temperature and the precipitate was collected by vacuum filtration. The solid was washed with ether and recrystallized in ethanol. White needles were

collected via vacuum filtration and washed with ether. Residual product remained in the filtrate and was precipitate with further addition of ether and collected via vacuum filtration and washed with ether. Combined total product massed to 9.7 g (41 mmol, 82% yield). ^{1}H NMR (400 MHz, DMSO-d_6) δ 8.83 (d, 2H), 7.96 (d, 2H), 4.28 (s, 3H), 2.60 (s, 3H).

1,4-dimethylpyridin-1-ium-3-sulfonate (5.17). Procedures were adopted from the works of Webb and Corwin, and Shabat and coworkers.[256,260] Iodomethane (10.0 mL, 160 mmol, 11.0equiv) was added to a solution of 4-methylpyridine-3-sulfonic acid (2.52 g, 14.6 mmol, 1.00 equiv.) and DMF (30 mL). The solution was stirred at 90 °C for 48 hours and then allowed to cool to room temperature. Ethyl acetate (150 mL) was added to the solution to force precipitation. A beige solid was collect via vacuum filtration and washed with ethyl acetate (2.53 g, 13.5 mmol, 93% yield). ^{1}H NMR (500 MHz, DMSO-d_6) δ 9.03 (s, 1H), 8.78 (d, 1H), 7.95 (d, 1H), 4.29 (s, 3H), 2.78 (s, 3H).

4,4'-((1E,1'E)-(5-carboxy-2-hydroxy-1,3-phenylene)bis(ethene-2,1-diyl))bis(1-methylpyridin-1-ium) dichloride (5.18a). Procedures from Shabat and coworkers[256] were modified. Thoroughly dried (under vacuum) dialdehyde **5.13** (1.12 g, 5.78 mmol, 1.00 equiv.) and picolinium **5.15** (2.84 g, 12.1 mmol, 2.09 equiv.) were added to a dry RBF. Anhydrous, 200 proof ethanol (20 mL) was added and stirring was commenced. Piperidine (1.20 mL, 12.1 mmol, 2.10 equiv.) was added. After 18 hours, concentrated hydrochloric acid was added dropwise with stirring; the solution changes from purple to orange, and a suspension of precipitate appears. The precipitate was collected via vacuum filtration, and washed with slightly acidic ethanol and then slightly acidic methanol (approximately 10

drops of concentrated hydrochloric acid per 100 mL of solvent). The yellow powder was dried under reduced pressure (2.58 g, 5.78 mmol, quantitative yield). ^{1}H NMR (400 MHz, DMSO-d_6) δ 13.11 (broad, 1H), 11.16 (broad, 1H), 8.89 (d, 4H), 8.38 (s, 2H), 8.28 (coalescing, 6H), 7.61 (d, 2H), 4.28 (s, 6H).

4,4'-((1E,1'E)-(5-((2-ammonioethyl)carbamoyl)-2-hydroxy-1,3-phenylene)bis(ethene-2,1-diyl))bis(1-methylpyridin-1-ium) trifluoroacetate dichloride (5.19a). Procedures from Shabat and coworkers[257] were modified. Thoroughly dried (under vacuum) quinone cyanine dye **5.18a** (0.521 g, 1.17 mmol, 1.00 equiv.) was added to a dry RBF. Dimethylformamide (40 mL) was added and stirring coerced the starting material to dissolve partially. Addition of *N*-Boc-ethylenediamine (0.374 g, 2.33 mmol, 1.99 equiv.) swiftly turned the dark green solution to an indigo hue. Addition of *N*,*N*,*N*′,*N*′-tetramethyl-*O*-(1*H*-benzotriazol-1-yl)uronium hexafluorophosphate (0.848 g, 2.24 mmol, 1.91 equiv.) and TEA (130 μL, 0.933 mmol, 0.797 equiv.) turned the solution to a violet hue over an hour. After 105 minutes, additional *N*-Boc-ethylenediamine (0.897 g, 5.60 mmol, 4.78 equiv.) and *N*,*N*,*N*′,*N*′-tetramethyl-*O*-(1*H*-benzotriazol-1-yl)uronium hexafluorophosphate (0.865 g, 2.28 mmol, 1.95 equiv.) were introduced. Reaction was stirred for 255 additional minutes and then concentrated under vacuum. The viscous tar sat for 18 hours. Then dichloromethane (30 mL) and trifluoroacetic acid (20 mL) was added and the solution was stirred for 30 minutes. The solution was removed under vacuum. To remove residual trifluoroacetic acid, the product was co-distilled with dichloromethane under vacuum three times. The orange solid was washed with acidic ethanol (few drops of trifluoroacetic acid per 100 mL of ethanol) and collected via vacuum

filtration in a fritted funnel. The orange powder massed to 0.309 g (0.514 mmol, 44% yield). ^{1}H NMR (400 MHz, DMSO-d_6) δ 10.97 (broad, 1H), 8.86 (d, 4H), 8.75 (broad, 1H), 8.33 (s, 2H), 8.24 (coalescing, 6H), 7.86 (broad, 3H), 7.59 (d, 2H), 4.27 (s, 6H), 3.55 (q, 2H), 3.02 (t, 2H).

4,4'-((1E,1'E)-(5-carboxy-2-hydroxy-1,3-phenylene)bis(ethene-2,1-diyl))bis(1-methylpyridin-1-ium-3-sulfonate) (5.18b). Thoroughly dried (under vacuum) dialdehyde **5.13** (0.692 g, 3.57 mmol, 1.00 equiv.) and picolinium sulfonate **5.17** (1.36 g, 7.24 mmol, 2.03 equiv.) were added to a dry RBF. Anhydrous, 200 proof ethanol (20 mL) was added and stirring was commenced. Piperidine (0.75 mL, 7.59 mmol, 2.13 equiv.) was added. After 18 hours, concentrated hydrochloric acid was added dropwise with stirring; the solution changes from purple to orange, and a suspension of precipitate appears. The precipitate was collected via vacuum filtration, and washed with slightly acidic ethanol and then slightly acidic methanol (approximately 10 drops of concentrated hydrochloric acid per 100 mL of solvent). The yellow powder is dried under reduced pressure (1.78 g, 3.35 mmol,94% yield). ^{1}H NMR (400 MHz, DMSO-d_6) δ 11.27 (broad, 1H), 9.08 (s, 2H), 8.84 (d, 2H), 8.50 (d, 2H), 8.34 (d, 2H), 8.22 (s, 2H), 8.15 (d, 2H), 4.30 (s, 6H).

4,4'-((1E,1'E)-(5-((2-ammonioethyl)carbamoyl)-2-hydroxy-1,3-phenylene)bis(ethene-2,1-diyl))bis(1-methylpyridin-1-ium-3-sulfonate) trifluoroacetate (5.19b). Thoroughly dried (under vacuum) quinone cyanine dye **5.18b** (0.410 g, 0.769 mmol, 1.00 equiv.) was added to a dry RBF. Dimethylformamide (40 mL) was added and stirring coerced the starting material to dissolve partially. Addition of *N*-

Boc-ethylenediamine (0.275 g, 1.71 mmol, 2.22 equiv.) swiftly turned the dark green solution to an indigo hue. Addition of *N*,*N*,*N*′,*N*′-tetramethyl-*O*-(1*H*-benzotriazol-1-yl)uronium hexafluorophosphate (0.637 g, 1.68 mmol, 2.18 equiv.) and TEA (105 μL, 0.753 mmol, 0.979 equiv.) turned the solution to a violet hue over an hour. After 10 minutes, additional *N*-Boc-ethylenediamine (0.521 g, 3.25 mmol, 4.23 equiv.) and *N*,*N*,*N*′,*N*′-tetramethyl-*O*-(1*H*-benzotriazol-1-yl)uronium hexafluorophosphate (0.581 g, 1.52 mmol, 1.99 equiv.) were introduced. Reaction was stirred for 18 additional hours and then concentrated under vacuum. The viscous tar sat for 18 hours. Then dichloromethane (5 mL) and trifluoroacetic acid (15 mL) was added and the solution was stirred for 30 minutes, and concentrated under reduced vacuum. To remove residual trifluoroacetic acid, the product was co-distilled with dichloromethane under vacuum three times. The orange solid was collect via vacuum filtration and rinsed with acidic methanol (several drops of concentrated hydrochloric acid per 100 mL of methanol). The orange powder massed to 0.503 g (0.730 mmol, 95% yield).^{1}H NMR (400 MHz, DMSO-d_6) δ 10.98 (broad, 1H), 9.10 (s, 2H), 8.84 (coalescing, 3H), 8.47 (d, 2H), 8.26 (d, 2H), 8.12 (coalescing, 4H), 7.78 (broad, 3H), 4.31 (s, 6H), 3.54 (q, 2H), 3.02 (m, 2H).

4,4'-((1E,1'E)-(2-acetoxy-5-carboxy-1,3-phenylene)bis(ethene-2,1-diyl))bis(1-methylpyridin-1-ium) dichloride (5.21). Triethylamine was added (1.0 mL, 7.2 mmol, 4.3 equiv.) to a stirring solution of acetic anhydride (10.0 mL, 106 mmol, 63.1 equiv.) and thoroughly dried (under vacuum) quinone cyanine dye **5.18a** (0.747 g, 1.68 mmol, 1.00 equiv.). The reaction was stirred for 24 hours at room temperature. Dichloromethane (150 mL) was used to dilute the solution and forcing precipitation. The purple precipitate was

collected via vacuum filtration and washed with dichloromethane. Then the precipitate was dissolved with methanol and diluted hydrochloric acid was added until the purple solution turned orange. (0.775 g, 1.59 mmol, 95% yield). ^{1}H NMR (400 MHz, DMSO-d_6) δ 8.95 (d, 4H), 8.53 (s, 2H), 8.41 (d, 4H), 7.88 (d, 2H), 7.72 (d, 2H), 4.31 (s, 6H), 2.62 (s, 3H).

4,4'-((1E,1'E)-(2-acetoxy-5-((2-((tert-butoxycarbonyl)amino)ethyl)carbamoyl)-1,3-phenylene)bis(ethene-2,1-diyl))bis(1-methylpyridin-1-ium) dichloride (5.21). Oxalyl chloride (1.0 mL, 12 mmol, 7.3 equiv.) was added to the acetoxy quinone cyanine dye **5.20** (0.755 g, 1.59 mmol, 1.00 equiv.) in dichloromethane (10 mL). The reaction was concentrated under vacuum after 24 hours of stirring. The yellow solid was partially dissolved in acetonitrile (25 mL). Then *N*-Boc-ethylenediamine (0.255 g, 1.59 mmol, 1.00 equiv.) and triethylamine (429 μL, 3.08 mmol, 1.94 equiv.) was added; upon addition, the solution immediately turned dark green, but within an hour returned yellow. Byproduct was removed via vacuum filtration, and the filtrate was concentrated under vacuum to a brown tacky tar. Water was added to the brown tacky tar and vigorously shaken until a brown precipitate formed. The brown precipitate was collected via vacuum filtration (0.144 g, 0.23 mmol, 14% yield). ^{1}H NMR (500 MHz, DMSO-d_6) of impure sample δ 90-6.9 (~16H), 4.29 (s, 6H), 3.20-3.06 (4H), 2.58 (s, 3H), 1.36 (s, >9).

3-(2,3,3-trimethyl-3H-indol-1-ium-1-yl)propane-1-sulfonate (5.23). The procedure developed by Balasubramanian and coworkers was slightly modified.[138] Dichlorobenzene (25 mL) was dried with molecular sieves, and heated to 90 °C. Without removing the molecular sieves, 2,3,3-trimethylindolenine (1.66 mL, 10.3 mmol, 1.00 equiv.) was added

while stirring. A stock bottle of 1,3-propane sultone was brought to 40 °C such that the solid melted (b.p. = 31 °C) and 0.91 mL (10.4 mmol, 1.00 equiv.) of warmed, liquid 1,3-propane sultone was added to the 2,3,3-trimethylindolenine solution. The reaction was stirred at 90 °C for 24 hours. The molecular sieves were removed by vacuum filtration and washed with ethanol. Ether was added to the ethanol filtrate to precipitate a purple solid. The purple solid was isolated via vacuum filtration. The solid was too tacky to remove from the filter paper and so the solid was dissolved with ethanol and concentrated under vacuum (2.506 g, 8.906 mmol, 86% yield). The crude product was used without purification and thus the anomalies in the NMR were due to the impurities. ^{1}H NMR (400 MHz, CH_3OD) δ 7.95 (complex, 1H), 7.72 (complex, 1H), 7.60 (complex, 2H), 4.71 (t, 2H), 3.30 (s, 2H, should be 3H), 2.97 (t, 2H), 2.33 (p, 2H), 1.57 (s, 6H).

(E)-3-(2-(2-hydroxystyryl)-3,3-dimethyl-3H-indol-1-ium-1-yl)propane-1-sulfonate (5.24). Followed Liao and coworkers procedures with slight modifications.[258] Salicyclaldehyde (0.15 mL, 1.4 mmol, 1.2 equiv.) was added to a stirring solution of crude indolinium (**5.23**, 0.3308 g, 2.28 mmol, 1.00 equiv.) and anhydrous ethanol (10 mL, 200 proof). The reaction was refluxed for 24 hours. An orange solid was collected via vacuum filtration and rinsed with ethanol and dichloromethane (0.227 g, 0.588 mmol, 50% yield). ^{1}H NMR (400 MHz, DMSO-d_6) δ 11.03 (s, 1H), 8.60 (d, 1H), 8.28 (d, 1H), 8.02 (d, 1H), 7.87 (m, 2H), 7.62 (m, 2H), 7.48 (t, 2H), 7.03 (d, 1H), 6.99 (t,1H), 4.81 (t,2H), 2.65 (t,2H), 2.18 (p, 2H), 1.77 (s, 6H).

2-((2,3,3-trimethyl-3H-indol-5-yl)methyl)isoindoline-1,3-dione (5.25). The procedure developed by Waggoner and Mujumdar was slightly modified.[261] The *N*-(hydroxymethyl)phthalimide (9.31 g, 52.6 mmol, 1.00 equiv.) solid was added to 2,3,3-trimethylindolenine (9.38 mL, 58.4 mmol, 1.11 equiv.) stirring in concentrated sulfuric acid (50 mL). The reaction was stirred for 72 hours at room temperature, and then poured into a 600 mL beaker containing 200 mL of ice. With rapid stirring, ammonium hydroxide (28%, ~300 mL) was slowly added to force precipitation. The orange solid was collected via vacuum filtration, and washed with water (16.4 g, 51.5 mmol, 98% yield). ^{1}H NMR (500 MHz, DMSO-d_6) δ 7.90 (coalescing, 2H), 7.85 (coalescing, 2H), 7.38 (s, 1H), 7.35 (d, 1H), 7.19 (d, 1H), 4.78 (s, 2H), 2.18 (s, 3H), 1.21 (s, 6H).

3-(5-((1,3-dioxoisoindolin-2-yl)methyl)-2,3,3-trimethyl-3H-indol-1-ium-1-yl)propane-1-sulfonate (5.26). Pre-dried indolenine **5.25** (15.0 g, 47.2 mmol, 1.00 equiv.) was added to a mixture of 1,2-dichlorobenzene (3 mL) and toluene (75 mL) in a pre-dried RBF. The RBF was equipped with a Dean-Stark trap and the reaction was heated at 106 °C for an hour. A heat gun was used to evaporate water from the sides of the RBF into the trap. With oven gloves, the Dean-Stark trap was removed. Then 1,3-propane sultone (5.77 g, 47.2 mmol, 1.00 equiv.) was added to the hot, stirring solution and the RBF was equipped with a pre-dried reflux condenser. The temperature was brought to 140 °C and stirred for 53 hours. A precipitate had formed, which was collect via vacuum filtration and washed with toluene. The powder was purified by a pseudo-recrystallization. The powder was dissolved in a minute amount of methanol and then precipitated out with the addition of ethanol. The pink powder was collected via vacuum filtration (16.1 g, 36.6 mmol, 78%

yield). ^{1}H NMR (500 MHz, DMSO-d_6) δ 8.00 (d, 1H), 7.92 (coalescing, 2H), 7.86 (coalescing, 2H), 7.78 (s, 1H), 7.56 (d, 1H), 4.89 (s, 2H), 4.63 (t, 2H), 2.80 (s, 3H), 2.60 (t, 2H), 2.13 (p, 2H), 1.50 (s, 6H).

(E)-3-(5-((1,3-dioxoisoindolin-2-yl)methyl)-2-(2-hydroxystyryl)-3,3-dimethyl-3H-indol-1-ium-1-yl)propane-1-sulfonate (5.27). Salicylaldehyde (1.12 g, 9.20 mmol, 1.00 equiv.) was added to dry indolenine **5.26** (4.04 g, 9.17 mmol, 1.00 equiv.) in anhydrous ethanol. The solution was refluxed for 16 hours and then concentrated under vacuum with the heat. The powder was redissolved in methanol, and precipitated with the addition of ether. The orange powder was collected via vacuum filtration, and washed with ether (4.40 g, 8.08 mmol, 88% yield). ^{1}H NMR (500 MHz, DMSO-d_6) δ 11.00 (s, 1H), 8.57 (d, 1H), 8.27 (d, 1H), 7.96 (d, 1H), 7.92 (coalescing, 2H), 7.85 (coalescing, 4H), 7.56 (d, 1H), 7.46 (t, 1H), 7.02 (d, 1H), 6.97 (t, 1H), 4.91 (s, 2H), 4.78 (t, 2H), 2.63 (t, 2H), 2.16 (p, 2H), 1.74 (s, 6H).

(2,3,3-trimethyl-3H-indol-5-yl)methanamine (5.29). The procedure developed by Waggoner and Mujumdar was slightly modified.[261] Hydrazine (50-60% in water, ~900 mmol, ~8 equiv.) was added to a suspension of phthalimide **5.25** (34.1 g, 107 mmol, 1.00 equiv.) in methanol (200 mL). The solution was stirred for 22 hours and then titrated to pH 1 with aqueous 6 M hydrochloric acid. The solution was concentrated under vacuum, redissolved in aqueous 1 M hydrochloric acid, and filtered through celite. The filtrate was washed with dichloromethane (50 mL ×4), titrated to pH 12 with aqueous 6 M NaOH, and extracted with dichloromethane (50 mL ×4). The combined organic layers were concentrated under vacuum to a yellow oil (17.1 g, 80.6 mmol, 85% yield). ^{1}H NMR (500

MHz, DMSO-d_6) δ 7.28 (s, 1H), 7.24 (d, 1H), 7.23 (d, 1H), 3.75 (s, 2H), 2.20 (s, 3H), 1.24 (s, 6H).

2,3,3-trimethyl-5-nitro-3H-indole (5.30). The procedure developed by Vincent and coworkers was slightly modified.[262] The liquid, 2,3,3-trimethylindolenine (1.20 mL, 7.48 mmol, 1.00 equiv.) was diluted in concentrated sulfuric acid (50 mL), and chilled on ice to < 5 °C. A separate solution of sodium nitrate (0.655 g, 7.71 mmol, 1.03 equiv.) was dissolved in concentrated sulfuric acid (50 mL), and chilled on ice to < 5 °C. The indolenine solution was slowly added to the stirring solution of sodium nitrate. The solution was stirred for one hour at < 5 °C. Ice (200 mL) was added directly to the solution. Then water (100 mL) was added. Sodium hydroxide pellets were added to the solution until full precipitation of the product occurred. An orange powder was collected via vacuum filtration and washed with water. The product was further purified by dissolving the powder in ethyl acetate and washing with water. The ethyl acetate was concentrated under vacuum and an orange powder formed (1.21 g, 5.94 mmol, 79% yield). ^{1}H NMR (500 MHz, $CDCl_3$) δ 8.27 (dd, 1H), 8.17 (d, 1H), 7.65 (d, 1H), 2.39 (s, 3H), 1.39 (s, 6H).

3-formyl-4-hydroxybenzoic acid (5.31). Hexamethylenetetramine (25.4 g, 181 mmol, 4.56 equiv.) and 4-hydroxybenzoic acid (5.49 g, 39.7 mmol, 1.00 equiv.) were dissolved in trifluoroacetic acid (40 mL, 500 mL RBF). The solution was stirred for 23 hours at 80 °C and then allowed to cool. An aqueous acid solution (10 mL of concentrated sulfuric acid added to 100 mL of water) was added to flask, and the solution was stirred for an additional 4 hours. A yellow powder was collected by vacuum filtration, rinsed with water

(100 mL × 2) and methanol (75 mL × 3), and dried under reduced pressure (5.28 g, 31.8 mmol, 80% yield). ^{1}H NMR (500 MHz, DMSO-d_6) δ 12.73 (broad, 1H), 111.47 (s, 1H), 10.29 (s, 1H), 8.23 (s, 1H), 8.04 (d, 1H), 7.08 (dd, 1H).

(E)-3-(2-(5-carboxy-2-hydroxystyryl)-3,3-dimethyl-3H-indol-1-ium-1-yl)propane-1-sulfonate (5.32). Aldehyde **5.31** (1.55 g, 9.33 mmol, 1.00 equiv.) was added to a stirring solution of crude indolinium (**5.23**, 0.3.15 g, 11.2 mmol, 1.20 equiv.) and anhydrous ethanol (10 mL, 200 proof). The reaction was refluxed for 24 hours. An orange solid was collected via vacuum filtration and rinsed with ethanol (1.50 g, 3.50 mmol, 38% yield). ^{1}H NMR (500 MHz, DMSO-d_6) of a sample too concentrated prevented resolution of splitting patterns δ 12.85 (broad, 1H), 11.99 (broad, 1H), 8.68 (s, 1H), 8.54 (d, 1H), 8.20-7.82 (coalescing, 4H), 7.64 (2H), 7.13 (1H), 4.80 (2H), 2.64 (2H), 2.20 (2H), 1.80 (s, 6H).

5-methoxy-1-(4-methoxyphenyl)indoline-2,3-dione (5.36). Procedure was adopted from Weeks and coworkers.[263] Oxalyl chloride (2.7 mL, 31.5 mmol, 2.24 equiv.) was added to dichloromethane (70 mL) contained in a RBF. The RBF was then equipped with a stir bar, Claisen adaptor, reflux condenser, and addition funnel. Bis(4-methoxyphenyl)amine (3.22 g, 14.1 mmol, 1.00 equiv.) was dissolved in dichloromethane (40 mL) and placed into the addition funnel. The oxalyl chloride solution was refluxed with vigorous stirring, and the diluted bis(4-methoxyphenyl)amine solution was added dropwise at a rate of ~1 drop per 3 seconds such that the addition was complete after ~40 minutes. The solution was stirred at reflux for an additional 1.5 hours. The solution was concentrated under vacuum to remove the excess oxalyl chloride, and then redissolved in dichloromethane (100 mL). With stirring, anhydrous aluminum trichloride (4.34 g, 32.5 mmol, 2.31 equiv.) was added

portion-wise over 10 minutes. The solution was refluxed for 1.5 hours, and then concentrated under vacuum to a brown powder. Addition of aqueous, 1 M hydrochloric acid (100 mL) was used to decompose and dissolve aluminum species; the brick-red solution was stirred for 50 minutes. Dichloromethane (30 mL × 3) was used to extract the compound. The organic extracts were combined and concentrated under vacuum. The brown powder was purified via column chromatography (eluted with dichloromethane, and then with mixtures of dichloromethane and increasing volumes of acetonitrile). Combined fractions were concentrated under vacuum and a brown powder solid was isolated (2.081 g, 7.35 mmol, 52% yield). ^{1}H NMR (500 MHz, $CDCl_3$) δ 7.30 (dt, 2H), 7.18 (d, 1H), 7.06 (dd, 1H), 7.03 (dt, 2H), 6.75 (d, 1H), 3.84 (s, 3H), 3.80 (s, 3H).

2,7-dimethoxyacridine-9-carboxylic acid (5.37). Procedure was adopted from Weeks and coworkers.[263] Potassium hydroxide (10.0 g, 178 mmol, 24.3 equiv.) was dissolved in water (100 mL) and added to isatin **5.36** (2.081 g, 7.35 mmol, 1.00 equiv.), brought to 140 °C, and then stirred for 80 hours. Concentrated hydrochloric acid (30.0 mL, 350 mmol, 47.6 equiv.) was added to ice (50 g); the chilled acid solution was added slowly isatin solution to coerce precipitate of a chartreuse yellow powder. The powder was collected via vacuum filtration, washed with water, and then washed with dichloromethane (2.00 g, 7.05 mmol, 96% yield). ^{1}H NMR (400 MHz, DMSO-d_6) δ 8.09 (d, 2H), 7.51 (d, 2H), 7.23 (s, 2H), 3.94 (s, 6H).

2-(2,7-dimethoxyacridine-9-carboxamido)ethan-1-aminium trifluoroacetate (5.38). Carboxylic acid **5.37** (0.994 g, 3.51 mmol, 1.00 equiv.) was dried in an oven set to 110 °C

for 24 hours, and then dried under high vacuum for 2 hours. Anhydrous thionyl chloride (10.0 mL, 138 mmol, 39.3 equiv.) was cannula-transferred to the dry carboxylic acid, refluxed for 5.5 hours, and then concentrated under vacuum to remove residual thionyl chloride. The remaining solid was dissolved dichloromethane (20 mL), and a solution of *N*-Boc-ethylenediamine (2.8 g, 17 mmol, 5.0 equiv.) in dichloromethane (5 mL) was added. The solution was refluxed for 18 hours, and then allowed to cool to room temperature. The *N*-Boc-ethylenediamine salt was removed via vacuum filtration, and the dichloromethane filtrate was washed with water (100 mL × 3). The dichloromethane was concentrated under vacuum, and resulted in the formation of a yellow solid (1.24 g, 2.92 mmol, 83% yield). ^{1}H NMR (500 MHz, $CDCl_3$) δ 7.85 (d, 2H), 7.22 (d, 2H), 7.09 (s, 2H), 5.47 (broad, 1H), 3.97 (s, 3H), 3.92 (t, 2H), 3.63 (t, 2H), 1.38 (s, 9H).

2-(2,7-dimethoxyacridine-9-carboxamido)ethan-1-aminium trifluoroacetate (5.39). Trifluoroacetic acid (10.0 mL, 131 mmol, 44.8 equiv.) was added to a suspension of carbamate **5.38** (1.241 g, 2.92 mmol, 1.00 equiv.) in dichloromethane (80 mL). The solution was stirred at room temperature for 2 hours, and then concentrated under vacuum. Dichloromethane and then methanol was used to co-distill (under vacuum) residual acid. A yellow powder was obtained (0.952 g, 2.17 mmol, 74% yield). ^{1}H NMR (500 MHz, DMSO-d_6) δ 9.07 (s, 1H), 8.09 (d, 2H), 8.02 (broad, 3H), 7.53 (d, 2H), 7.13 (s, 2H), 3.94 (s, 6H), 3.77 (broad, 2H), 3.17 (broad, 2H).

4-acetamidophenyl acetate. Triethylamine (20.0 mL, 143 mmol, 1.31 equiv.) was added to 4-aminophenol (8.23 g, 109 mmol, 1.00 equiv.). Acetic anhydride (30.0 mL, 317 mmol,

2.91 equiv.) was added slowly to the stirring solution. After the vigorous bubbling seized, the reaction was heated to 80 °C. The reaction was stirred for 48 hours, cooled, and diluted with water (300 mL). Solid was collected via vacuum filtration and washed with water. Solid resembles coarse beach sand (13.8 g, 71.3 mmol, 65% yield). ^{1}H NMR (400 MHz, DMSO-d_6) δ 9.97 (s, 2H), 7.58 (d, 2H), 7.03 (d, 2H), 2.24 (s, 3H), 2.03 (s, 3H).

Conclusion.

This Thesis showed the seminal work towards the development of new technologies for ionic power generation and solar saltwater desalination. Central to the approach is the transformation of optically-inactive ion-exchange membranes used in electrochemical technologies into optically-active power-producing membranes. Studies were presented showing that ion transport initiated by photoacids bonded to mesoporous materials will require careful molecular engineering to enable efficient light-to-ionic energy conversion. Shown was the first demonstration of photovoltaic action from a covalently sensitized ion-exchange membrane. The sensitized monopolar membrane generated no net power because of a rapid and continuous ion crossover across the membrane due to use of a single monopolar ion-exchange membrane with a large pH gradient across it. The use of a sensitized bipolar membrane showed enhanced photovoltaic efficiencies as compared to the monolithic counterpart and analogies from the physics of solar cells was used to elucidate the mechanism of photovoltaic action. The obtained photovoltages are more than half that needed to desalinate the sodium chloride in sea water to potable water and all that needed to convert moderately saline brackish water to potable water. Ongoing optimization studies were presented. Ultimately, power-conversion efficiencies large enough to desalinate ocean water should be attainable with our proposed direct solar desalination devices.

References.

(1) International Energy Outlook Executive Summary https://www.eia.gov/outlooks/ieo/pdf/exec_summ.pdf (accessed Jan 1, 2017).

(2) Hawkswoth, J.; Clarry, R.; Audino, H. The Long View: How will the global economic order change by 2050? https://www.pwc.com/gx/en/world-2050/assets/pwc-the-world-in-2050-full-report-feb-2017.pdf (accessed Jan 1, 2017).

(3) International Energy Outlook 2017 https://www.eia.gov/outlooks/ieo/pdf/0484(2017).pdf (accessed Jan 1, 2017).

(4) Côme, G.-M. *Gas-Phase Thermal Reactions: Chemical Engineering Kinetics*, 1st ed.; Kluwer Academic Publishers: Dordrecht, 2001.

(5) Sunlight https://en.wikipedia.org/wiki/Sunlight (accessed Jan 1, 2017).

(6) Lewis, N. S.; Nocera, D. G. *Proc. Natl. Acad. Sci.* **2006**, *103* (43), 15729–15735.

(7) Moriarty, P.; Honnery, D. *Renew. Sustain. Energy Rev.* **2012**, *16* (1), 244–252.

(8) Total Energy https://www.eia.gov/totalenergy/data/browser/?tbl=T01.03#/?f=M (accessed Jan 1, 2017).

(9) Doran, P. T.; Zimmerman, M. K. *Eos (Washington. DC).* **2009**, *90* (3), 22–23.

(10) Cook, J.; Nuccitelli, D.; Skuce, A.; Jacobs, P.; Painting, R.; Honeycutt, R.; Green, S. A.; Lewandowsky, S.; Richardson, M.; Way, R. G. *Energy Policy* **2014**, *73*, 706–708.

(11) Tol, R. S. J.; Carlton, J. S.; Perry-Hill, R.; Huber, M. .

(12) Cook, J.; Oreskes, N.; Doran, P. T.; Anderegg, W. R. L.; Verheggen, B.; Maibach, E. W.; Carlton, J. S.; Lewandowsky, S.; Skuce, A. G.; Green, S. A.; Nuccitelli, D.; Jacobs, P.; Richardson, M.; Winkler, B.; Painting, R.; Rice, K. *Environ. Res. Lett.* **2016**, *11* (4), 48002.

(13) *IPCC, 2013: Summary for Policymakers. In: Climate Change 2013: The Physical Science Basis. Contribution of Working Group I to the Fifth Assessment Report of the Intergovernmental Panel on Climate Change*; Midgley, S. T. F. . D. Q. G. K. P. M. T. S. K. A. J. B. A. N. Y. X. V. B. ; P. M., Ed.; Cambridge University Press: Cambridge, United Kingdom and New York, NY, USA, 2013.

(14) O'Neel, W. T. P. J. T. H. S. *Science (80-.).* **2008**, *321* (September), 1340–1343.

(15) Vermeer, M.; Rahmstorf, S. *Proc. Natl. Acad. Sci. U. S. A.* **2009**, *106* (51), 21527–21532.

(16) Weaver, I. A. N. L. B. R. A. B. P. M. C. N. de N. M. H. E. J. E. F. N. G. A. M. H. D. J. K. G. K. C. L. Q. T. M. L. M. E. M. B. I. M. A. J. P. S. R. E. R. H. J. S. *The Copenhagen Diagnosis, 2009: Updating the World on the Latest Climate Science*; The University of New South Wales Climate Change Research Centre (CCRC): Sydney, Australia, 2009.

(17) Siler-evans, K.; Lima, I.; Morgan, M. G.; Apt, J. *Proc. Natl. Acad. Sci.* **2013**, *110* (29), 11768–11773.

(18) Proistosescu, C.; Huybers, P. J. *Sci. Adv.* **2017**, *3*, e1602821.

(19) Marsh, G. E. *J. Climatol.* **2014**, 1–7.

(20) Shakun, J. D.; Clark, P. U.; He, F.; Marcott, S. A.; Mix, A. C.; Liu, Z.; Otto-Bliesner, B.; Schmittner, A.; Bard, E. *Nature* **2012**, *484* (7392), 49–54.

(21) Martin, P.; Archer, D.; Lea, D. W. *Paleoceanography* **2005**, *20* (2), 1–10.

(22) Toggweiler, J. R. *Paleoceanography* **1999**, *14* (5), 571–588.

(23) Cuffey, K. M.; Vimeux, F. *Nature* **2001**, *412* (6846), 523–527.

(24) Stott, L.; Timmermann, A.; Thunell, R. *Science.* **2007**, *318* (5849), 435–439.

(25) Lüthi, D.; Le Floch, M.; Bereiter, B.; Blunier, T.; Barnola, J.-M.; Siegenthaler, U.; Raynaud, D.; Jouzel, J.; Fischer, H.; Kawamura, K.; Stocker, T. F. *Nature* **2008**, *453*

(7193), 379–382.

(26) Masson-Delmotte, V.; Stenni, B.; Pol, K.; Braconnot, P.; Cattani, O.; Falourd, S.; Kageyama, M.; Jouzel, J.; Landais, A.; Minster, B.; Barnola, J. M.; Chappellaz, J.; Krinner, G.; Johnsen, S.; Röthlisberger, R.; Hansen, J.; Mikolajewicz, U.; Otto-Bliesner, B. *Quat. Sci. Rev.* **2010**, *29* (1–2), 113–128.

(27) Huber, M.; Knutti, R. *Nat. Geosci.* **2012**, *5* (1), 31–36.

(28) Climate Change 2014 Synthesis Report https://www.ipcc.ch/news_and_events/docs/ar5/ar5_syr_headlines_en.pdf (accessed Jan 1, 2017).

(29) *Comparison of Lifecycle Greenhouse Gas Emissions of Various Electricity Generation Sources*; World Nuclear Association: London, 2011.

(30) Denholm, P.; Margolis, R. M. *Energy Policy* **2008**, *36* (9), 3531–3543.

(31) Loster, M. Total Primary Energy Supply — From Sunlight http://www.ez2c.de/ml/solar_land_area/ (accessed Jan 1, 2017).

(32) 2020 Utility-Scale Solar Goal Achieved https://energy.gov/eere/solar/articles/2020-utility-scale-solar-goal-achieved (accessed Jan 1, 2017).

(33) Jelle, B. P. *Energies* **2016**, *9* (1), 1–30.

(34) Maehium, M. A. How much do solar panels cost http://energyinformative.org/solar-panels-cost/ (accessed Jan 1, 2017).

(35) Chapin, D. M.; Fuller, C. S.; Pearson, G. L. *J. Appl. Phys.* **1954**, *25* (5), 676–677.

(36) Green, M. A.; Emery, K.; Hishikawa, Y.; Warta, W.; Dunlop, E. D.; Levi, D. H.; Ho-Baillie, A. W. Y. *Prog. Photovolt Res. Appl.* **2017**, *15* (25), 3–13.

(37) Fonash, S. J. *Solar Cell Device Physics*, 2nd ed.; Academic Press/Elsevier Inc.:

Burlington, MA, 2010.

(38) Vos, A. De. *J. Phys. D. Appl. Phys.* **1980**, *13* (5), 839–846.

(39) Tributsch, H. *Ionics (Kiel).* **2000**, *6* (3–4), 161–171.

(40) Ross, R. T.; Hsiao, T. *J. Appl. Phys.* **1977**, *48* (12), 4783–4785.

(41) Reece, S. Y.; Hamel, J. A.; Sung, K.; Jarvi, T. D.; Esswein, A. J.; Pijpers, J. J. H.; Nocera, D. G. *Science (80-.).* **2011**, *334* (6056), 645–648.

(42) Noorden, R. Van. "Artificial leaf" faces economic hurdle http://www.nature.com/news/artificial-leaf-faces-economic-hurdle-1.10703 (accessed Jan 1, 2017).

(43) Verlage, E.; Hu, S.; Liu, R.; Jones, R. J. R.; Sun, K.; Xiang, C.; Lewis, N. S.; Atwater, H. A. *Energy Environ. Sci.* **2015**, *8* (11), 3166–3172.

(44) Sun, K.; Liu, R.; Chen, Y.; Verlage, E.; Lewis, N. S.; Xiang, C. *Adv. Energy Mater.* **2016**, *6* (13), 1–7.

(45) Zhou, X.; Liu, R.; Sun, K.; Chen, Y.; Verlage, E.; Francis, S. A.; Lewis, N. S.; Xiang, C. *ACS Energy Lett.* **2016**, *1* (4), 764–770.

(46) Xie, X.; Crespo, G. a; Mistlberger, G.; Bakker, E. *Nat. Chem.* **2014**, *6* (3), 202–207.

(47) Memming, R. *Semiconductor electrochemistry*, 2nd ed.; Memming, R., Ed.; Wiley-VCH: Weinheim, 2015.

(48) Yasui, M.; Hazama, a; Kwon, T. H.; Nielsen, S.; Guggino, W. B.; Agre, P. *Nature* **1999**, *402* (6758), 184–187.

(49) Jiang, Y.; Lee, A.; Chen, J.; Ruta, V.; Cadene, M.; Chait, B. T.; MacKinnon, R. *Nature* **2003**, *423* (6935), 33–41.

(50) Bean, B. P. *Nat. Rev. Neurosci.* **2007**, *8* (6), 451–465.

(51) Andérasson, L. E.; Vänngård, T. *Ann. Rev. Plant Physiol. Plant Mol. Biol.* **1998**, *39*, 379–411.

(52) Furshpan, E. J.; Potter, D. D. *J. Physiol.* **1959**, *145*, 289–325.

(53) Phelan, P.; Goulding, L. A.; Tam, J. L. Y.; Allen, M. J.; Dawber, R. J.; Davies, J. A.; Bacon, J. P. *Curr. Biol.* **2008**, *18* (24), 1955–1960.

(54) Glaaser, I. W.; Slesinger, P. A. *Sci. Rep.* **2017**, *7* (1), 4592.

(55) Lee, I.; Lee, J. W.; Greenbaum, E. *Phys. Rev. Lett.* **1997**, *79*, 3294–3297.

(56) Lovreček, B.; Despić, A.; Bockris, J. O. *J. Phys. Chem.* **1959**, *63* (5), 750–751.

(57) Mafé, S.; Ramírez, P. *Acta Polym.* **1997**, *48*, 234–250.

(58) Chen, P.; Mitsui, T.; Farmer, D. B.; Golovchenko, J.; Gordon, R. G.; Branton, D. *Nano Lett.* **2004**, *4* (7), 1333–1337.

(59) Li, J.; Stein, D.; McMullan, C.; Branton, D.; Aziz, M. J.; Golovchenko, J. A. *Nature* **2001**, *412* (6843), 166–169.

(60) Kong, Y.; Fan, X.; Zhang, M.; Hou, X.; Liu, Z.; Zhai, J.; Jiang, L. *ACS Appl. Mater. Interfaces* **2013**, *5* (16), 7931–7936.

(61) Siwy, Z.; Heins, E.; Harrell, C. C.; Kohli, P.; Martin, C. R. *J. Am. Chem. Soc.* **2004**, *126*, 10850–10851.

(62) Siwy, Z.; Gu, Y.; Spohr, H. A.; Baur, D.; Wolf-Reber, A.; Spohr, R.; Apel, P.; Korchev, Y. E. *Europhys. Lett.* **2002**, *60* (3), 349–355.

(63) Siwy, Z.; Dobrev, D.; Neumann, R.; Trautmann, C.; Voss, K. *Appl. Phys. A Mater. Sci. Process.* **2003**, *76* (5), 781–785.

(64) Siwy, Z.; Apel, P.; Baur, D.; Dobrev, D. D.; Korchev, Y. E.; Neumann, R.; Spohr, R.; Trautmann, C.; Voss, K. O. *Surf. Sci.* **2003**, *532–535*, 1061–1066.

(65) Chtanko, N.; Molares, M. E. T.; Cornelius, T.; Dobrev, D.; Neumann, R. *J. Phys. Chem. B* **2004**, *108* (pH 7), 9950–9954.

(66) Siwy, Z. S. *Adv. Funct. Mater.* **2006**, *16*, 735–746.

(67) Kalman, E.; Healy, K.; Siwy, Z. S. *Europhys. Lett.* **2007**, *78*, 28002.

(68) Nguyen, G.; Vlassiouk, I.; Siwy, Z. S. *Nanotechnology* **2010**, *21*, 265301.

(69) Wei, C.; Bard, A. J.; Feldberg, S. W. *Anal. Chem.* **1997**, *69* (22), 4627–4633.

(70) Bruckbauer, A.; Ying, L.; Rothery, A. M.; Zhou, D.; Shevchuk, A. I.; Abell, C.; Korchev, Y. E.; Klenerman, D. *J. Am. Chem. Soc.* **2002**, *124* (30), 8810–8811.

(71) Piper, J. D.; Clarke, R. W.; Korchev, Y. E.; Ying, L.; Klenerman, D. *J. Am. Chem. Soc.* **2006**, *128* (51), 16462–16463.

(72) Umehara, S.; Pourmand, N.; Webb, C. D.; Davis, R. W.; Yasuda, K.; Karhanek, M. *Nano Lett.* **2006**, *6* (11), 2486–2492.

(73) Sun, K.; Mauzerall, D. *Proc. Natl. Acad. Sci. U. S. A.* **1996**, *93* (20), 10758–10762.

(74) Steinberg-Yfrach, G.; Liddell, P. a.; Hung, S.-C.; Moore, A. L.; Gust, D.; Moore, T. A. *Nature* **1997**, *385* (6613), 239–241.

(75) Bhosale, S.; Sisson, A. L.; Talukdar, P.; Fürstenberg, A.; Banerji, N.; Vauthey, E.; Bollot, G.; Mareda, J.; Röger, C.; Würthner, F.; Sakai, N.; Matile, S. *Science (80-.).* **2006**, *313* (5783), 84–86.

(76) White, W.; Sanborn, C. D.; Reiter, R. S.; Fabian, D. M.; Ardo, S. *J. Am. Chem. Soc.* **2017**, *139* (34), 11726–11733.

(77) White, W.; Sanborn, C. D.; Fabian, D.; Ardo, S. *Joule* **2017**, *2*, 1–17.

(78) Würfel, P. *Physics of Solar Cells*, 1st ed.; Wiley-VCH: Weinheim, 2005.

(79) Gutman, M.; Huppert, D. *J. Biochem. Biophys. Methods* **1979**, *1*, 9–19.

(80) Gutman, M.; Huppert, D.; Pines, E. *J. Am. Chem. Soc.* **1981**, *103* (13), 3709–3713.

(81) Mauritz, K. A.; Moore, R. B. *Chem. Rev.* **2004**, *104*, 4535–4585.

(82) Gaieck, W.; Ardo, S. *Rev. Adv. Sci. Eng.* **2014**, *3* (4), 277–287.

(83) Onufriev, A.; Case, D. A.; Ullmann, G. M. *Biochemistry* **2001**, *40* (12), 3413–3419.

(84) Finkler, B.; Spies, C.; Vester, M.; Walte, F.; Omlor, K.; Riemann, I.; Zimmer, M.; Stracke, F.; Gerhards, M.; Jung, G. *Photochem. Photobiol. Sci.* **2014**, *13*, 548–562.

(85) David M. Hercules, L. B. R. *J. Phys. Chem.* **1959**, *64* (4), 397–400.

(86) Wehry, E. L.; Rogers, L. B. *Variation of excited-state pKa values with method of measurement*; Elsevier, 1965; Vol. 21.

(87) Apel, P. *Radiat. Meas.* **2001**, *34* (1–6), 559–566.

(88) Apel, P. Y.; Korchev, Y. E.; Siwy, Z.; Spohr, R.; Yoshida, M. *Nucl. Instruments Methods Phys. Res. Sect. B Beam Interact. with Mater. Atoms* **2001**, *184*, 337–346.

(89) Vlassiouk, I.; Siwy, Z. S. *Nano Lett.* **2007**, *7* (3), 552–556.

(90) Siwy, Z.; Fuliński, A. *Am. J. Phys.* **2004**, *72* (2004), 567.

(91) Constantin, D.; Siwy, Z. S. *Phys. Rev. E - Stat. Nonlinear, Soft Matter Phys.* **2007**, *76* (October), 1–10.

(92) Xue, J. M.; Zou, X. Q.; Xie, Y. B.; Wang, Y. G. *J. Phys. D. Appl. Phys.* **2009**, *42* (10), 105308.

(93) Kovarik, M. L.; Zhou, K.; Jacobson, S. C. *J. Phys. Chem. B* **2009**, *113*, 15960–15966.

(94) Siwy, Z. S.; Howorka, S. *Chem. Soc. Rev.* **2010**, *39* (3), 1115–1132.

(95) Berezkin, V. V; Volkov, V. I.; Kiseleva, O. A.; Mitrofanova, N. V; Sobolev, V. D. **2003**, *65* (1), 129–131.

(96) Siwy, Z., Kosińska, I. D.; Fuliński, A.; Martin, C. R. *Phys. Rev. Lett.* **2005**, *94* (48102), 1–

4.

(97) Kalman, E. B. Controlling Ionic Transport for Device Design in Synthetic Nanopores, University of California, Irvine, 2010.

(98) He, Y.; Gillespie, D.; Boda, D.; Vlassiouk, I.; Eisenberg, R. S.; Siwy, Z. S. *J. Am. Chem. Soc.* **2009**, *131* (27), 5194–5202.

(99) Ali, M.; Schiedt, B.; Healy, K.; Neumann, R.; Ensinger, W. *Nanotechnology* **2008**, *19* (8), 85713.

(100) Ali, M.; Ramirez, P.; Mafé, S.; Neumann, R.; Ensinger, W. *ACS Nano* **2009**, *3* (3), 603–608.

(101) Yameen, B.; Ali, M.; Neumann, R.; Ensinger, W.; Knoll, W.; Azzaroni, O. *Nano Lett.* **2009**, *9* (7), 2788–2793.

(102) Yameen, B.; Ali, M.; Neumann, R.; Ensinger, W.; Knoll, W.; Azzaroni, O. *Chem. Commun. (Camb).* **2010**, *46* (11), 1908–1910.

(103) Gilles, F. M.; Tagliazucchi, M.; Azzaroni, O.; Szleifer, I. *J. Phys. Chem. C* **2016**, *120* (9), 4789–4798.

(104) Tagliazucchi, M.; Azzaroni, O.; Szleifer, I. *J. Am. Chem. Soc.* **2010**, *132* (35), 12404–12411.

(105) He, Y.; Gillespie, D.; Boda, D.; Vlassiouk, I.; Eisenberg, R. S.; Siwy, Z. S. *J. Am. Chem. Soc.* **2009**, *131* (14), 5194–5202.

(106) Spry, D. B.; Goun, A.; Glusac, K.; Moilanen, D. E.; Fayer, M. D. *J. Am. Chem. Soc.* **2007**, *129* (26), 8122–8130.

(107) Spry, D. B.; Fayer, M. D. *J. Phys. Chem. B* **2009**, *113* (30), 10210–10221.

(108) Piletic, I. R.; Tan, H. S.; Fayer, M. D. *J. Phys. Chem. B* **2005**, *109* (45), 21273–21284.

(109) Tan, H. S.; Piletic, I. R.; Fayer, M. D. *J. Chem. Phys.* **2005**, *122* (17), 0–9.

(110) Tan, H. S.; Piletic, I. R.; Riter, R. E.; Levinger, N. E.; Fayer, M. D. *Phys. Rev. Lett.* **2005**, *94* (5), 1–4.

(111) Spohr, R. Methods for producing nuclear traces or microholes originating from nuclear traces of an individual ion, United States Patent 4369370, 1983.

(112) Nakajima, N.; Ikada, Y. *Bioconjug. Chem.* **1995**, *6* (1), 123–130.

(113) Chen, H.; Gratton, E.; Digman, M. A. *Microsc. Res. Tech.* **2015**, *78* (4), 283–293.

(114) Lakowicz, J. R. *Principles of Fluorescence Spectroscopy*, 3rd ed.; Springer: New York, 2006.

(115) O 'Donnell, R. M.; Sampaio, R. N.; Li, G.; Johansson, P. G.; Ward, C. L.; Meyer, G. J. *J. Am. Chem. Soc.* **2016**, *138* (2), 3891–3903.

(116) Das, I.; Panja, S.; Halder, M. *J. Phys. Chem. B* **2016**, *120* (29), 7076–7087.

(117) Weller, A. *Z. Elektrochem.* **1952**, 662–668.

(118) Pines, D.; Pines, E. *Solvent Assisted Photoacidity*; 2007; Vol. 1.

(119) Richtol, H. H.; R., F. B. *Anal. Chem.* **1974**, *46* (12), 1749–1754.

(120) Arnaut, L. G.; Formosinho, S. J. *J. Photochem. Photobiol. A Chem.* **1993**, *75* (1), 1–20.

(121) Ireland, J. F.; Wyatt, P. A. H. *Adv. Phys. Org. Chem.* **1976**, *12*, 131–221.

(122) Kambhamptai, P. *J. Phys. Chem. Lett.* **2013**, *4* (2), 3316–3318.

(123) Kambhamptai, P. *J. Phys. Chem. Lett.* **2014**, *4* (2), 3497.

(124) Crosby, G. A.; Demas, J. N. *J. Phys. Chem.* **1971**, *75*, 991–1024.

(125) Hammett, L. P.; Deyrup, A. J. *J. Am. Chem. Soc.* **1932**, *54* (7), 2721–2739.

(126) Jorgenson, M. J.; Hartter, D. R. *J. Am. Chem. Soc.* **1963**, *85* (7), 878–883.

(127) Olsen, A. L.; Washburn, E. R. *J. Am. Chem. Soc.* **1932**, *54* (3212), 117–126.

(128) Paul, M. A.; Long, F. A. *Chem. Rev.* **1957**, *57* (1), 1–45.

(129) Bell, R. P.; Dowding, A. L.; Noble, J. A. *J. Chem. Soc.* **1955**, 3106–3110.

(130) Trefalt, G.; Behrens, S. H.; Borkovec, M. *Langmuir* **2016**, *32*, 380–400.

(131) Astumian, R. D. *Science* **1997**, *276* (5314), 917–922.

(132) Siwy, Z.; Apel, P.; Dobrev, D.; Neumann, R.; Spohr, R.; Trautmann, C.; Voss, K. *Nucl. Instr. Meth. Phys. Res. B* **2003**, *208*, 143–148.

(133) Yameen, B.; Ali, M.; Neumann, R.; Ensinger, W.; Knoll, W.; Azzaroni, O. *J. Am. Chem. Soc.* **2009**, *131* (6), 2070–2071.

(134) Ali, M.; Yameen, B.; Cervera, J.; Ramírez, P.; Neumann, R.; Ensinger, W.; Knoll, W.; Azzaroni, O. *J. Am. Chem. Soc.* **2010**, *132*, 8338–8348.

(135) Weisstein, E. W. Conical Frustum http://mathworld.wolfram.com/ConicalFrustum.html (accessed Jan 7, 2017).

(136) Grabowski, Z. R.; Rubaszewska, W. *J. Chem. Soc., Faraday Trans.* **1977**, *1* (73), 11–28.

(137) Michaelis, L. *Chem. Rev.* **1935**, *16* (2), 243–286.

(138) Robertso.Re; Rossall, B. *Can. J. Chem.* **1971**, *49* (9), 1441–1450.

(139) Oae, S.; Kadoma, Y. *Can. J. Chem* **1986**, *64* (6), 1184–1188.

(140) Li, M. *Organic Chemistry of Drug Degradation*, 1st ed.; Royal Society of Chemistry: Cambridge, 2012.

(141) Ali, M.; Bayer, V.; Schiedt, B.; Neumann, R.; Ensinger, W. *Nanotechnology* **2008**, *19* (48), 485711.

(142) Ali, M.; Mafe, S.; Ramirez, P.; Neumann, R.; Ensinger, W. *Langmuir* **2009**, *25* (21), 11993–11997.

(143) Nakajima, N.; Ikada, Y. *Bioconjug. Chem.* **1995**, *6*, 123–130.

(144) Han, J.; Tao, F.-M. *J. Phys. Chem. A* **2006**, *110* (1), 257–263.

(145) Ames, D. E.; Grey, T. F. *J. Chem. Soc.* **1955**, *0*, 631–636.

(146) Cuatrecasas, P.; Parikh, I. *Biochemistry* **1972**, *11* (12), 2291–2299.

(147) Lomant, A. J.; Fairbanks, G. *J. Mol. Biol.* **1976**, *104* (1), 243–261.

(148) Staros, J. V.; Wright, R. W.; Swingle, D. M. *Anal. Biochem.* **1986**, *156* (1), 220–222.

(149) Bulpitt, P.; Aeschlimann, D. *J Biomed Mater Res* **1999**, *47*, 152–69.

(150) Grabarek, Z.; Gergely, J. *Anal. Biochem.* **1990**, *185* (1), 131–135.

(151) Spry, D. B.; Fayer, M. D. *J. Chem. Phys.* **2008**, *128*, 84508.

(152) Abbasian, M.; Aali, N. K. *J. Nanostruct.* **2016**, *6* (1), 35–42.

(153) Lu, Y.; Pelton, R.; Brook, M. A. *Langmuir* **2007**, *23* (10), 5630–5637.

(154) Zhao, J.; Milanova, M.; Warmoeskerken, M. M. C. G.; Dutschk, V. *Colloids Surfaces A Physicochem. Eng. Asp.* **2012**, *413*, 273–279.

(155) Dijksman, A.; Elzinga, J. M.; Li, Y. X.; Arends, I. W. C. E.; Sheldon, R. A. *Tetrahedron Asymmetry* **2002**, *13* (8), 879–884.

(156) Nelson, David L.; Cox, M. M. *Lehninger Principles of Biochemistry*, 6th ed.; W.H. Freeman, 2012.

(157) Skulachev, V. P.; Bogachev, A. V.; Kasparinsky, F. O. *Principles of Bioenergetics*; Springer Science & Business Media, 2012.

(158) Bard, A. J.; Memming, R.; Miller, B. *Pure Appl. Chem.* **1991**, *63* (4), 569–596.

(159) Singh, K.; Korenstein, R.; Lebedeva, H.; Caplan, S. R. *Biophys. J.* **1980**, *31* (3), 393–401.

(160) Eisenbach, M.; Weissmann, C.; Tanny, G.; Caplan, S. R. **1977**, *81* (1), 77–80.

(161) Chu, L.; Yen, C.; El-sayed, M. A. **2010**, *26*, 620–626.

(162) Gust, D.; Moore, T. A.; Moore, A. L. *Acc. Chem. Res.* **2001**, *34* (1), 40–48.

(163) Gust, D.; Moore, T. A.; Moore, A. L.; Liddell, P. A.; Kuciauskas, D.; Sumida, J. P.; Nash, B.; Nguyen, D.; Moore, A. L.; Moore, T. A.; Gust, D.; Mathis, P.; Mialocq, J.-C.; Chachaty, C.; Bensasson, R. V.; Land, E. J.; Doizi, D.; Liddell, P. A.; Lehman, W. R.; Nemeth, G. A.; Moore, A. L. *J. Am. Chem. Soc.* **1997**, *307* (1), 1400–1405.

(164) Moore, T. A.; Gust, D.; Mathis, P.; Mialocq, J.-C.; Chachaty, C.; Bensasson, R. V.; Land, E. J.; Doizi, D.; Liddell, P. A.; Lehman, W. R.; Nemeth, G. A.; Moore, A. L. *Nature*. 1984, pp 630–632.

(165) Fonash, S. *Solar Cell Device Physics*, 2nd ed.; Elsevier, 2010.

(166) Sun, K.; Mauzerall, D. *Proc. Natl. Acad. Sci.* **1996**, *93*, 10758–10762.

(167) Bhosale, S.; Sisson, A. L.; Talukdar, P.; Fürstenberg, A.; Banerji, N.; Vauthey, E.; Bollot, G.; Mareda, J.; Röger, C.; Würthner, F.; Sakai, N.; Matile, S. *Science (80-.).* **2006**, *313* (5783), 84–86.

(168) Ardo, S.; Meyer, G. J. *Chem. Soc. Rev.* **2009**, *38* (1), 115–164.

(169) Donten, M. L.; Hamm, P.; VandeVondele, J. *J. Phys. Chem. B* **2011**, *115* (5), 1075–1083.

(170) Natzle, W. C.; Moore, C. B. *J. Phys. Chem.* **1985**, *89* (12), 2605–2612.

(171) Henrich, J. D.; Suchyta, S.; Kohler, B. *J. Phys. Chem. B* **2015**, *119*, 2737–2748.

(172) Banerjee, S.; Curtin, D. E. *J. Fluor. Chem.* **2004**, *125* (8), 1211–1216.

(173) Würfel, P. *Physics of Solar Cells: From Principles to New Concepts*; Wiley-VCH, 2005.

(174) Abraham John, S.; Ramaraj, R. *J. Electroanal. Chem.* **2004**, *561* (SUPPL. 1), 119–126.

(175) John, S. A.; Ramaraj, R. *Langmuir* **1996**, *12* (23), 5689–5695.

(176) García-Fresnadillo, D.; Marazuela, M. D.; Moreno-Bondi, M. C.; Orellana, G. *Langmuir* **1999**, *15* (19), 6451–6459.

(177) Sabatani, E.; Nikol, H. D.; Gray, H. B.; Anson, F. C. *J. Am. Chem. Soc.* **1996**, *118* (5),

1158–1163.

(178) Chen, T. Y.; Leddy, J. *Langmuir* **2000**, *16* (6), 2866–2871.

(179) Ma, L.; Li, J.; Xu, G.; Xiong, J.; Cai, W. *RSC Adv.* **2016**, *6* (115), 114899–114905.

(180) Schulze, M.; Lorenz, M.; Wagner, N.; Gülzow, E. *Fresenius. J. Anal. Chem.* **1999**, *365* (1–3), 106–113.

(181) Greso, A. J.; Moore, R. B.; Cable, K. M.; Jarrett, W. L.; Mauritz, K. A. *Polymer (Guildf).* **1997**, *38* (6), 1345–1356.

(182) Gruger, A.; Régis, A.; Schmatko, T.; Colomban, P. *Vib. Spectrosc.* **2001**, *26* (2), 215–225.

(183) Perusich, S. A. *J. Appl. Polym. Sci.* **2011**, *120* (1), 165–183.

(184) Hillman, D. M.; Stephens, S. H.; Poynton, S. D.; Murphy, S.; Ong, A. L.; Varcoe, J. R. *J. Mater. Chem. A* **2013**, *1* (4), 1018–1021.

(185) Ariese, F.; Kok, S. J.; Verkaik, M.; Hoornweg, G. P.; Gooijer, C.; Velthorst, N. H.; Hofstraatt, J. W. *Anal. Chem.* **1993**, *65* (14), 1100–1106.

(186) Chen, C.; Levitin, G.; Hess, D. W.; Fuller, T. F. *J. Power Sources* **2007**, *169* (2), 288–295.

(187) Liu, X.; Gao, H.; Chen, X.; Hu, Y.; Pei, S.; Li, H.; Zhang, Y. *J. Memb. Sci.* **2016**, *515*, 268–276.

(188) Salerno, H. L. S.; Elabd, Y. A. *J. Appl. Polym. Sci.* **2013**, *127* (1), 298–307.

(189) Silverstien, R. M.; Webster, F. X.; Kiemle, D. J. *Spectrometric Idenitfication of Organic Compounds*, 7th ed.; John Wiley & Sons, Inc., 2005.

(190) Hoffmann, E. A.; Fekete, Z. A.; Korugic-karasz, L. S.; Karasz, F. E.; Wilusz, E. *J. Polym. Sci. Part A* **2003**, *42*, 551–556.

(191) Lopez, G. P.; Castner, D. G.; Ratner, B. D. *Surf. Interface Anal.* **1991**, *17*, 267–272.

(192) Chien, H. C.; Tsai, L. D.; Kelarakis, A.; Lai, C. M.; Lin, J. N.; Fang, J.; Zhu, C. Y.; Chang, F. C. *Polym. (United Kingdom)* **2012**, *53* (22), 4927–4930.

(193) Haghighat, S.; Ostresh, S.; Dawlaty, J. M. *J. Phys. Chem. B* **2016**, *120* (5), 1002–1007.

(194) Reiter, R. S.; White, W.; Ardo, S. *J. Electrochem. Soc.* **2016**, *163* (4), H3132–H3134.

(195) Bard, J. A.; Faulkner, R. L. *Electrochemical Methods: fundementals and applications*, 2nd ed.; John Wiley & Sons, Inc.: New York, 1980.

(196) Shockley, W.; Queisser, H. J. *J. Appl. Phys.* **1961**, *32* (3), 510–519.

(197) Chang, W. B.; Evans, C. M.; Popere, B. C.; Russ, B. M.; Liu, J.; Newman, J.; Segalman, R. A. *ACS Macro Lett.* **2016**, *5* (1), 94–98.

(198) Ishida, H.; Tobita, S.; Hasegawa, Y.; Katoh, R.; Nozaki, K. *Coord. Chem. Rev.* **2010**, *254* (21–22), 2449–2458.

(199) Resch-Genger, U.; Rurack, K. *Pure Appl. Chem.* **2013**, *85* (10), 2005–2026.

(200) Pardo, A.; Reyman, D.; Poyato, J. M. L.; Medina, F. *J. Lumin.* **1992**, *51* (5), 269–274.

(201) Melhuish, W. H. *J. Phys. Chem.* **1961**, *65* (6), 229–235.

(202) Herráez, J. V.; Belda, R. *J. Solution Chem.* **2006**, *35* (9), 1315–1328.

(203) White, W.; Sanborn, C. D.; Fabian, D. M.; Ardo, S. *Joule* **2017**, *2*, 1–17.

(204) Lashkaryov, V. E. *Izv. Akad. Nauk SSSR, Ser. Fiz.* **1941**, *5* (4–5), 442–446.

(205) Fuller, C. S. *Rec. Chem. Prog.* **1956**, *17* (2), 75–93.

(206) Chapin, D. M.; Fuller, C. S.; Pearson, G. L. *J. Appl. Phys.* **1954**, *25* (5), 676–677.

(207) *Look Magazine*. 1956.

(208) Lovrecek, B.; Despic, A.; Bockris, J. O. *J. Phys. Chem.* **1959**, *63*, 750.

(209) Maslov, V.; Zotov, Y. *Russ. Chem. Rev.* **1968**, *37* (4), 310–315.

(210) Murphy, G. W. *Sol. Energy* **1978**, *21*, 403–407.

(211) McNaught, A. D.; Wilkinson, A. In *IUPAC Compendium of Chemical Terminology*; IUPAC: Research Triagle Park, NC, 2014; Vol. 1533, p 5591.

(212) Pearson, G. L.; Bardeen, J. *Phys. Rev.* **1949**, *75* (5), 865.

(213) Rosés, M.; Ràfols, C.; Bosch, E. *Anal. Chem.* **1993**, *1003* (23), 2294–2299.

(214) Fonash, S. J. *Solar Cell Device Physics*; Elsevier, 2010.

(215) Bockris, J.; Reddy, A. *Modern Electrochemistry*, second.; Kluwer Academic Publishers: New York, 2002.

(216) Kittel, C. *Introduction to Solid State Physics*, 8th ed.; Wiley, 2005.

(217) Rondinini, S.; Longhi, P.; Mussini, P. R.; Mussini, T. *Pure Appl. Chem.* **1987**, *59* (12), 1693–1702.

(218) Battaglia, C.; Cuevas, A.; De Wolf, S. *Energy Environ. Sci.* **2016**, *9* (5), 1552–1576.

(219) Sze, S. M.; Ng, K. K. *Physics of Semiconductor Devices*, 3rd ed.; John Wiley & Sons, Inc.: Hoboken, NJ, USA, 2007.

(220) Würthner, F.; Kaiser, T. E.; Saha-Möller, C. R. *Angew. Chemie Int. Ed.* **2011**, *50* (15), 3376–3410.

(221) Ardo, S.; Sun, Y.; Castellano, F. N.; Meyer, G. J. *J. Phys. Chem. B* **2010**, *114* (45), 14596–14604.

(222) Ardo, S.; Sun, Y.; Staniszewski, A.; Castellano, F. N.; Meyer, G. J. *J. Am. Chem. Soc.* **2010**, *132* (19), 6696–6709.

(223) Pensack, R. D.; Banyas, K. M.; Barbour, L. W.; Hegadorn, M.; Asbury, J. B. *Phys. Chem. Chem. Phys.* **2009**, *11* (15), 2575.

(224) Zhang, F.; Zhang, H.; Qu, C. *J. Mater. Chem.* **2011**, *21* (34), 12744.

(225) Wang, G.; Weng, Y.; Chu, D.; Xie, D.; Chen, R. *J. Memb. Sci.* **2009**, *326*, 4–8.

(226) Luo, J.; Wu, C.; Wu, Y.; Xu, T. *J. Memb. Sci.* **2010**, *347*, 240–249.

(227) Khan, M. I.; Mondal, A. N.; Tong, B.; Jiang, C.; Emmanuel, K.; Yang, Z.; Wu, L.; Xu, T. *Desalination* **2016**, *391*, 61–68.

(228) Astom Corporation. **2013**, 40.

(229) Merle, G.; Wessling, M.; Nijmeijer, K. *J. Memb. Sci.* **2011**, *377* (1–2), 1–35.

(230) Reiter, R. S.; White, W.; Ardo, S. *J. Electrochem. Soc.* **2016**, *163* (4), H3132–H3134.

(231) Ünlü, M.; Zhou, J.; Kohl, P. A. *J. Phys. Chem. C* **2009**, *113* (26), 11416–11423.

(232) Grew, K. N.; McClure, J. P.; Chu, D.; Kohl, P. A.; Ahlfield, J. M. *J. Electrochem. Soc.* **2016**, *163* (14), F1572–F1587.

(233) Hegedus, L.; Kirschner, N.; Wittmann, M.; Noszticzius, Z. *J. Phys. Chem. A* **1998**, *102* (32), 6491–6497.

(234) Warrick, P.; Auborn, J. J.; Eyring, E. M. *J. Phys. Chem.* **1972**, *76* (8), 1184–1191.

(235) Eames, C.; Frost, J. M.; Barnes, P. R. F.; O'Regan, B. C.; Walsh, A.; Islam, M. S. *Nat. Commun.* **2015**, *6*, 7497.

(236) Bag, M.; Renna, L. A.; Adhikari, R. Y.; Karak, S.; Liu, F.; Lahti, P. M.; Russell, T. P.; Tuominen, M. T.; Venkataraman, D. *J. Am. Chem. Soc.* **2015**, *137* (40), 13130–13137.

(237) Fabian, D. M.; Ardo, S. *J. Mater. Chem. A* **2016**, *4* (18), 6837–6841.

(238) **2016**.

(239) WorldBank. **2017**, 1–2.

(240) Ardo, S. *Distinctive voices : Development of a plastic water bottle for sunlight-driven desalination*; National Academy of Sciences, 2017.

(241) WHO. *Heal. criteria other Support. Inf.* **1996**, *2*, 8.

(242) California Department of Water Resources. *Desalination (Brackish and Sea Water) A*

Resource Management Strategy of the California Water Plan; 2016.

(243) Ramírez, P.; Rapp, H. J.; Reichle, S.; Strathmann, H.; Mafé, S. *J. Appl. Phys.* **1992**, *72* (1), 259–264.

(244) Mafé, S.; Ramírez, P.; Alcaraz, A. *Chem. Phys. Lett.* **1998**, *294* (4–5), 406–412.

(245) Spies, C.; Shomer, S.; Finkler, B.; Pines, D.; Pines, E.; Jung, G.; Huppert, D. *Phys. Chem. Chem. Phys.* **2014**, *16* (19), 9104.

(246) Kiefer, P. M.; Hynes, J. T. *J. Phys. Chem. A* **2002**, *106* (9), 1834–1849.

(247) Marcus, R. A. *J. Phys. Chem.* **1968**, *72* (3), 891–899.

(248) Marcus, R. A. *J. Am. Chem. Soc.* **1969**, *91* (26), 7224–7225.

(249) Cohen, A. O.; Marcus, R. A. *J. Phys. Chem.* **1968**, *72* (1), 4249–4256.

(250) Pines, E. *Isotope Effects In Chemistry and Biology*; Kohen, A., Limbach, H., Eds.; CRC Press, 2005.

(251) Simkovitch, R.; Kisin-Finfer, E.; Shomer, S.; Gepshtein, R.; Shabat, D.; Huppert, D. *J. Photochem. Photobiol. A Chem.* **2013**, *254*, 45–53.

(252) Green, O.; Gajst, O.; Simkovitch, R.; Shabat, D.; Huppert, D. *J. Phys. Chem. A* **2017**, *121* (16), 3079–3087.

(253) Presiado, I.; Karton-Lifshin, N.; Erez, Y.; Gepshtein, R.; Shabat, D.; Huppert, D. *J. Phys. Chem. A* **2012**, *116*, 7353–7363.

(254) Simkovitch, R.; Shomer, S.; Gepshtein, R.; Shabat, D.; Huppert, D. *J. Phys. Chem. A* **2014**, *118* (10), 1832–1840.

(255) Silverman, L. N.; Spry, D. B.; Boxer, S. G.; Fayer, M. D. *J. Phys. Chem.* **2008**, *112*, 10244–10249.

(256) Karton-Lifshin, N.; Albertazzi, L.; Bendikov, M.; Baran, P. S.; Shabat, D. *J. Am. Chem.*

Soc. **2012**, *134*, 20412–20420.

(257) Hananya, N.; Eldar Boock, A.; Bauer, C. R.; Satchi-Fainaro, R.; Shabat, D. *J. Am. Chem. Soc.* **2016**, *138* (40), 13438–13446.

(258) Shi, Z.; Peng, P.; Strohecker, D.; Liao, Y. *J. Am. Chem. Soc.* **2011**, *133* (37), 14699–14703.

(259) Sharrett, Z.; Gamsey, S.; Hirayama, L.; Vilozny, B.; Suri, J. T.; Wessling, R. A.; Singaram, B. *Org. Biomol. Chem.* **2009**, No. 7, 1461–1470.

(260) Webb, J. L.; Corwin, A. H. *J. Am. Chem. Soc.* **1944**, *66* (9), 1456–1459.

(261) Waggoner, A. S.; Mujumdar, R. Rigidized Trimethine Cyanine Dyes. WO1999031181 A1, 1999.

(262) Marie-Noelle, R.; Francois, S.; Vincent, G. Markers, their manufacturing process and their applications. CA 2618217 A1, 2007.

(263) Browne, K. A.; Deheyn, D. D.; El-Hiti, G. A.; Smith, K.; Weeks, I. *J. Am. Chem. Soc.* **2011**, *133* (37), 14637–14648.

Nuclear Magenetic Resonance and Mass Spectras.

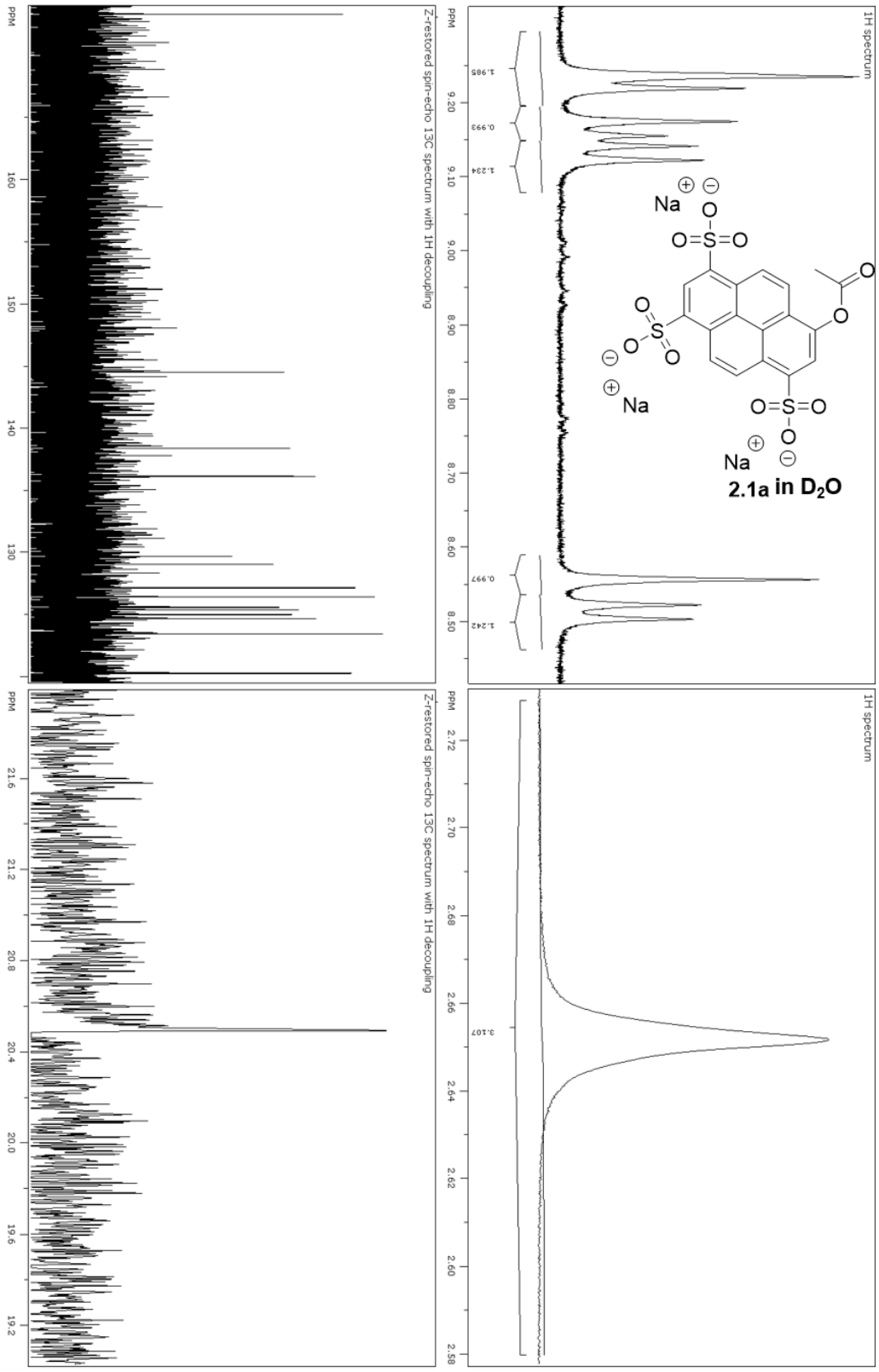

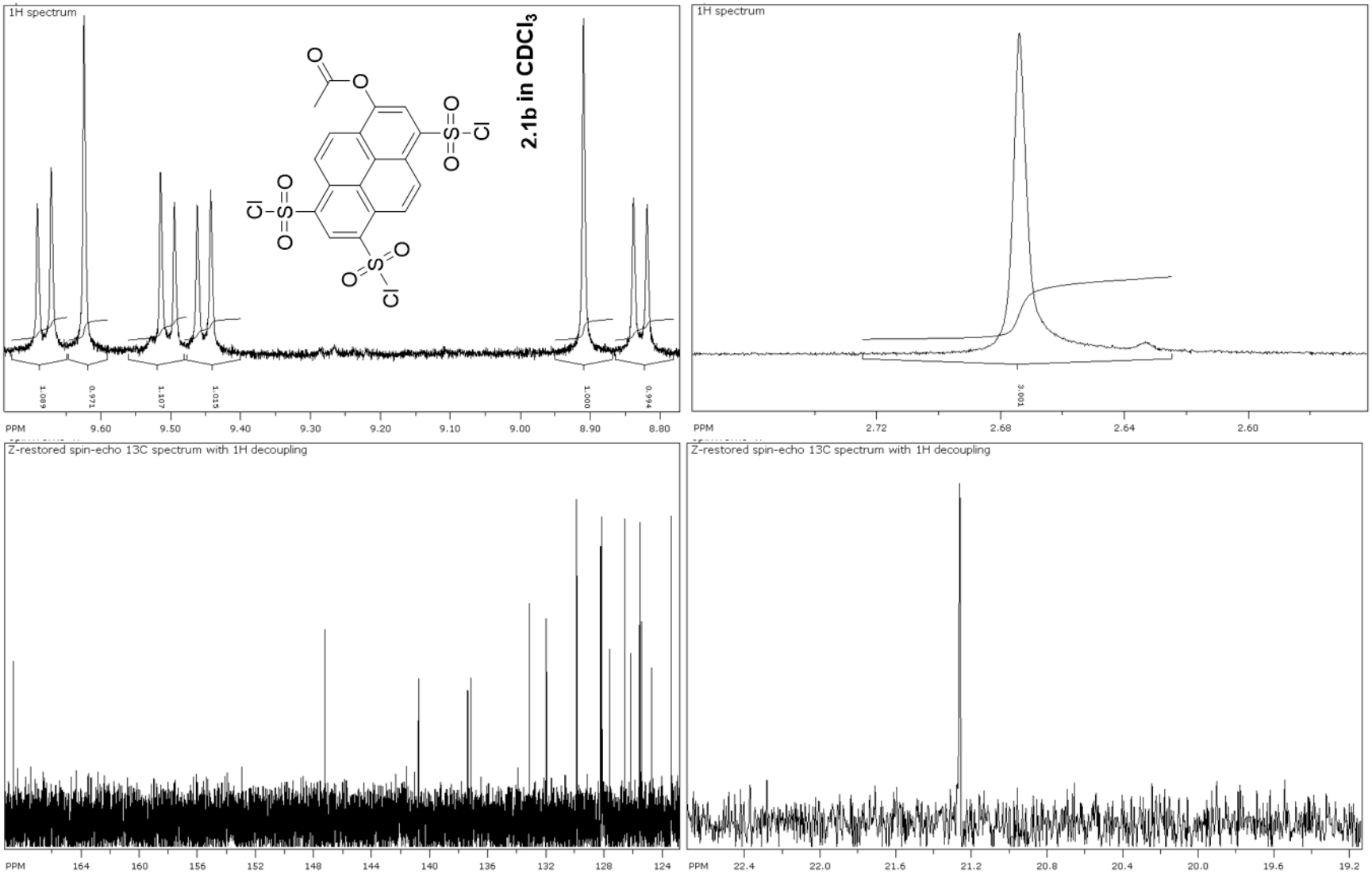
1H spectrum
2.1b in CDCl3
1.089
0.971
1.107
1.015
1.000
0.994
PPM
9.60
9.50
9.40
9.30
9.20
9.10
9.00
8.90
8.80
1H spectrum
3.001
PPM
2.72
2.68
2.64
2.60
Z-restored spin-echo 13C spectrum with 1H decoupling
PPM
164
160
156
152
148
144
140
136
132
128
124
Z-restored spin-echo 13C spectrum with 1H decoupling
PPM
22.4
22.0
21.6
21.2
20.8
20.4
20.0
19.6
19.2

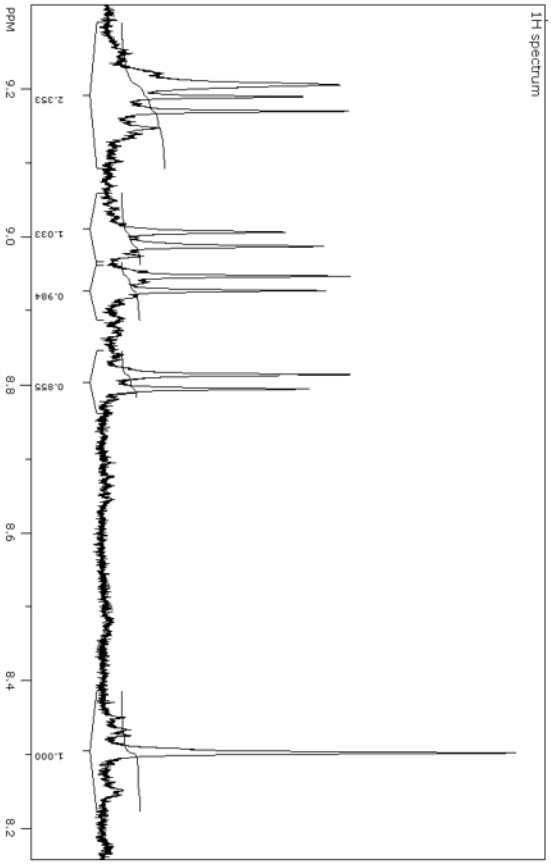
1H spectrum
PPM
9.2
9.0
8.8
8.6
8.4
8.2
2.353
1.033
0.984
0.855
1.000

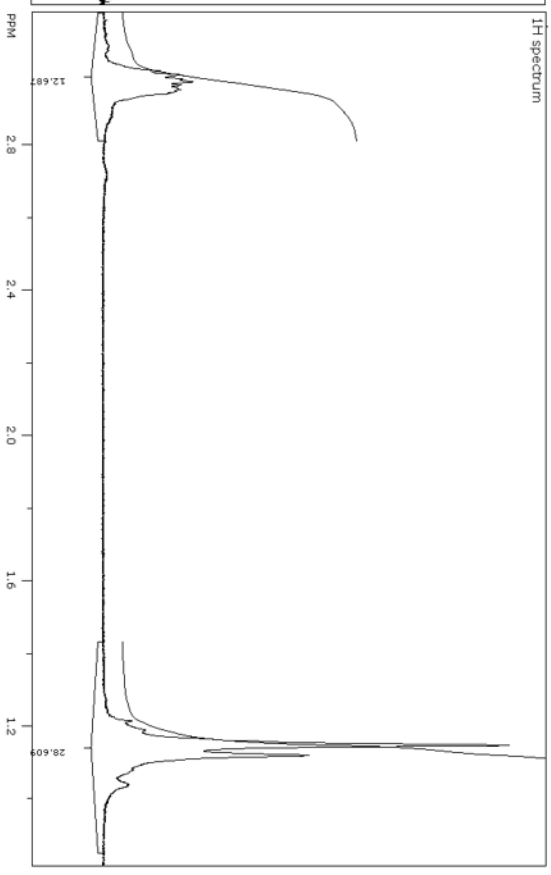
1H spectrum
PPM
2.8
2.4
2.0
1.6
1.2
12.687
28.609

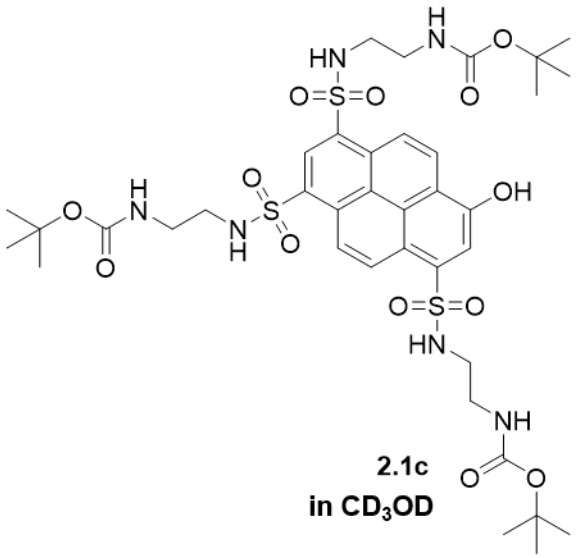
HN
O=S=O
O
H
N
O
O
H
N
O
O
S
O
N
H
OH
O=S=O
HN
NH
O
O

2.1c
in CD_3OD

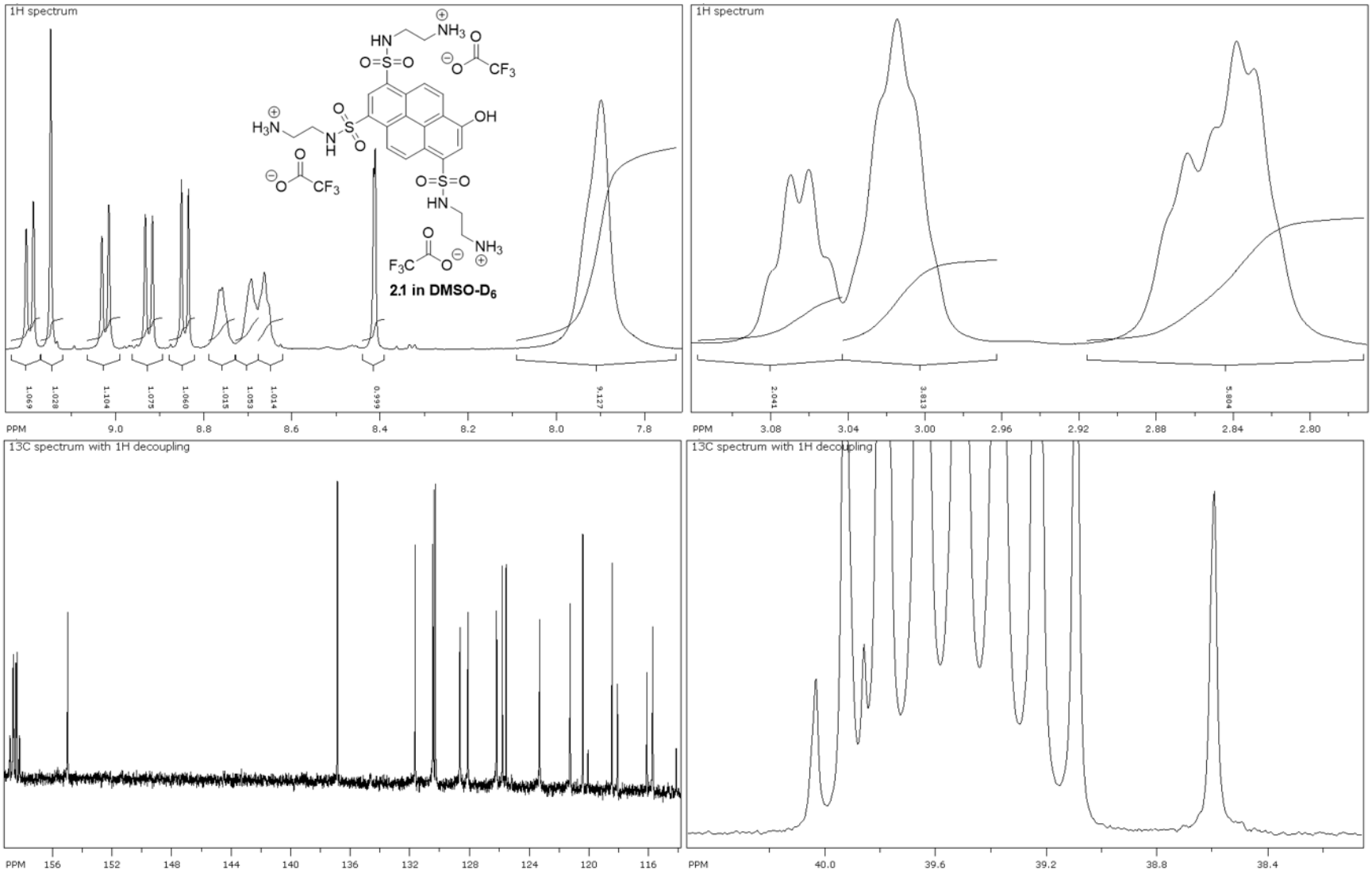
1H spectrum
2.1 in DMSO-D6
1.069
1.028
1.104
1.075
1.060
1.015
1.093
1.014
0.999
9.127
PPM
9.0
8.8
8.6
8.4
8.2
8.0
7.8
1H spectrum
2.041
3.813
5.804
PPM
3.08
3.04
3.00
2.96
2.92
2.88
2.84
2.80
13C spectrum with 1H decoupling
PPM
156
152
148
144
140
136
132
128
124
120
116
13C spectrum with 1H decoupling
PPM
40.0
39.6
39.2
38.8
38.4

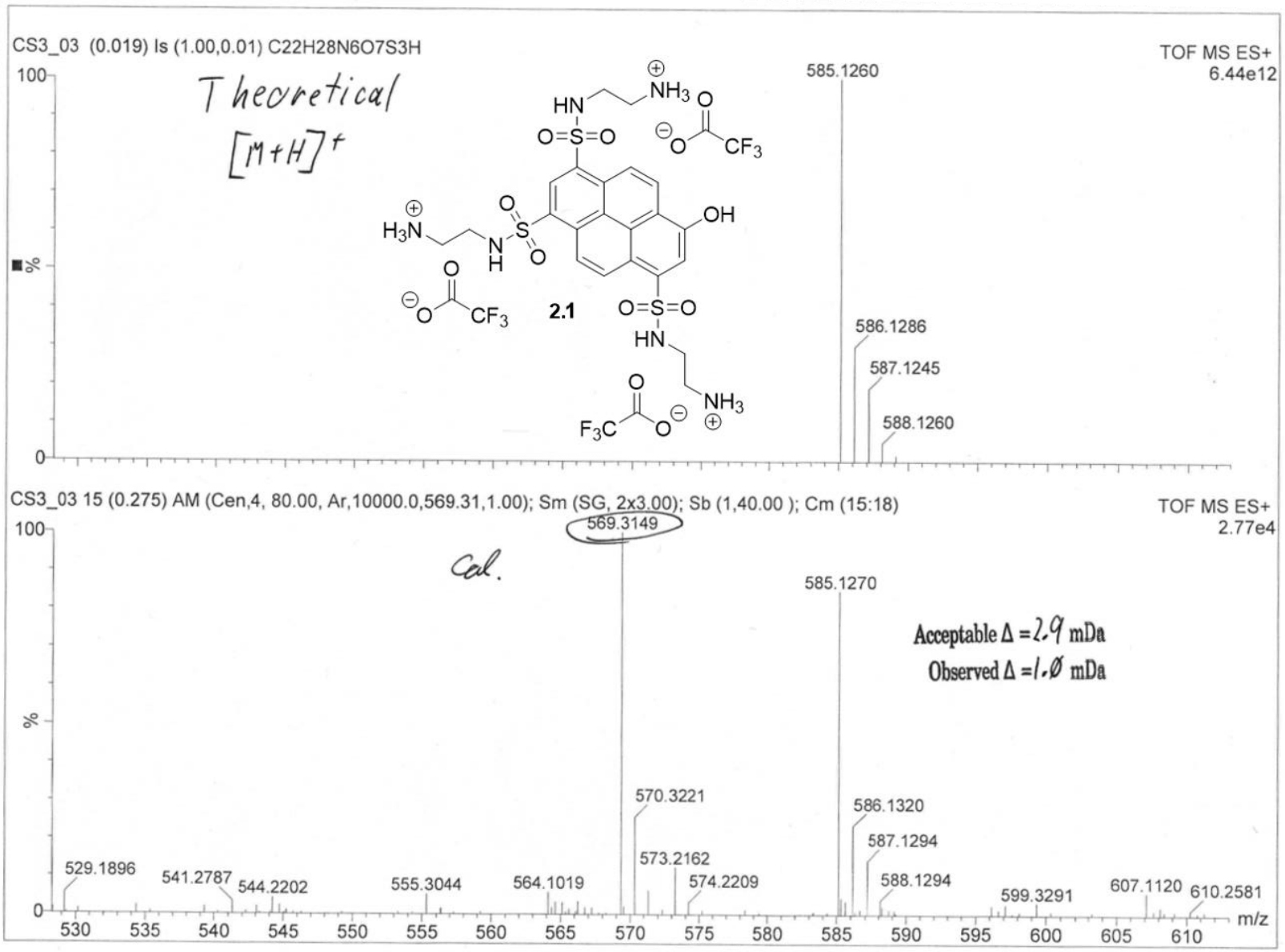
CS3_03 (0.019) Is (1.00,0.01) C22H28N6O7S3H
Theoretical
[M+H]+
TOF MS ES+
6.44e12
585.1260
586.1286
587.1245
588.1260
2.1
CS3_03 15 (0.275) AM (Cen,4, 80.00, Ar,10000.0,569.31,1.00); Sm (SG, 2x3.00); Sb (1,40.00); Cm (15:18)
TOF MS ES+
2.77e4
569.3149
Cal.
585.1270
Acceptable Δ = 2.9 mDa
Observed Δ = 1.0 mDa
570.3221
586.1320
587.1294
573.2162
588.1294
574.2209
529.1896
541.2787
544.2202
555.3044
564.1019
599.3291
607.1120
610.2581
m/z

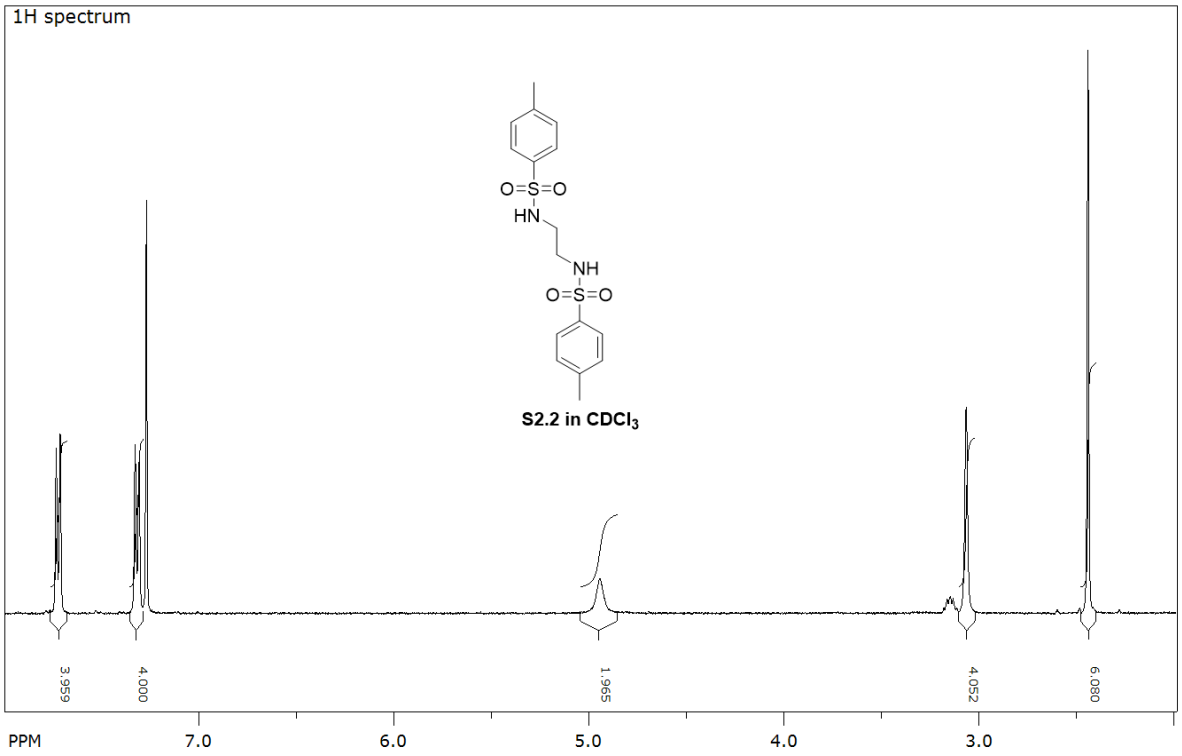
1H spectrum
O=S=O
HN
NH
O=S=O
S2.2 in CDCl3
3.959
4.000
1.965
4.052
6.080
PPM
7.0
6.0
5.0
4.0
3.0

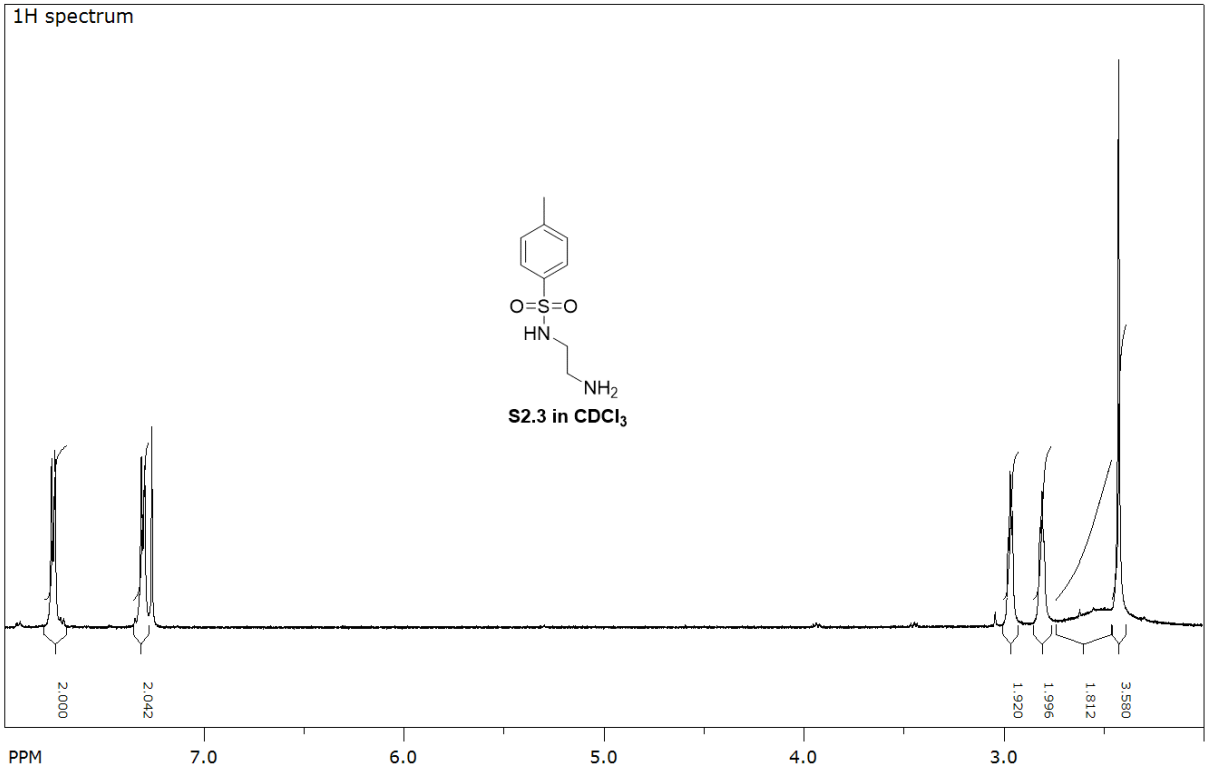
1H spectrum
O=S=O
HN
NH2
S2.3 in CDCl3
2.000
2.042
1.920
1.996
1.812
3.580
PPM
7.0
6.0
5.0
4.0
3.0

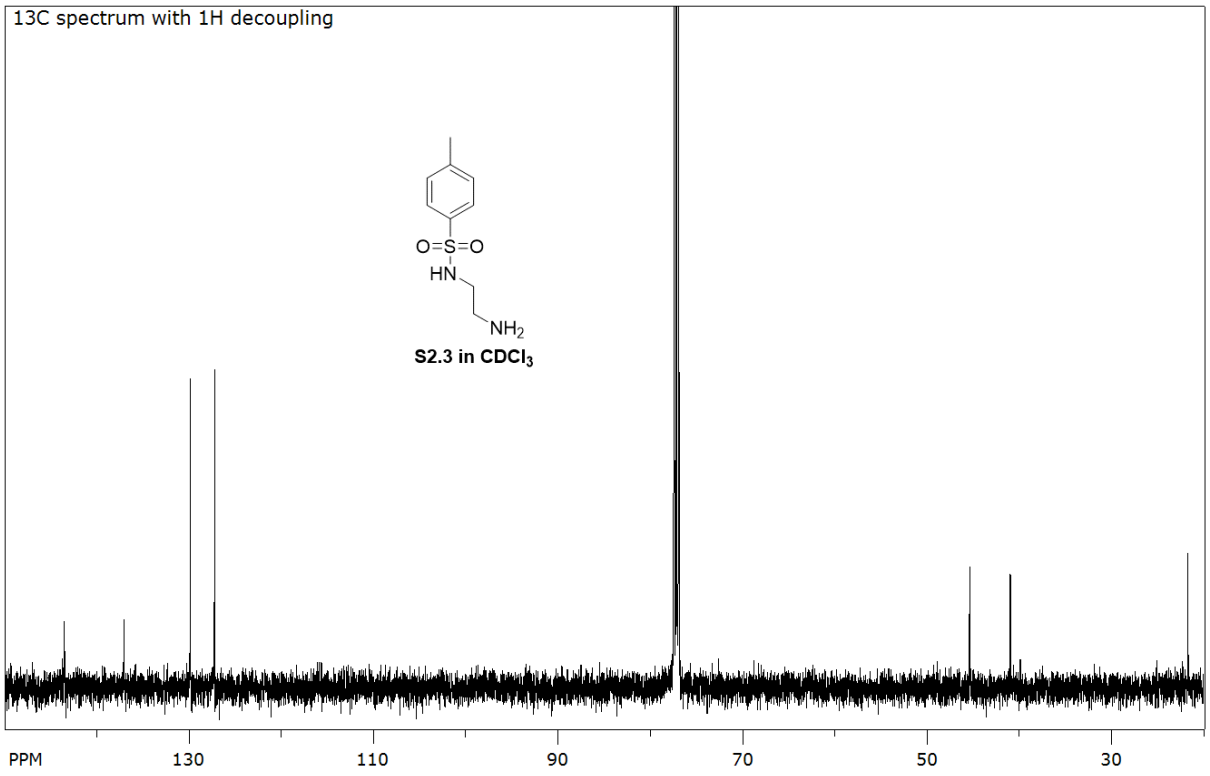
13C spectrum with 1H decoupling
O=S=O
HN
NH2
S2.3 in CDCl3
PPM
130
110
90
70
50
30

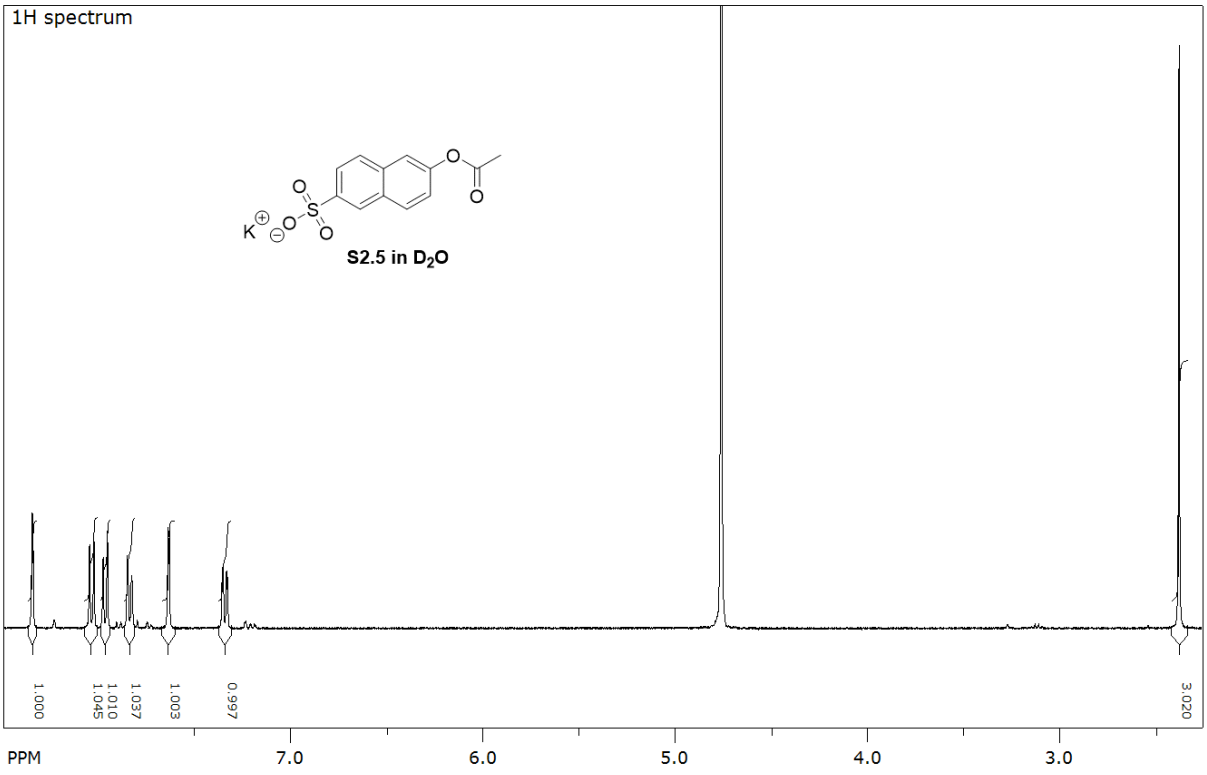
1H spectrum
K
O
S
O
S2.5 in D2O
1.000
1.045
1.010
1.037
1.003
0.997
3.020
PPM
7.0
6.0
5.0
4.0
3.0

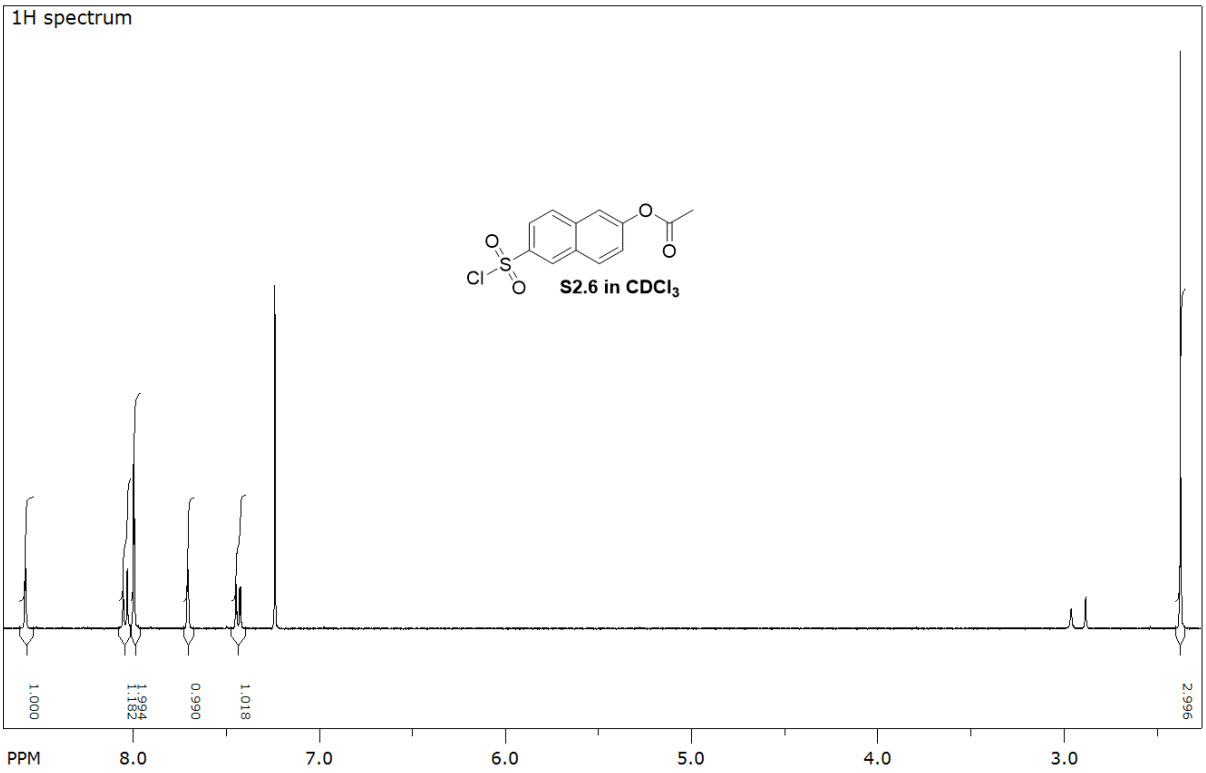
1H spectrum
S2.6 in CDCl3
1.000
1.994
1.182
0.990
1.018
2.996
PPM
8.0
7.0
6.0
5.0
4.0
3.0

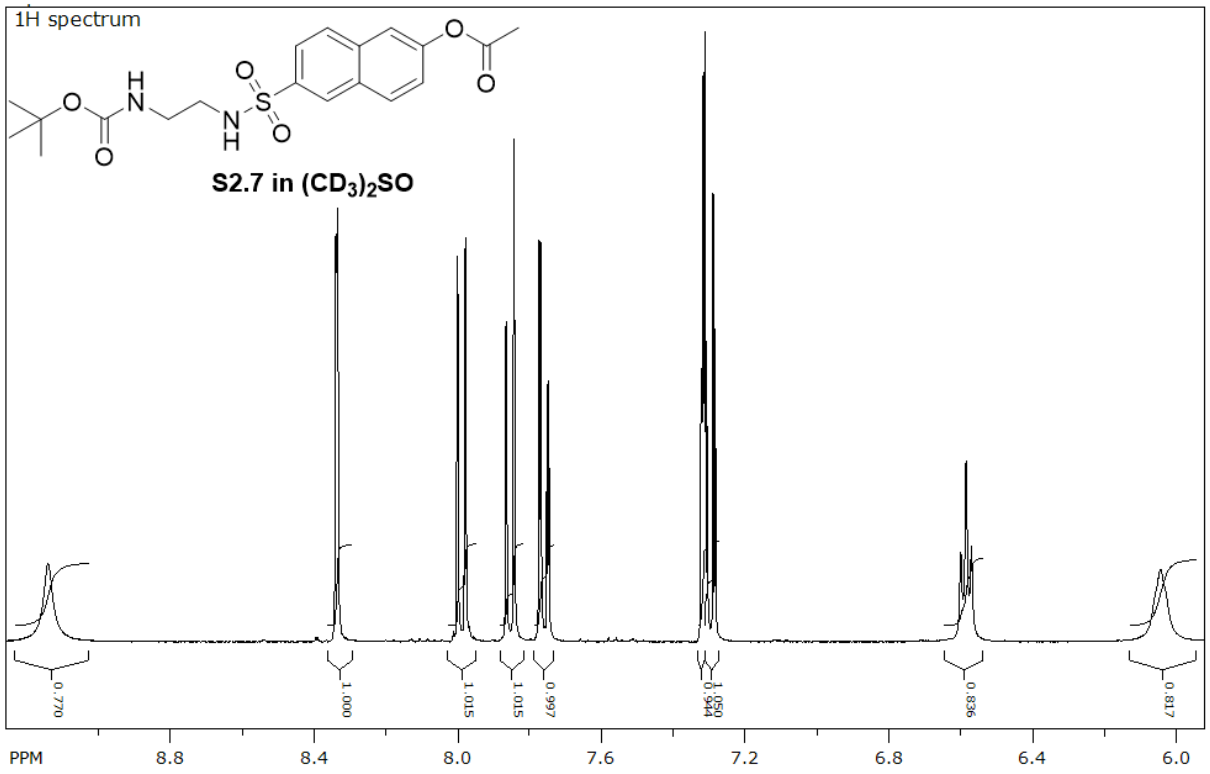
1H spectrum
S2.7 in (CD3)2SO
0.770
1.000
1.015
1.015
0.997
1.050
0.944
0.836
0.817
PPM
8.8
8.4
8.0
7.6
7.2
6.8
6.4
6.0

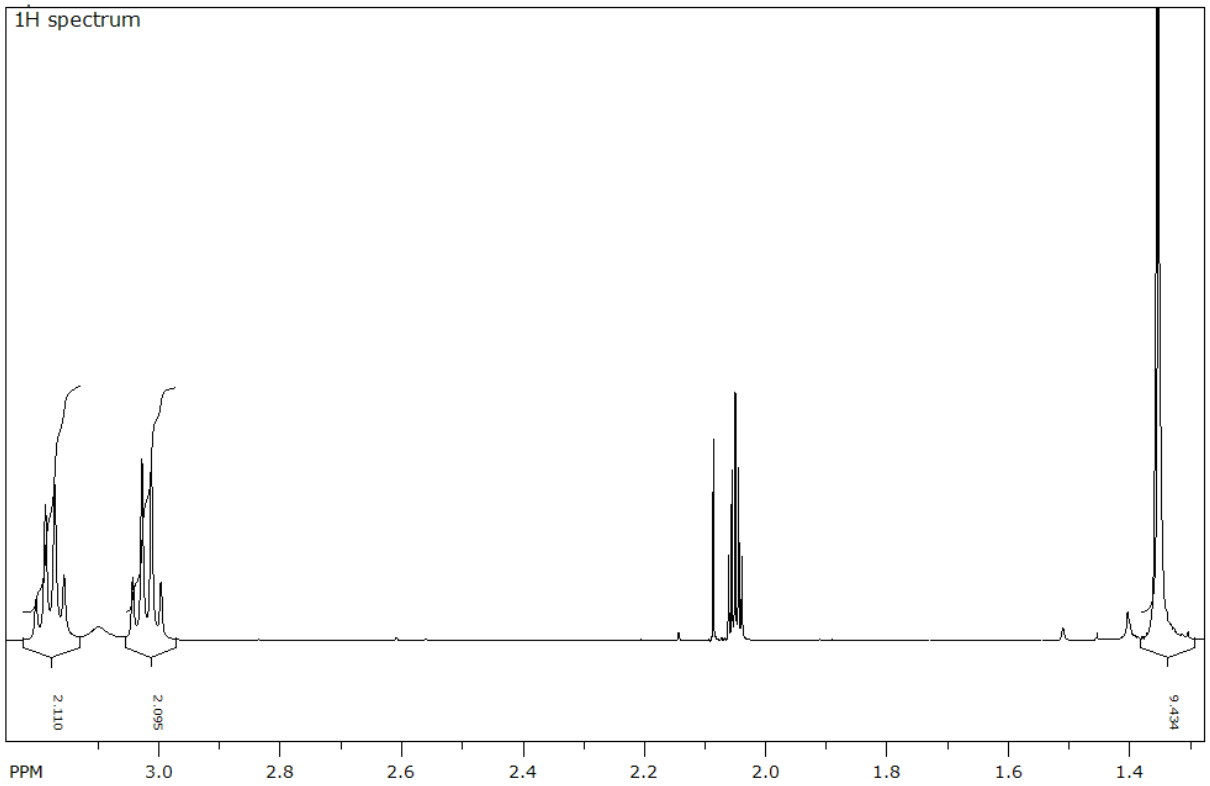
1H spectrum
2.110
2.095
9.434
PPM
3.0
2.8
2.6
2.4
2.2
2.0
1.8
1.6
1.4

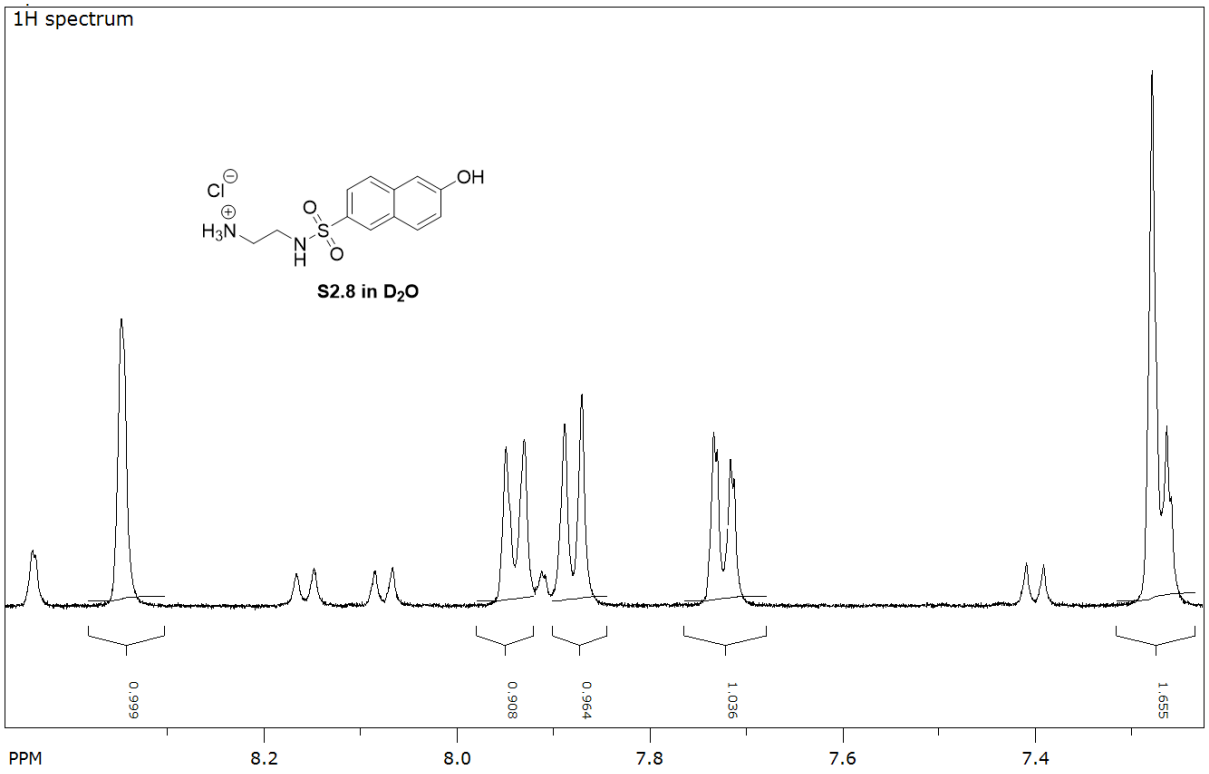
1H spectrum
Cl
H3N
O
S
N
H
O
OH
S2.8 in D2O
0.999
0.908
0.964
1.036
1.655
PPM
8.2
8.0
7.8
7.6
7.4

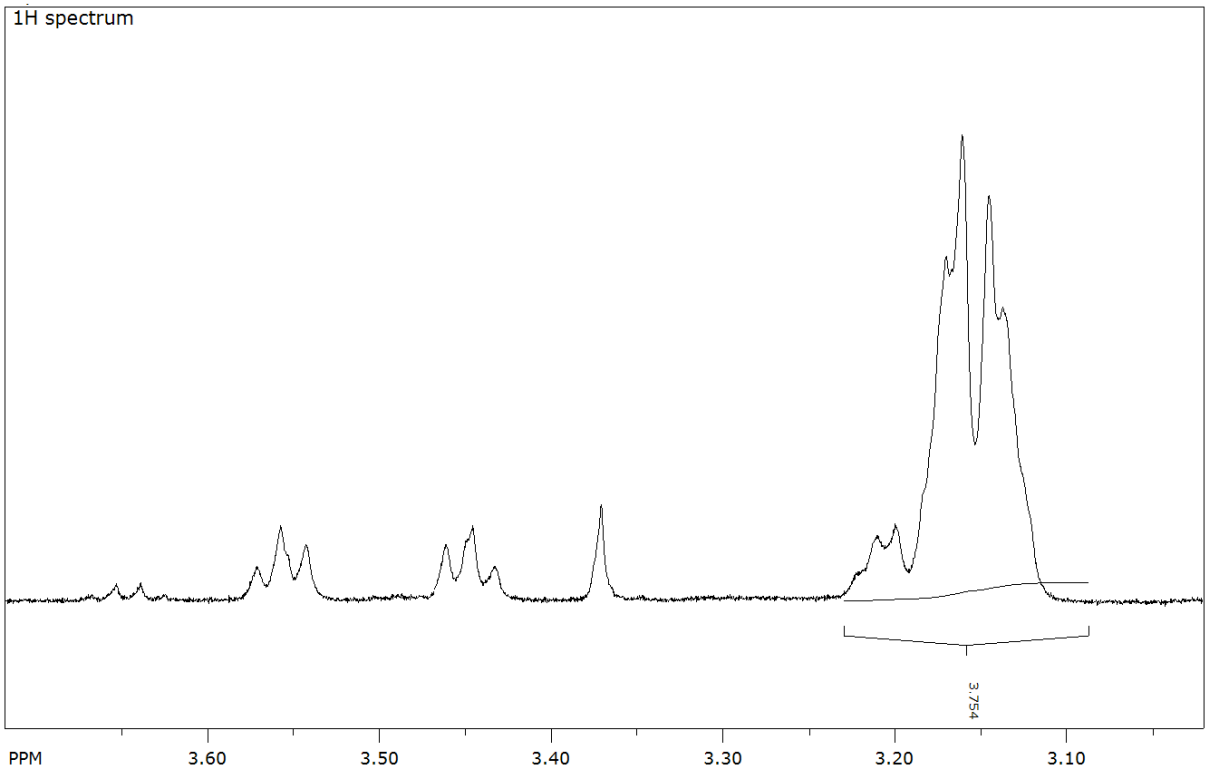
1H spectrum
3.754
PPM
3.60
3.50
3.40
3.30
3.20
3.10

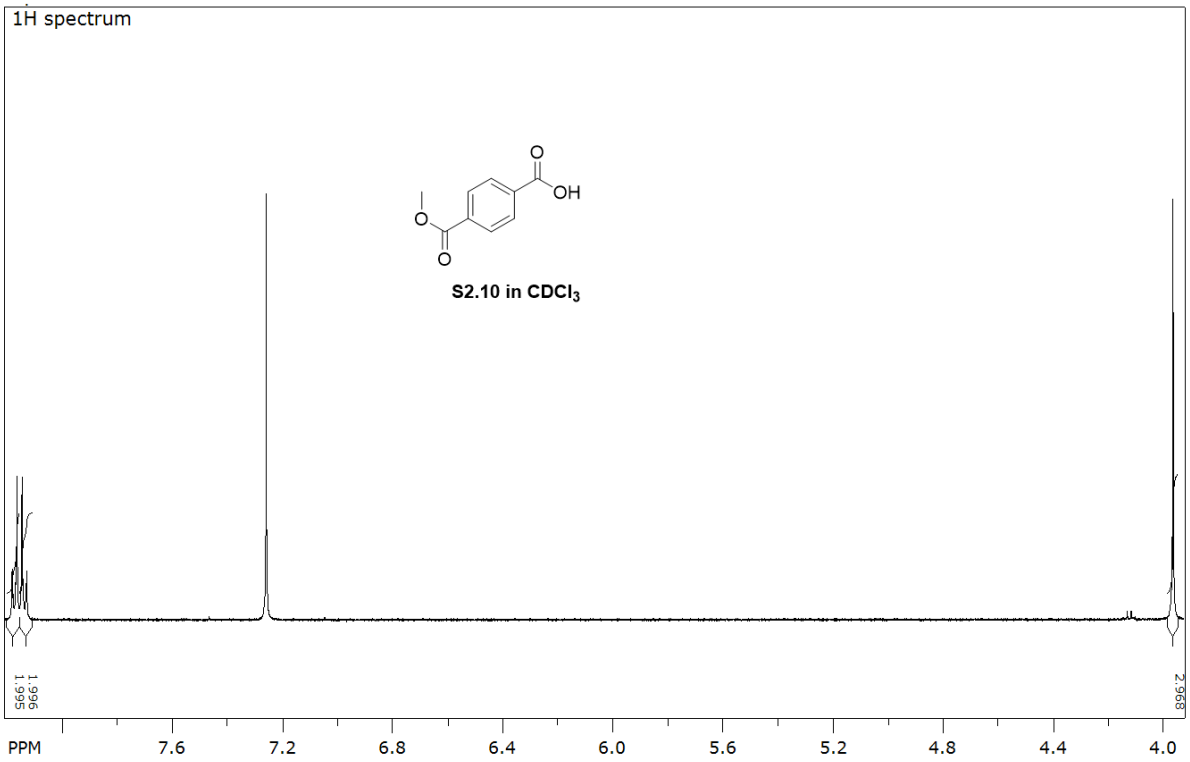
1H spectrum
O
OH
O
O
S2.10 in CDCl3
1.996
1.995
2.968
PPM
7.6
7.2
6.8
6.4
6.0
5.6
5.2
4.8
4.4
4.0

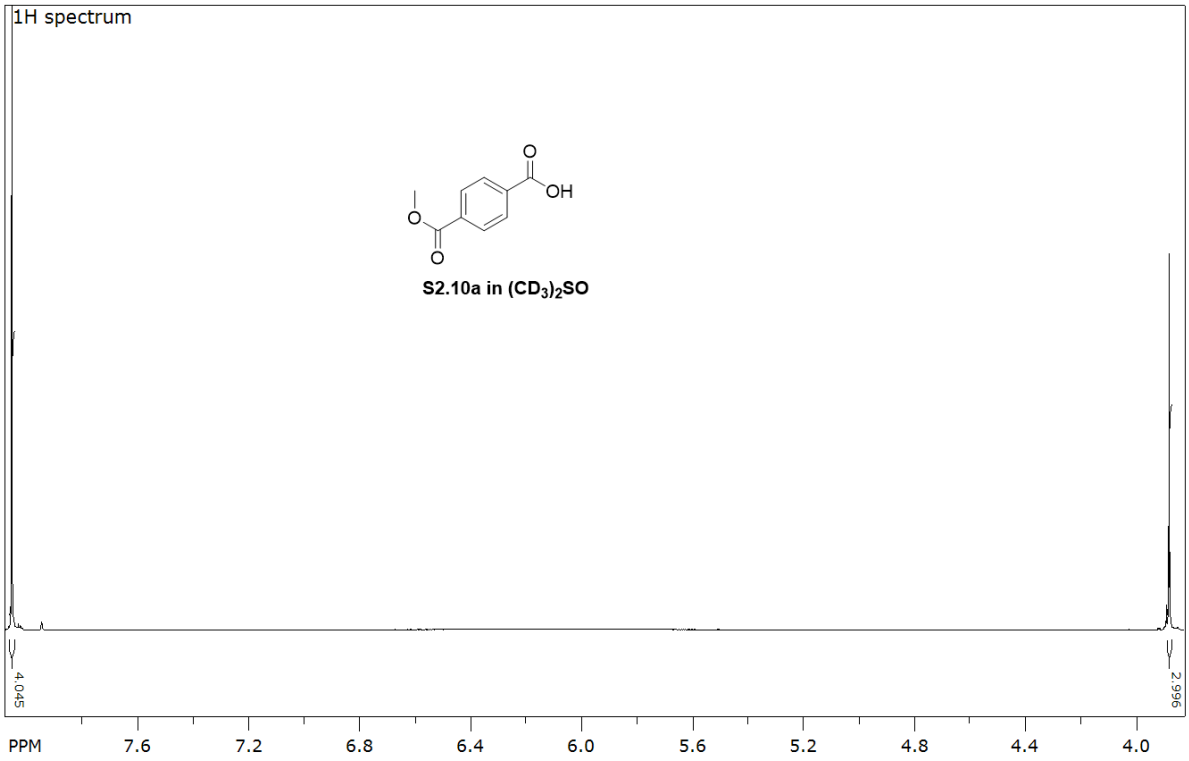
1H spectrum
O
OH
O
O
S2.10a in (CD3)2SO
4.045
2.996
PPM
7.6
7.2
6.8
6.4
6.0
5.6
5.2
4.8
4.4
4.0

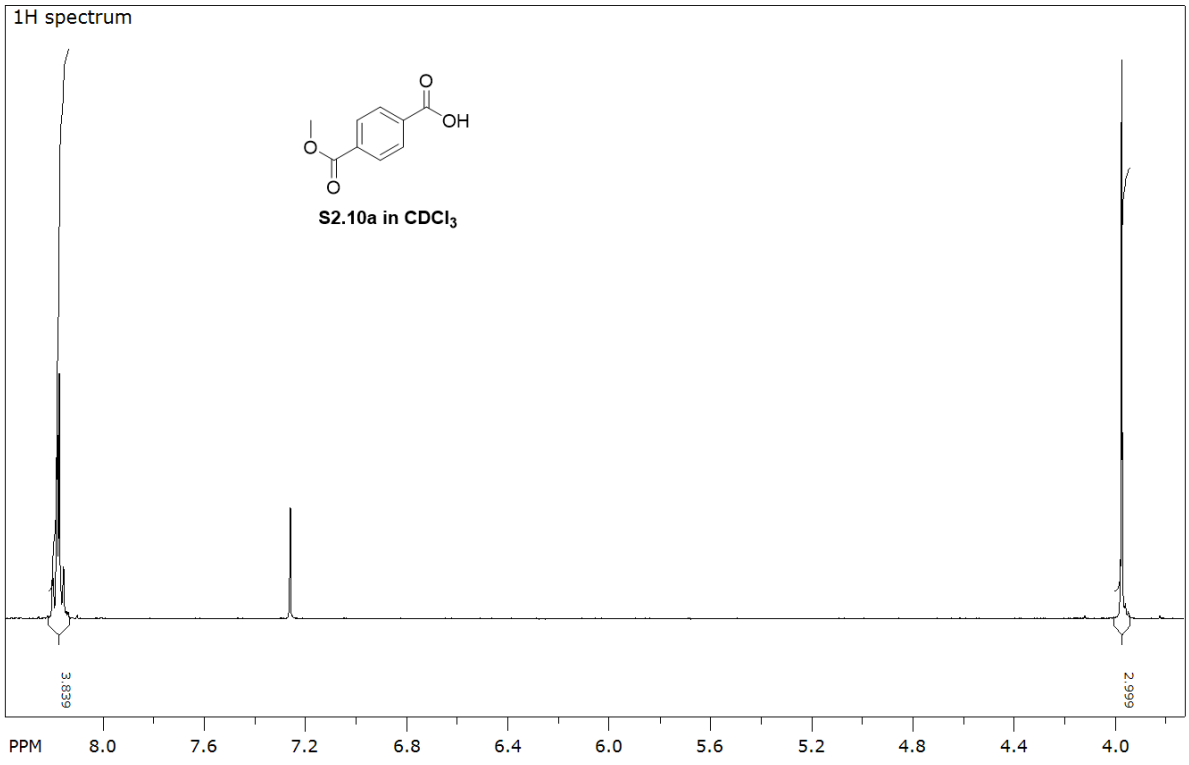
1H spectrum
O
OH
O
O
S2.10a in CDCl3
3.839
2.999
PPM
8.0
7.6
7.2
6.8
6.4
6.0
5.6
5.2
4.8
4.4
4.0

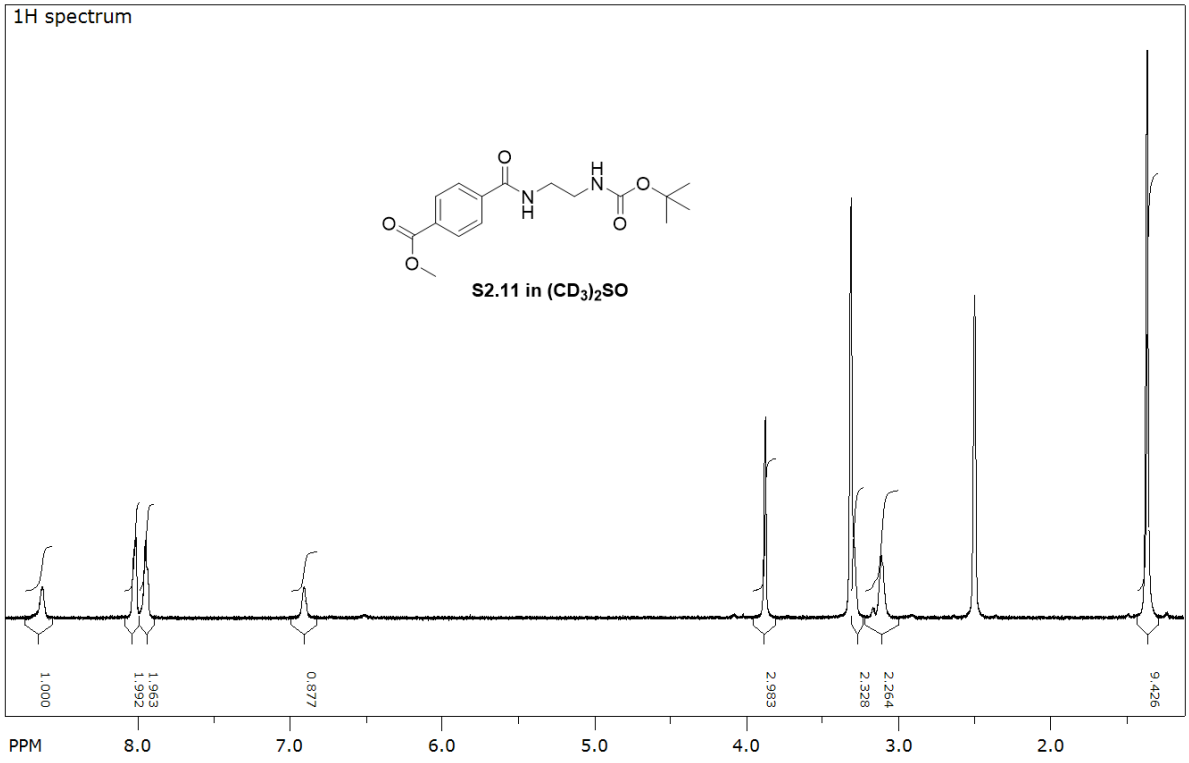
1H spectrum
O
N
H
H
N
O
O
O
O
S2.11 in (CD3)2SO
1.000
1.963
1.992
0.877
2.983
2.328
2.264
9.426
PPM
8.0
7.0
6.0
5.0
4.0
3.0
2.0

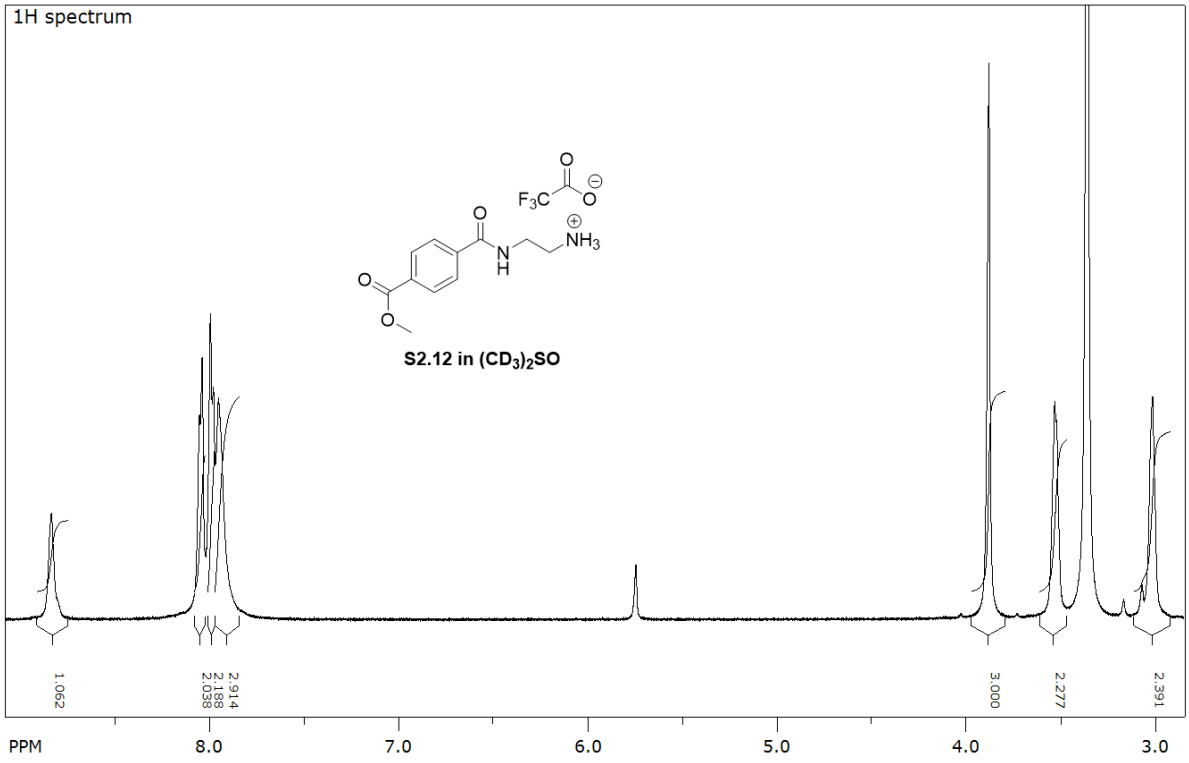
1H spectrum
S2.12 in (CD3)2SO
1.062
2.914
2.188
2.038
3.000
2.277
2.391
PPM
8.0
7.0
6.0
5.0
4.0
3.0

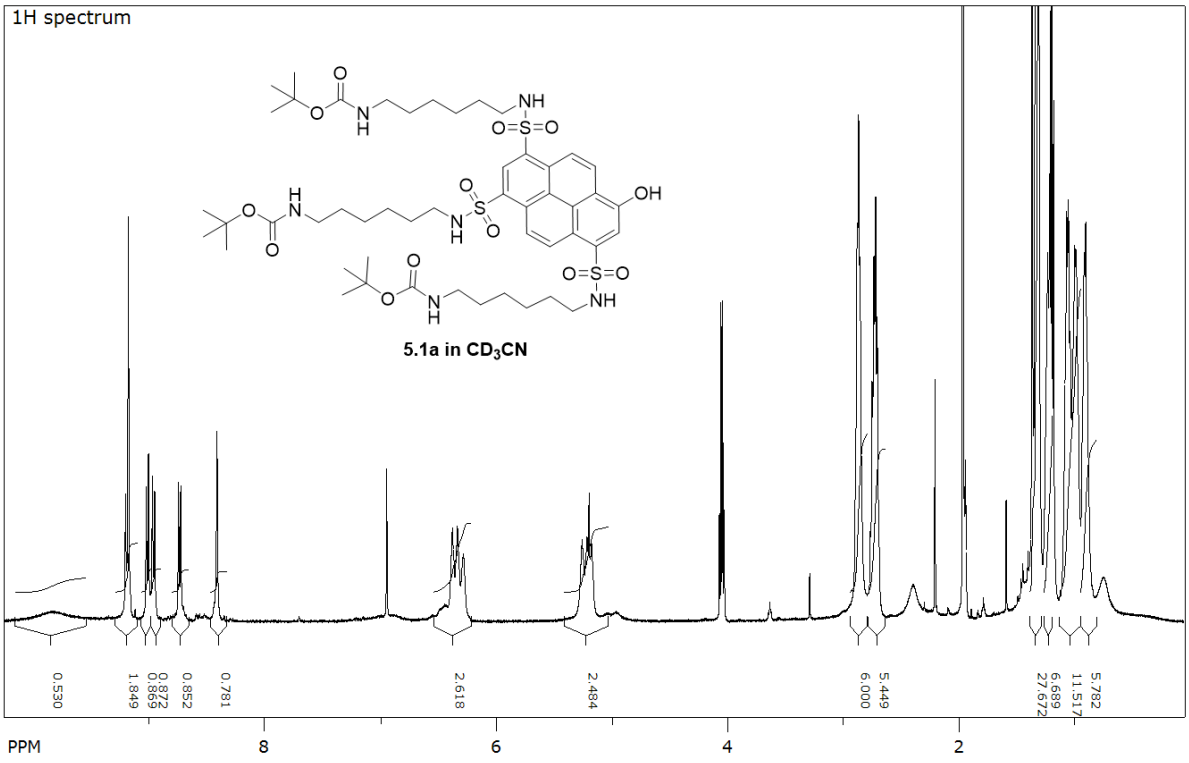
1H spectrum
5.1a in CD3CN
0.530
1.849
0.872
0.865
0.852
0.781
2.618
2.484
6.000
5.449
27.672
6.689
11.517
5.782
PPM
8
6
4
2

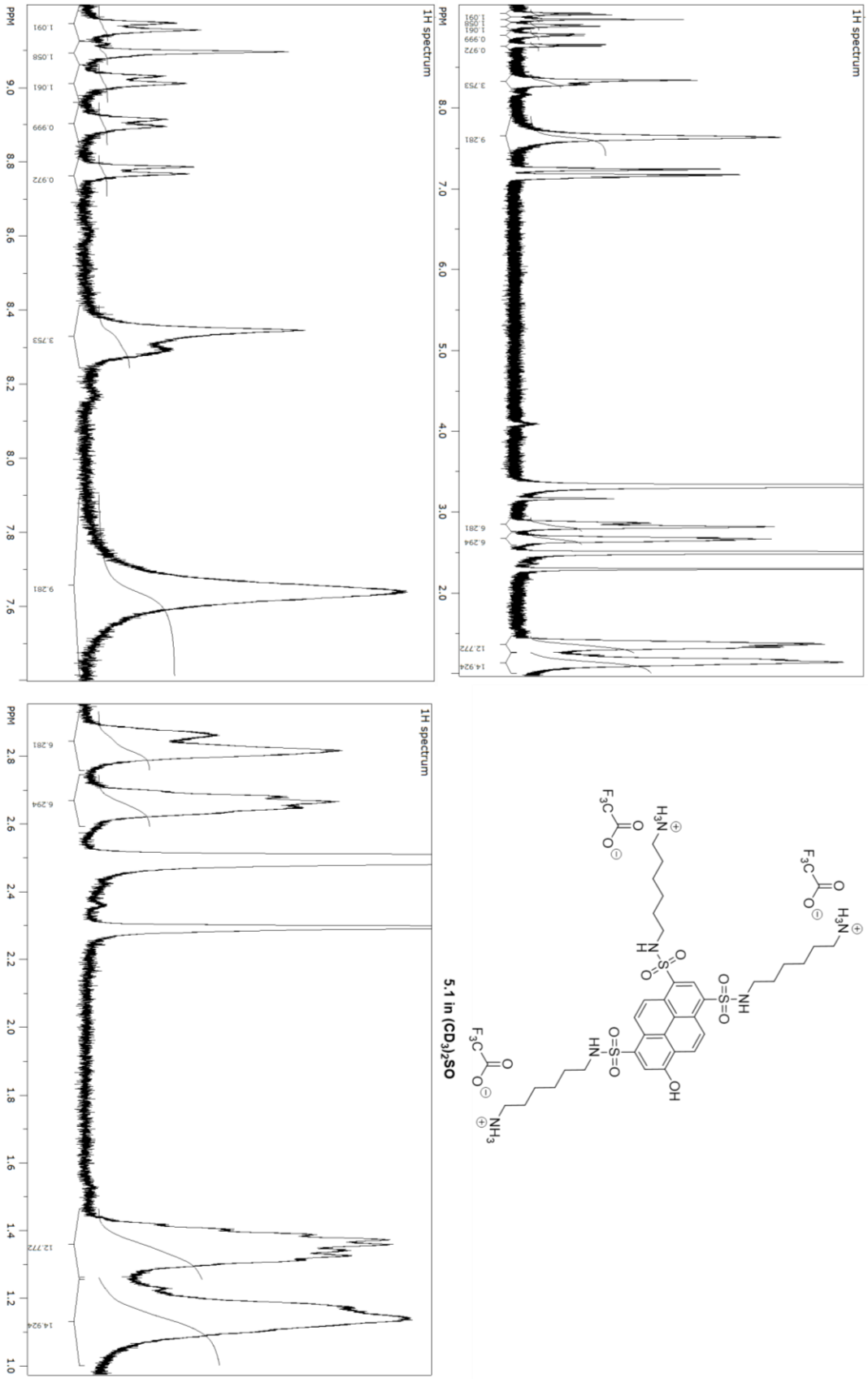
1H spectrum
PPM
14.924
12.772
9.281
6.294
6.281
3.753
0.972
0.999
1.061
1.058
1.091
5.1 in (CD3)2SO

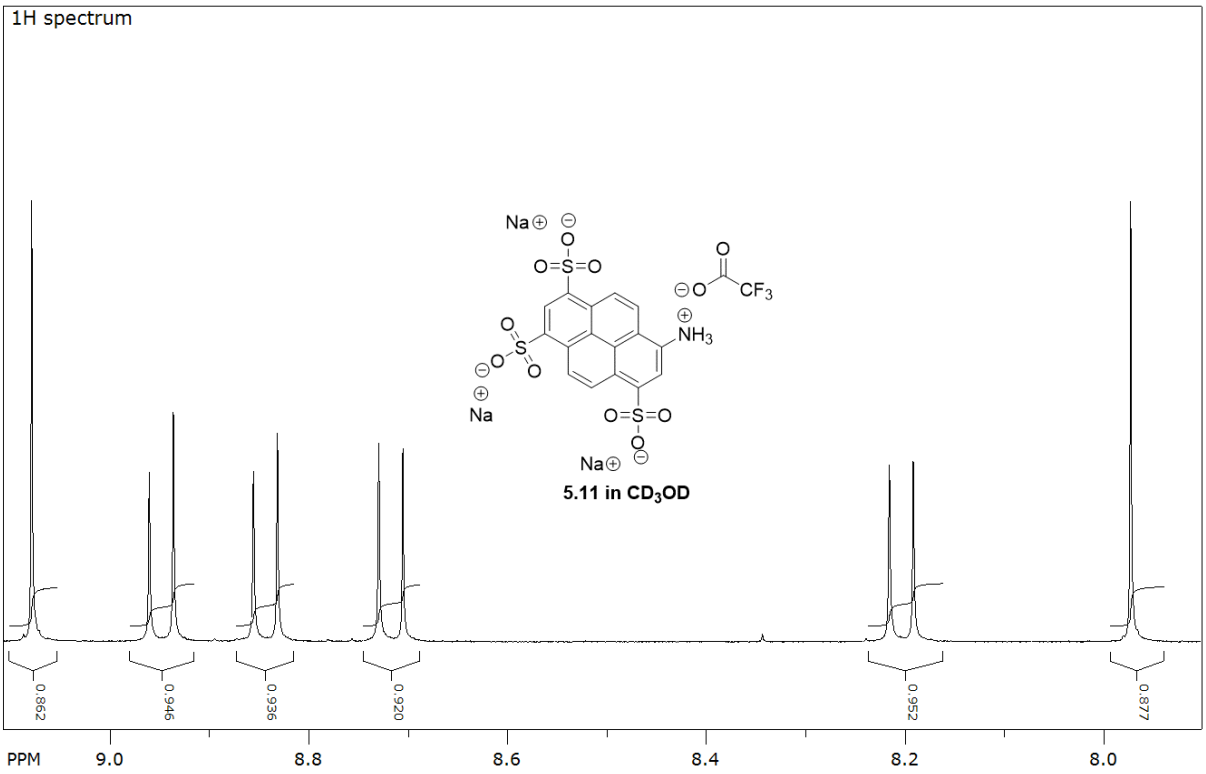

5.11 in CD_3OD

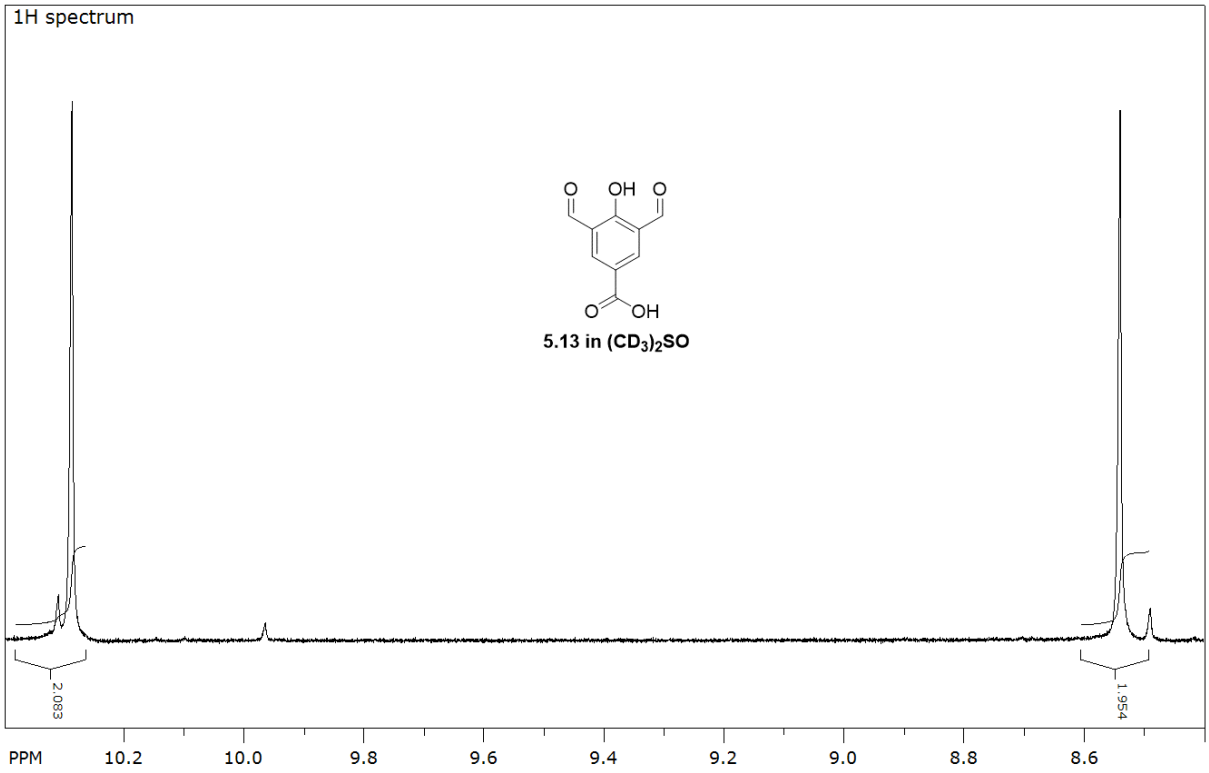

5.13 in $(CD_3)_2SO$

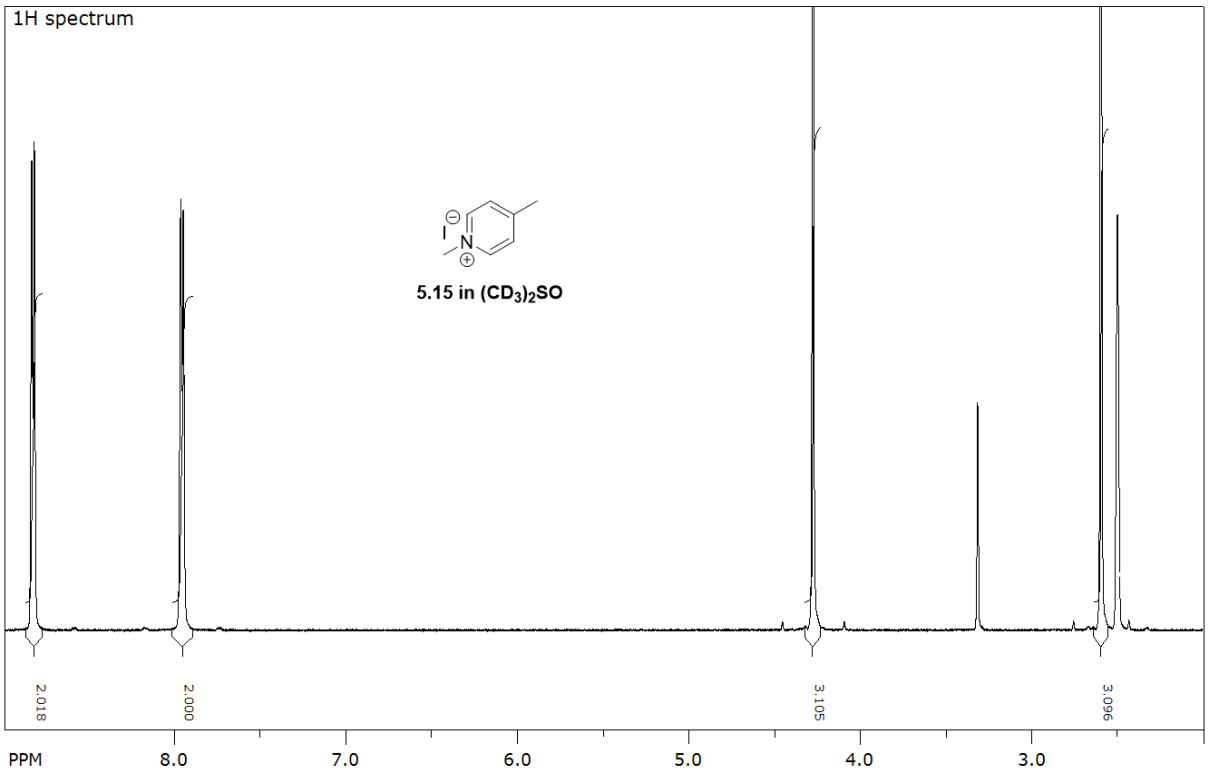
1H spectrum
5.15 in (CD3)2SO
2.018
2.000
3.105
3.096
PPM
8.0
7.0
6.0
5.0
4.0
3.0

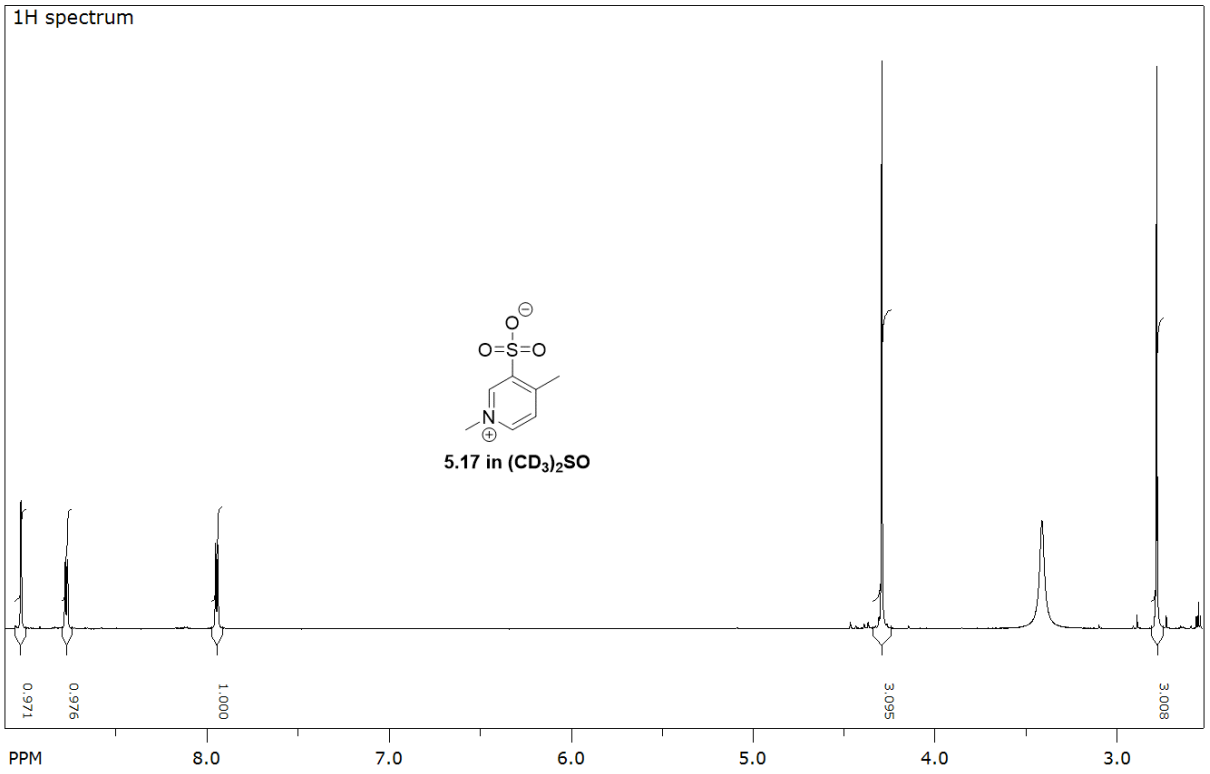
1H spectrum
5.17 in (CD3)2SO
0.971
0.976
1.000
3.095
3.008
PPM
8.0
7.0
6.0
5.0
4.0
3.0

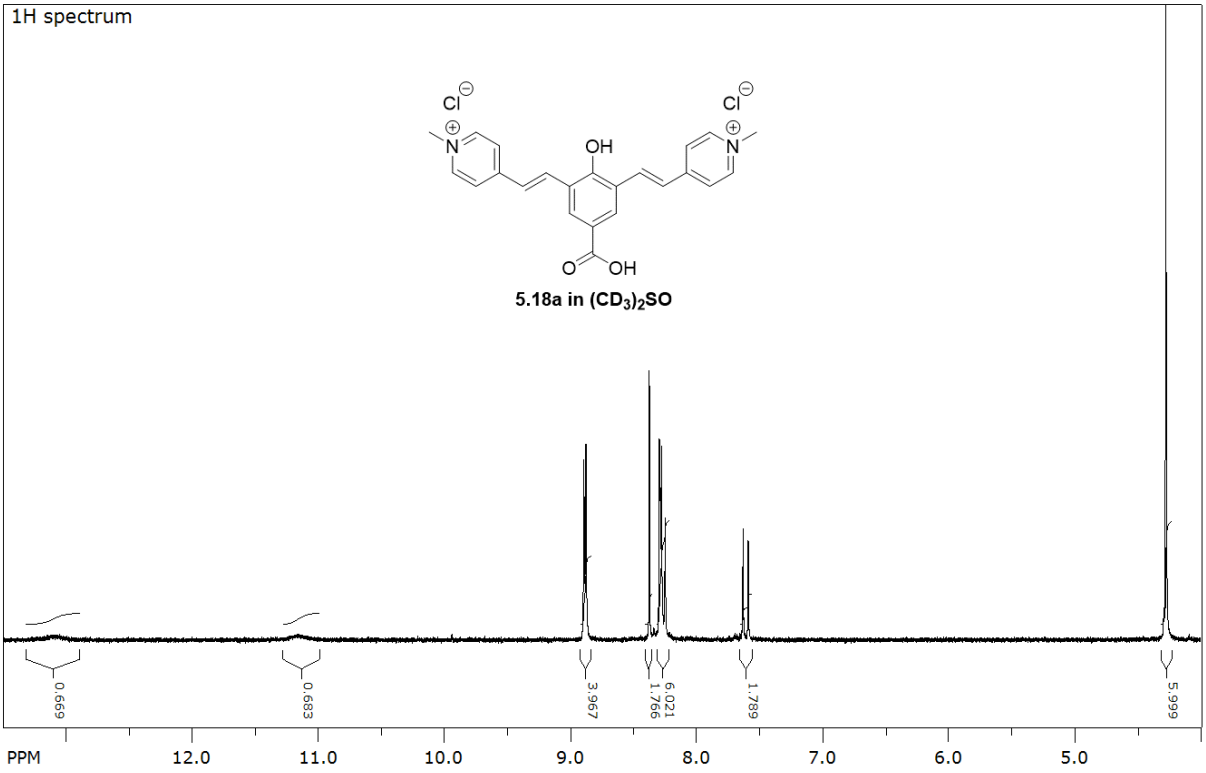

5.18a in $(CD_3)_2SO$

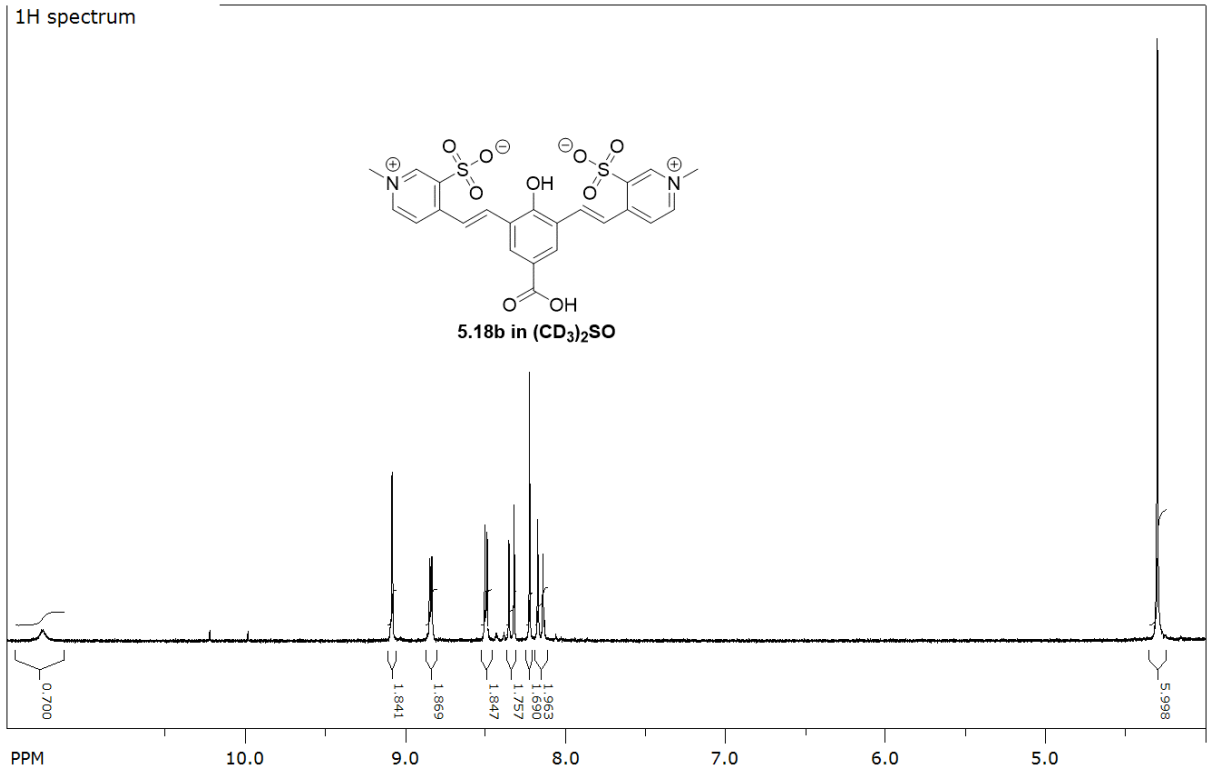

5.18b in $(CD_3)_2SO$

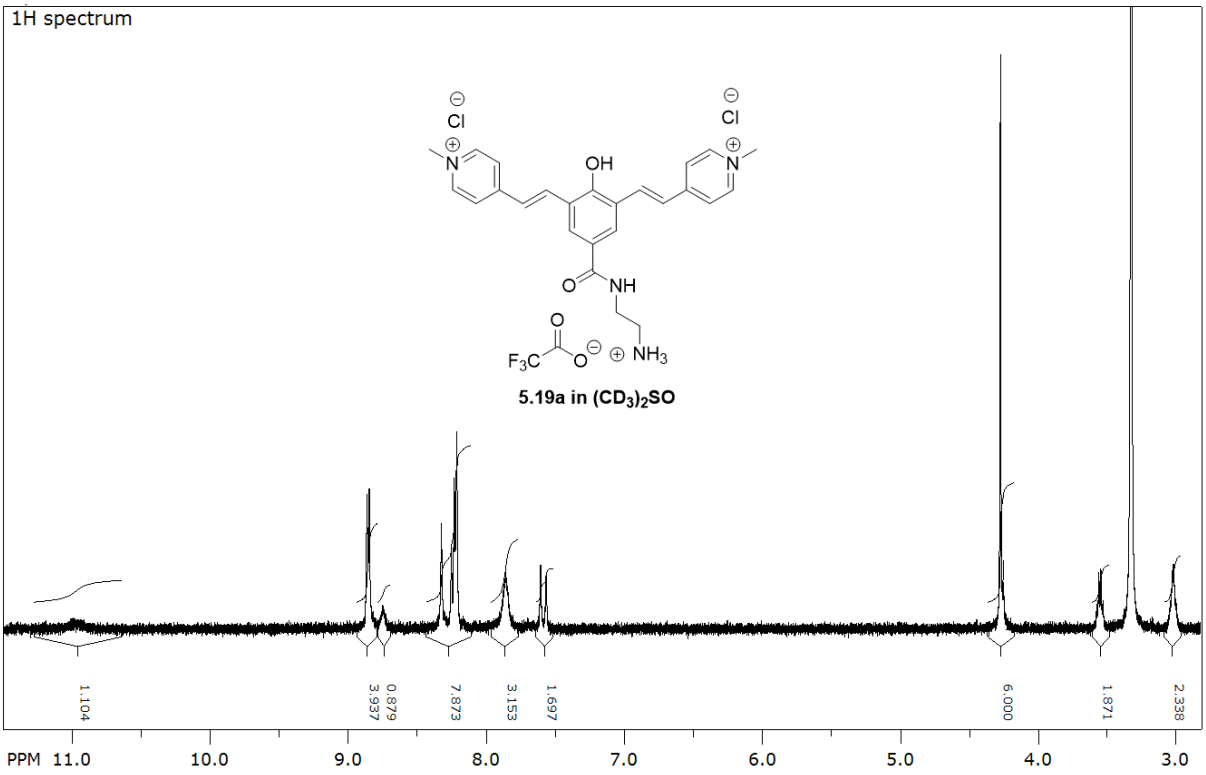
1H spectrum
Cl
Cl
OH
NH
NH3
F3C
5.19a in (CD3)2SO
1.104
3.937
0.879
7.873
3.153
1.697
6.000
1.871
2.338
PPM 11.0
10.0
9.0
8.0
7.0
6.0
5.0
4.0
3.0

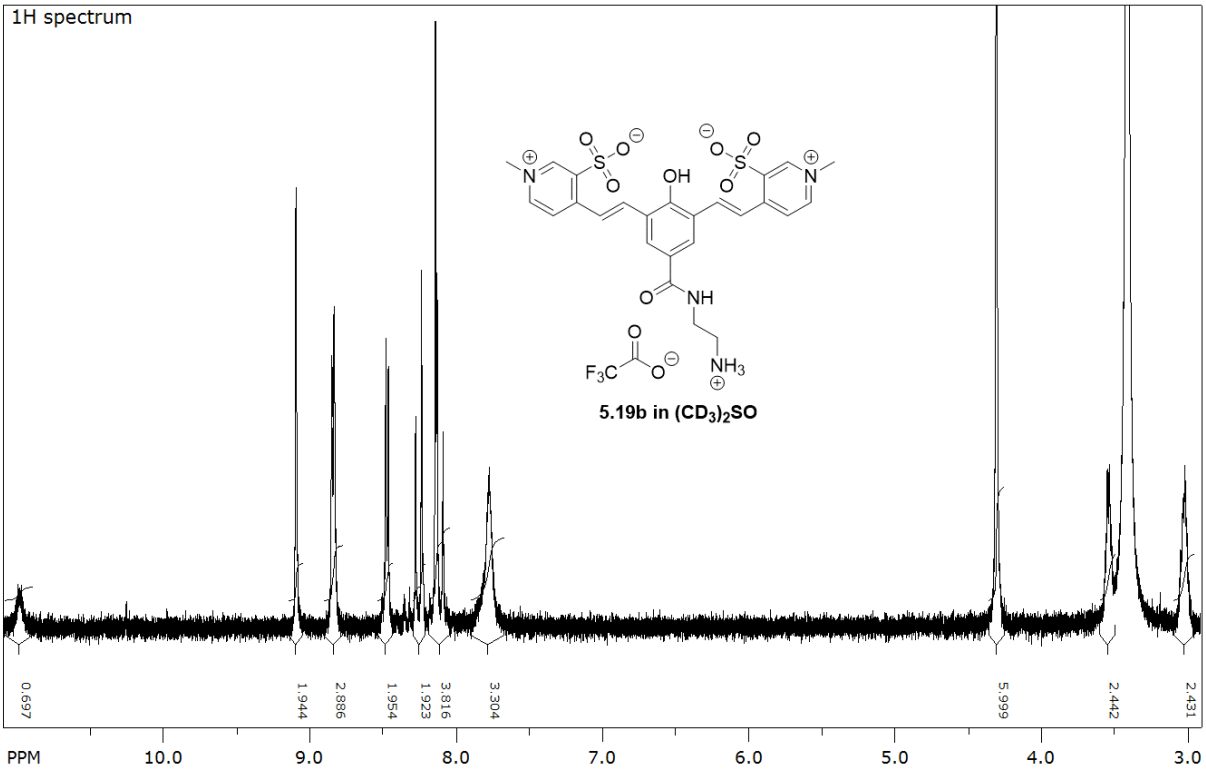
1H spectrum
OH
NH
NH3
F3C
5.19b in (CD3)2SO
0.697
1.944
2.886
1.954
1.923
3.816
3.304
5.999
2.442
2.431
PPM
10.0
9.0
8.0
7.0
6.0
5.0
4.0
3.0

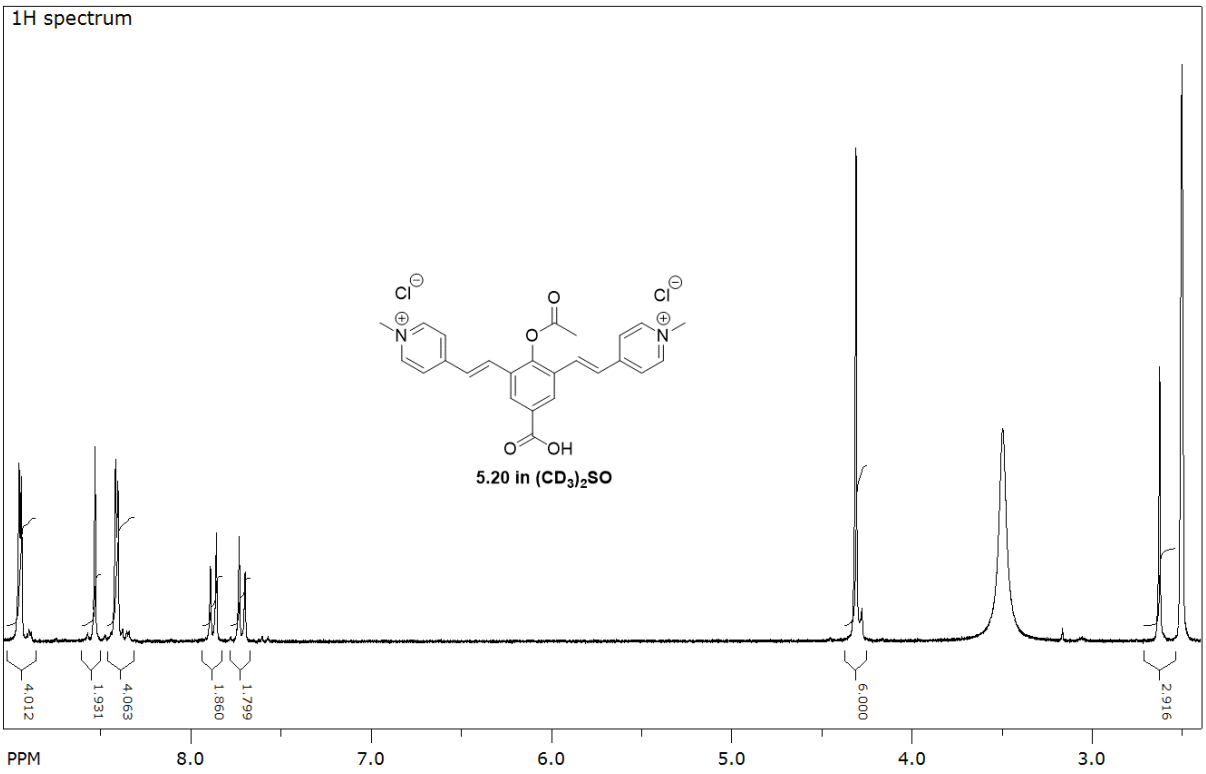
1H spectrum
Cl
N
O
O
Cl
N
O
OH
5.20 in (CD3)2SO
4.012
1.931
4.063
1.860
1.799
6.000
2.916
PPM
8.0
7.0
6.0
5.0
4.0
3.0

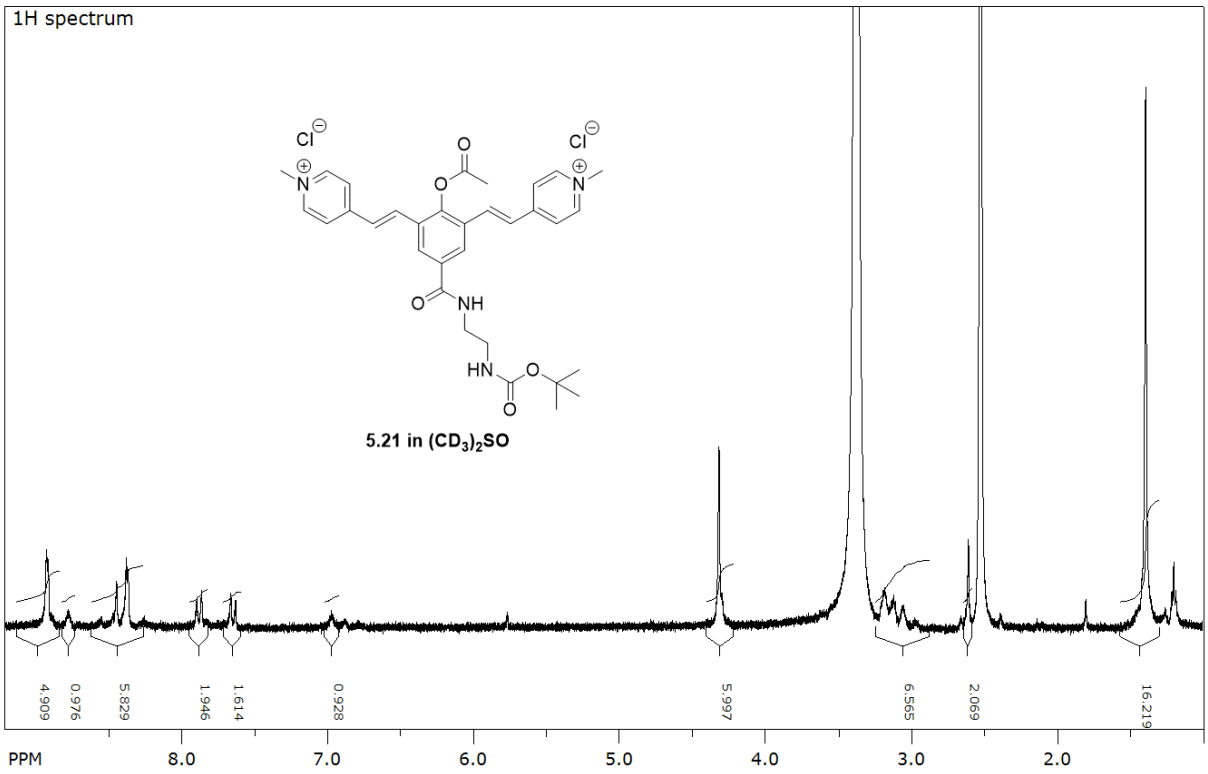
1H spectrum
Cl
N
O
O
Cl
N
O
NH
HN
O
O
5.21 in (CD3)2SO
4.909
0.976
5.829
1.946
1.614
0.928
5.997
6.565
2.069
16.219
PPM
8.0
7.0
6.0
5.0
4.0
3.0
2.0

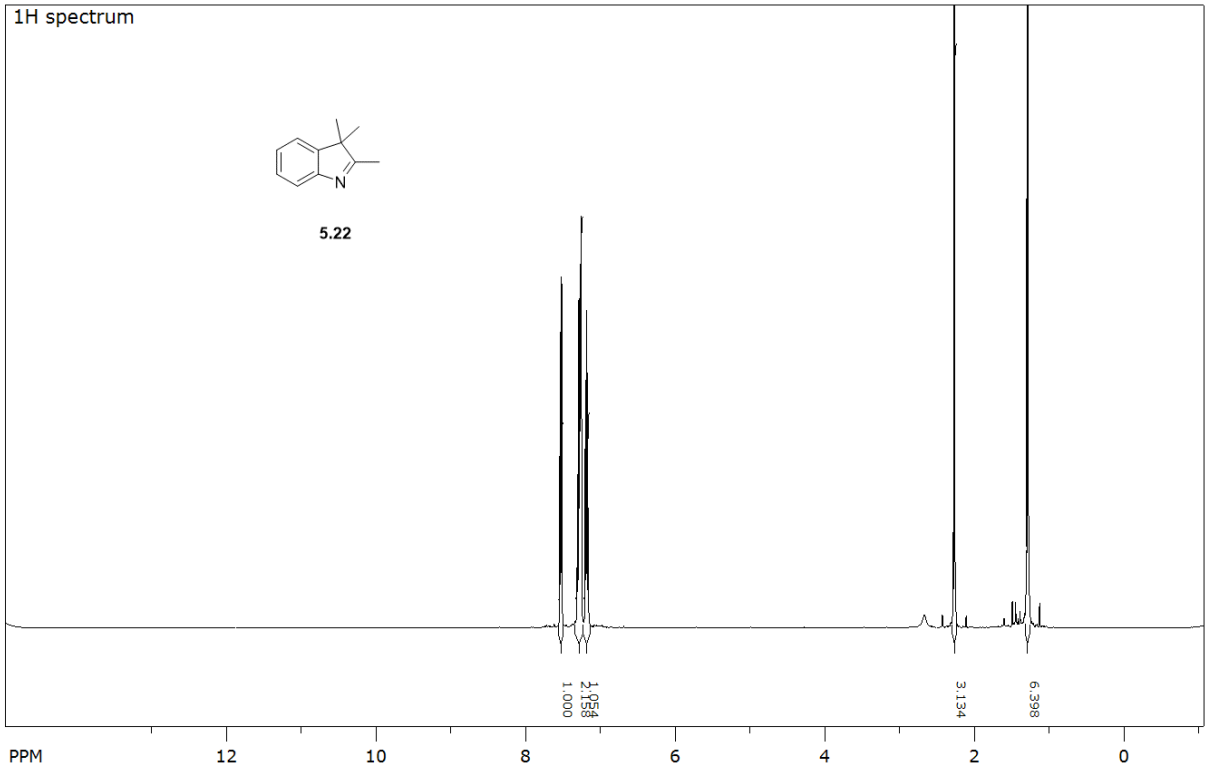
1H spectrum
5.22
1.000
2.158
1.054
3.134
6.398
PPM
12
10
8
6
4
2
0

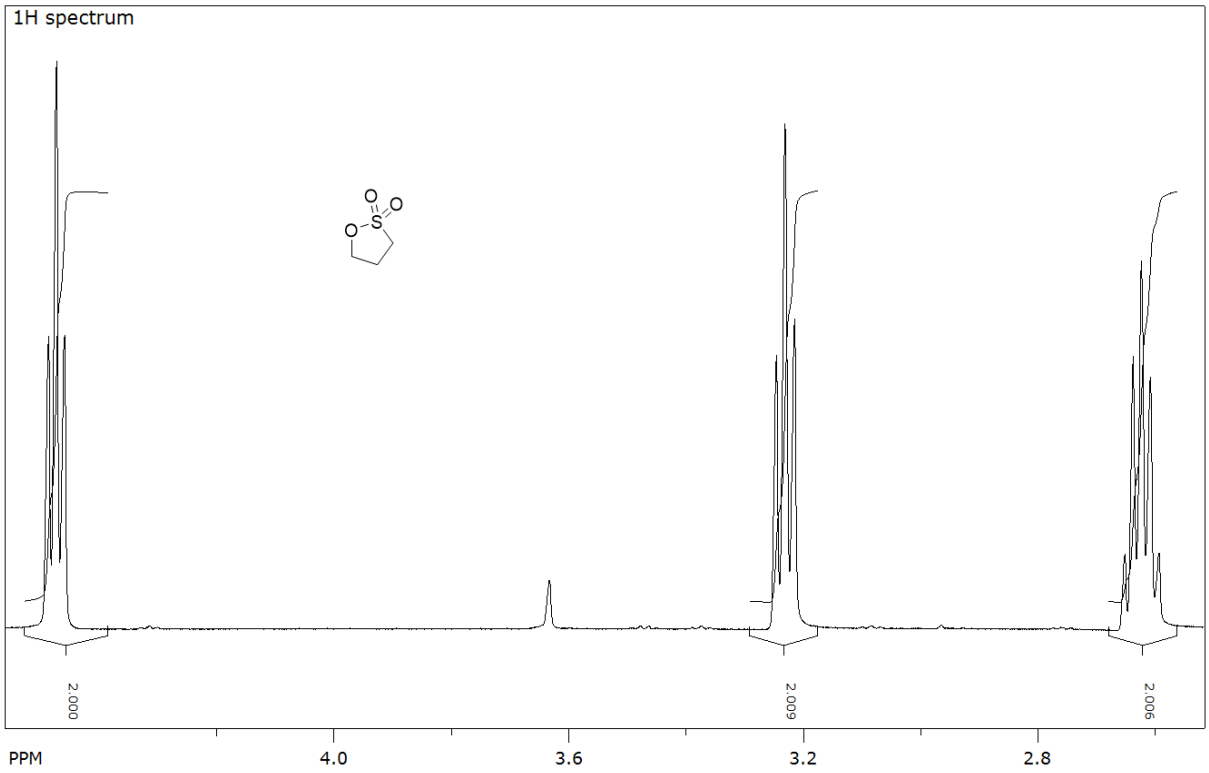
1H spectrum
2.000
2.009
2.006
PPM
4.0
3.6
3.2
2.8

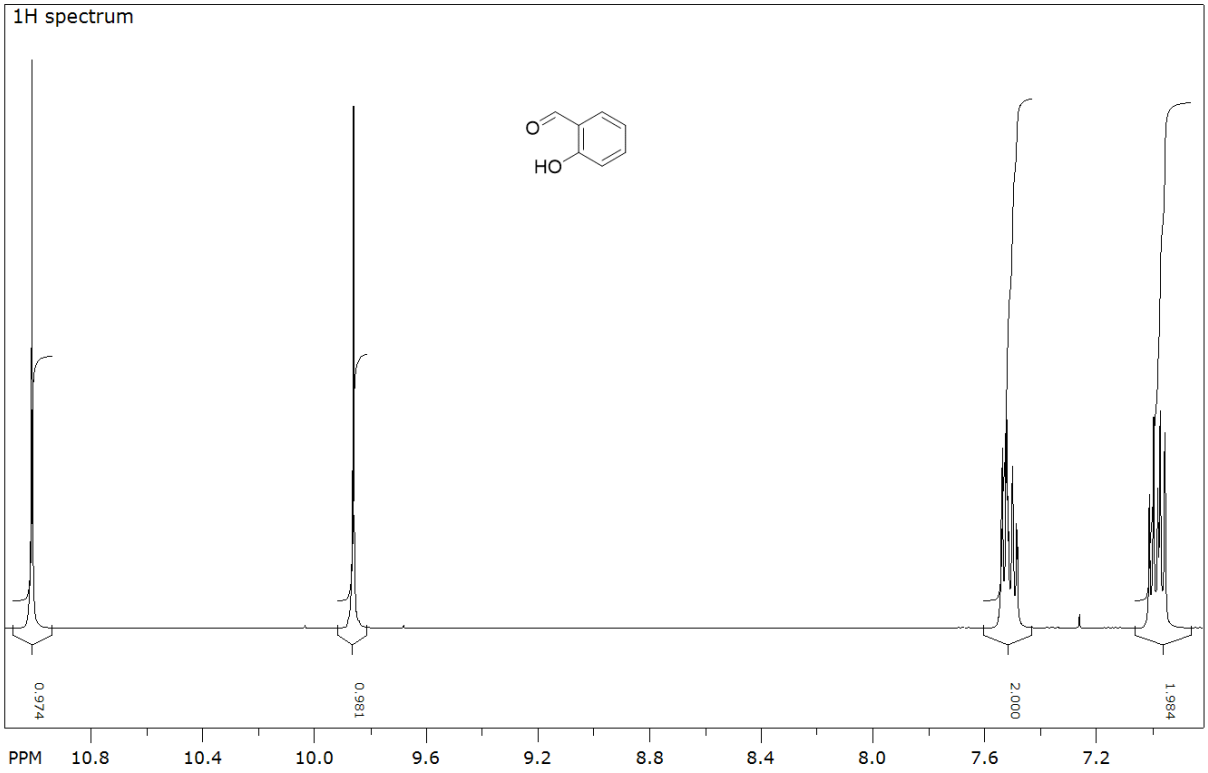
1H spectrum
O
HO
0.974
0.981
2.000
1.984
PPM
10.8
10.4
10.0
9.6
9.2
8.8
8.4
8.0
7.6
7.2

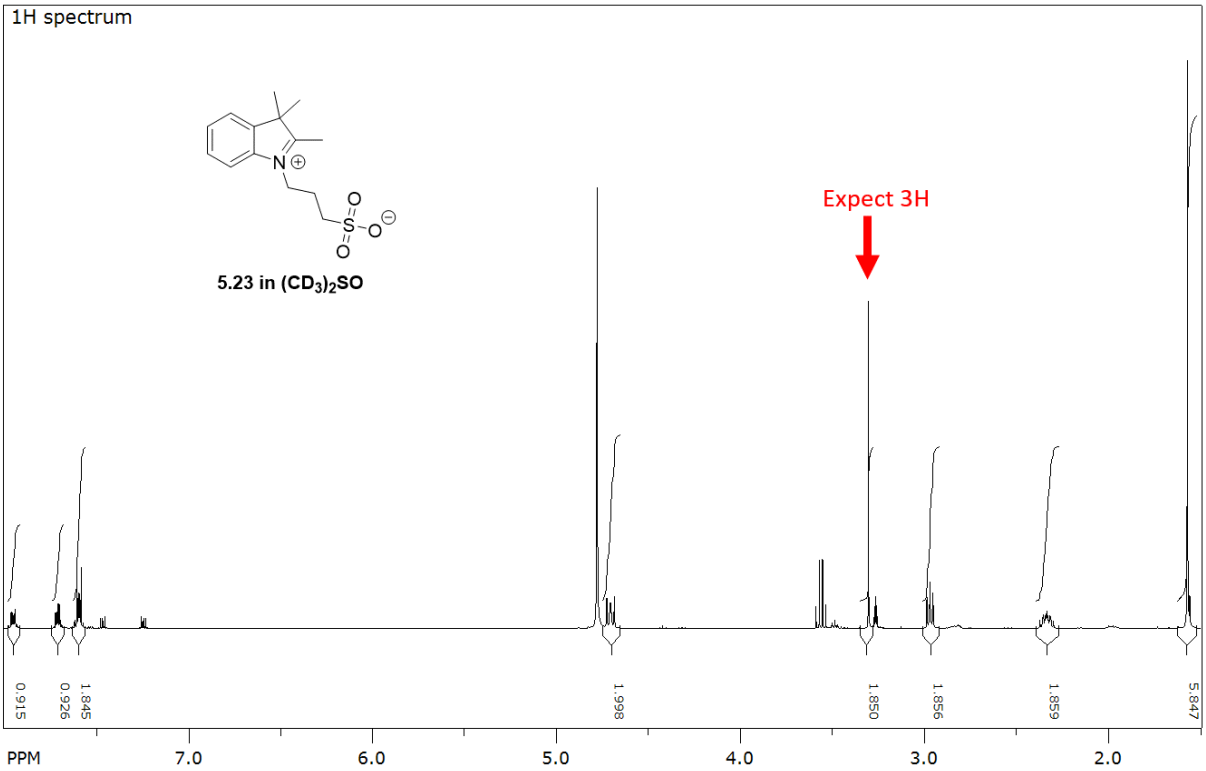
1H spectrum
N
O
S
O
O
5.23 in (CD3)2SO
Expect 3H
0.915
0.926
1.845
1.998
1.850
1.856
1.859
5.847
PPM
7.0
6.0
5.0
4.0
3.0
2.0

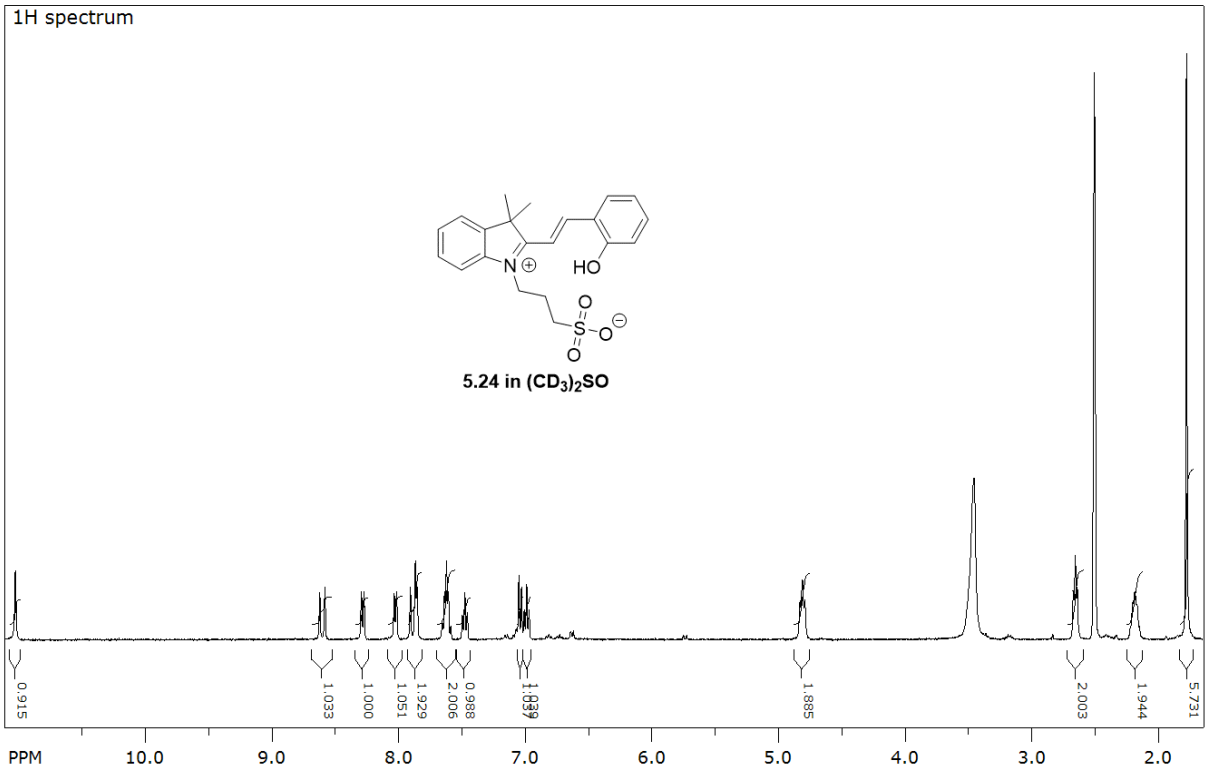
1H spectrum
HO
N
S
O
O
O
5.24 in (CD3)2SO
0.915
1.033
1.000
1.051
1.929
2.006
0.988
1.885
2.003
1.944
5.731
PPM
10.0
9.0
8.0
7.0
6.0
5.0
4.0
3.0
2.0

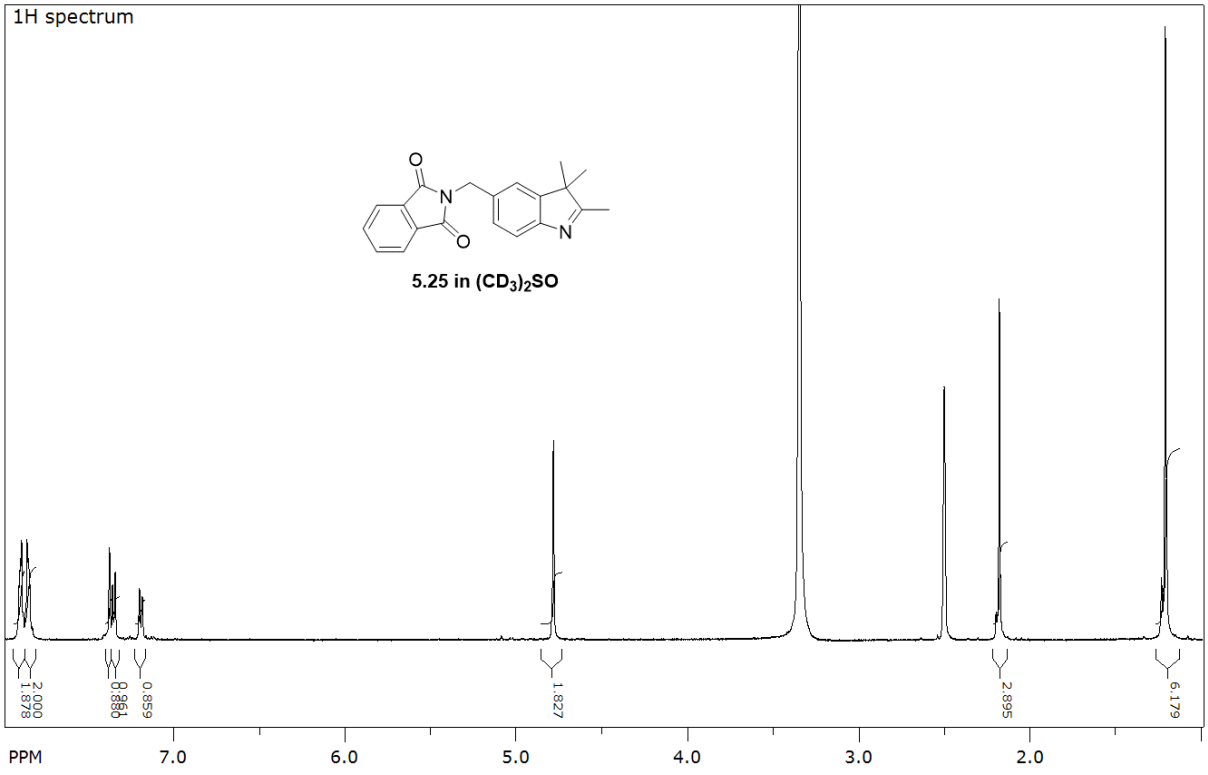
1H spectrum
O
N
O
N
5.25 in (CD3)2SO
2.000
1.878
0.861
0.859
1.827
2.895
6.179
PPM
7.0
6.0
5.0
4.0
3.0
2.0

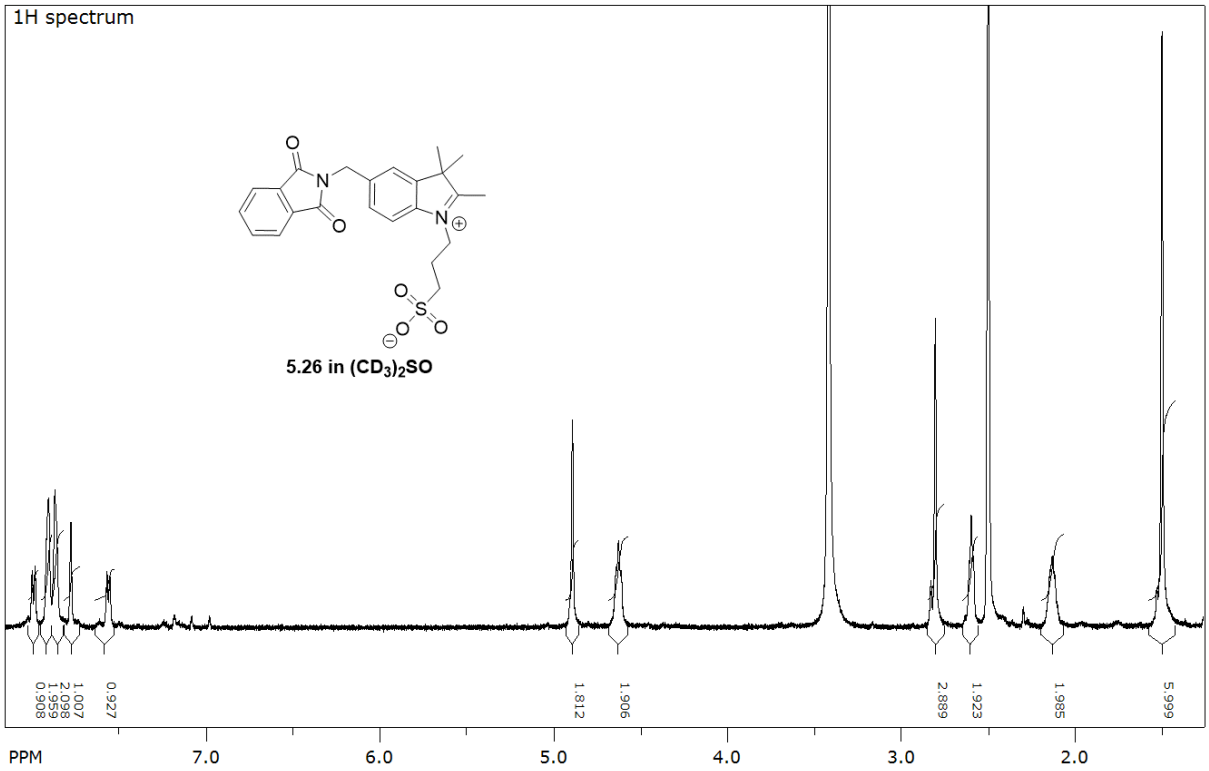
1H spectrum
5.26 in (CD3)2SO
0.908
1.007
1.959
2.008
0.927
1.812
1.906
2.889
1.923
1.985
5.999
PPM
7.0
6.0
5.0
4.0
3.0
2.0

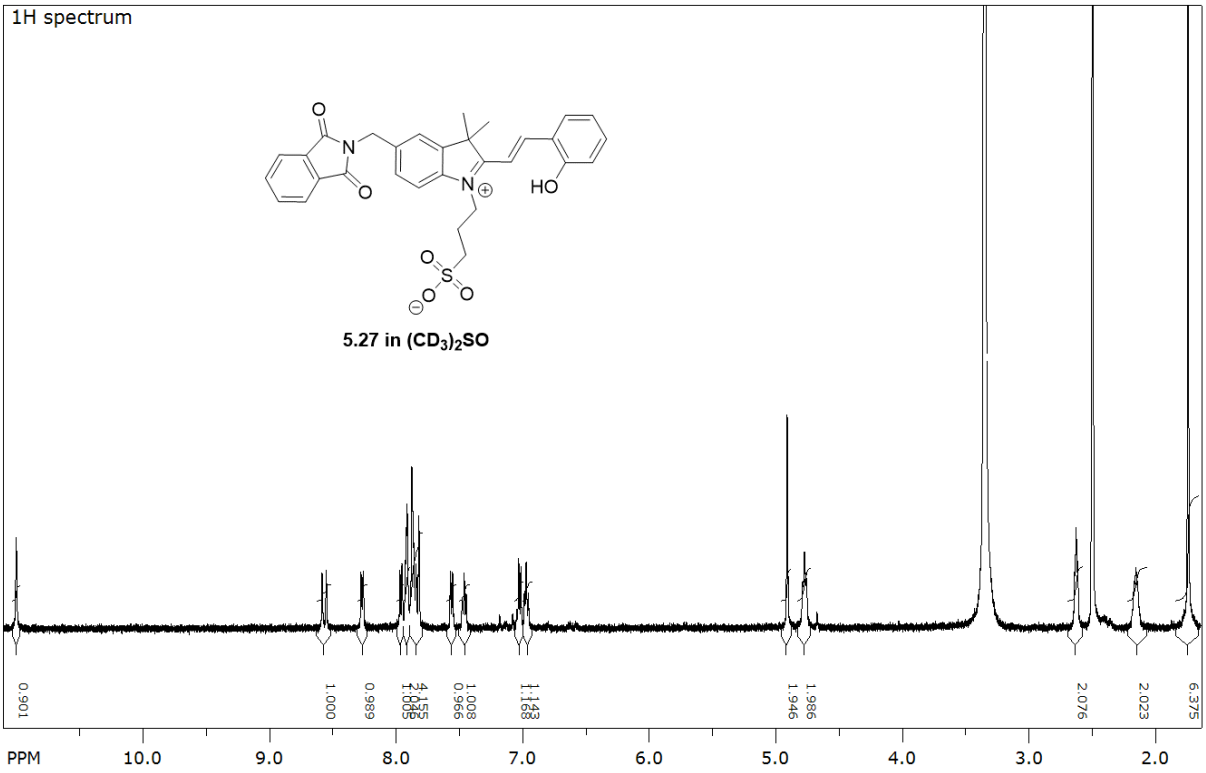
1H spectrum
HO
5.27 in (CD3)2SO
0.901
1.000
0.989
1.008
0.966
1.946
1.986
2.076
2.023
6.375
PPM
10.0
9.0
8.0
7.0
6.0
5.0
4.0
3.0
2.0

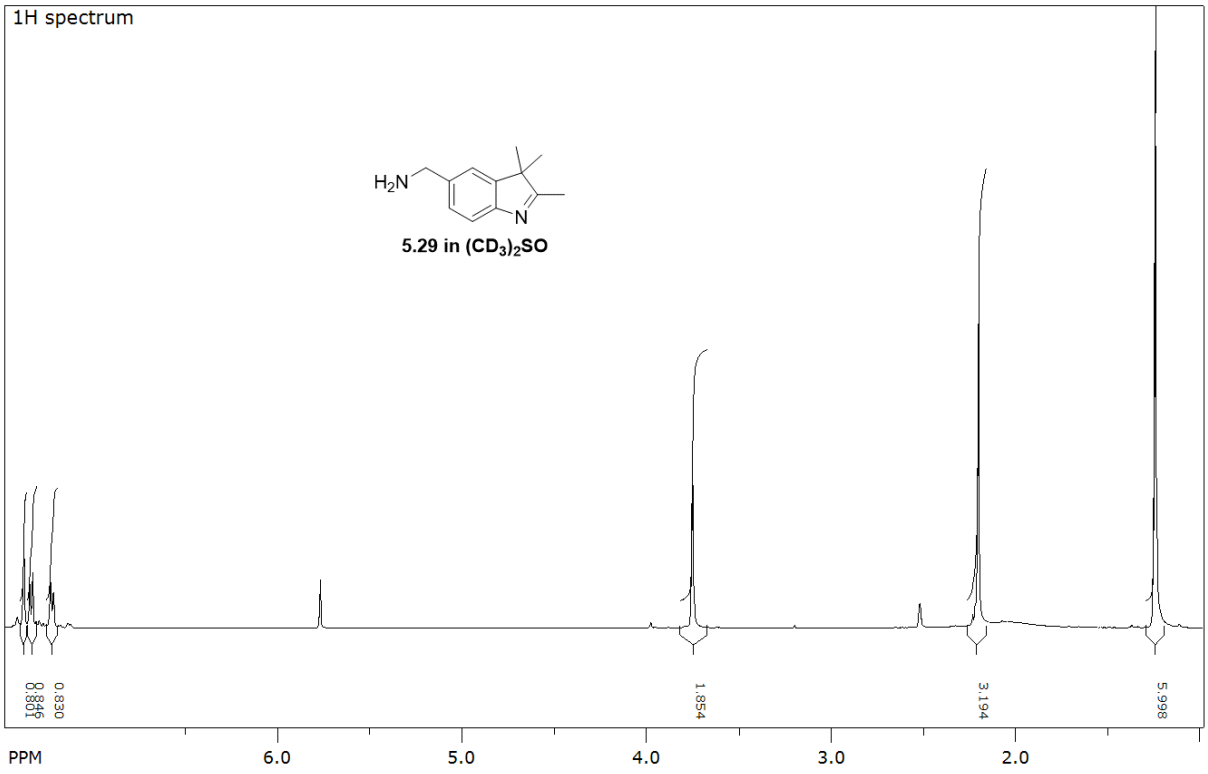
1H spectrum
H_2N
N
5.29 in $(CD_3)_2SO$
0.801
0.846
0.830
1.854
3.194
5.998
PPM
6.0
5.0
4.0
3.0
2.0

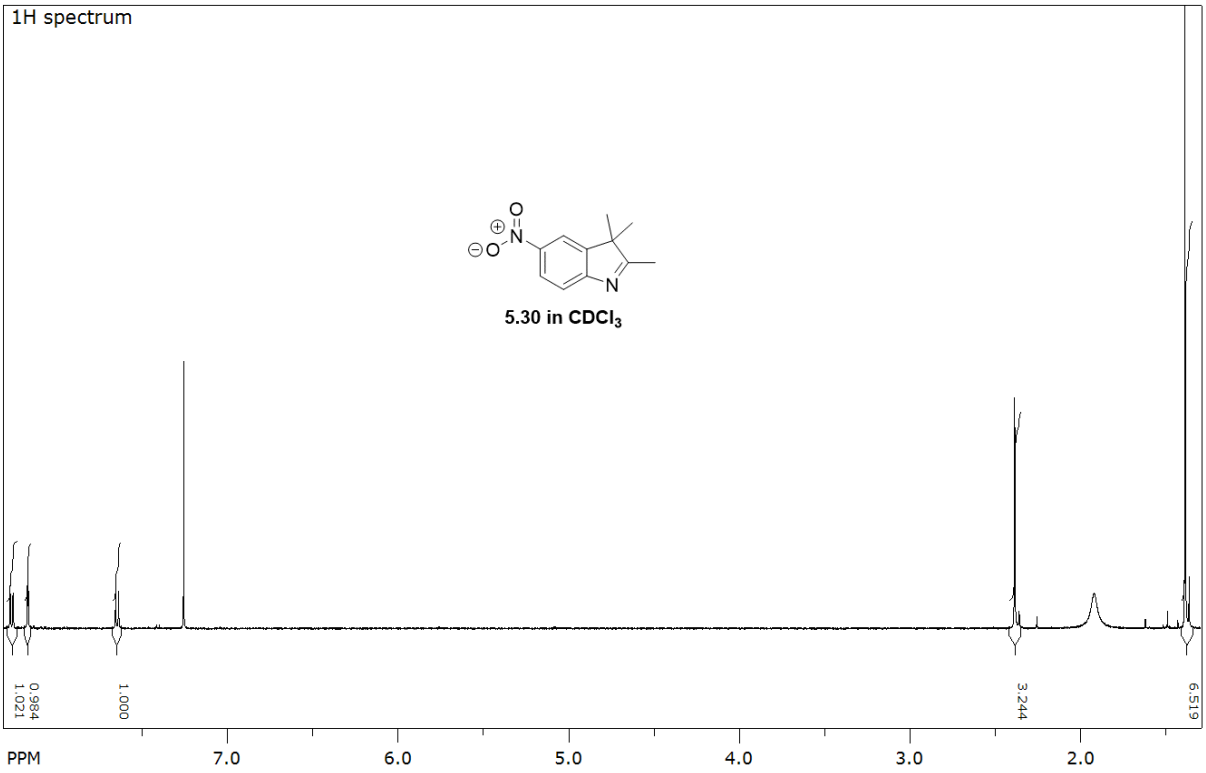
1H spectrum
O
N
O
N
5.30 in $CDCl_3$
1.021
0.984
1.000
3.244
6.519
PPM
7.0
6.0
5.0
4.0
3.0
2.0

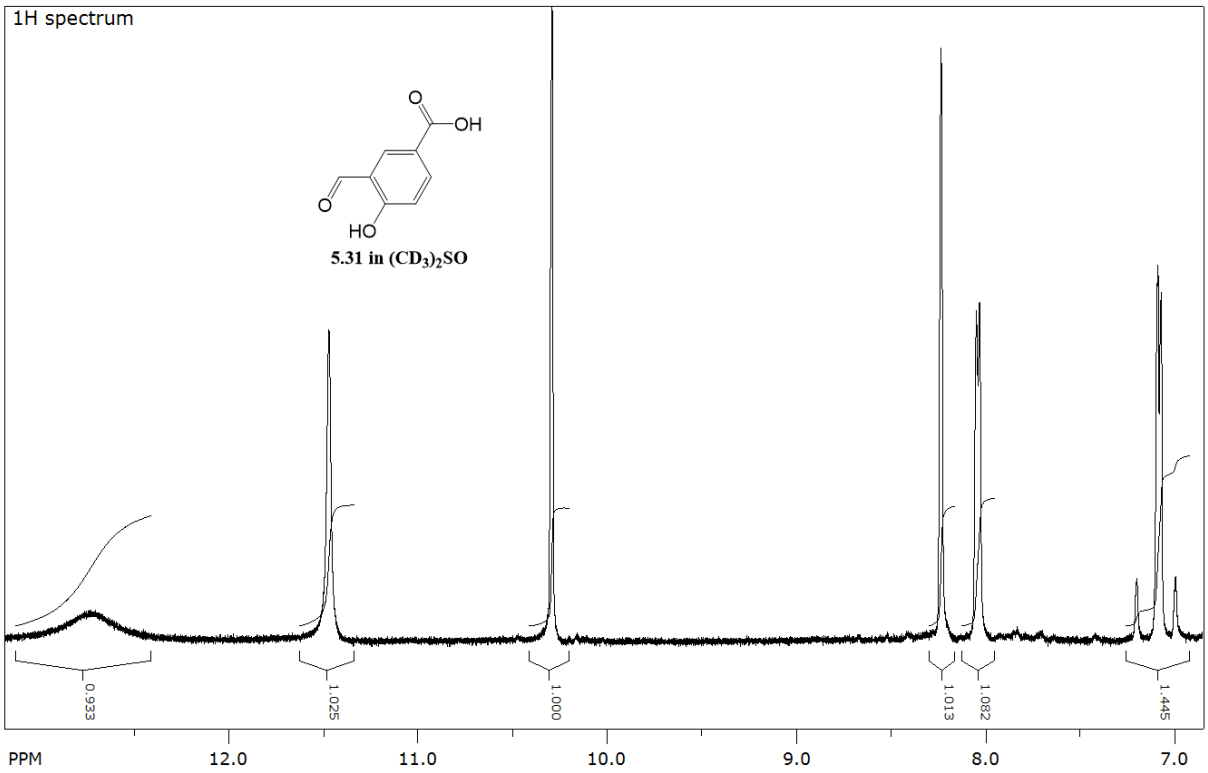
1H spectrum
O
OH
O
HO
5.31 in (CD3)2SO
0.933
1.025
1.000
1.013
1.082
1.445
PPM
12.0
11.0
10.0
9.0
8.0
7.0

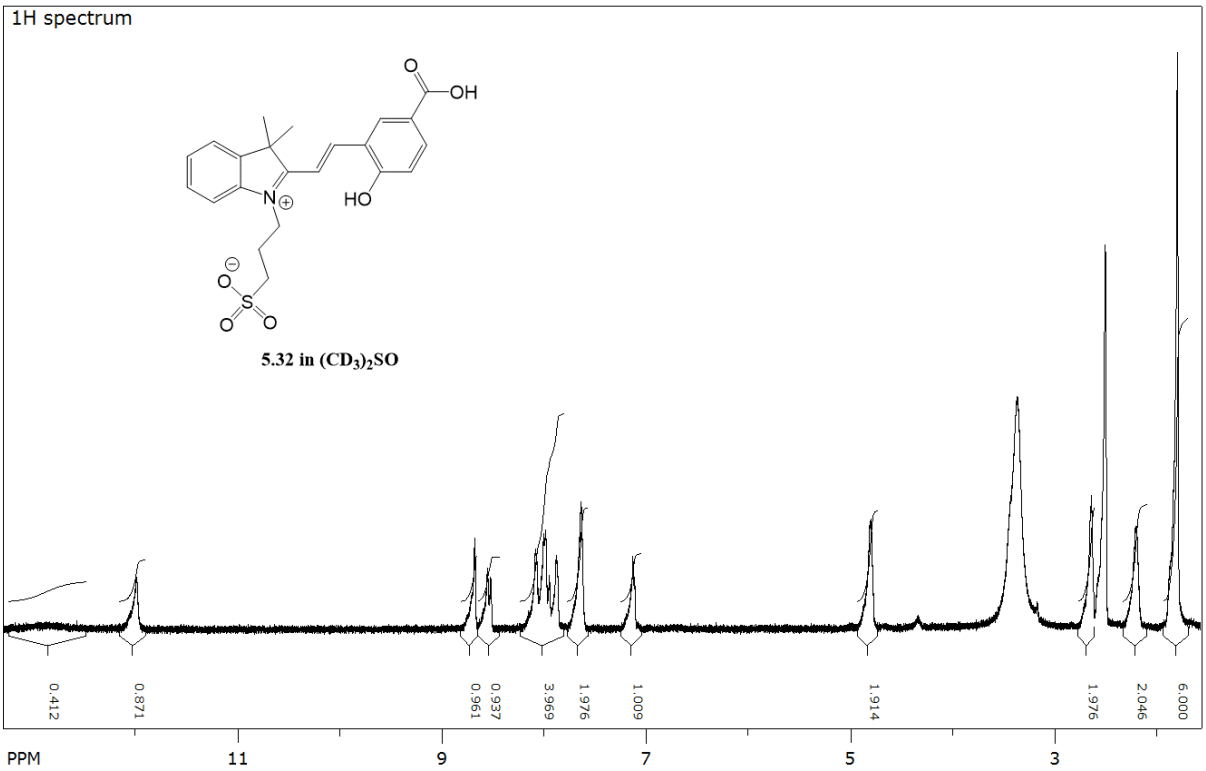
1H spectrum
O
OH
HO
N
O
S
O
O
5.32 in (CD3)2SO
0.412
0.871
0.961
0.937
3.969
1.976
1.009
1.914
1.976
2.046
6.000
PPM
11
9
7
5
3

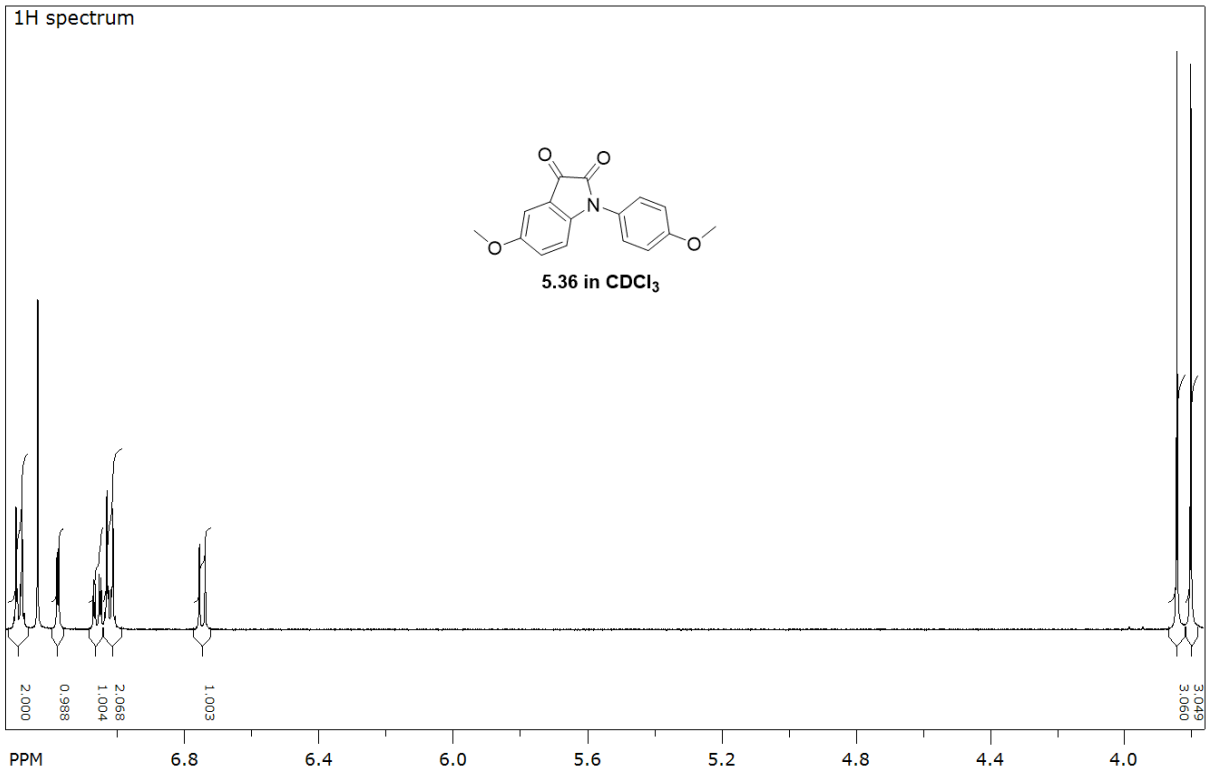
1H spectrum
5.36 in CDCl3
2.000
0.988
2.068
1.004
1.003
3.060
3.049
PPM
6.8
6.4
6.0
5.6
5.2
4.8
4.4
4.0

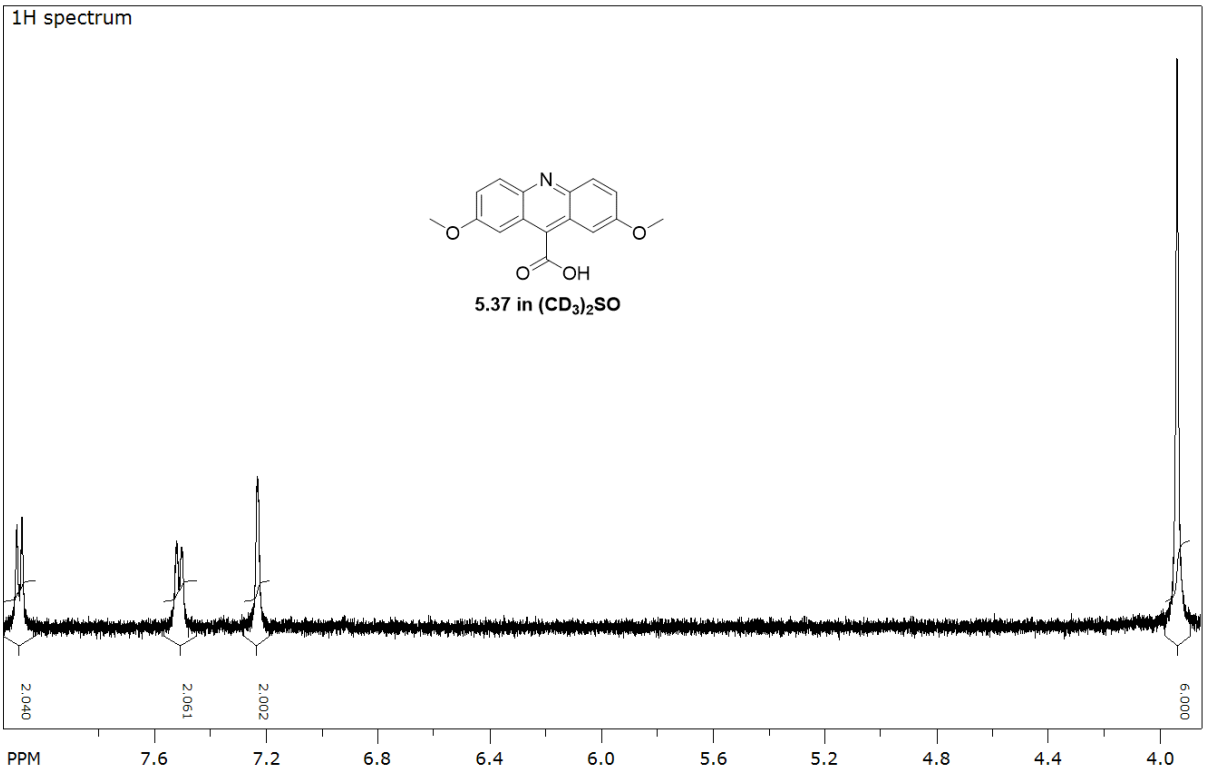
1H spectrum
5.37 in (CD3)2SO
2.040
2.061
2.002
6.000
PPM
7.6
7.2
6.8
6.4
6.0
5.6
5.2
4.8
4.4
4.0

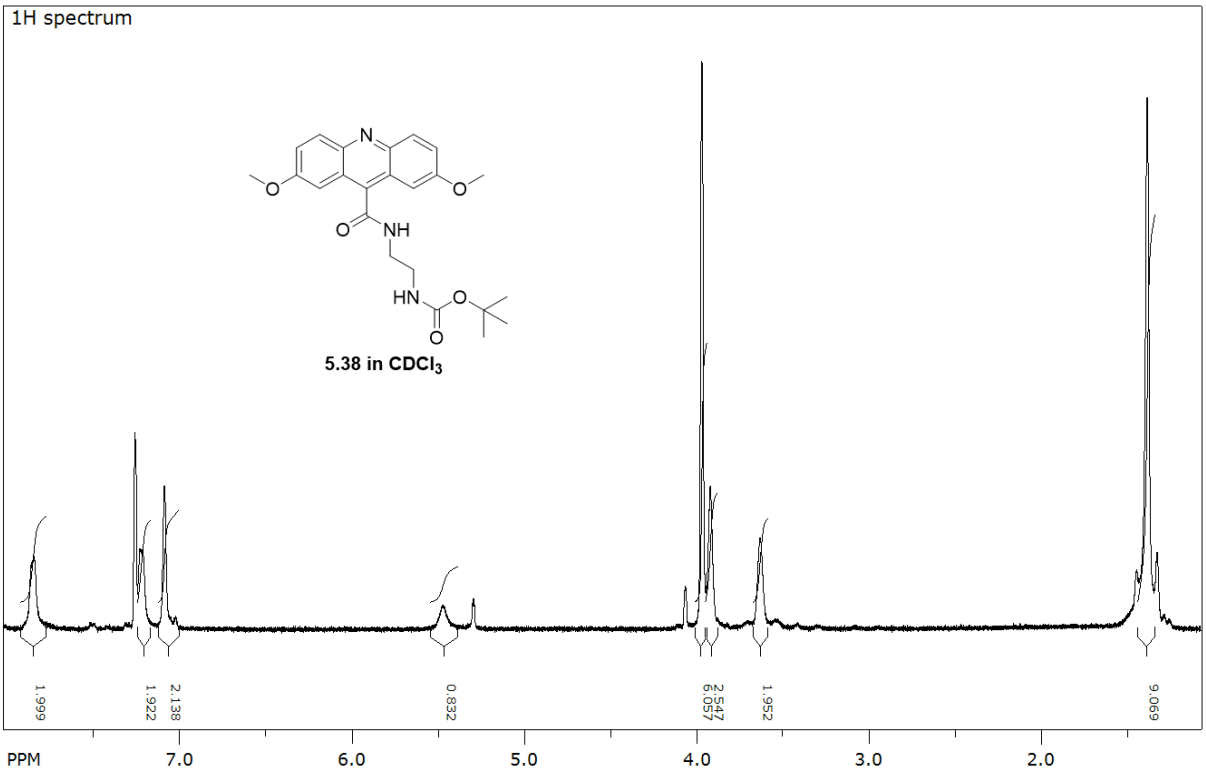
1H spectrum
N
O
O
NH
HN
O
O
O
5.38 in CDCl3
1.999
1.922
2.138
0.832
2.547
6.057
1.952
9.069
PPM
7.0
6.0
5.0
4.0
3.0
2.0

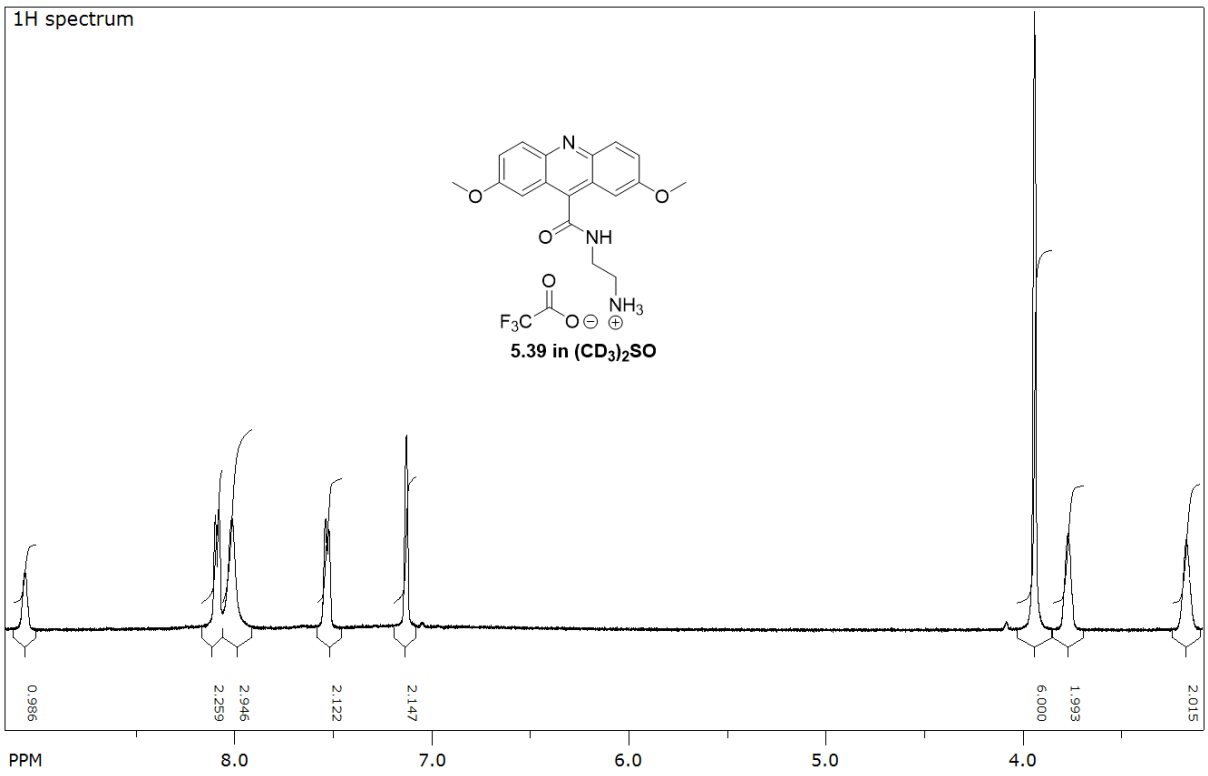
1H spectrum
N
O
O
NH
O
F3C
O
NH3
5.39 in (CD3)2SO
0.986
2.259
2.946
2.122
2.147
6.000
1.993
2.015
PPM
8.0
7.0
6.0
5.0
4.0

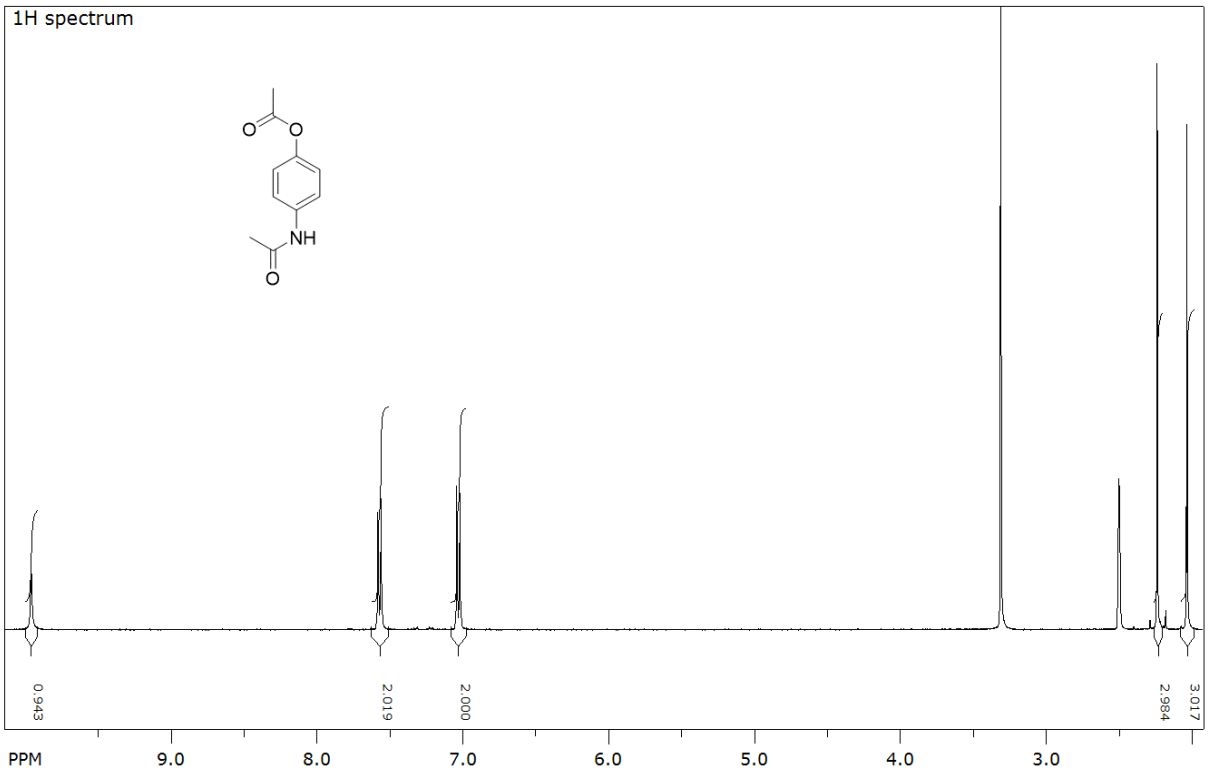
1H spectrum
O
O
NH
O
0.943
2.019
2.000
2.984
3.017
PPM
9.0
8.0
7.0
6.0
5.0
4.0
3.0